
About the specificity of epidural field potentials recorded with high-density multi-electrode arrays from the primary visual cortex

A thesis submitted in the fulfillment of the requirements for the degree of

Doctor of Natural Sciences (Dr. rer. nat)

by Benjamin Fischer

to the Faculty 2 (Biology/Chemistry) at the University of Bremen

August, 2020

Betreuer: *Dr. Detlef Wegener*

Erstgutachter: *Dr. Detlef Wegener*

Zweitgutachter: *Prof. Dr. Michael Koch*

Dissertationskolloquium: *30.10.2020*

s d g

Table of contents

1. Summary	1
1.1 Summary.....	1
1.2 Zusammenfassung.....	3
2. Preface	8
3. Introduction	12
3.1 The early visual system.....	12
3.1.1 Overview.....	12
3.1.2 Parallel pathways: retina and LGN.....	12
3.1.3 The primary visual cortex.....	15
3.1.4 Spatial scales of electrophysiological signals.....	18
3.1.5 Neuronal responses of V1 to visual stimulation.....	21
3.1.6 Visual attention in V1.....	26
3.2 Brain-Computer Interfaces.....	31
3.2.1 Data acquisition methods for BCIs.....	33
3.2.2 Visual BCI control based on exogenous and endogenous signals.....	40
3.2.3 Locked-In Syndrome.....	42
3.2.4 BCIs for the restoration of communication.....	43
3.3 Towards the objective of this thesis.....	46
4. General Materials and Methods	47
4.1 Legal permission.....	47
4.2 Subjects.....	47
4.3 Multi-electrode array.....	48
4.4 Surgical procedures.....	48
4.5 Recording chamber and monitor setup.....	50
4.6 Eye-tracking.....	50
4.7 Data acquisition.....	50
4.8 Receptive field mapping.....	51
4.9 General data processing.....	51
4.9.1 Preprocessing.....	51
4.9.2 Wavelet transformation.....	52
4.10 Receptive field analysis.....	52
4.10.1 Electrode selection.....	53
4.11 Support Vector Machines.....	53

5. Visual epidural field potentials possess high functional specificity in single trials.....	55
5.1 Abstract.....	56
5.2 New & Noteworthy.....	56
5.3 Introduction.....	57
5.4 Materials and Methods.....	59
5.4.1 <i>Subjects</i>	59
5.4.2 <i>Surgical Procedures</i>	59
5.4.3 <i>Data Acquisition</i>	60
5.4.4 <i>Visual Stimulation and Behavioral Task</i>	61
5.4.5 <i>Data Analysis</i>	63
5.4.6 <i>Experimental design and statistical analysis</i>	68
5.5 Results.....	68
5.5.1 <i>ERF Coverage of the Epidural Multielectrode Array</i>	69
5.5.2 <i>Time Course-Based Classification of Single Trials</i>	71
5.5.3 <i>Identification of Most Informative Features and Time Bins Across the Entire Array</i>	75
5.5.4 <i>Classification Performance for ROC-Based Feature Selection</i>	77
5.5.5 <i>Learning-Free Decoding and Implications for Future Development of Epidural Arrays</i>	80
5.6 Discussion.....	83
5.6.1 <i>Methodological and technical considerations</i>	83
5.6.2 <i>Functional Specificity of EFPs</i>	85
6. Modulation of epidural field potentials from macaque V1 evoked by stimulus size, shape and color.....	88
6.1 Abstract.....	89
6.2 Introduction.....	89
6.3 Materials and Methods.....	91
6.3.1 <i>Subjects</i>	91
6.3.2 <i>Data acquisition</i>	92
6.3.3 <i>Visual stimulation</i>	92
6.3.4 <i>Data preprocessing</i>	93
6.3.5 <i>Wavelet transformation</i>	93
6.3.6 <i>Electrode selection</i>	94
6.3.7 <i>Trial rejection</i>	94
6.3.8 <i>Statistics</i>	95
6.3.9 <i>Selection of most-informative signal features and position-selective electrodes</i>	96
6.3.10 <i>Support Vector Machine-based classification</i>	97
6.4 Results.....	98
6.4.1 <i>EFP responses evoked by stimulus size, shape and color</i>	98
6.4.2 <i>Classification of stimulus attributes from single-trial and trial-averaged EFP features</i>	106

6.5 Discussion.....	108
6.5.1 Stimulus size.....	109
6.5.2 Stimulus shape and shape-class.....	109
6.5.3 Stimulus color.....	110
6.5.4 Outlook.....	111
7. Preliminary results: Modulation of EFPs from macaque V1 evoked by stimulus contrast.....	113
7.1 Motivation.....	113
7.2 Materials and Methods.....	113
7.2.1 Subjects.....	113
7.2.2 Visual stimulation.....	113
7.2.3 Experiment 1 – Large area stimulation.....	114
7.2.4 Experiment 2 – Rapid local stimulation.....	115
7.2.5 Data preprocessing and wavelet transformation.....	115
7.2.6 Removal of electrodes and trials with artifactual high γ -activity.....	116
7.2.7 Data analysis.....	116
7.2.8 Statistics and measurement of correlation.....	119
7.3 Results.....	119
7.3.1 Experiment 1.....	119
7.3.2 Experiment 2.....	124
7.4 Discussion.....	127
7.4.1 Evoked broadband EFP modulations.....	128
7.4.2 The influence of stimulus contrast and luminance onto the EFP.....	128
7.4.3 Increased γ -power response with increasing stimulus contrast/luminance.....	129
7.4.4 Shorter response latencies with increasing stimulus contrast/luminance.....	130
7.4.5 Conclusion and outlook.....	130
8. Preliminary results: Attentional modulation of EFPs from V1, and correlation of EFPs and response time.....	131
8.1 Motivation.....	131
8.2 Materials and Methods.....	132
8.2.1 Subject.....	132
8.2.2 Visual stimulation.....	133
8.2.3 Task.....	134
8.2.4 Behavioral analysis.....	135
8.2.5 Preprocessing of EFPs.....	135
8.2.6 Electrode and trial rejection.....	135
8.2.7 Analysis of attention.....	136
8.2.8 Statistics.....	137
8.3 Results.....	137

8.3.1 Behavioral results.....	137
8.3.2 Attentional modulation of EFPs.....	138
8.3.3 Visual evoked EFP latencies correlate with RT.....	142
8.4 Discussion.....	145
9. Emphasizing the “positive” in positive reinforcement: using nonbinary rewarding for training monkeys on cognitive tasks.....	150
9.1 Abstract.....	151
9.2 New & Noteworthy.....	151
9.3 Introduction.....	152
9.4 Material and Methods.....	154
9.4.1 Subjects.....	154
9.4.2 Visual stimulation, reward schedule, and behavioral paradigms.....	155
9.4.3 Data analysis.....	158
9.5 Results.....	159
9.5.1 Example 1: Preventing high error rates.....	159
9.5.2 Example 2: Improving feedback and increasing alertness.....	164
9.5.3 Example 3: Teaching abstract cues.....	168
9.5.4 Example 4: Fine-shaping of behavior.....	171
9.6 Discussion.....	176
9.6.1 Potential and benefits of NB-PRT.....	177
9.6.2 Limitations and side aspects of NB-PRT.....	179
10. General conclusion and outlook.....	181
10.1 The specificity of EFPs.....	181
10.2 EFP modulation is correlated to behavior and spatial attention.....	182
10.3 Optimization of information decoding.....	182
10.4 Transfer to the human brain.....	183
10.5 Outlook.....	184
11. References.....	186
12. Appendix.....	211
12.1 Abbreviations.....	211
12.2 Danksagungen.....	214
Versicherung an Eides Statt.....	215
Erklärungen zur elektronischen Version und zur Überprüfung einer Dissertation.....	216
Hinweis über den Umfang der Überarbeitung der Dissertation.....	217

1. Summary

1.1 Summary

Superficial extracortical recordings of neuronal activity have gained interest in neuroscience, especially in the field of Brain-Computer Interfacing. High-density multi-electrode arrays have been developed to study brain functions and to investigate signals for Brain-Computer Interface (BCI) control. Subdural electrocorticography (ECoG) is more commonly used, while epidural recordings from the cortex are less present in research. Epidural field potentials (EFPs) promise high-quality electrophysiological data with high spatial resolution while being less invasive than ECoG. Only a few studies, however, have focused on the investigation of the information content of EFPs about cortical processes. In order to study the specificity of EFPs, the objective of this thesis has been to study the representation of sensory and cognitive information in epidural signals recorded with a high-density multi-electrode array. Therefore, a cortical area was targeted that is easily accessible with an epidural electrode array: the primary visual cortex (V1). V1 has a large exposed area and therefore enables the coverage with a high number of electrodes. In addition, visual stimulation evokes precise spatio-temporal cortical activation patterns in V1 that allow an association of cortical activity to visual information. The EFP from macaque V1 was recorded using high-density multi-electrode arrays to investigate its information content about visual stimulus attributes and cognitive processes.

The first study investigated to which degree the spatial location of a stimulus can be decoded from single-trial EFPs. The study is included as it was published previously [Fischer et al. 2019]. The peripheral visual field of monkeys fixating a central fixation square was rapidly stimulated with small visual stimuli at nine spatially close locations. Support Vector Machines (SVM) were utilized to identify the spatial location of the visual stimulation on a single-trial basis. Using a combination of different signal features, each extracted by a Receiver-Operator Characteristics (ROC) based method, as SVM input, led to classification

rates $> 95\%$. Furthermore, classification rates $> 90\%$ have also been achieved by using ROC-based features from the high γ -band without applying advanced Machine Learning techniques for the classification of single locations. These results provide evidence that the spatial cortical processing of V1 is well represented in high-density single-trial EFPs.

In the second study, the EFP modulation evoked by different stimulus attributes was investigated. While monkeys performed a fixation task, the periphery of the visual field was stimulated with small objects that differed in their position, size, shape and color. The previously established ROC-based feature extraction method was used to extract most informative features for each stimulus attribute which enable the differentiation between the categories of the stimulus attribute (e.g., to differentiate between different sized stimuli). Stimulus size and shape elicited significant differences in the mean γ -response recorded by the majority of electrodes. Stimuli consisting of the same but differently rotated geometrical shape caused a similar modulation of EFP transients. In addition, stimulus size and shape were classified with rates above chance level using EFP ROC-features. These results show that signals recorded with epidural electrodes are sensitive to changes in stimulus size and shape. The modulation of the EFP from V1 caused by small changes in the visual stimulation demonstrates the degree of detailed information that can be extracted from EFPs.

A third study was conducted to investigate the EFP response modulation caused by stimulus contrast. While the animals did a fixation task, either multiple equiluminant stimuli were flashed at once or the stimulus contrast of single stimuli within the stimulus display was changed sequentially. A higher stimulus contrast in the first stimulation procedure evoked shorter onset latencies and higher absolute mean amplitudes in the broadband EFP and the broadband γ -power response over all electrodes. Furthermore, γ -power peak amplitudes decreased for highest contrasts. The second stimulus procedure evoked higher γ -power amplitudes and shorter onset latencies for both EFP and γ -power in the signal of single electrodes with the rising magnitude of the increase in contrast. These results illustrate the sensitivity of epidurally recorded signals to stimulus contrast. In addition, the similarity of these results to intracortical studies point out the high accuracy of epidural signals and the precise imprint of neuronal activity in the γ -response of EFPs.

In the fourth electrophysiological study, a monkey performed covert spatial attentional shifts to single target stimuli within a multi-stimulus display. The monkey was trained to respond

fast to the luminance change at a cued target stimulus. Simultaneously, the EFP was recorded in V1. A small attentional modulation was found in the γ -band activity shortly before the luminance change of the target stimulus. Electrodes with a receptive field (RF) located close to the target stimulus showed higher γ -power when attention was focused onto the target. In contrast, electrodes with an RF located far from the target stimulus showed higher γ -power when attention was focused onto a distractor stimulus located far from the target stimulus. Additionally, the attentional modulation was highest when the delay in time between the cue onset and the target stimulus change onset was long or when the monkey responded fast. The same data was analyzed to investigate the relation between the evoked broadband EFP response post target change and the corresponding response time (RT) of the animal. Shorter EFP response latencies occurred when the monkey responded fast. These preliminary results demonstrate that the EFP recorded from V1 is modulated by visual spatial attention and correlates with behavior.

The fifth and last study is a methodological study regarding the training of macaque monkeys. A method called “non-binary positive reinforcement training” (NB-PRT) was developed. The study is included as published [Fischer & Wegener 2018]. In short, NB-PRT provides not only a reward for the desired behavior as in classical positive reinforcement training (PRT), but a reward of a smaller amount is given also for semi-optimal or even unwanted behavior. The study illustrates that monkeys adapt to the desired behavior while maximizing the received reward. Thereby, NB-PRT supports a high task confidence and the motivation of the animals because it offers an additional, more encouraging feedback for the monkey besides errors. Thus, NB-PRT can be considered as an additional component for PRT-based training protocols.

All in all, this thesis provides evidence for the specificity of high-density EFPs and provides a new effective strategy for training macaque monkeys in cognitive tasks.

1.2 Zusammenfassung

Im Bereich der Neurowissenschaften, insbesondere im Themenfeld des Brain-Computer Interfacings, haben Aufnahmen der neuronalen Aktivität der Oberfläche des Kortex an Interesse gewonnen. Für die Untersuchung von Gehirnfunktionen und von Signalen zur

Steuerung von Brain-Computer Interfaces (BCIs) wurden Multielektrodenarrays mit hoher Elektrodendichte entwickelt. Während häufiger subdurale Elektrokortikographie (ECoG) genutzt wird, sind epidurale Aufnahmen vom Kortex in der Forschung weniger präsent. Epidurale Feldpotentiale (EFPs) verheißen hochqualitative elektrophysiologische Daten mit hoher räumlicher Auflösung bei einer geringeren Invasivität im Vergleich zum ECoG. Jedoch haben nur wenige Studien den Informationsgehalt der EFPs über kortikale Prozesse untersucht. Das Ziel dieser Dissertation war es, die Repräsentation sensorischer und kognitiver Informationen in epiduralen Aufnahmen mit hoher räumlicher Auflösung zu untersuchen, um damit die Spezifität des EFPs zu charakterisieren. Aus diesem Grund wurde ein kortikales Areal untersucht, welches leicht zugänglich für ein epidurales Elektrodenarray ist: der primäre visuelle Kortex (V1). Dieser weist eine große, offenliegende Fläche auf, welche eine Abdeckung mit vielen Elektroden ermöglicht. Zudem evoziert visuelle Stimulation präzise raumzeitliche Muster kortikaler Aktivität in V1, welche die Assoziation von kortikaler Aktivität und visueller Information ermöglichen. Das EFP von V1 von Makakenaffen wurde mit Hilfe von Multielektrodenarrays mit hoher Elektrodendichte aufgenommen, um dessen informativen Gehalt über visuelle Stimulusattribute und kognitive Prozesse zu untersuchen.

In der ersten Studie wurde untersucht, in welchem Maß die räumliche Position eines Stimulus aus dem EFP einzelner Präsentationsdurchläufe dekodiert werden kann. Die Studie ist so, wie sie publiziert wurde [Fischer et al. 2019], in der Dissertation dokumentiert. Das periphere visuelle Feld von Makaken, die einen zentralen Punkt fixierten, wurde rasch mit kleinen visuellen Stimuli an neun räumlich nah beieinanderliegenden Positionen stimuliert. Mit Hilfe von Support Vector Maschinen (SVMs) wurde die Identifizierbarkeit der räumlichen Position auf Basis einzelner Präsentationsdurchläufe untersucht. Höchst informative Signalmerkmale wurden mit Hilfe eines Verfahrens basierend auf der Operationscharakteristik eines Beobachters (ROC) extrahiert. Wenn Kombinationen dieser Merkmale als SVM Input genutzt wurden, führte dies zu Klassifikationsraten $> 95\%$. Des Weiteren wurden durch die Nutzung von ROC-basierten Merkmalen des hohen γ -Frequenzbandes und ohne die Nutzung von fortschrittlichen Klassifikationsverfahren des maschinellen Lernens Klassifikationsraten $> 90\%$ für einzelne räumliche Positionen erzielt. Zusammengefasst belegen die Ergebnisse, dass die räumlich kortikale Verarbeitung von V1 gut im hochauflösendem EFP einzelner Präsentationsdurchläufe abgebildet wird.

In der zweiten Studie wurde die EFP Modulation, welche von verschiedenen visuellen Reizen evoziert wurde, untersucht. Während die Tiere eine Fixationsaufgabe ausführten, wurde die Peripherie des visuellen Feldes mit Objekten stimuliert, die sich in ihrer Position, Größe, Form und Farbe unterschieden. Das zuvor etablierte ROC-basierte Merkmalsextraktionsverfahren wurde genutzt, um Merkmale mit höchstem Informationsgehalt für jedes Stimulusattribut zu extrahieren, welche die Unterscheidung zwischen den Kategorien eines Attributes ermöglichen (z.B. die Unterscheidung zwischen unterschiedlich großen Stimuli). Bei einem Großteil der Elektroden riefen Stimulusgröße und -form signifikante Unterschiede in der mittleren γ -Antwort hervor. Stimuli der selben Form, die jedoch verschiedentlich gedreht waren, evozierten ähnliche Modulationen der transienten EFP Antwort. Zudem konnte die Stimulusgröße und -form mit höheren Klassifikationsraten als die Zufallswahrscheinlichkeit aus ROC-basierten Signalmerkmalen des EFP klassifiziert werden. Diese Ergebnisse zeigen, dass Signale, die durch epidurale Elektroden aufgenommen wurden, empfindlich für die Änderung in Stimulusgröße und -form sind. Die durch kleine Änderungen in der visuellen Stimulation verursachten Modulationen des EFPs demonstrieren den Grad an detaillierter Information, die aus dem EFP extrahiert werden kann.

Eine dritte Studie wurde durchgeführt, um die Modulation der EFP-Antwort durch den Stimuluskontrast zu untersuchen. Während die Makakenaffen eine Fixationsaufgabe durchführten, wurden entweder mehrere equiluminante Stimuli gleichzeitig aufgeleuchtet oder der Stimuluskontrast einzelner Stimuli des Stimulusdisplays wurde sequenziell verändert. Die Analyse der Signale, die durch die erste Stimulationsprozedur evoziert wurden, zeigte, dass ein höherer Objektkontrast kürzere Latenzen und höhere absolute mittlere Amplituden der Signalantwort im Breitband-EFP und der Energie im Breitband γ -Energie über alle Elektroden evozierte. Des Weiteren sank die Maximalamplitude der γ -Energie bei den höchsten Kontraststufen. Die zweite Stimulationsprozedur evozierte mit steigender Magnitude der Kontrasterhöhung höhere γ -Energie und ein früheres Auftreten der Signalantwort im EFP und der γ -Energie im Signal einzelner Elektroden. Die Ergebnisse veranschaulichen die Empfindlichkeit epidural aufgenommener Signale gegenüber dem Stimuluskontrast. Die Ähnlichkeit der Ergebnisse zu intrakortikalen Studien zeigt die hohe Genauigkeit epiduraler Signale und den präzisen Abdruck neuronaler Aktivität in der γ -Antwort des EFPs.

In der vierten elektrophysiologischen Studie richtete ein Affe seine verdeckte räumliche Aufmerksamkeit auf einzelne Zielstimuli eines Multistimulusdisplays aus. Der Affe war darauf trainiert, rasch auf die Luminanzänderung am Zielstimulus, der zuvor durch einen Hinweisreiz angegeben wurde, zu reagieren. Gleichzeitig wurde das EFP in V1 aufgenommen. Es wurde kurz vor der Luminanzänderung des Zielbuchstabens eine kleine aufmerksamkeitsbedingte Modulation der Aktivität im γ -Band gefunden. Elektroden, deren rezeptives Feld (RF) nah am Zielstimulus lag, zeigten eine erhöhte γ -Energie, wenn die Aufmerksamkeit auf den Zielstimulus gerichtet war. Im Gegensatz dazu zeigten Elektroden, deren RF weit entfernt vom Zielbuchstaben lag, erhöhte γ -Energie, wenn die Aufmerksamkeit auf einen Distraktorstimulus fokussiert wurde, der weit entfernt vom Zielstimulus lag. Zusätzlich war die Aufmerksamkeitsmodulation am Größten, wenn die Zeitverzögerung zwischen dem Auftreten des Hinweisreizes und dem Auftreten der Änderung am Zielstimulus groß war oder wenn der Affe schnell reagierte. Die selben Daten wurden im Hinblick auf den Zusammenhang zwischen der evozierten Breitband-EFP Antwort nach der Zielstimulusänderung und der dazugehörigen Reaktionszeit (RT) des Tieres untersucht. Kürzere EFP Antwortlatenzen traten auf, wenn der Affe schnell reagierte. Diese vorläufigen Ergebnisse demonstrieren, dass das EFP, welches von V1 aufgenommen wurde, durch visuelle räumliche Aufmerksamkeit moduliert wird und mit Verhalten korreliert.

Die fünfte und letzte Studie ist eine methodische Studie, die sich mit dem Training von Makakenaffen befasst. In diesem Rahmen entstand eine Methode namens „Nicht-binäres positiv verstärkendes Training“ (NB-PRT). Die Studie ist so, wie sie publiziert worden ist [Fischer & Wegener 2018], in der Dissertation enthalten. Verkürzt dargestellt, gibt NB-PRT eine Belohnung nicht nur beim gewünschten Verhalten wie im klassischen positiv verstärkendem Training (PRT), sondern gibt eine kleinere Belohnung auch bei suboptimalem oder auch bei nicht gewünschtem Verhalten. Die Studie zeigt, dass Affen ihr Verhalten dem gewünschten Verhalten anpassen, während sie zugleich die erhaltene Belohnung maximieren. Dabei wird eine hohe Aufgabensicherheit und die Motivation des Tieres gefördert, da den Affen neben Fehlern ein zusätzliches, ermutigenderes Feedback geboten wird. Daher kann NB-PRT als eine zusätzliche Komponente des PRT-basierten Trainings betrachtet werden.

1.2 Zusammenfassung

Zusammengefasst liefert diese Dissertation Beweise für die Spezifität von hochauflösendem EFP und stellt eine neue effektive Strategie für das Training kognitiver Aufgaben von Makakenaffen zur Verfügung.

2. Preface

Decades of neuroscientific research have led to a broader understanding of the anatomy and the physiology of the brain. This knowledge has given insight into the functionality of the healthy and the pathological brain. For scientific investigations and the application of clinical procedures based on the brain's functionality, superficial extracortical recordings have become an important tool. A common way to record superficial extracortical activity is to use surface electrodes which are placed on top of the cortical tissue below the dura mater, usually denoted as ECoG. Due to the fact that ECoG is less invasive than intracortical recordings and provides a higher spatial resolution than electroencephalography (EEG), it enables meso-invasive large-scale cortical recordings (as reviewed in [Parvizi & Kastner 2018; Schalk & Leuthardt 2011]). The spatial resolution of ECoG recordings mainly depends on the electrode density. The inter-electrode distance of clinically used and commercially available electrode stripes and arrays is usually 1 cm (low-density arrays) [Lesser et al. 2010]. In clinical settings, subdural low-density arrays have become a standard tool for the invasive detection of epileptogenic zones [Enatsu & Mikuni 2016; Penfield & Jaspers 1954; Yang et al. 2014] and for electrical stimulation mapping [Ritaccio et al. 2018]. Lately, multi-electrode arrays with smaller inter-electrode distance in comparison to low-density arrays were developed predominantly for scientific research (high-density arrays) [Shokouejad et al. 2019]. Despite the advantages resulting from their higher spatial resolution, high-density arrays are sparsely used for clinical applications [Shokouejad et al. 2019].

In recent years, studies have also investigated whether ECoG enables BCI control [Schalk & Leuthardt 2011]. BCIs are developed to restore communication and motor functions of paralyzed patients [Birbaumer 2006; Birbaumer & Cohen 2007]. A BCI gets input from a neuronal signal source (e.g., ECoG) and converts it into meaningful actions [Wolpaw et al. 2002]. Therefore, BCI research aims to identify cortical activity evoked by intrinsic or extrinsic processes that can be precisely extracted from single-trial recordings. In the best case, a BCI user is able to modulate his cortical activity, which is translated into a command that executes an action of a computer or a machine. The accuracy of BCI control increases utilizing ECoG instead of EEG [Grazimann et al. 2005]. Interestingly, ECoG-based BCIs

benefit from a higher spatial resolution of ECoG recordings because the decoding performance increases with an increase in electrode density of the multi-electrode array [Hermiz et al. 2018; Wang et al. 2016]. Despite the benefits of high-density multi-electrode arrays for BCI accuracy, many ECoG-based studies are based on clinical electrode arrays because most human subjects are patients undergoing a clinical procedure [Hill et al. 2012; Parvizi & Kastner 2018].

Apart from the advantages that ECoG offers for BCI applications, a major issue for a long-term application of ECoG is the risk resulting from the implantation. Postoperative infections occurred in ~8% of patients that were subdurally implanted for a long-term treatment of epileptic seizures [Bergey et al. 2015; Cook et al. 2013]. A less invasive approach which could alleviate these complications is the recording of the EFP from the top of the dura. The application of long-term epidural electrodes resulted in less complications like infections in comparison to the application of long-term subdural electrodes (for an overview, see Table 1 in [Shimoda et al. 2012]). EFPs and ECoG recorded with clinical standard electrode arrays were found to possess similar signal quality [Bundy et al. 2014]. Regrettably, when using high-density arrays, EFPs have been found to have a lower signal quality in comparison to ECoG [Bundy et al. 2014]. Nevertheless, high-density EFPs could still hold specific information about cortical processing. This assumption is underlined by recent studies decoding movement-related parameters from high-density EFPs recorded from the motor and sensorimotor cortex (e.g., [Farrokhi & Erfanian 2018; Flint et al. 2012, 2017; Marathe & Taylor 2013; Shimoda et al. 2012; Slutzky et al. 2011]). The decoding was predominantly based on features which were averaged over long periods of time. As a matter of fact, this procedure impedes a detailed investigation of the temporal modulation of EFP activity. In addition, some studies applied advanced signal filtering methods onto EFP leading to signal features that do not allow for a direct interpretation of the original EFP signal. Thus, many of these studies provide only limited insight into the specificity of high-density EFP activity. Besides the effort in motor-related cortical areas (for a review, see [Slutzky & Flint 2017]), there is marginal knowledge about the specificity of EFP from other cortical areas. Thus, despite of the ability to decode information from predominantly motor-related EFPs, little is known about the specificity of high-density EFPs and whether they contain precise information about the underlying cortical processes.

In this thesis, I investigated EFPs recorded with high-density multi-electrode arrays from the macaque cortex. The objective was to investigate the specificity of high-density EFPs by studying the information content extractable from epidurally recorded cortical activity. A special focus is the decoding of information from single trials because, if possible, EFP would not only be an alternative for scientific research but also for innovative online BCI applications.

To cope with the purpose of investigation, V1 was chosen as the target area for EFP recordings. Macaque V1 can be easily accessed with multi-electrode arrays because large parts of it are exposed on the cortical surface [Blasdel & Campbell 2001]. The large exposed area also enables a coverage with a high number of electrodes. Moreover, V1 is suitable for the purpose of investigation because of the well-controllable cortical activation. This is mainly due to the retinotopic architecture of V1 [Tootell et al. 1988], meaning that input from neighboring locations in the visual field is processed by neighboring neural populations. Despite the specific spatial cortical processing in V1, neurons located in V1 are responsive to a variety of extrinsic influences, such as features of visual stimuli (e.g., [Lashgari et al. 2012]), and intrinsic influences like visual attention (for a review, see [Posner & Gilbert 1999]). Finally, previous studies using penetrating electrodes have investigated V1 extensively (for a review [Carandini et al. 2005; Posner & Gilbert 1999]) which enables the comparison of EFPs from V1 to a variety of intracortical studies. This thesis makes use of the properties of V1 to investigate how different sensory, attentional and behavioral states modulate cortical activity recorded by epidural electrodes. Single-trial and trial-averaged epidural activity was studied to investigate the specificity, robustness and reliability of EFPs.

This thesis is structured into four main parts:

- An introduction (Chapter 3), containing a general overview about the main topics, aspects and the corresponding literature associated with the research question of this thesis.
- A methodological section (Chapter 4), which explains and introduces methods that are commonly used in the following chapters to prohibit a redundancy of methodological descriptions.

- Chapters 5-9 contain the experimental results including two research papers and a draft of a paper manuscript. Due to the different formats of the chapters, they are structured differently.
 - ♦ Chapter 5: The retinotopic organization of V1 enables the investigation of spatial activity patterns in EFPs. A study investigating the possibility to decode the spatial location of visual stimulation based on single-trial EFPs from V1 is reported in this chapter. The study has been previously published and is documented as published [Fischer et al. 2019].
 - ♦ Chapter 6 and 7: Two studies investigating whether stimulus size, shape, and color (Chapter 6) or stimulus contrast (Chapter 7) systematically modulate visually evoked EFPs from V1 are reported. Chapter 6 is prepared as a paper manuscript.
 - ♦ Chapter 8: The attentional modulation of EFPs recorded from V1 evoked by covert spatial attention is investigated in this chapter. In addition, the relation of task-relevant visually evoked EFP modulations and the response time of the monkeys is studied.
 - ♦ Chapter 9: While humans can be instructed directly, monkeys need to be trained over many weeks or even months in small steps to perform a sophisticated task (such as the task necessary for Chapter 8). Hence, an effective animal training is highly relevant for the successful conduction of research studies that are based on the behavior of animals. To optimize macaque training in cognitive tasks, this chapter introduces a new training method which maintains the task confidence and a high motivation of the animals while they learn the new, desired behavior. The study has been previously published and is documented as published [Fischer & Wegener 2018].
- Chapter 10 provides a general conclusion that summarizes and brings together the main findings from Chapters 5-9.

3. Introduction

3.1 The early visual system

3.1.1 Overview

Before visual information is processed by a manifold of cortical areas, the vast majority of visual information is transferred from the retina via the lateral geniculate nucleus (LGN) to V1 [Callaway 2005]. The information is kept in parallel pathways containing different kinds of visual information [Dacey 2000]. This separated projection of visual information influences the processing of visual information in V1, which is the targeted cortical area of this thesis. For a better understanding of the functional architecture of V1, I introduce the routing of visual information from the retina to the LGN in the next section.

3.1.2 Parallel pathways: retina and LGN

Parallel processing starts as soon as the light meets the retina. The retina contains two different types of photoreceptors: cones and rods. While rods are not sensitive to the wavelength of light, cones can be divided into three wavelength-sensitive classes: short-, medium- and long-wavelength cones [Jacobs 2008; Wässle 2004]. In the case of a photon activating a photoreceptor, a change in membrane potential occurs which is passed onto postsynaptic neuronal cells by a decrease of the synaptic transmission of neurotransmitters [Sung & Chuang 2010; Wässle 2004; Yau & Hardie 2009]. This signal converges from the photoreceptors via diverse neuronal cell types (horizontal, bipolar and amacrine cells) onto ganglion cells [Wässle 2004], where the change in membrane potential is translated into action potentials. The amount of cells carrying the visual signal decreases by a factor of ~ 110 when comparing the number of photoreceptors and the number of ganglion cells [Barlow 1981]. During the convergence of the signal, visual information is separated because the signal of different assemblies of photoreceptors is projected onto distinct types of ganglion

cells [Dacey 2000; Wässle 2004]. While there are various ganglion cell types projecting to the LGN [Dacey et al. 2003], the three most prominent types of ganglion cells are [Callaway 2005; Dacey 2000]:

- midget ganglion cells, carrying red/green color-opponent information [Gouras 1968],
- parasol ganglion cells, carrying broadband achromatic information [Kaplan & Shapley 1986],
- and bistratified ganglion cells, carrying blue/yellow color-opponent information [Dacey & Lee 1994].

These ganglion cell types also differ in their morphology, RF characteristics and response properties to various stimulus features (for reviews, see [Dacey 2000; Nassi & Callaway 2009; Schiller 2010]).

From the three ganglion cell types, three separate visual pathways emerge: the parvocellular, magnocellular and koniocellular pathway (P-, M- and K-pathway) [Callaway 2005]. Ganglion cells belonging to a pathway project into specific layers of the LGN:

- The P-pathway is formed by midget ganglion cells projecting into the parvocellular layers of the LGN (layer 1 and 2) [Michael 1988; Perry et al. 1984].
- The M-pathway is formed by parasol ganglion cells projecting into the magnocellular layers of the LGN (layer 3 to 6) [Michael 1988; Perry et al. 1984].
- The K-pathway is formed by bistratified ganglion cells projecting both in between LGN layers (intercalated layers) and into LGN layers ([Hendry & Yoshioka 1994], for a review, see [Hendry & Reid 2000]).

The proportion of retinal ganglion cell types projecting to the LGN are 70% midget, 10% parasol and 8% bistratified ganglion cells [Nassi & Callaway 2009].

LGN neurons have differently structured RFs [Reid & Shapley 2002]. Historically, two concepts regarding the visual RF arose from different experimental procedures. The classical visual RF of a neuron was predominantly mapped by visual stimulation of the retina and simultaneous recording of the neuronal activity of the targeted cell [Spillmann 2014]. The stimulated area evoking a response in the target neuron was defined as the visual RF (for a review, see [Spillmann 2014]). In contrast, the extra-classical RF describes a region larger

than the classical RF. Stimulation within this region does not generate action potentials but modulates the neuronal response evoked by stimulation in the classical RF (for reviews, see [Jeffries et al. 2014; Spillmann et al. 2015]). Ganglion cells and postsynaptic connected LGN cells have similar classical RFs and response characteristics [Cleland & Lee 1985]. The classical RF of LGN M-cells, which receive non-chromatic input signals from parasol ganglion cells, is structured as on-center and off-center RF [Lee 1996]. The area of these RFs can be divided into a center and a surround [Hubel & Wiesel 1961; Wiesel & Hubel 1966]: An on-center RF is organized such that light emitted onto the center of the RF will lead to an excitation and light emitted onto the surround will lead to an inhibition of the ganglion cell, while the opposite is the case for off-center RFs. The classical RF of LGN cells receiving color-opponent input has either a center and surround structure (Type I) or none (Type II) [Lee 1996; Reid & Shapley 1992; Wiesel & Hubel 1966]: Considering a Type I RF, a certain wavelength leads to an excitation of the cell when emitted to the center, while another wavelength leads to an inhibition when emitted to the surround. Type II RFs are also excited and inhibited by different wavelengths but the response is independent of the spatial location of light emission.

Before projecting into the LGN, the two optical nerves containing the axons of ganglion cells cross in the optic chiasm [Hubel & Wiesel 1977]. Axons from the right and left half of the retina are separated in the optic chiasm, leading to nerves containing only information from one side of the visual field [Hubel & Wiesel 1977]. For example, light coming from the left side of an object which is centered in the visual field is seen on the right half of the retina of each eye. The side-separated nerves project to the LGN ipsilateral to the retinal representation, thus the contralateral visual field is represented in each of the bilateral LGN [Hubel & Wiesel 1977]. Each LGN layer gets input from a single eye and the input of the retina into the LGN is arranged in a way that the spatial topography of the retina is maintained in each layer of the LGN [Kaas et al. 1972], which is called retinotopy.

From the LGN, the visual signal is projected into V1. As part of the neocortex, V1 consists of six vertically arranged layers differing in cell types and density [Brodman 1909]. Layer 4 of V1 is divided into four sub-layers (4A, 4B, 4C α and 4C β) varying in their input and output connections [Lund 1988]. Neurons of the LGN project to different V1 layers:

- magnocellular neurons of the LGN (M-pathway) project into layer 4C α and 6 of V1 [Henderickson et al. 1978; Hubel & Wiesel 1972],
- parvocellular neurons of the LGN (P-pathway) project to layer 4A, 4C β and 6 of V1 [Henderickson et al. 1978; Hubel & Wiesel 1972]
- and K-pathway neurons of the LGN project into layer 1 and 2/3 of V1 [Hendry & Reid 2000; Hendry & Yoshioka 1994].

This structured parallel projection of visual information shapes the functional architecture of V1, thereby defining its spatially structured response to visual stimulation. The functional architecture of V1 and its differentiated response patterns to different stimulus features are described in the next sections (Chapters 3.1.3 and 3.1.5).

3.1.3 The primary visual cortex

As it receives the main visual information output from the LGN, V1 is the first cortical stage of visual processing [Nassi & Callaway 2009]. The amount of neurons increases by a factor of > 130 from the LGN to V1 in macaque monkeys [Chow et al. 1950], causing a divergence of visual information. Macaque V1 has a size of $\sim 1,200$ mm², half of which is exposed on the brain's surface [Blasdel & Campbell 2001]. In contrast, only a small proportion of V1 is exposed on the surface of the human brain [Van Essen et al. 2001]. The representation of the visual field is similar in V1 and LGN: The left visual field is represented in V1 of the right hemisphere and vice versa [Hubel & Wiesel 1977]. The anterior part of V1 of each hemisphere represents the lower quadrant and the posterior part represents the upper quadrant of the visual field [Tootell et al. 1988]. Similar to the LGN, V1 has a retinotopic functional architecture [Tootell et al. 1988; Wandell et al. 2007]. Not every part of the visual field, however, is represented by the same amount of neurons. With greater distance from the spatial representation of the fovea, the visual field is represented by a smaller volume of cortical tissue [Daniel & Whitteridge 1961; Hubel & Wiesel 1974b]. This phenomenon, called cortical magnification, is likely to be the consequence of the high ganglion cell density in the fovea of the retina [Wässle et al. 1990]. Furthermore, the RF size of neurons gets larger with an increasing RF eccentricity from the fovea [Hubel & Wiesel 1974b].

As the RF of LGN ganglion cells, the RF of V1 neurons is divided into a classical and an extra-classical RF. Two cell type can be characterized in V1 by the response properties of their classical RF: simple and complex cells [Hubel & Wiesel 1962, 1968]. The classical RF of simple cells is divided into a center and a surround: Light emission onto the center increases the activity of the neuron while light emission onto the surround leads to a decrease in the activity of the neuron or vice versa [Hubel & Wiesel 1962, 1968]. In contrast, the classical RF of complex cells cannot be divided into an excitatory or inhibitory region [Hubel & Wiesel 1962, 1968]. Both simple and complex cells can be end-stopping, which means that a stimulus larger than the classical RF inhibits the evoked response (for a review, see [Spillmann 2014]). As for LGN neurons, the activity evoked by the stimulation of the classical RF of V1 neurons is also modulated by the stimulation of the extra-classical RF which is much larger than the classical RF (for a review, see [Spillmann et al. 2015]).

As a result of the retinotopy and the structured projections from the LGN, different properties of visual information are processed in segregated neuronal populations which are arranged spatially within V1 (which is referred to as “maps”). V1 maps of ocular dominance, orientation, color and spatial frequency are well studied.

- *Ocular Dominance*: Many neurons in layer 4 of V1 are only responsive to signals from one eye [Hubel & Wiesel 1968]. This single-eye dominance is organized in alternating stripes over the surface of V1 [Hubel & Wiesel 1972; LeVay et al. 1975, 1985]. The stripes emerge from the ordered LGN input into V1 because the different layers of the LGN receive input from a single eye in an alternating sequence [Hubel & Wiesel 1972]. Such a stripe has a thickness of $\sim 400 \mu\text{m}$ in the macaque monkey [Hubel et al. 1977; Hubel & Wiesel 1977]. Maps of ocular dominance are most prominent in layer 4 of V1 but are also present in other layers [Hubel & Wiesel 1972].
- *Orientation*: Orientation maps emerge from populations of cells with the same orientation tuning. Orientation-selective neurons show an increased response to a visual stimulus with a certain orientation in comparison to stimuli with other orientations [Hubel & Wiesel 1962, 1968, 1974a]. These neurons are arranged in local orientation columns which were named pinwheels because of their distinct organization [Bartfeld & Grinvald 1992; Bonhoeffer & Grinvald 1991]: Within a pinwheel, which includes all orientation preferences, neurons with a similar

- orientation preference are located close to each other and are arranged circularly around a center. Neurons with orthogonal orientation preference lie on opposing sites from the center of the pinwheel. In the primate brain, the change of the preferred orientation within the pinwheel was found to be smooth [Bartfeld & Grinvald 1992]. Orientation-selective cells are found in all layers of V1 [Ringach et al. 2002].
- *Color*: Color maps arise from color selective but poorly orientation-selective cells in the superficial layers of V1 [Livingstone & Hubel 1984]. They have been discovered by using the enzyme cytochrome oxidase. Regions showing a dense staining are called cytochrome oxidase blobs (size $\sim 0.3\text{-}0.7\text{ mm}^2$, depending on the distance to the fovea, [Livingstone & Hubel 1984]). Recently, an alternative color map in primate V1 was found. These so called “hue maps” are represented by a cortical area with a diameter of $\sim 160\text{ }\mu\text{m}$ [Xiao et al. 2007]. Within such a map, different spatial activity patterns were found for a visual stimulation with objects that were shown at the same spatial location but differed in their hue value. These hue-wise spatial activation patterns overlap to a large extent. The authors of this study argued that hue maps possibly overlap with blobs.
 - *Spatial frequency*: Neurons in V1 were found to selectively respond to certain spatial frequencies [Bredfeldt & Ringach 2002; De Valois et al. 1982]. This selectivity is spatially organized in V1: spatial frequency maps were found to intersect orthogonally with orientation maps [Nauhaus et al. 2012] and neurons with a preference for low spatial frequencies cluster at the center of blobs [Silverman et al. 1989].

Besides these, V1 neurons of non-human primates process a variety of other visual properties, for example, spatial phase tuning [Aronov et al. 2003], motion direction [Dow 1974; Lu et al. 2010] and disparity [Poggio & Fischer 1977]. These were, however, not described as being spatially and functionally arranged in maps yet.

V1 maps do not only overlap but are also arranged in dependence of each other. While blobs and orientation pinwheels are distributed independently from each other, they are both centered on the mid-line of the ocular dominance stripes [Bartfeld & Grinvald 1992]. Furthermore, the found topography of orientation and spatial frequency maps is maintained between neighboring cells showing slight differences in their response preference [DeAngelis

et al. 1999]. The same study found RF characteristics of neighboring cells to be similar, but not equal. These findings indicate a smooth functional topography of V1 at the level of neighboring cells rather than a patchy functional topography of neuronal populations containing neurons with similar response properties.

The spatial arrangement of V1 maps leads to a modular organization of its response properties. Therefore, small units of the cortical area of V1, representing a small part of the visual field, process a manifold of visual features [Hubel & Wiesel 1977; Livingstone & Hubel 1984]. A cortical region containing a full set (180°) of orientation-selective neuronal populations, one left and one right ocular dominance stripe and blobs is called a hypercolumn [Hubel & Wiesel 1974b; Livingstone & Hubel 1984]. While the functional importance of the columnar organization of V1 is debatable [Horton & Adams 2005; Landisman & Ts'o 2002], the structure of hypercolumns reflects the local arrangement of V1 maps.

V1 channels the signals coming from different pathways to other brain areas. Three main informational streams are projected: motion, form and color [Livingstone & Hubel 1988]. V1 projects signals from the blobs (color information) to the thin stripes and inter-blob signals (form information) into the pale stripes of the secondary visual cortex (V2; for a review, see [Sincich & Horton 2005]). In addition, motion information is projected directly and also via the thick stripes of V2 to the middle temporal visual area (MT) [Sincich & Horton 2005; Yabuta et al. 2001]. From this separated projection of visual information, two different streams of visual information processing diverge: the dorsal (how) and the ventral (what) stream, described by Goodale and Milner [1992]. They propose that the ventral stream processes and identifies objects (color and form information), while the dorsal stream mediates visually guided actions (motion information). It is important to note that these two streams are not an extension of the parallel projections from the retina via LGN to V1, because they receive mixed inputs from the parallel sub-cortical pathways [Merigan & Maunsell 1993].

3.1.4 Spatial scales of electrophysiological signals

Before approaching to a detailed description of how V1 neurons respond to visual stimulation, this section summarizes main techniques for recording electrophysiological signals and electrophysiological signal types for a better understanding of the findings

reported in the following chapters. The emphasis is laid on extracellular electrophysiological measurements, because this type of recording was used in the experiments reported later.

Electrophysiological recordings measure the electrical activity produced by physiological processes in the body [Buzsáki et al. 2012]. The electrical potential (or voltage) is measured as the difference between a recording and a reference electrode. All extracellular electrophysiological measurements have high temporal resolution in comparison to brain imaging methods like functional magnet resonance imaging (fMRI) [Fukushima et al. 2015]. Electrophysiological measurements can be realized on different spatial scales [Lewis et al. 2015]. I use the term spatial scale in this thesis to denote the distance between an electrode and the source of the recorded signal (i.e., neurons): A low spatial scale indicates recordings performed near to, and a high spatial scale indicates recordings performed far from the actual signal source. Due to the fact that there are multiple layers of tissue covering the cortex, the location of the electrode within these layers influences the spatial scale. The main tissues covering the brain are the dura mater, the skull and the scalp.

Extracellular electrophysiological recordings are conducted by inserting thin electrodes into the cortical tissue. As a result, the activity of single cells or assemblies of cells is recorded. Different kinds of information can be obtained from intracortical recordings by filtering the signal. Usually, a frequency of ~300 Hz is used to create a high-pass and a low-pass filter [Logothetis 2003]. When using a high-pass filter, action potentials (spiking activity) are extracted [Logothetis 2003]. Different spike clustering methods are available to isolate the spiking activity of single units (single unit activity, SUA) [Lewicki 1998; Zhang et al. 2018]. The spiking activity of multiple neurons is called multi unit activity (MUA). Recently, a method for extracting MUA without clustering or thresholding has been introduced [Drebitz et al. 2019; Supèr & Roelfsema 2005]. Alternatively, a low-pass filter can be applied to obtain the local field potential (LFP) [Logothetis 2003]. The LFP is the summed extracellular potential from the cells surrounding the electrode which is caused by a manifold of processes like synaptic activity, spikes and intrinsic currents [Buzsáki et al. 2012]. While spikes are a precise measure of neuronal activity, the LFP is useful for investigating current changes in the extracellular medium caused by a neuronal population. The LFP (and spiking activity, depending on the size of the electrode; for a further discussion, see Chapter 3.2.1.1) can also be recorded from subdural and epidural electrodes. For subdural recordings, electrodes are

placed on top of the cortex, while electrodes are placed on top of the dura for epidural recordings. The difference between those measures is caused by the additional thin layer of tissue (dura mater, ~ 0.5 mm [Galashan et al. 2011]), which is passed by the signal before it is recorded by an epidural electrode [Moran 2010]. Besides these invasive measures, surface electrodes are placed on top of the scalp to record EEG. The multiple layers of tissue between scalp electrodes and the signal source act as capacitive-resistant membrane and, thereby, low-pass filter the signal [Nunez & Srinivasan 2006]. Thus, frequencies above 100 Hz are attenuated to a high extent in EEG [Nunez & Srinivasan 2006]. That is the reason why EEG is naturally a low-pass filtered signal.

The LFP, EFP, ECoG and EEG are band-pass filtered to obtain neuronal activity in certain frequency bands. Four major frequency bands are defined as θ (4-8 Hz), α (8-13 Hz), β (13-30 Hz) and γ (> 30 Hz) (as in [Groppe et al. 2013]). The γ -band is further differentiated into a low- (usually 30-80 Hz) and a high- γ (usually > 80 Hz) band because these bands show task-specific differences (e.g., [Hermes et al. 2015]) and respond differently to sensory stimulation (e.g., [Bartoli et al. 2019]). The exact definition of the frequency range of low- and high- γ , however, differs between studies [Crone et al. 2011]. While the functional role of these two bands is debatable, high- γ was found to reflect cortical activity in various ECoG studies (for a review, see [Crone et al. 2011]).

With an increase in the spatial scale of a recording technique, the extent of the integration over the cortical tissue (spatial spread) increases too [Buzsáki et al. 2012]. The difference in spatial spread between the introduced measures makes them suitable for different kinds of investigations. At a low spatial scale, the spatial spread is small. Thus, intracortical electrodes enable the recording of signals from very small neuronal populations. Various studies measured the spatial spread of the intracortical LFP between ~ 200 and 250 μm radius around the electrode's tip [Berens et al. 2008; Dubey & Ray 2016; Katzner et al. 2009; Xing et al. 2009]. In contrast, findings about the spatial spread of superficial extracortical recordings (EFP, ECoG) are less consistent. A recent study used MUA- and LFP-based RFs to estimate the spatial spread of ECoG [Dubey & Ray 2019]. It was estimated to be slightly larger than the diameter of the surface electrode (spatial spread: 3 mm, electrode diameter: 2.3 mm). Additionally, they found that the RF size was more than twice as large based on ECoG in comparison to MUA. Using smaller ECoG electrodes (electrode diameter: 250 μm),

Bockhorst and colleagues [2018] found that the RF width was smaller for RFs based on subdural recorded MUA in comparison to intracortical MUA. While these studies cannot be compared directly because of the different strategies to calculate RFs, the latter study indicates that smaller electrodes enable recordings that are more similar to intracortical recordings. This assumption is in line with another study that found the signal which was recorded with small subdural electrodes (made out of 40 μm thick wires) is more similar to the intracortical LFP in comparison to the signal recorded with larger subdural electrodes (2.3 mm diameter) [Kellis et al. 2016]. Thus, the size of the electrode has a huge impact onto the spatial spread. A study in the barrel cortex of rats, however, demonstrated that the signals of differently large ECoG electrodes (diameter 50-300 μm) did not differ when sensory evoked potentials were investigated [Vomero et al. 2018]. This finding indicates that electrodes with a size $< 300 \mu\text{m}$ could have a similar spatial spread. In summary, the spatial spread of ECoG is influenced by the size of the electrode but its exact extent differs between studies. On a high spatial scale, EEG electrodes integrate over large cortical areas. The spatial resolution of raw EEG allows to display source patches of $> 5 \text{ cm}$ [Nunez et al. 1994]. Despite the inability to display local cortical activity, EEG has the advantage that it is non-invasive and easy to use [Im & Seo 2016]. To overcome its poor spatial resolution, various techniques were applied on EEG signals (for a review, see [Srinivasan 1999]).

Having these facts in mind, I report electrophysiological findings about the response of V1 neurons to visual stimulation.

3.1.5 Neuronal responses of V1 to visual stimulation

The majority of studies within this thesis investigate EFP responses evoked by different visual stimulus attributes. As mentioned before, ECoG recorded with small electrodes shows visual response properties similar to intracortical recordings [Kellis et al. 2016]. EFP recordings reported in this thesis were performed by using a high-density multi-electrode array with small electrodes. In order to relate EFPs to intracortical and ECoG responses, this section reviews recent findings on intracortical and superficial extracortical signal modulations in V1 caused by different features of the visual stimulation.

In general, the neuronal response to visual stimulation can be divided into a fast transient response and a subsequent prolonged sustained response. The earliest visually evoked

response of a V1 neuron is a sharp increase in its firing rate which usually occurs around 30-50 ms post stimulus onset [Maunsell & Gibson 1992]. Depending on the stimulation parameters, the neuronal response is further modulated (sustained response) or decreases after the initial response to baseline activity (e.g., [Gawne & Martin 2002; Huang & Paradiso 2008]). In comparison to the firing rate, the LFP response to visual stimulation is modulated in a more complex way and is dependent on the depth of the intracortical recording [Kraut et al. 1985; Schroeder et al. 1991]. I focus onto the LFP activity in superficial layers because they influence superficial extracortical recordings as ECoG to a large degree [Buzsáki et al. 2012]. The visually evoked LFP from superficial layers or the cortical surface of V1 within ~150 ms post stimulus onset consists of distinct alternating peaks [Kraut et al. 1985; Schroeder et al. 1991]. The earliest peak, which is associated with the activity in layer 4 of V1, occurs ~40 ms post stimulus onset [Kraut et al. 1985; Schroeder et al. 1991]. The visually evoked response of V1 neurons recorded with ECoG shows similar modulations, however, a lower number of peaks occurs within 200 ms post stimulus onset and the first peak occurs ~75 ms post stimulus onset [Dagnelie et al. 1989; Dubey & Ray 2019].

V1 neurons were found to be responsive to a manifold of visual stimulus attributes. In the following, I describe the modulation of the neuronal response caused by example stimulus attributes.

- *Spatial frequency, orientation and movement direction:* As mentioned previously, neurons in V1 can be selectively responsive to the orientation or the spatial frequency of a stimulus. These neurons show maximal response to a certain (preferred) orientation/spatial frequency, while the response to other orientations/spatial frequencies decreases with decreasing similarity to the preferred orientation/spatial frequency [De Valois et al. 1982; Hubel & Wiesel 1968]. In a similar manner, some cells show a higher response to a certain stimulus movement direction [Dow 1974; Livingstone & Hubel 1984].
- *Contrast and luminance:* Many neurons in V1 show a modulation of their activity caused by stimulus contrast and luminance [Dai & Wang 2012]. The neuronal response increases in a hyperbolic fashion when the stimulus contrast is increased [Albrecht & Hamilton 1982]. In contrast, different response modulations were found for neurons with increasing luminance: the response was monotonically increasing,

monotonically decreasing or v-shaped with a trough when reaching the background luminance [Kinoshita & Komatsu 2001]. Some neurons were found to respond highest to intermediate luminance [Geisler et al. 2007; Peng & Van Essen 2005]. In addition, LFP γ -power recorded with penetrating electrodes was found to increase with increasing contrast, however, γ -power decreased for the highest contrast [Jia et al. 2013]. The latency of the neuronal response onset was found to be shorter when stimuli had a higher contrast or luminance [Geisler et al. 2007].

- *Color*: Some cells show higher response amplitudes to stimuli with a certain color [Friedman et al. 2003; Motokawa et al. 1962; Wachtler et al. 2003]. In general the neuronal response of a cell is defined by the cone input that is delivered via the parallel pathways [Conway 2001]. Color-selective neurons can be categorized into single-opponent, double-opponent and non-opponent cells based on the enhancement or inhibition caused by the specific wavelength emission onto the center and the surround of the RF [Motokawa et al. 1962; Shapley & Hawken 2011].
- *Disparity*: V1 neurons were found to be responsive to a certain range of disparities. Some were found to respond to stimulus disparities that are perceived as depth towards the subject while the response is inhibited when stimuli have disparities that are perceived as depth into the display. Others respond vice versa. [Poggio & Fischer 1977]
- *Stimulus size*: Larger sized stimuli evoked a lower spiking activity in V1 neurons [Gieselmann & Thiele 2008]. In addition, the same study found increased γ -oscillations for stimuli with increasing size that were larger than the classical RF of V1 neurons.

The neuronal response of V1 neurons is usually dependent on the combination of stimulus attributes. In the following, I give some examples to illustrate the manifold of distinct modulations of the neuronal response caused by multiple stimulus attributes. For some cells, tuning curves of orientation/direction and disparity, or orientation and spatial frequency emerge in a joint tuning curve resulting in a neuronal response that is dependent on both stimulus attributes [Grunewald & Skoumbourdis 2004; Mazer et al. 2002]. Furthermore, when stimulus contrast is increased, orientation selectivity of some color-selective cells was found to increase as well [Johnson et al. 2008]. In addition, responses to stimuli with

different luminance and contrast combinations were found to be separable by the response amplitude and the response latency [Geisler et al. 2007]. A change in luminance is represented earlier during the neuronal response when a change in luminance and contrast occurs simultaneously [Wang et al. 2015].

Clinical applications such as BCIs benefit from a precise decoding of neuronal signals. The influence of multiple stimulus attributes onto the neuronal response of single neurons, however, complicates the decoding of information from single cell activity. For example, the interpretation of the response amplitude of a cell which is responsive to multiple stimulus attributes can be misleading because a certain response amplitude is evoked by different combinations of stimulus attributes. An alternative approach for decoding information from neuronal activity is to take the signal of multiple neurons or of neuronal populations into account. On the one hand, different models were used to decode information from the coordinated activity of multiple neurons (e.g., [Quian Quiroga & Panzeri 2009]). On the other hand, information about stimulus attributes can be derived from the integrated response over neuronal populations in V1. The functional architecture of V1 leads to distinct spatial cortical activity patterns caused by the visual stimulation (see Chapter 3.1.3). These patterns carry information about the visual stimulation because the spatial arrangement of V1 response maps is known. A vivid example of a decoding approach using spatial activity patterns from V1 to decode information about the visual stimulation is provided by a previous fMRI study [Miyawaki et al. 2008]. The authors were able to reconstruct small objects (total size $1.15^\circ \times 1.15^\circ$, letters and symbols) that were shown for a few seconds to subjects from the high-resolution cortical activity patterns of V1. Besides fMRI signals, electrophysiological signals can also serve as a basis for such a decoding approach. Electrophysiological measures are advantageous because they offer a higher temporal resolution than fMRI [Fukushima et al. 2015] which enables the decoding of spatio-temporal activity patterns. ECoG and intracortical recordings possess a similar or better spatial resolution in comparison to fMRI, while EEG possesses a low spatial resolution [Fukushima et al. 2015]. A spatial activity pattern recorded with a low spatial resolution loses its information because it is under-sampled and therefore becomes less distinct. That is probably the reason why an EEG study did not find a statistical difference between the signal of occipital electrodes evoked by differently shaped stimuli [Duszyk et al. 2014], while a high-density EFP study successfully decoded the shape of large visual stimuli (4°) from single-trial

signals of V1 [Rotermund et al. 2009]. This advantage makes superficial extracortical recordings a promising candidate for real-time decoding of information from cortical activity patterns and could therefore be used for the development of BCIs. Only little is known, however, about the ability to decode different stimulus attributes from single-trial high-resolution superficial extracortical signals from V1.

An improvident interpretation of the studies reported in the previous section could lead to the assumption that V1 activity is a pure representation of the visual field seen by the retina. Nevertheless, another fMRI study trained their subjects to maintain an imaginary vivid image of a previously shown letter [Senden et al. 2019]. The authors were able to decode the previously shown letter from the time-averaged V1 activity during the imaginary maintenance. An activation of V1 during multiple seconds of imagination that allows for the decoding of the previously shown letter cannot be explained by a pure representation of the visual input, but rather by intrinsic cortical signals. Thus, V1 is not exclusively modulated by external, but also by intrinsic signals. This assumption is also in line with several electrophysiological studies revealing a differentiated V1 activity caused by intrinsic information (e.g., [Eriksson et al. 2010; Lee et al. 1998; Roelfsema et al. 2007]). Roelfsema and colleagues [2007], for example, investigated the response of V1 neurons that either covered a target stimulus, a distractor stimulus or the background display with their RF. Shortly after the onset of the stimulation display, all neurons showed an enhanced response due to the visual stimulation. A few milliseconds later, neurons that covered the target or the distractor stimulus with their RF, showed an enhanced response in comparison to neurons covering the background with their RF. Later, only neurons that covered the target stimulus with their RF showed a higher response in comparison to neurons covering the distractor stimulus with their RF. This study demonstrates that temporal changes in the neuronal response depend on the task-relevance of the stimulus covered by the RF of the neuron. The information about the task-relevance of a visual object cannot be derived from the pure sensory input. This differentiated response of V1 neurons requires information from other than sensory sources, for example, from other brain areas.

Besides the projections from the LGN, V1 receives projections via reciprocal and inter-areal connections from other visual areas [Felleman & Van Essen 1991; Rockland & Pandya 1979]. Top-down influences from higher visual areas deliver higher cognitive information to

V1 (for a review [Roelfsema & De Lange 2016]). Several kinds of top-down influences effecting visual processing have been investigated previously [Gilbert & Li 2013; Petro et al. 2014]. Amongst others, attention [Luck et al. 1997; Motter 1993; Roelfsema et al. 1998], perception [Murray et al. 2002; Parkkonen et al. 2008], perceptual learning [Li et al. 2008] and working memory [Supèr et al. 2001] were found to influence V1 activity. In the following section, the emphasis is laid onto visual attention because the attentional modulation of EFPs recorded from V1 is investigated in a study of this thesis.

3.1.6 Visual attention in V1

At any moment, our visual system is confronted with a massive visual input. The brain has only a limited capacity to process these signals. Thus, signals are in competition to be processed. Attention is a process that selects signals for priority processing. [Carrasco 2011; Katsuki & Constantinidis 2014]

Attention can be categorized into exogenous and endogenous attention. Exogenous (or bottom-up) attention is based on the differentiated saliency of stimuli [Katsuki & Constantinidis 2014]. This process is well described by a concept called “saliency map” [Katsuki & Constantinidis 2014]. It describes an activity map which integrates and displays all characteristics of visual information (e.g., stimulus location, stimulus features) of the visual field [Katsuki & Constantinidis 2014]. Attention is drawn to the most conspicuous location within this map [Koch & Ullman 1985]. Bottom-up attention can be well illustrated by picturing a single red flower in a field full of blue flowers. Here, attention is drawn from the stimulus features of the odd stimulus (red color), which is an involuntary process. It was hypothesized that a saliency map is realized in higher cortical areas like the prefrontal cortex (PFC) and the posterior parietal cortex (PPC) because neurons within these areas receive information from large parts of the visual field [Katsuki & Constantinidis 2014]. Different regions within these areas (e.g., the dorsolateral prefrontal cortex (dlPFC), the frontal eye fields (FEF), the lateral intraparietal area (LIP)) were found to be involved in bottom-up attention (for a review, see [Katsuki & Constantinidis 2014]). Recent findings, however, gave evidence that a saliency map could also be created by the neuronal activity of V1 indicating that the selection between competing stimuli could happen before the signal is processed in

PFC or PPC [Chen et al. 2016; Zhang et al. 2012]. Thus, the distinct mechanism of bottom-up attention is not fully understood yet.

Apart from that, the brain selects signals based on endogenous mechanisms, which is called endogenous (or top-down) attention [Carrasco 2011]. Endogenous attention is directed, for example, onto a spatial location, a specific object or an object feature that is chosen voluntarily by the subject [Katsuki & Constantinidis 2014]. It can be illustrated by a person observing a single red flower within a field of red flowers because he knows that it is about to bloom. Top-down attention was shown to predominantly originate in regions of the PFC and the PPC (for a review, see [Bisley 2011]). Microstimulation of the FEF, for example, led to increasing firing rates of neurons located in the fourth visual area (V4) that processed the presented stimulus [Moore & Armstrong 2003]. Recent findings, however, gave evidence that subcortical structures as the LGN, the superior colliculus (SC) and the pulvinar are also involved in attentional processing [Green et al. 2017; Schneider & Kastner 2009; Zhou et al. 2016]. Bottom-up and top-down attention interact [McMains & Kastner 2011] but are independent mechanisms [Pinto et al. 2013]. While there is evidence that top-down and bottom-up attention are partly processed by similar cortical areas, other results demonstrated an anatomical separation of cortical areas being involved in these two types of attention [Hahn et al. 2006; Kincade et al. 2005].

Furthermore, attention can be categorized into spatial, object-based and feature-based attention [Carrasco 2011].

- Spatial attention is leading to an increased processing of stimuli within a location in the visual field (for a review, see [Carrasco 2011]). Posner [1980] illustrated this mechanism as a spotlight that is directed to a region of interest. Over the years, other concepts of spatial attention were introduced because studies provided evidence that the focus of spatial attention is rather not explained by a simple spotlight. The focus of spatial attention was, for example, described as a gradient because the behavioral performance of subjects decreased in an attention task when the location of the to-be-detected stimulus change was moved away from the center of the attentional focus [Mangun & Hillyard 1988; Shulman et al. 1986]. Recent studies suggest that the modulation of neuronal activity due to spatial attention is distributed like a mexican hat function because the neuronal activity of the near surround of the attentional focus

was found to be suppressed by a larger degree than the activity of neurons in the extensive surround [Hopf et al. 2006].

- Object-based attention enhances visual processing of all neuronal populations that encode information about the attended object [Chen 2012]. Two different kinds of object-based attention were defined [Vecera & Farah 1994]: The first describes an attentional selection of spatial areas that belong to the attended object while the second one describes an attentional object selection based on non-spatial object attributes like color and orientation. It is debatable, whether the second type of selection is realized in object-based attention (for a review, see [Chen 2012]). Depending on the task paradigm and stimuli, only spatial attention, only object-based attention or both can be elicited [Hollingsworth et al. 2012; Müller & Kleinschmidt 2003; Vecera & Farah 1994].
- Feature-based attention increases the processing of stimuli with a certain feature like color or orientation, independent from their spatial location [Maunsell & Treue 2006]. Spatial and feature-based attention have been shown to potentiate the attentional effect of each other in LIP neurons in an attentional tasks where attention was needed to be drawn to both a spatial location and a stimulus feature [Ibos & Freedman 2016].

A study found combined interaction between spatial, object-based and feature-based attention, concluding that the interaction enables an attentional facilitation across various stimulus dimensions [Kravitz & Behrmann 2011].

Apart from these categories, the allocation of visual attention can be realized in two ways: overtly or covertly. While overt attention denotes that the direction of the gaze is focused onto the attentional target, covert attention denotes the allocation of attention to a location which is not in gaze direction [Carrasco 2011].

In the following, the attentional modulation of V1 activity is reviewed because it is the targeted cortical area of this thesis. A few decades ago, the existence of an attentional modulation of neuronal activity in V1 was a question of debate (for a review, see [Posner & Gilbert 1999; Slotnick 2013]). Many studies were able to find robust attentional effects in higher visual areas, while no effect was found in V1 (as reviewed in [Slotnick 2013]). Accumulative evidence from more recent studies investigating attentional mechanisms,

however, has demonstrated the existence of an attentional modulation of the neuronal activity in V1 [Posner & Gilbert 1999; Slotnick 2013]. In the following, I summarize results of studies which found an attentional modulation of the neuronal activity in V1 grouped by different kinds of signal acquisition.

- *Firing rates*: During the allocation of attention onto a spatial location which is covered by the RF of V1 neurons (attended condition), these neurons show an enhanced (transient or sustained) firing rate compared to the firing rate of the same neurons during the allocation of the spatial attentional focus onto another location (unattended condition) [Buffalo et al. 2010; Chalk et al. 2010; McAdams & Maunsell 1999; McAdams & Reid 2005; Motter 1993; Sharma et al. 2015; Vidyasagar 1998]. Enhanced firing rates were also found for evoked responses from the same object in object-based attention tasks [Roelfsema et al. 1998; Thiele et al. 2009] and for stimulus orientation in a feature-based attention task [Haenny & Schiller 1988]. In spatial attention tasks, this enhancement was larger when the attended stimulus was near to the optimal orientation of the V1 neuron [McAdams & Maunsell 1999; Motter 1993] and when the attended location was surrounded by other contextual stimuli [Ito & Gilbert 1999].
- *LFP*: The LFP from neuronal populations of V1 recorded with intracortical electrodes was also found to be modulated by spatial attention. Besides a decrease in γ - and α -band activity and an increase in γ -peak-frequency, a reduced γ -spike-field-coherence was found for the LFP activity of V1 neurons processing stimuli within the attended location in the attended condition in comparison to the unattended condition [Chalk et al. 2010; Das & Ray 2018].
- *ECoG*: As for the LFP, an increase in γ -peak-frequency was found for ECoG electrodes recording signals from neurons processing the attended location comparing the attended and unattended condition [Bosman et al. 2012]. The γ -power of ECoG recorded from V1 was found to be enhanced [Davidesco et al. 2013; Martin et al. 2019] or suppressed [Martin et al. 2019] by attention. The latter finding was argued to be possibly caused by the stimulation of the RF surround [Martin et al. 2019]. Additionally, a decrease in θ -activity [Spyropoulos et al. 2018] was found for ECoG

recorded from V1 neuronal populations that process stimuli within the attended location in the attended condition in comparison to the unattended condition.

- *EEG*: An increase in the earliest visual component (C1) of the evoked potential of EEG was found for the attended condition in comparison to the unattended condition using a spatial attention task [Kelly et al. 2008]. The C1 of the event-related potential (ERP) is associated with the evoked activity in V1 [Foxe & Simpson 2002; Jeffreys & Axford 1972]. Therefore, the previous finding regarding C1 indicates an attentional modulation of the activity of neuronal populations in V1.
- *fMRI*: A higher blood oxygenation level dependent (BOLD) response was found in V1 regions processing stimuli within the attended location [Gandhi et al. 1999; Gouws et al. 2014; Somers et al. 1999; Tootell et al. 1998], while a lower BOLD response was found for V1 regions processing stimuli within the non-attended location [Gouws et al. 2014; Somers et al. 1999; Tootell et al. 1998]. In addition, the baseline activity of V1 was found to be shifted by attention [Murray 2008].

While the attentional modulation of intracortical V1 signals is usually small, fMRI-based studies find predominantly larger modulations (as reviewed in [Boynton 2011]). Additionally, the degree of the neuronal modulation due to attention is increasing with the visual hierarchy [Buffalo et al. 2010; Luck et al. 1997; Martin et al. 2019; Mehta et al. 2000]. Thus, the attentional modulation of responses of neurons located in V1 is small in comparison to neurons located in higher visual areas. In addition, the attentional modulation occurs later in neurons located in V1 in comparison to neurons located in higher visual areas like V2 and V4 [Buffalo et al. 2010]. Some studies, however, found an early attentional modulation in V1 which suggests a greater importance of V1 in attentional processing than commonly assumed (for a review, see [Slotnick 2013]).

V1 receives projections from various areas, thus, signals that cause the attentional modulation in V1 can originate from different sources. Signals that cause an attentional modulation are delivered by feedback connections from higher visual areas (e.g., V4), which themselves receive attentional input from PFC and PPC regions (for review, see [Baluch & Itti 2011; Noudoost et al. 2010]). V1 could also receive signals that cause an attentional modulation via sparse projections directly from higher cortical areas (e.g., FEF and LIP, [Barone et al. 2000]). Additionally, V1 gets input from the LGN which itself shows an enhanced neuronal

activity caused by spatial attention [McAlonan et al. 2008]. Thus, signals from the LGN entering V1 can already be modulated by attention. V1 could also receive signals that cause an attentional modulation by the pulvinar because it is connected to visual cortices, LIP and FEF [Gutierrez et al. 2000; Kaas & Lyon 2007; Romanski et al. 1997; Selemon & Goldman-Rakic 1988; Ungerleider et al. 1983]. In addition, the functional coupling of the pulvinar, and LIP and FEF was found to increase during the allocation of spatial attention [Fiebelkorn et al. 2019].

Apart from research studies regarding the understanding of different attentional mechanisms and anatomical circuits of attention, other studies investigated the possibility of decoding the location of the focus of spatial covert visual attention from brain signals for BCI control [Allison et al. 2010; Aloise et al. 2012a; Andersson et al. 2011; Ekanayake et al. 2018; Gunduz et al. 2012; Marchetti et al. 2013; Treder et al. 2011b, 2011a; Zhang et al. 2010]. The modulation of activity in V1 caused by shifts of covert spatial visual attention could potentially be used for BCI control. The decreasing level of attentional modulation from higher to lower visual areas [Buffalo et al. 2010; Luck et al. 1997; Martin et al. 2019; Mehta et al. 2000], however, could impede this approach. Recently, the identity of two spatial locations of covert visual attention was decoded from EFP signals recorded from V1 and V4 [Rotermund et al. 2013]. This finding provides evidence for the potential usage of EFPs from visual cortices to control a BCI via shifts of covert spatial attention. Only two stimulus positions, however, were decoded in the last mentioned study. Multiple stimulus locations would be favorable to ensure high degrees of freedom for the BCI user. Hence, a study of this thesis aimed to decode the spatial location of multiple covert attentional foci.

The next chapter focuses on types of BCIs and how BCIs have been used to restore communication in paralyzed patients.

3.2 Brain-Computer Interfaces

A major goal of developing BCIs is the reestablishment of communication and motor functions for paralyzed patients [Birbaumer 2006; Birbaumer & Cohen 2007]. A BCI converts brain signals into commands for a computer or a device. In order to function

precisely, the different parts of a BCI (signal acquisition, signal processing and command execution) need to compliment each other to provide a well-functioning BCI [Wolpaw et al. 2002]. Each part can be realized in different ways and faces its own challenges. In the first place, different kinds of recording techniques spanning from intracortical electrodes to brain imaging methods as fMRI can be used for recording neuronal signals for a BCI [Nicolas-Alonso & Gomez-Gil 2012]. Each of these techniques has its advantages and disadvantages which need to be considered when developing a BCI (this topic is further reviewed in Chapter 3.2.1). Furthermore, different neuronal signals that a user is capable to modulate voluntarily can be used as a BCI control signal (different types of control signals for visual BCIs are reviewed in Chapter 3.2.2). Once the signal is recorded, signal-specific data analysis is applied to read out the specific BCI control signal [Nicolas-Alonso & Gomez-Gil 2012]. Issues like artificial signal modulation, inter-subject variability and trial-to-trial variability need to be compensated to reliably extract the desired control signal (e.g., [Blankertz et al. 2011; Fatourechhi et al. 2007; Saha et al. 2017; Saha & Baumert 2020]). In addition, data analysis for online BCIs is challenged by the huge amount of data that needs to be analyzed in real-time (e.g., [Hosseini et al. 2017]). After analysis, the desired action or command is executed in real-time provided a fast and reliable feature interpretation. The accuracy of BCI control, however, does not only rely on technical aspects. For example, BCI users usually need to be trained to control their neuronal signals to execute a desired action [Wolpaw et al. 2002].

Over the past decades, different approaches and types of BCIs were developed coping with the mentioned and other challenges. While a review of all kinds of BCIs is beyond the scope of this thesis, the focus is laid predominantly onto visual BCIs based on electrophysiological signals because one study of this thesis investigates the modulation of EFPs from V1 caused by visual attention because of its potential use for BCI control (Chapter 8). Previously, many visual BCIs were developed to enable paralyzed patients to communicate (for a review, see [Rezeika et al. 2018]). Visual BCIs are advantageous because they can be controlled by a majority of BCI users, provide a reliable and robust performance, and need less training of BCI users in comparison to other BCIs [Fazel-Rezai et al. 2012; Gao et al. 2014; Wang et al. 2008; Wolpaw et al. 2002].

In the following, I describe different recording methods for BCI applications. Afterwards, main signal types for visual BCI control are introduced. Finally, I review current BCIs used for the reestablishment of the communication of paralyzed patients.

3.2.1 Data acquisition methods for BCIs

In general, BCIs can be categorized by their level of invasiveness. Non-invasive BCIs rely on recording techniques like EEG, magnetoencephalography (MEG) and fMRI, while invasive BCIs rely on invasive recording techniques like ECoG and intracortical electrodes. Non-invasive BCIs offer the advantage that their usage does not need a surgical intervention. However, fMRI and MEG recordings are locally bound to large immobile scanners. In contrast, EEG-based BCIs are portable and can, for example, be easily recorded at bedside. [Nicolas-Alonso & Gomez-Gil 2012]

In the following I focus onto portable electrophysiological recording methods, starting with EEG.

Besides the benefit of non-invasiveness and portability, EEG offers the opportunity to record simultaneously from electrodes placed over the whole head. Nevertheless, EEG has a low spatial resolution, is sensitive to muscle activity like eye blinks and is also influenced by electromagnetic disturbing signals from outside the body [Burle et al. 2015; Urigüen & Garcia-Zapirain 2015; Usakli 2010]. In order to handle these issues, many techniques and algorithms were developed to optimize the signal quality of EEG leading to higher signal-to-noise ratios and a more accurate detection of signal sources (i.e., brain areas) causing the modulation of the EEG signal [Blankertz et al. 2008; Grech et al. 2008; Hallez et al. 2007; Michel et al. 2004; Srinivasan 1999; Urigüen & Garcia-Zapirain 2015]. This effort has led, for example, to an increase in the spatial resolution of EEG from > 5 cm to 2-3 cm (for a review, see [Burle et al. 2015]). Still, the low spatial resolution of EEG impedes the detection of the activity of small neuronal populations. Furthermore, a common drawback of BCIs based on non-invasive recordings is that they usually need long periods of training before a user is capable of autonomous BCI control [Birbaumer 2006]. Relying on long training periods is sub-optimal because it limits the time of autonomous BCI usage.

Alternatively, intracortical and superficial extracortical signals are considered as an input signal for BCIs [Schalk & Leuthardt 2011; Slutzky & Flint 2017]. Invasive recordings need a

previous surgical implantation of electrodes. Once chronically implanted, however, recordings are easily accessible because the electrodes do not need to be placed before each session as in EEG-based BCI setups. In addition, these electrodes are more isolated from outer disturbances due to the coverage by the scalp, the skull and other tissue.

Recently, ECoG has become a popular choice of data acquisition for BCI research [Schalk & Leuthardt 2011]. Many studies utilized ECoG signals from the cortex of epilepsy patients undergoing a localization of epileptic foci [Parvizi & Kastner 2018]. In comparison to EEG, ECoG has many advantages:

- a higher spatial resolution [Buzsáki et al. 2012; Schalk & Leuthardt 2011],
- a higher signal-to-noise ratio [Ball et al. 2009],
- a higher signal amplitude [Petroff et al. 2016],
- a larger bandwidth [Staba et al. 2002],
- and the signal is less affected by muscle activity and eye blinks [Ball et al. 2009].

Previously, it was demonstrated that ECoG-based BCIs outperform EEG-based BCIs applying the same data processing on both signal types [Grazimann et al. 2005]. Due to the better signal quality, BCI training is faster with ECoG signals in comparison to EEG [Birbaumer 2006]. The quality of ECoG signals remains stable over long periods of time (e.g. steady signal-to-noise ratio and mean power for up to 776 days, [Nurse et al. 2018]). Thus, ECoG can be applied for long-term recordings. For example, a patient was able to use an ECoG-based BCI for 36 months without a decrease in BCI control [Pels et al. 2019]. In addition, long-term animal studies demonstrated that ECoG grids affect the neuronal tissue only marginally [Degenhart et al. 2016; Henle et al. 2011; Romanelli et al. 2018]. These studies found no macroscopic cortical damage, only a mild chronic inflammatory response, a low foreign body response, an encapsulation of the array in collagenous or new dural tissue, and a mechanically cortical depression which had almost no effect onto the cortex in terms of cytology. However, two long-term studies found that around 8% of the implanted ECoG grids in humans led to infections [Bergey et al. 2015; Cook et al. 2013].

Depending on the array design, a single multi-electrode grid can be used to record ECoG from multiple neighboring cortical areas. ECoG also yields the opportunity for intrasulcal

recordings [Fukushima et al. 2014; Matsuo et al. 2011; Yanagisawa et al. 2009]. While electrode grids can be produced to contain a high amount of electrodes (e.g., > 300 electrodes, [Viventi et al. 2011]), current data acquisition systems are a limiting factor because of their limited capacity to process multiple signals [Chang 2015].

Apart from ECoG, intracortical electrodes were used to establish BCI control. The signal quality of intracortical recordings is high because the activity of single cells or a small population of neurons can be recorded. This enables precise BCI control (for a review, see [Slutzky & Flint 2017]). Despite its high signal quality, the local nature of intracortical recordings impedes a simultaneous recording from different (and distant) cortical areas in comparison to ECoG. In addition, especially for spiking activity, signal quality decreases over time [Chestek et al. 2011; Slutzky & Flint 2017; Szostak et al. 2017]. This is partly caused by the immune response which is triggered by the insertion of an electrode into the cortical tissue [Fernández et al. 2014; Grill et al. 2009; Polikov et al. 2005]. After insertion, microglial cells and astrocytes migrate to surround the electrode leading to an increase in electrode impedance (for a review, see [Campbell & Wu 2018]). However, electrode failure over time is also caused by abiotic issues like the degradation of the electrode's material (for a review, see [Campbell & Wu 2018]). Despite these issues, a study found intracortical LFP and spiking activity to remain stable for 3 months to 3 years enabling long-term motor BCI control [Flint et al. 2016]. Another study showed for a single macaque monkey that the recording of SUA and MUA is possible for more than 7 years using the same intracortical electrodes [Krüger et al. 2010].

In general, non-invasive data acquisition techniques are more favorable than invasive techniques provided that these enable sufficient BCI control. Non-invasive BCIs reach high accuracy when used by healthy subjects (e.g., [Xing et al. 2018]), however, the accuracy decreases when being employed by patients which are the main target group for BCI development (e.g., [Li et al. 2014; Piccione et al. 2006], for more details, see Chapter 3.2.4.1). Due to the fact that signals from invasive recordings have been proven to enable a more accurate decoding in comparison to decoding based on non-invasive signals (e.g., [Grimann et al. 2005]; for a review, see [Waldert et al. 2009]), invasive BCIs could be a solution for cases where the won freedom in communication or movement of a patient justifies the risk of an invasive implantation. Patient surveys revealed that many patients

would consider invasive methods for using a BCI besides a general preference for non-invasive methods [Blabe et al. 2015; Collinger et al. 2013a; Huggins et al. 2011]. The development of invasive BCIs could help to improve the quality of life of impaired and/or paralyzed patients. Due to the lower acceptance by patients but beneficial properties of invasive BCIs, issues like the cortical damage caused by the implantation and the longevity of implants need to be improved [Waldert 2016]. For a long-term application of BCIs, ECoG is more favorable than intracortical recordings because it triggers a milder inflammatory response, is less invasive and provides the possibility to record easily from multiple cortical areas (as described above). An even better option for long-term invasive BCIs could be provided by using epidural electrodes because neither the cortical tissue nor the dura is damaged during the implantation of these electrodes. After implantation, scar tissue growth onto epidural arrays was found in rats [Schendel et al. 2013, 2014]. The implantation of epidural electrodes, however, has caused less complications like infections after surgery in long-term application in comparison to subdural electrodes (for an overview, see Table 1 in [Shimoda et al. 2012]). Furthermore, epidural electrode arrays anchored by tracts that penetrate the skull do not influence movements of the brain inside the skull, while subdural implants lead to an interference of the natural movement buffer function of the dura [Moran 2010]. Epidural recordings can be realized utilizing similar multi-electrode arrays as for ECoG recordings. Therefore, EFPs and ECoG potentially have similar spatial and temporal resolution provided that similar arrays are used. Despite its advantages, the EFP is used in less studies in comparison to ECoG (e.g., see Table 1 in [Wang et al. 2017] or as reviewed in [Slutzky & Flint 2017]). Furthermore, only a few studies have compared the signal quality between EFPs and ECoG which is of importance to clarify whether EFPs are useful for BCI control and other clinical applications. Previous comparative investigations of EFPs and ECoG have led to controversial findings. Some studies found that ECoG has higher spectral amplitudes, higher signal amplitudes and a higher signal-to-noise ratio in comparison to EFPs [Bundy et al. 2014; Torres Valderrama et al. 2010]. Other studies demonstrated a similar signal quality of EFPs and ECoG [John et al. 2018; Slutzky et al. 2010]. In addition, a study that used cortical activity from the motor cortex to distinguish between two cognitive states (rest vs. imagination of a movement) did not find a negative influence of the human dura onto the classification performance [Torres Valderrama et al. 2010]. Furthermore, the accuracy of decoding continuous grasp kinematics was similar using either epidural or

subdural recordings from human motor and somatosensory areas [Flint et al. 2017]. Thus, despite their difference in signal quality, these findings demonstrate a similar decoding accuracy based on either EFPs or ECoG. Apart from the signal quality, a few studies have investigated the temporal stability of EFPs or ECoG which is of high importance in order to use these techniques for long-term recordings. These studies found, that both EFPs and ECoG show an increase in electrode impedance shortly after implantation which is followed by a stable impedance over weeks and months [Henle et al. 2011; Sauter-Starace et al. 2019; Schendel et al. 2014; Sillay et al. 2013]. Nevertheless, a general conclusion about the difference in the temporal stability between ECoG and EFPs is impeded by the sparseness of long-term studies, especially for epidural arrays [Slutzky & Flint 2017].

In brief, epidural recordings are less invasive while subdural recordings have a better signal quality because the dura mater increases the distance to the signal source and is an additional barrier which needs to be passed by the to-be-recorded signal. In the case of epidural signals containing similar information as ECoG about cortical processing, they would provide a promising less invasive basis for long-term BCI applications. In the motor domain, EFPs were used to decode movement-related information (e.g., [Flint et al. 2012; Gomez-Rodriguez et al. 2010; Marathe & Taylor 2013; Shimoda et al. 2012; Slutzky et al. 2011]). Most of these studies reveal only limited information about the spatial and temporal EFP activity caused by movement-related actions because signal features for decoding were either averaged over large time windows or extracted by algorithms that prevent a direct association between signal features and the original signal.

A few studies used epidural recordings to establish motor BCI control (e.g., [Benabid et al. 2019; Gomez-Rodriguez et al. 2010; Spüler et al. 2014]). Seven different hand movement intentions, for example, were decoded with an accuracy of 61% using EFPs recorded from the motor cortex [Spüler et al. 2014]. In addition, exoskeleton control was established for a single tetraplegic patient for 2 years using epidural signals from the sensorimotor cortex [Benabid et al. 2019]. After progressive training of the patient in different tasks with increasing degrees of freedom over 16 months, he was trained to control an exoskeleton with eight degrees of freedom and reached an accuracy of 70.9%. Despite the intermediate level of accuracy achieved by these individual studies, they demonstrate the potential of epidural signals from motor-related cortices. Apart from the research in motor areas, epidural

recordings were rarely used to investigate EFPs from cortical areas like visual areas [Grothe et al. 2012; Rotermund et al. 2009, 2013; Taylor et al. 2005]. Until now, the specificity and characteristics of the EFP from other than motor areas and its usefulness for BCI control is sparsely investigated.

3.2.1.1 High- and low-density multi-electrode arrays for superficial extracortical recordings

Multi-electrode arrays with different geometries (e.g., electrode size, inter-electrode distance and electrode arrangement) can be used for both subdural and epidural data acquisition. In the following, I describe the differences between classical clinically-used arrays and recently developed high-density arrays. Due to the predominant usage of ECoG in scientific and clinical studies, most of the below cited findings regarding different array geometries were carried out using ECoG.

Most human ECoG research is carried out with epilepsy patients which are implanted with electrodes for a clinical purpose [Parvizi & Kastner 2018]. Clinical standard electrode arrays usually have an electrode diameter of 2-5 mm and inter-electrode distance of 10 mm [Lesser et al. 2010; Parvizi & Kastner 2018]. While the signal of ECoG recorded with these electrodes and the intracortical LFP was found to be similar in their response tuning [Dubey & Ray 2020], the size of subdural electrodes and the corresponding spatial spread impedes the investigation of the activity of small neuronal populations. Recently, advances in microelectronics enabled the development of high-density multi-electrode arrays which allow for extracortical recordings with a high spatial resolution [Shokouejad et al. 2019]. A study, for example, used high-density ECoG recorded from electrodes with a size of $10 \times 10 \mu\text{m}$ and an inter-electrode distance of $30 \mu\text{m}$ to extract spikes from superficial cortical neurons [Khodagholy et al. 2015]. Besides these properties, high-density ECoG was found to have similar response characteristics in comparison to intracortical MUA recordings, and ECoG-recorded MUA was found to be less noisy in comparison to intracortically recorded MUA [Bockhorst et al. 2018]. Additionally, the enhanced resolution of high-density ECoG leads to a higher decoding performance [Hermiz et al. 2018; Wang et al. 2016] and to field potentials which are more similar to intracortical recordings in comparison to clinical ECoG arrays [Kellis et al. 2016]. For both high- and low-density multi-electrode arrays, the coherence in the high frequency range between electrodes decreases with increasing inter-

electrode distance [Wang et al. 2009]. Nevertheless, the coherence in the high frequency range between electrodes is significantly lower in high-density arrays in comparison to low-density arrays when investigating similar inter-electrode distances [Wang et al. 2009]. Thus, in multiple ways, the signal quality is higher for high-density in comparison to low-density multi-electrode arrays. There are, however, two important factors to be considered when the electrode density of an array is increased.

- An increase in the spatial resolution is frequency dependent: The increase in the correlation between electrodes caused by a decrease in the inter-electrode distance is smaller for higher frequencies [Chang 2015]. Therefore, the recording of differentiated neuronal activity between closely located electrodes is superior when filtering for the high frequency range.
- Both the spatial coverage and the electrode density of an array influence the decoding performance. Hermiz and colleagues [2018] tested different geometries of multi-electrode arrays. By sub-sampling electrodes from a high-density array, they changed the number of electrodes, the electrode density and the array-covered area to investigate the influence of these parameters onto information decoding. While keeping the number of electrodes constant between grids with a different inter-electrode distance, they found low-density grids to outperform high-density grids in identifying the state of the neuronal activation. Consequently, the coverage of larger areas was beneficial for decoding of the neuronal activity regardless of the electrode density. Nevertheless, when these electrode arrays covered a fixed area with equally spaced electrodes, high-density grids (i.e., low inter-electrode distance and high number of electrodes) outperformed low-density grids. Thus, a larger spatial coverage and a higher electrode density of multi-electrode arrays are both important factors to increase the decoding performance.

High-density arrays have not been introduced in clinical setups yet but are rather used in basic and pre-clinical research studies [Shokouinejad et al. 2019]. In the future, high-density arrays could potentially replace low-density arrays due to their increased spatial resolution [Shokouinejad et al. 2019]. Furthermore, increasing the density of multi-electrode arrays might be of particular importance for a EFP-based applications because the higher electrode density could compensate for the lower signal quality in comparison to ECoG. Further

investigations are necessary to pave the way for a more common usage of high-density arrays, especially regarding the development of EFP-based applications.

3.2.2 Visual BCI control based on exogenous and endogenous signals

The modulation of neuronal signals required for BCI control can be caused by either exogenous or endogenous processes [Gao et al. 2014]. A widely used visual BCI based on exogenous control signals is the steady state visual evoked potential (SSVEP)-based BCI speller [Rezeika et al. 2018]. The user of an SSVEP-based BCI speller selects one visual object out of a multi-object display by fixating the eye's gaze onto the desired object (e.g., onto the letter that should be typed next) [Rezeika et al. 2018]. The various objects arranged on the display flicker differently, which is realized in three different ways [Bin et al. 2009]:

- objects flicker in different frequencies (frequency modulated visual evoked potential, f-VEP),
- objects flicker separated in time but not frequency-locked (time modulated visual evoked potential, t-VEP)
- or objects flicker in form of different pseudo-randomized sequences (pseudo-random code modulated visual evoked potential, c-VEP).

As for all three cases, the focused gaze onto an object leads to a unique activity pattern of visual evoked potentials (VEPs) [Bin et al. 2009]. The activity patterns are identified by the BCI which enables the execution of a command associated with the fixated object [Rezeika et al. 2018]. c-VEP-based BCIs reach highest performance, followed by f-VEP-based BCIs, while t-VEP-based BCIs reach lowest performance (92.8, 39.7 and < 30 bits/min [Bin et al. 2009], the bit rate [bits/min] or information transfer rate (ITR) is used as measure of BCI communication performance [Wolpaw et al. 2002]). The number of targets in f-VEP-based BCIs is limited by the frame rate of the monitor used for the visual presentation [Wang et al. 2010]. This limitation can be overcome by, for example, using an alternative visual stimulation design [Rezeika et al. 2018; Wang et al. 2010].

In contrast, signal modulations used for the control of BCIs can also be caused by endogenous processes like voluntary mental activities (e.g., a shift of covert spatial attention).

A commonly used endogenous signal for visual BCI control is the P300 response [Rezeika et al. 2018]. The P300 is a component of the ERP which occurs ~300-400 ms post onset of a rare stimulus when recorded with EEG [Patel & Azzam 2005]. Its amplitude is modulated, for example, by attention, stimulus frequency and stimulus sequence (for a review, see [Patel & Azzam 2005]). Many types of P300 BCI spellers originate from the experiment of Farwell and Donchin [1988]. For their P300 BCI speller, letters of the alphabet are arranged in a grid. In each trial, the rows and columns are intensified sequentially for a brief duration in time. The subject has to focus on one letter and count the number of its intensifications. The intensification of the focused letter manipulates the P300. The focused object is detected by analyzing the amplitude of the P300 with regard to the row-/column that was intensified. In this way, a user spells words by focusing on the desired letters, one after another. The original P300 speller from Farwell and Donchin [1988] reached a classification accuracy of 95% with an ITR of 12 bits/min. P300-based BCIs were further improved in ITR and/or accuracy (e.g., mean accuracy 84%, mean bit rate: 53.7 bits/min [Yeom et al. 2014]; 100% accuracy and 71.9 bits/min for a single subject [Käthner et al. 2015]). This improvement was achieved by, for example, varying and optimizing the stimulation pattern, using different visual presentations of letters, using other changes of stimuli instead of intensifying and/or using a virtual-reality headset for the visual stimulation [Käthner et al. 2015] (for a review, see [Abiri et al. 2019; Rezeika et al. 2018]). P300-based BCI speller usually rely on multiple intensifications of each row/column for extracting the P300. This circumstance decreases the P300-based BCI spelling speed in comparison to SSVEP-based BCIs [Rezeika et al. 2018]. In addition, an increased number of objects presented on the monitor naturally causes an increased duration of trials of P300-based BCI spellers because more rows/columns need to be intensified. However, larger amounts of objects can be easily implemented in P300-based spellers which needs advanced methods to be realized in SSVEP-based spellers due to the limitations caused by the refresh rate of the monitor [Rezeika et al. 2018; Wang et al. 2010]. Over the years, hybrid BCIs were developed to combine the advantages of both BCI types. Chang and colleagues [2016], for example, developed a hybrid BCI enabling the presentation of as much objects as in a P300-based speller while the spelling speed was increased in comparison to both a P300- and a SSVEP-based speller.

Regrettably, the classical setup of SSVEP- and P300-based BCIs (as described above) is relying on the direction of the gaze, prohibiting BCI control of paralyzed patients. Therefore,

gaze-independent visual BCIs were developed that do not rely on eye movements or on the location of the gaze. Gaze-independent BCIs were realized for example by modifying SSVEP-based, P300-based or hybrid BCIs, and/or by utilizing concepts like covert shifts of visual attention for BCI control (e.g., [Aloise et al. 2012b; Egan et al. 2017; Lesenfants et al. 2014; Liu et al. 2011; Treder et al. 2011b]). In general, both the gaze-independency and the usage of spatial attentional shifts for BCI control were found to decrease the performance of BCIs [Aricò et al. 2014; Brunner et al. 2010]. Despite the lower performance of gaze-independent BCI spellers in comparison to gaze-dependent BCI spellers, these BCIs provide a channel of communication for paralyzed patients who would otherwise remain mute.

Before tuning into current BCI solutions for reestablishing communication for paralyzed patients, the Locked-In Syndrome (LIS) is introduced. Patients suffering from LIS are a main target group for the development of BCI spellers.

3.2.3 Locked-In Syndrome

LIS is a state of full or almost full paralysis of the voluntary musculature while consciousness is preserved. LIS is categorized into three sub-types defined by the residual muscle control [Bauer et al. 1979]:

- Classic LIS (cLIS) patients are able to move muscles that are involved in vertical eye movements and blinking.
- Incomplete LIS (iLIS) patients are able to control the same muscles as cLIS patients. Furthermore, they are able to control additional muscles.
- Complete or total LIS (tLIS) patients have no residual voluntarily muscle control.

In the majority of cases, LIS is caused by a lesion of the ventral lower pons or other structures of the brainstem [Laureys et al. 2005; Posner et al. 2007; Smith & Delargy 2005]. LIS can, for example, also be caused by amyotrophic lateral sclerosis (ALS) [Hayashi & Kato 1989], multiple sclerosis [Forti et al. 1982] or the Guillain-Barré syndrome [Ragazzoni et al. 2000]. While some LIS patients die shortly after entering the LIS-state, others survive many years, many of them with a need for artificial respiration or respiratory assistance [Bauer et al. 1979; Laureys et al. 2005; Patterson & Grabis 1986]. Over time, some cLIS/iLIS patients enter the tLIS state (e.g., [Murguialday et al. 2011]). The restriction in

communication and movement causes social isolation [Ganzini & Block 2002] and difficulties in clinical care [Chisholm & Gillett 2005]. Many patients, however, report a rather good quality of life and the will to live [Lulé et al. 2009]. In order to improve the quality of life, BCIs were developed to enable the communication of LIS patients [Lulé et al. 2009].

3.2.4 BCIs for the restoration of communication

The following sections review current BCI spellers. Also, the emphasis is laid onto the patient usage of these BCI spellers regarding their effectiveness to restore the patients communication.

3.2.4.1 *Non-invasive BCIs*

To reestablish patient communication and motor control, many non-invasive BCIs were developed. Recent gaze-dependent non-invasive BCIs were tested with healthy subjects and reached a high speed and a high accuracy [Chen et al. 2015; Nakanishi et al. 2014; Spüler 2017; Xing et al. 2018; Yao et al. 2018; Yin et al. 2013]. Unfortunately, BCI control is often worse for patients [Hill et al. 2006; Li et al. 2014; Ortner et al. 2011; Piccione et al. 2006]. In order to enable BCI control for paralyzed patients, gaze-independent non-invasive visual BCI spellers were developed (e.g., [Acqualagna & Blankertz 2013; Aloise et al. 2012b, 2012a; Hwang et al. 2015; Lesenfants et al. 2014; Lin et al. 2018; Treder et al. 2011b; Won et al. 2018]). Highest spelling speed among these studies was established for a healthy subject by the BCI developed by Lin and colleagues [2018] (10 s/character, based on a bit rate of 20.26 bits/min). In comparison, gaze-dependent BCIs can reach a spelling speed of less than 1 s per character (e.g., [Yao et al. 2018]). Even though the BCI speller developed by Lin et al. [2018] reached highest spelling speed for the class of gaze-independent BCIs, the spelling speed is insufficient for a regular usage because spelling a short sentence would need plenty of minutes. Furthermore, in case of BCI usage by a patient, the spelling speed could further decrease because of the patient's state of health. Similar to gaze-dependent BCIs, gaze-independent BCIs show a lower performance for patients in comparison to healthy subjects (compare [Marchetti et al. 2012, 2013]; [Kaufmann et al. 2013; Lesenfants et al. 2014]). A meta analysis comparing studies involving ALS patients to communicate via non-invasive BCIs found that all analyzed tLIS patients were not able to control a BCI [Kübler &

Birbaumer 2008]. Since then, only a few studies were able to establish yes/no communication for tLIS patients via a EEG-based BCI [Guger et al. 2017; Okahara et al. 2018] and a BCI based on functional near-infrared spectroscopy [Gallegos-Alaya et al. 2014].

In summary, the reduced performance for patients, the drastic decrease in spelling speed for gaze-independent systems and the current limitation to yes/no communication for tLIS patients make current non-invasive BCIs unsuitable for the restoration of fast and reliable communication of paralyzed patients.

3.2.4.2 Invasive BCIs

In the domain of invasive BCIs, a large branch of research and development focused on motor and sensorimotor areas [Birbaumer 2006; Schalk & Leuthardt 2011; Slutzky & Flint 2017; Volkova et al. 2019]. Signals from these areas were used to decode or predict covert and overt movements, and to establish motor control of external devices like robotic limbs (e.g., [Collinger et al. 2013b; Hochberg et al. 2012; Velliste et al. 2008; Wodlinger et al. 2015; Yanagisawa et al. 2011]), for a review [Schwartz et al. 2006]). Furthermore, they were used for cursor control and communication [Bacher et al. 2015; Hinterberger et al. 2008; Jarosiewicz et al. 2015; Leuthardt et al. 2004; Nuyujukian et al. 2018; Pandarinath et al. 2017; Schalk et al. 2008; Vansteensel et al. 2016; Wang et al. 2013]. A commonly used control signal is the imagination of movements (motor imagery) [Hwang et al. 2013]. Motor-imagery-based BCI control is superior for non-paralyzed patients in comparison to paralyzed patients [Hill et al. 2006], and the accuracy varies between subjects [Marchesotti et al. 2016]. Furthermore, motor signals are not intuitively connected to communication and need to be learned by the user. Other studies utilized speech-involved brain areas and the decoding of covert speech for developing invasive BCI spellers for the paralyzed [Martin et al. 2018; Rabbani et al. 2019]. Regrettably, these suffer from poorly controllable signals in terms of time-locked activity [Martin et al. 2018]. Further technical and analytical improvement is necessary to cope with the current issues before covert speech can be decoded with high accuracy [Martin et al. 2018; Rabbani et al. 2019].

Alternatively, some studies used ECoG from various areas (including visual areas) as input for previously established visual BCIs (e.g., SSVEP- and P300-based BCIs) to enable communication of patients [Brunner et al. 2011; Kapeller et al. 2014; Speier et al. 2013]. These studies used signals from clinical ECoG grids resulting in a sparse coverage of the

targeted cortical areas. Despite the low electrode-density, these studies provide two important findings.

- Firstly, the superior performance of ECoG in comparison to EEG was shown for these BCI spellers. In contrast to EEG-based BCIs, ECoG-based BCIs reached a higher decoding accuracy [Speier et al. 2013] and faster spelling/bit rates [Brunner et al. 2011; Speier et al. 2013], while less subject training was needed [Kapeller et al. 2014].
- Secondly, these studies demonstrated that signals from electrodes covering the visual cortex or the occipital pole held important information for decoding [Brunner et al. 2011; Speier et al. 2013].

In addition, the usage or the investigation of epidural recordings for future invasive BCI applications was suggested to decrease their invasiveness [Brunner et al. 2011; Speier et al. 2013].

These findings point out the advantages of superficial extracortical data acquisition for visual BCI spellers, especially in the case of recording neuronal signals from the visual cortex. The subdural electrode placement was sparse in all studies because the signal was recorded from low-density electrode arrays. Due to the fact that an increase in electrode density improves the decoding performance based on ECoG [Hermiz et al. 2018; Wang et al. 2016], the utilization of high-density arrays at specific visual cortices could further improve decoding and open new possibilities for high-accuracy visual BCI spellers. In addition, especially for long-term BCI applications, EFPs could be used instead of ECoG because of their lower invasiveness which decreases the risk of the occurrence of infections after implantation (for an overview, see Table 1 in [Shimoda et al. 2012]). Despite its possible relevance for long-term BCI applications, EFPs could be of importance for basic brain research and other clinical applications in the case of high-density EFPs containing meaningful information about cortical processing. Thus, investigations regarding the specificity of EFPs and the degree of decodable information from EFPs are necessary to clarify the potential benefits of epidural signals for research and clinical applications.

3.3 Towards the objective of this thesis

Superficial extracortical recordings are promising for the development of BCI spellers to enable the communication of paralyzed patients. More importantly, information decoding and therefore BCI speller control could be similarly well established using EFPs in comparison to ECoG. This approach would be advantageous for long-term applications because of the reduced invasiveness. In addition, (visual) BCIs, which are suitable to restore communication for able-vision but paralyzed patients, could benefit from a dense electrode coverage of the (visual) cortical region of interest. EFPs recorded with high-density multi-electrode arrays could therefore enable precise BCI control of paralyzed patients. In the circumstance of EFPs providing reliable information about cortical processing, they would not only serve as an input signal for less-invasive high-accuracy BCIs but would also provide less-invasive cortical signals for brain research and other clinical applications. Further investigations are necessary to quantify the characteristics and the specificity of EFPs.

The objective of this thesis was to investigate whether and to what extent sensory and cognitive information is extractable from high-density EFPs. Therefore, EFPs were recorded from macaque V1 using high-density multi-electrode arrays. Different visual and cognitive tasks were performed by the monkeys during the recordings, aiming to modulate the sensory and attentional processing of V1. Based on the evoked EFPs, the representation of sensory, attentional and behavioral information in trial-averaged and single-trial signals was investigated. The results demonstrate the specific imprint of information about the spatial location of the visual stimulation in single-trial EFPs. Trial-averaged EFPs also reflect modulations of the activity of neuronal populations in V1 evoked by different visual attributes (stimulus size, shape and contrast), as well as by attentional and behavioral conditions. Besides the electrophysiological investigations, this thesis includes a study demonstrating a new method for optimizing macaque training in cognitive tasks. This training method enabled the training of a complex task used for a study of this thesis. In summary, the results provide evidence for the precise representation of information about cortical processing in EFPs and document a new method for training macaques in cognitive tasks.

4. General Materials and Methods

This chapter deals with methodological aspects of the subsequent chapters. In this chapter I describe only methods which are used in multiple chapters. Each subsequent chapter has its own Materials and Methods section describing chapter-specific methods. Due to the fact that Chapter 5 and Chapter 9 are research papers, and Chapter 6 is a draft of a paper manuscript, redundant methodological descriptions are unavoidable.

4.1 Legal permission

All experimental and surgical procedures followed the *Directive 2010/63* issued by the European Commission and the *Regulation for the Welfare of Experimental Animals* issued by the Federal Government of Germany and were approved by the local authorities.

4.2 Subjects

For the studies in Chapter 5-8, epidural recordings were carried out with four male macaque monkeys (*Macaca mulatta*). For the behavioral study documented in Chapter 9, an additional monkey was trained. The animals were either housed separately in indoor animal compartments, where they had visual and auditory contact to other animals, or housed in a group of two to four animals. Groups of animals were housed in a large compartment which was divided into an equally sized in- and outdoor section. Climbing opportunities and animal toys were provided in both sections. All animals were used to the laboratory procedures and visual tasks. Monkeys were rewarded with water or diluted fruit juice during training and recording sessions. Outside recording sessions, free fruits and water were provided in their home compartment. Daily monitoring of the behavior in the stables and monitoring of the behavior during training/recording sessions, monitoring of the body weight multiple times a week, and regularly checks by veterinarians ensured the well-being of the monkeys.

The nomenclature for the monkeys is not uniform within this thesis. Each abbreviation for a monkey (*M1*, *M2*,...) is used for each chapter individually. Thus, the same abbreviation in different chapters does not necessarily refer to the same monkey.

4.3 Multi-electrode array

The multi-electrode array was developed (Brain Research Institute - Section Theoretical Neurobiology, Institute for Microsensors, -actuators and -systems (IMSAS), University of Bremen) and produced (IMSAS) at the University of Bremen. A detailed technical documentation can be found elsewhere [Schander et al. 2019; Stokov et al. 2017]. Briefly, the array was designed to cover the cortical surface of macaque V1/V2 and V4 of one hemisphere densely with surface electrodes. The array contained 202 gold electrodes for recording and a large surface reference electrode positioned on top of the array which was oriented towards the skull. Electrodes were covered in poly(3,4-ethylenedioxythiophene): polystyrene sulfonate (PEDOT:PSS). The carrier material was a single polymer layer on both sides. The electrode diameter was 560 μm and electrodes were arranged hexagonally with equal distance of 1.8 mm from center to center. The signal of the electrodes was transferred via conductor tracts to soldered OMNETICS connectors (MSA-Components, Attendorn, Germany). Ground electrodes were PEDOT:PSS covered 0.5 mm thick and winded gold wires.

4.4 Surgical procedures

The animals were implanted with a cap, a head holder, an epidural multi-electrode array and epidural ground electrodes. All surgeries were performed under strict sterile conditions. Anesthesia was initialized using Ketamine and Medetomidine. For surgeries longer than one hour, anesthesia was maintained by Propofol, Remifentanil and Isoflurane. Otherwise, anesthesia was maintained with about 1% Isoflurane. Rimadyl was used for post-operative analgesia. In order to anchor a cap of acrylic cement (Palamed/Paladur, Kulzer, Hanau, Germany), cortical screws were inserted. Afterwards, a head holder was fixated onto the cap

using acrylic cement (Paladur). After finishing the behavioral training, monkeys participating in electrophysiological experiments were implanted with a multi-electrode array and ground electrodes. A small trepanation of approximately 10×10 mm was cut over the prefrontal cortex of the right hemisphere with a piezoelectric device (Piezosurgery®, Mectron, Köln, Germany) using a 0.3 mm cutter. Two or three ground electrodes were placed between the skull and the dura mater. Afterwards, the trepanation was closed by re-inserting the (fit) bone piece (kept in Ringer-Lactate during the procedure), filling the gap between bone and bone piece with Gelastypt (Sanofi-Aventis, Frankfurt, Germany) and covering the area with acrylic cement (Palamed/Paladur), while maintaining access to the plugs of the electrodes. The location of the lunate sulcus of the left hemisphere was estimated by using data of a pre-surgical structural MRI scan which was carried out at the University of Bremen. A trepanation of $\sim 25 \times 30$ mm was cut over the left hemisphere using a piezoelectric cutter (0.3 mm) based on the stereotactic information. The trepanation was chosen to be located a few mm anterior to the estimated location of the lunate sulcus and ~ 2 mm lateral from the midline. The anterior edge of the trepanation included an extension of about 10×15 mm (aligned at the anterior/medial border crossing of the trepanation) to provide an exit for the tracts of the array. The bone piece was kept in Ringer-Lactate after being disconnected from the skull. The array was placed to sit slightly above the estimated location of the lunate sulcus. Due to the trepanation being smaller than the array, the array was guided between the skull and the dura with thin spatulas. Pictures were taken to document the position of the array. Afterwards, the trepanation was closed by re-inserting the bone piece into the trepanation. The gap between the skull and the bone piece was filled with bone cement (usually chronOS Inject Bone Filler (DePuy Synthes, Umkirch, Germany) or DirectInject (Stryker, Duisburg, Germany), depending on the animal). In addition, the bone piece was equipped with a stripe of titanium which was fixated by cortical screws located on the bone piece and on the surrounding skull. The connectors at the end of the tracts (OMNETICS, MSA Components, Attendorn, Germany) were placed within a trough of the acrylic cement cap (Paladur) and fixated via a two component adhesive (UHU 300 ENDFEST). The connector was covered with a metallic cap for protection, which was fixated by a metallic frame that was embedded in the acrylic cap.

4.5 Recording chamber and monitor setup

Unless otherwise stated, the monkeys sat head fixated and with a distance of ~70 cm in front of a CRT monitor (resolution: $1,152 \times 864$ pixels, refresh rate: 100 Hz) in a separated room with a dimmed light source. The background color of the monitor was black (0 cd/m^2). A lever within the monkey's primate chair was used as a manipulandum.

4.6 Eye-tracking

For recording eye-tracking data, the animals left eye was illuminated by one or two infra-red diodes. The movement of the left eye was recorded by a camera (usually VRmC-6pro, VRmagic, Mannheim, Germany; or TVCCD 240, Monacor, Bremen, Germany). A custom-made eye tracker monitored the pupil diameter and the gaze direction of the monkey, and transmitted the data into the visual stimulation system for online comparison with the eye position requirements.

4.7 Data acquisition

In the following, all parts of the recording chain documented in brackets were originating from Multichannel Systems (Reutlingen, Germany). The EFP signal of the multi-electrode array was recorded simultaneously via seven 32-channel head stages (MPA 32, amplification factor: 10) wired to four signal collectors (Sc2x32). The signal was fed into four main amplifiers (PGA64, amplification factor: 5,000). Finally, the amplified signal of the multi-electrode array, the pupil diameter and gaze direction signal from the eye tracker, and a 50 Hz signal from a socket were fed into an USB box (USB-ME256), and from there to a windows PC. The EFP was recorded at 25 kHz sampling rate.

4.8 Receptive field mapping

For all electrophysiological studies, only electrodes recording visually modulated EFPs were considered for the analysis. In order to select electrodes by this criterion, the RF of each electrode was measured using a RF-mapping procedure that was previously described by Drebitz et al. [2019]. A monkey started a trial of the RF-mapping task by fixating the fixation spot (FS) and pressing a lever within two seconds. Precise fixation (within $\sim 1^\circ$ around the FS) needed to be maintained throughout the trial. After pressing the lever, a 750 ms long baseline interval with only the FS on screen followed. In the next interval, one bar was shown for 2.5 to 3 s or two bars were shown subsequently, each for 1.5 s. The stimulation parameters differed between the monkeys but usually a bar size of $\sim 24^\circ \times 0.24^\circ$, a trajectory length of 19° , and a bar luminance of $\sim 8 \text{ cd/m}^2$ was used. Bars differed in their orientation by 30° and moved into one out of 12 directions. Movement trajectories were chosen to overlap with a large area of the lower right quadrant of the visual field. If two bars were shown in the same trial, they were separated by 500 ms. The bar's motion direction was randomized in each experimental round. One experimental round consisted of 12 or six trials (dependent on the number of bars per trial) which included all bar orientations. The combination of bar orientations in a trial in which two bars were shown was pre-defined in six different combinations. These occurred randomly in an experimental round. After the bar (or the last bar) disappeared, a pseudo-randomized time window started, where only the FS was visible. Afterwards, the FS changed its luminance and the monkey had to respond by releasing the lever to receive a reward. After a successful response, an inter-trial interval (ITI) of usually 1.5 s length started.

4.9 General data processing

4.9.1 Preprocessing

Unless otherwise stated, the data of each experiment was preprocessed in the following way: The recorded EFP was low-pass filtered (finite impulse response filter in both forward and backward direction, 150 Hz cutoff) and down-sampled from 25 to 1 kHz. If available, the 50

Hz disturbing noise was removed from the EFP by using the recorded 50 Hz power line signal.

4.9.2 Wavelet transformation

In order to receive frequency specific activity of the EFP signal, a wavelet transformation was performed on the preprocessed EFP signal of each electrode. Morlet wavelets with a mean of zero and a localization in time and space were used. A Morlet wavelet is defined as [Torrence & Compo 1998]:

$$\psi_0(\eta) = \pi^{-\frac{1}{4}} e^{i\omega_0\eta} e^{-\frac{\eta^2}{2}}$$

where ω_0 is the non-dimensional frequency and η the non-dimensional time parameter. To extract 35 exponentially increasing frequency bands of the EFP from 5-160 Hz, ω_0 was set to six. The wavelet transformation is defined as [Torrence & Compo 1998]:

$$W_n(s) = \sum_{n'=0}^{N-1} x_{n'} \psi^* \left[\frac{(n' - n) \delta t}{s} \right]$$

where * indicates a complex conjugation. x_n is the time series, δt is the time step and s is the scale of the wavelet. Spacing of δt was equal. Wavelet power at any frequency and time bin was calculated as:

$$WLpower = (2|W_n(s)|)^2.$$

The wavelet transformed data was, frequency-wise, baseline normalized by subtracting the mean wavelet power of a baseline time window and then dividing the result by the mean wavelet power baseline activity. The low pass filtered signal (EFP) was usually baseline corrected by subtracting the mean baseline activity.

4.10 Receptive field analysis

Each RF-mapping was recorded in a single session for each monkey. At least ten trials per bar motion direction were recorded. Previous to the RF analysis, two different kinds of trial

rejection were performed to sort out artifacts in the signal. Firstly, trials with miss-matching time triggers and missing time bins were sorted out. Secondly, trials showing high continuous activity during the course of the movement of a bar were rejected.

A more detailed description of the RF-mapping analysis is given elsewhere [Drebitz et al. 2019]. Briefly, for calculating the RF of each electrode, the mean wavelet power between 60 and 150 Hz over all trials was calculated for each bar's motion direction separately. The mean signal was z-normalized for each direction. Each mean wavelet power trajectory was expressed as a matrix of the size [trajectory length \times bar length]. To spatially align these trajectory matrices, they were fit into a large matrix considering the spatial orientation and spatial extent of each trajectory. In addition, a delay of 80 ms was applied for each trajectory, to consider the response delay of the EFP from V1 for the RF calculation. Whenever all trajectories overlapped at a single position in space, the overlapping wavelet power values were multiplied. The product was divided by the 12th root resulting in the geometric mean of the analyzed spatial position. The spatial map of the geometric mean was used to define the RF of an electrode. All spatial locations ≥ 1 z-score were considered for defining the RF. The largest patch of connected spatial locations above threshold was chosen as the RF. The activity center of the RF was defined as the location of the peak z-value within the previously defined patch.

4.10.1 Electrode selection

For further analysis, only electrodes located over V1 were considered. Electrodes located anterior to the lunate sulcus, judged from array placement in the surgery, were rejected. Furthermore, electrodes which showed no RF or an RF with a size < 1 dva² (squared degree of visual angle) were rejected.

4.11 Support Vector Machines

In order to decode the class identity of a single trial, Support Vector Machines (SVM) were applied. The libsvm library for Matlab [Chang & Lin 2011] was used to perform the SVM classification based on the implemented radial basis function kernel. Unless otherwise stated,

the classification procedure of a set of test trials (consisting of one trial of each class) was done as follows. For each class, a “one vs. rest” SVM was trained with a set of 50 randomly chosen training trials per class. After SVM training, each trial of the test set was applied to each of the SVMs. Each SVM calculated the probability that the test trial has the class identity which the SVM was previously trained on. The class identity of the SVM providing the highest probability value was assigned to the tested trial. Usually, the classification procedure was repeated until all available trials were used once for testing. SVM performance was calculated by dividing the number of correctly classified trials by the number of tested trials.

Before SVM training, hyperparameters γ and C of the SVM were optimized by grid search in the range of 2^{-10} to 2^3 and 2^{-2} to 2^8 respectively for all randomly chosen training trials, using multi-class cross-validation as implemented in libsvm [Chang & Lin 2011].

In general, an SVM tries to find the most optimal hyperplane (or decision boundary) between data points (support vectors) of different classes. In simplified terms, the hyperplane of a non-linear SVM (as used in this thesis) can be illustrated as a curved line which separates two populations of dots (support vectors) in 2D space. C is a constant defining a soft-margin around the hyperplane, thereby defining the minimal distance between the hyperplane and support vectors. To ensure this distance, outliers of the support vectors within the margin are labeled as an error and thereby excluded from defining the hyperplane. A low C will exclude more support vectors to ensure the broadness of the margin. The γ -parameter controls the flexibility of the hyperplane by defining an expansion around every support vector. The expansion of every support vector leads to a more patchy representation of neighboring support vectors. The higher γ is chosen, the smaller is the expansion. Provided that γ is chosen too high, the hyperplane winds around groups of support vectors leading to an overfitting of the data. [Ben-Hur & Weston 2010]

5. Visual epidural field potentials possess high functional specificity in single trials

Declaration of the contribution of the candidate to a multi-author article which is included as a chapter in the submitted doctoral thesis.

Task	Contribution [%]
Experimental concept and design:	ca. 50
Data acquisition:	ca. 90
Data analysis and interpretation:	ca. 75
Preparation of figures and tables:	ca. 50
Drafting the manuscript:	ca. 40

Date:

Signature:

This chapter was previously published. Citation: Fischer B, Schander A, Kreiter A K, Lang W & Wegener D (2019), "Visual epidural field potentials possess high functional specificity in single trials." *J Neurophysiol*, 122 (4): 1634–1648, doi:10.1152/jn.00510.2019

Link: <https://journals.physiology.org/doi/full/10.1152/jn.00510.2019>

Authors

Benjamin Fischer¹, Andreas Schander², Andreas K. Kreiter¹, Walter Lang², Detlef Wegener¹

Affiliation

¹Brain Research Institute, Center for Cognitive Sciences, University of Bremen, Germany

²Institute for Microsensors, -Actuators, and -Systems, University of Bremen, Germany

5.1 Abstract

Recordings of epidural field potentials (EFPs) allow neuronal activity to be acquired over a large region of cortical tissue with minimal invasiveness. Because electrodes are placed on top of the dura and do not enter the neuronal tissue, EFPs offer intriguing options for both clinical and basic science research. On the other hand, EFPs represent the integrated activity of larger neuronal populations and possess a higher trial-by-trial variability and a reduced signal-to-noise ratio due to the additional barrier of the dura. It is thus unclear whether and to what extent EFPs have sufficient spatial selectivity to allow for conclusions about the underlying functional cortical architecture, and whether single EFP trials provide enough information on the short timescales relevant for many clinical and basic neuroscience purposes. We used the high spatial resolution of primary visual cortex to address these issues and investigated the extent to which very short EFP traces allow reliable decoding of spatial information. We briefly presented different visual objects at one of nine closely adjacent locations and recorded neuronal activity with a high-density epidural multielectrode array in three macaque monkeys. With the use of receiver operating characteristics (ROC) to identify the most informative data, machine-learning algorithms provided close-to-perfect classification rates for all 27 stimulus conditions. A binary classifier applying a simple max function on ROC-selected data further showed that single trials might be classified with 100% performance even without advanced offline classifiers. Thus, although highly variable, EFPs constitute an extremely valuable source of information and offer new perspectives for minimally invasive recording of large-scale networks.

5.2 New & Noteworthy

Epidural field potential (EFP) recordings provide a minimally invasive approach to investigate large-scale neural networks, but little is known about whether they possess the required specificity for basic and clinical neuroscience. By making use of the spatial selectivity of primary visual cortex, we show that single-trial information can be decoded

with close-to-perfect performance, even without using advanced classifiers and based on very few data. This labels EFPs as a highly attractive and widely usable signal.

5.3 Introduction

The acquisition of spatiotemporally highly resolved activity from large neuronal populations has opened new possibilities for studying the distributed neuronal processes underlying the brain's cognitive and executive functions [Siegel et al. 2012; Varela et al. 2001]. A closer understanding of their spatiotemporal dynamics and discrimination of critical patterns within this activity offers promising perspectives for the diagnosis, treatment, and therapy of nervous system diseases [Engel et al. 2005; Lebedev & Nicolelis 2017; Murphy et al. 2016; Parvizi & Kastner 2018]. Intracerebral recordings, with the use of microelectrode arrays [Suner et al. 2005; Vetter et al. 2004] or microwire bundles [Nicolelis et al. 2003; Schwarz et al. 2014; Williams et al. 1999], provide access to single-cell activity within a designated cortical region. Electrocorticography (ECoG), on the other hand, with the use of subdural electrode grids, allows a large extent of the cortical surface to be covered and provides access to measurements at a mesoscopic scale.

ECoG was introduced during the early 1950s to identify epileptogenic zones before surgical intervention [Penfield & Jaspers 1954], and later on became the gold standard for perioperative functional mapping [Palmini 2006; Yang et al. 2014]. ECoG arrays for clinical purposes mostly use electrodes with large diameters and large interelectrode distances [Lesser et al. 2010; Schalk & Leuthardt 2011]. More recently, however, several research groups developed high-density arrays that allow analysis of neural signals on a finer spatial scale [Fukushima et al. 2014; Rubehn et al. 2009; Schander et al. 2019; Tolstosheeva et al. 2015]. Because ECoG provides better spatial resolution, better signal-to-noise ratio, and higher frequency components (> 40 Hz) than electroencephalography [Ball et al. 2009; Ray et al. 2008], and constitutes a probably more durable recording approach than intracerebral electrodes [Chao et al. 2010], it has now become an increasingly interesting technique for both basic research on the dynamics of large-scale networks [Lewis et al. 2015] and brain-computer interfacing [Schwartz et al. 2006].

A major challenge in ECoG research is to extract useful information from short data fragments (i.e., single trials), due to the strong trial-by-trial fluctuations in both distributed and local brain activity underlying different perceptual and cognitive states [Fox & Raichle 2007; Garrett et al. 2013] and the short timescales on which neuronal signals need to be classified for clinically relevant brain-computer interfaces (BCI). To increase the signal-to-noise ratio, ECoG arrays are mostly placed below the dura mater, to avoid attenuation of the signal by the barrier of the dura. Opening the dura usually does not constitute a limiting factor for perioperative ECoG, whereas it may create a significant drawback for long-term recordings with regard to invasiveness and related clinical complications [Lesser & Arroyo 2005]. As an alternative, multielectrode arrays may be placed on top of the dura to record the epidural field potential (EFP), thus minimizing the risk of side effects for chronic applications.

In the motor domain, EFPs were successfully used to decode hand and arm movements [Flint et al. 2012; Marathe & Taylor 2013; Shimoda et al. 2012], and accurate decoding of motor commands with epidural signals was suggested as an important next step for viable long-term BCIs [Flint et al. 2017]. Yet, little is known about the selectivity and reliability of EFPs from other cortical domains and how specific single-trial EFPs reflect the local functional circuitry.

In the present study we make use of the high spatial resolution of primary visual cortex (V1) to investigate the functional specificity of single-trial EFPs recorded with a high-density epidural multielectrode array. Because visual stimulation elicits clearly localized neuronal activations, V1 is particularly suited to study whether these are preserved in the EFP response. We show that despite its obvious limitations, the EFP allows close-to-perfect classification of the spatial information of nine closely adjacent stimuli at the single-trial level. The results suggest a strong potential of EFPs for both the trialwise investigation of neuronal processes during sensory and cognitive processing and the further development of minimally invasive clinical approaches.

5.4 Materials and Methods

5.4.1 Subjects

All experimental and surgical procedures followed Directive 2010/63 issued by the European Commission and the Regulation for the Welfare of Experimental Animals issued by the Federal Government of Germany, and were approved by the local authorities. EFP recordings were performed in three male macaque monkeys (*Macaca mulatta*) ages 13, 11, and 11 yr old. All monkeys were familiar with laboratory standard procedures and a dimming task at fixation, and took part in additional projects not reported here. *Monkey 1 (M1)* and *monkey 3 (M3)* were separately housed in indoor compartments, in visual and auditory contact with other animals. *Monkey 2 (M2)* was housed in a group of four animals, in a large indoor room with daily access to an equally large outer compartment. All compartments were enriched by a manifold of monkey toys, puzzles, and climbing opportunities. During training and recording sessions, monkeys received water or diluted fruit juice as reinforcer for performing the behavioral task in the recording chamber. At nonrecording days, they received free fruits and liquid in their home compartment. Health and well-being was checked by daily monitoring and regular visits by veterinarians, and body weight was checked several times a week.

5.4.2 Surgical Procedures

For anchoring a head holder and the connector of the electrode array, all monkeys were implanted with a cap of acrylic cement (Palamed/Paladur), fixed by cortical screws to the animals' skull, following a previously published protocol [Wegener et al. 2004]. The EFP array was implanted after monkeys had been familiarized with the task and stimulus conditions reported below. Surgeries were performed under strictly sterile conditions. Anesthesia was initialized by a mixture of ketamine-medetomidine, maintained by propofol and remifentanyl, and supplemented by isoflurane. Postoperative analgesia was maintained by carprofen. For epidural implantation of the multielectrode array over V1, the stereotaxic location of the lunate sulcus was estimated before surgery on the basis of structural MRI scans. A trepanation over the left hemisphere was made using an ultrasonic bone-cutting device with a 0.3-mm cutter, ranging from a few millimeters anterior to the lunate sulcus to

the occipital ridge, and from 2 mm lateral to the midline to the lateral surface of the skull. The trepanation was extended in frontal direction into a $10 \times 15\text{-mm}^2$ stripe to place the flat ribbon cables connecting the electrodes with OMNETICS connectors (MSA-Components, Attendorn, Germany). After the array was placed in its desired position, the location of some spatially characteristic electrodes was stereotactically determined and/or photographed. Ribbon cables left the cranium through a small gap in the skull. The trepanation was closed by reinserting the bone piece (kept in Ringer lactate during the meantime) and kitting with bone cement, and additionally fixing the bone flap with a stripe of titanium, anchored by cortical screws. OMNETICS connectors were placed in a trough of the Paladur cap, filled with two-component glue (UHU 300 Endfest). Finally, a frame to hold a protective cap covering the connector was anchored. Additional ground electrodes were implanted over frontal cortex.

5.4.3 Data Acquisition

The multielectrode array (Fig. 1A) was developed, designed, and manufactured at the University of Bremen [Schander et al. 2019]. The design purpose was to match the size and shape of the macaque brain's occipital surface for covering V1/2 and part of V4 in one hemisphere with a high number of electrodes. Each array consisted of 202 gold electrodes with a $560\text{-}\mu\text{m}$ diameter, arranged in a hexagonal pattern with 1.8 mm center-to-center distance. The reference electrode was placed on top of the array and faced the skull. Electrodes were coated with poly(3,4-ethylenedioxythiophene) polystyrene sulfonate (PEDOT:PSS) to reduce the electrode/tissue impedance [Pranti et al. 2018]. The substrate material was the polymer polyimide with a total layer thickness of 10 μm . Ground electrodes over frontal cortex were coated with PEDOT:PSS, too.

Recordings were performed with a sampling rate of 25 kHz. Pre- and main amplification (10 times, 5,000 times) and filtering (1 Hz to 5 kHz) was performed using equipment from Multichannel Systems (Reutlingen, Germany). The EFP signal, the analog eye position channels from a custom-made video-oculography system, and a 50-Hz power line-derived signal were stored on a computer for offline analysis. Data were recorded in multiple sessions for up to several weeks. The first session was recorded 2 (*M3*), 5 (*M1*), and 18 weeks (*M2*) after array implantation.

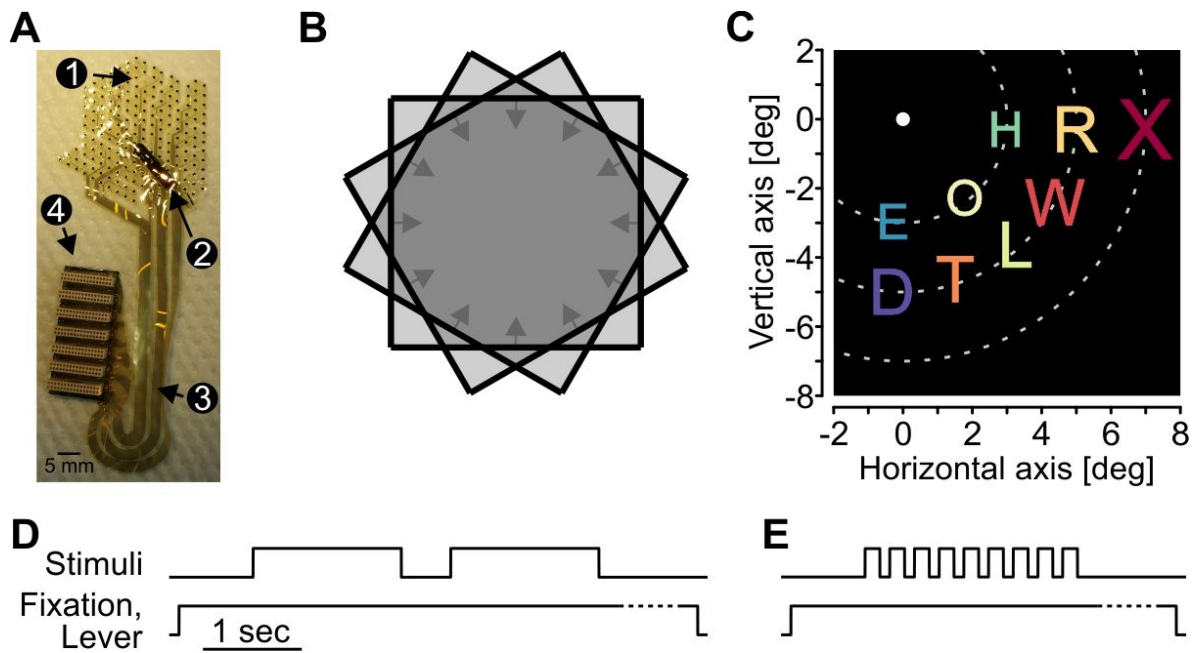


Fig 1: Epidural multielectrode array and visual stimulation. *A*: multielectrode array with 202 poly(3,4-ethylenedioxythiophene) polystyrene sulfonate (PEDOT:PSS)-covered gold electrodes (1), reference electrode (2), conductor tracks (3), and OMNETICS connectors (4). *B*: scheme of bar trajectories for the epidural field potential receptive field (ERF) mapping procedure. Black lines indicate differently oriented bar stimuli, arrows indicate motion directions, light gray-shading indicates areas covered by motion trajectories, and dark gray-shading shows overlap of all trajectories. *C*: spatial stimulus arrangement in the letter presentation procedure. Dotted lines indicate isoeccentricity lines used for stimulus placing and were not shown on the display. *D* and *E*: time course of trials in the mapping (*D*) and letter presentation procedure (*E*). During the mapping procedure, either 1 (*monkeys 1* and *3*) or 2 bars per trial (*monkey 2*; as shown in *D*) were presented. Dotted lines indicate randomized period at end of trial, after disappearance of visual stimuli.

5.4.4 Visual Stimulation and Behavioral Task

Visual stimuli were presented on a 21-in. cathode ray-tube monitor (resolution: $1,152 \times 864$ pixels, refresh rate: 100 Hz) placed 70 cm in front of the animal. Stimulation consisted of an automatic mapping procedure to characterize the size and location of EFP receptive fields (ERFs) and rapid presentation of nine different letter stimuli in the lower right quadrant of the visual field to investigate the spatial selectivity of single-trial EFP traces. The ERF mapping procedure was similar to a method recently introduced by Fiorani et al. [2014], described in detail in Drebitz et al. [2019]. Briefly, an array of 12 oriented, moving bars (size: *M1*, $0.24 \times 16.1^\circ$; *M2* and *M3*, $0.24 \times 24.2^\circ$) was placed over the lower right quadrant (centered at $8.1/-4.0^\circ$ for *M1* and at $2.4/-3.6^\circ$ for *M2* and *M3*). Bars were shown against a gray or black background (luminance: 2.5, 0, and 0 cd/m^2) with suprathreshold contrast (4.15, 7.85, and 7.85 cd/m^2 for *M1*, *M2*, and *M3*, respectively). Each bar moved along a trajectory of fixed length (20.2° , 19.4° , and 19.4°) in 1 of 12 directions, spaced by 30° , with a velocity of 8.1,

12.9, and 6.5°/s for *M1*, *M2*, and *M3*, respectively. The bars' motion trajectories formed a regular, 12-sided area of overlap with polygonal shape (Fig. 1*B*).

To investigate spatial stimulus selectivity of single-trial EFPs, differently colored, isoluminant (10 cd/m²) stimuli were shown at one of nine adjacent locations in the visual quadrant covered by the electrode array. Background luminance was the same as during the receptive field mapping procedure. Stimuli consisted of the letters D, E, H, L, O, R, T, W, and X in Arial font. Letters were placed on three imaginary rings around the center of the screen (Fig. 1*C*), with a center distance of 3.5°, 5.9°, and 8.2° for *M1* and 3°, 5°, and 7° for *M2* and *M3*. Letter stimuli in the inner imaginary ring had a height of 1.25° for *M1* and 0.95° for *M2* and *M3*. Stimulus size on the middle and outer imaginary ring increased by factors of 1.2 and 1.5, to account for the increase in receptive field size with increasing eccentricity [Hubel & Wiesel 1974b]. During presentation of visual stimuli, monkeys performed a dimming task at fixation. Monkeys were required to initiate a stimulus sequence by gazing at a central fixation spot (0.2° × 0.2°) and pressing a lever, and to respond to the dimming of the fixation spot by releasing the lever within 200-750 ms. Lever release outside the response window and eye movements of more than 1° away from the fixation spot caused termination of the trial. The temporal sequence in the mapping and letter presentation procedure is depicted in Fig. 1, *D* and *E*, respectively. Each stimulus sequence started with a blank screen of 750-ms duration, to provide a baseline period without visual stimulation for baseline correction of responses. During the mapping procedure, either one (*M1*, *M3*) or two bars after each other (*M2*) were shown, depending on the length of the motion trajectory. If two bars were shown in a single trial, they were separated by a blank interval of 500 ms. Motion directions were chosen randomly, and each direction was presented at least 10 times. During letter presentation, all nine stimuli were shown per sequence, each for 150 ms, separated by a blank interval of 100 ms, in pseudorandom order. For both the mapping procedure and the letter presentation, dimming of the fixation point occurred during an interval 0.1-1.1 s after disappearance of the last object shown. Subsequent sequences were separated by an intertrial interval of maximally 1.5 s. For *M1* and *M3*, fixation point dimming occurred during letter stimulus presentation in ~5% of the trials (catch trials). These trials did not enter data analysis.

5.4.5 Data Analysis

5.4.5.1 Preprocessing

All recorded signals were low-pass filtered (finite impulse response filter in forward and backward direction, 150-Hz cutoff frequency) and downsampled to 1 kHz. If applicable, 50-Hz noise was removed, based on the phase of the recorded power line signal. Electrodes located anterior to the lunate sulcus and electrodes with no or strongly noise-disturbed signals were excluded. The final database included 88 (*M1*), 174 (*M2*), and 137 electrodes (*M3*) delivering a significant ERF (see below) and covering V1.

5.4.5.2 EFP signals

We use the term EFP to denote single-trial signals at any given electrode following the onset of a stimulus. At each electrode, EFPs were baseline-corrected by subtracting the prestimulus signal amplitude (averaged over time and trials) from each trial's stimulus response. EFPs were then smoothed with a Loess filter with $\lambda = 2$ and $\alpha = 0.04$. All response features of the EFP that were used for classification (see below) were computed either from the whole time course of the trial between 25 and 175 ms after stimulus onset or, alternatively, from a shorter time period estimated by receiver operating characteristic (ROC) analysis (see below). EFP features that were tested included maximal amplitude and maximal absolute amplitude, averaged over the respective time bins, and negativity (most negative peak during the respective time period). Alternatively, the time course of the EFP modulation during the entire trial was used as feature.

5.4.5.3 Wavelet transformation

To obtain spectral information, EFPs of each electrode and stimulus sequence were wavelet-transformed using Morlet wavelets [Torrence & Compo 1998], defined as

$$\psi_0(\eta) = \pi^{-\frac{1}{4}} e^{i\omega_0\eta} e^{-\frac{\eta^2}{2}},$$

where ω_0 refers to the nondimensional frequency (set to 6 to cover 5-160 Hz in 35 exponentially increasing steps) and η refers to the nondimensional time parameter. The wavelet transform is defined as

$$W_t(s) = \sum_{t'=0}^{N-1} x_{t'} \psi_0^* \left[\frac{(t'-t) \Delta_t}{s} \right],$$

where x_t indicates the time series, Δ_t is the time step, s is the scale of the wavelet, and $*$ denotes complex conjugation. Wavelet transformation was performed on raw EFPs, as obtained after preprocessing. The resultant complex numbers W_t can be written as

$$W_t = at + ibt,$$

where a refers to the real part $Re\{W_t\}$ and b refers to the imaginary part $Im\{W_t\}$, both of which were used as candidate features for classification (see below). Wavelet power WP_t for each time bin t was calculated by

$$WP_t(s) = (2|W_t(s)|)^2.$$

For each frequency band, baseline correction was done by subtracting mean baseline WP from the mean WP_t during stimulus presentation, and subsequently dividing through it. Time-trigger information was used to cut the continuous data into stimulus-specific data fragments. Features extracted from the time course of the wavelet-transformed data included mean power in a given time-frequency range, their real and imaginary parts, and phase angle. Mean power was calculated by averaging over all bins of a given frequency range of the entire trial, from 25 to 175 ms after onset or, alternatively, over a limited time-frequency window estimated by ROC analysis (see below). Mean real or imaginary parts of W_t were computed accordingly. The phase angle of a given time-frequency range was expressed as the circular mean over the phase angles of individual bins, using the CircStat toolbox for MATLAB [Berens 2009]. Alternatively, the trial's time course of the mean power between 60 and 150 Hz (broadband gamma power, BGP) was used as a feature for classification (see below).

5.4.5.4 Receptive field mapping

Before computation of ERF maps, data with extraordinarily high continuous activity throughout the trial were excluded using an automated trial-rejection procedure. Subsequently, ERF calculation for each electrode was performed by first averaging mean WP_t across the BGP frequency range of all trials of a given motion direction. The response R at each location (x, y) was expressed as the geometric mean over the Z -transformed responses to the $n = 12$ motion directions at the time the bars crossed that location plus a constant value

of $c = 80$ ms to account for response latency. ERFs were defined as area of R_{map} with Z scores > 1 and minimal size > 1 deg² (Fig. 2, *A* and *B*). If more than one area was found, only the largest was chosen. A detailed description of the procedure is provided in Drebitz et al. [2019]. As a measure for the strength of the response relative to the background activity, we calculated the signal-to-background ratio (SBR) of ERFs by weighting power inside the ERF against power of the background:

$$SBR = \frac{\overline{WP}_{ERP} - \overline{WP}_{Base}}{\overline{WP}_{Base}}$$

where \overline{WP}_{ERP} and \overline{WP}_{Base} indicate mean power inside and outside ERF, respectively. All analytical procedures taking into account the ERF center refer to the center of activation (peak activation).

5.4.5.5 Support vector machines

Investigation of the spatial selectivity of single trials was performed by training support vector machines (SVMs) on data from the letter presentation procedure. No trial rejection for exclusion of data with artifacts was performed, to more closely simulate clinical conditions. Throughout the remainder of this article, we use the term “trial” to denote the response to a single stimulus in a stimulus sequence, between 25 and 175 ms after stimulus onset. Multiclass classification was based on radial basis function kernel, one-vs.-rest SVMs, as implemented in “libsvm” [Chang & Lin 2011]. For classifying single trials, we randomly chose 50 trials per stimulus condition for training one SVM for each of the nine stimulus conditions. If not stated differently, SVM parameters C and γ were chosen optimal for each training set using grid search with cross-validation (C represents the cost function and can be thought of as the penalty for misclassification during training, γ is the free parameter of the Gaussian radial basis function and can be thought of as the spread of the decision region). For each of the nine stimulus conditions, one test trial, not used in any of the training sets, was assigned to the stimulus with the highest probability for class identity. This procedure was repeated for each of the trials in the database. Per monkey, stimulus, and (where applicable) electrode, SVM classification performance was calculated by comparing assigned vs. real identity over all test trials.

5.4.5.6 Single-trial classification based on time course

To investigate the stimulus specificity of single trials, we first tested a signal's time course at individual electrodes of the three arrays. This was done by training SVMs as described above, using first the baseline-corrected EFP time course and second, the BGP time course of the wavelet-transformed data, recorded between 25 and 175 ms after stimulus onset. To keep computations within reasonable time, we initially used a limited range for SVM parameters C and γ for single-electrode classification. On the basis of these results, we then selected the best-performing electrode per stimulus (Best1 condition) or the concatenated response of the best three or best five electrodes per stimulus [Best3 (Best5) condition] for optimized classification, using a wider range of parameters C and γ (as explained earlier). We additionally concatenated the response vectors of all the best-performing electrodes into one long vector (Best1paired condition).

5.4.5.7 Single-trial classification based on distributed activity

As an alternative to using the time course of the signal, each trial was expressed as the distributed activity over the entire array. To this end, each electrode's time course was collapsed to a single value (using different response features, e.g., mean EFP amplitude or mean BGP power over time) such that each trial was now represented by a vector of length N , where N corresponds to the number of electrodes (see Fig. 4B). Training and testing of SVMs was performed as described earlier.

5.4.5.8 Initial selection of informative response features

t -Distributed stochastic neighborhood embedding (t-SNE; [Van Der Maaten & Hinton 2008]) was used for initial visual exploration of various candidate features (e.g., power in a specific frequency range). t-SNE is an unsupervised, nonlinear machine learning algorithm for dimensionality reduction, improving clustering of high-dimensional data in low-dimensional space by minimizing the distance of neighboring data points and maximizing the distance of distant points. The Perplexity parameter was set to 30, and maximal number of iterations was limited to 1,000.

5.4.5.9 Selection of most informative time (-frequency) windows

Much of the variability of neuronal responses is explained by internally driven activity [Fiser et al. 2004], and intrinsic signal fluctuations may cause stronger response modulations than

does the visual input [Lee et al. 2019]. To isolate informative, stimulus-specific time periods during stimulus responses from nonspecific intrinsic fluctuations in the signal, we applied ROC analysis. For each monkey, ROC curves were computed by testing the trials of one condition against the trials of all other conditions for each individual time bin. To improve reliability, temporal resolution of the data was averaged within successive bins of 5-ms length. The time course of the variance of the area-under-the-ROC curve (AUC) was then used to select putatively most informative time bins. For individual time bins, AUC variance is low in the absence of a visual response to any of the stimuli, when the ROC classifier is guessing and AUC values for all nine stimuli are close to 0.5. In contrast, AUC variance is increasing in the presence of a selective visual response, when there is good classification for one (or a small number) out of all stimulus conditions. Empirically, we found AUC variance to be more selective and more indicative of putatively informative time bins than were other measures such as mean or maximal AUC.

The time-resolved ROC analysis was performed separately for the EFP and for the power, phase angle, $Re\{W_t\}$, and $Im\{W_t\}$ of the individual frequency bands of the wavelet-transformed data. Subsequently, for each of the different measures, the grand variance of AUC values was calculated bin by bin over all stimulus conditions and electrodes of each array such that for each of the measures, high variance indicates bins with strong signal differences between electrodes and conditions, i.e., presumably more distinct responses to the test stimulus. All values were then Z-transformed to allow for a single selection criterion across features and electrode arrays. Aggregates of three or more bins with a Z score > 1.5 were chosen for further analysis. If more than one such aggregate was found for a given feature, the one with the highest peak variance was selected. Per electrode, final features are expressed as means over the selected time (or time-frequency) bins (e.g., mean power in a specific time-frequency cluster).

5.4.5.10 Selection of most informative electrodes

In analogy to identifying the most informative time bins, we identified electrodes carrying most of the information in the distributed activity vectors using the same ROC-AUCs. For each electrode, AUC values of the most-informative time (or time-frequency) bins were averaged for each stimulus and expressed as absolute deviation (Δ) from 0.5 (guessing). Electrodes were then ranked from maximum to minimum Δ for each stimulus, resulting in

nine different stimulus-specific rank orders. Most informative electrodes were selected on the basis of their rank for the response feature under investigation. Alternatively, to test the combination of different features, ranking could be based on the mean AUC values over these features.

5.4.6 Experimental design and statistical analysis

For each of the three monkeys, all electrodes delivering a significant visual response during the ERF mapping procedure were considered. Statistical analysis was performed by first testing for normal distribution of the data using Shapiro-Wilk tests. Nonparametric tests were used if the Shapiro-Wilk test rejected the null hypothesis of normal distribution at the $\alpha = 5\%$ significance level for at least one of the data sets. Effect size ω^2 [Hays 1963; Lakens 2013] for both parametric and nonparametric ANOVA (Kruskal-Wallis) was calculated by

$$\omega^2 = \frac{SS_b - df_b MS_w}{SS_t + MS_w}$$

with all values for calculation derived from the statistics of the preceding test. ω^2 ranges between 0 (no effect) and 1. For Wilcoxon signed-rank tests, effect size R was calculated by

$$R = \frac{|Z|}{\sqrt{N}},$$

where Z was derived from the Wilcoxon test statistics and N indicates the total number of samples. As a benchmark, effect size is considered to be small for $R = \sim 0.1$ and large for $R \geq \sim 0.5$ [Cohen 1988; Field 2013]. Where applicable, post hoc analyses were corrected for multiple comparison using Tukey's honestly significant difference criterion.

5.5 Results

The goal of the study was to assess the spatial specificity of visually driven EFPs from primary visual cortex and to quantify whether, and how reliable, spatial information can be drawn from single trials lasting no longer than 150 ms. To this end, we recorded visual responses from three monkeys with epidurally implanted multielectrode arrays over V1 and visually stimulated at nine close-by locations in one visual quadrant. In the following, we

first analyze size and coverage of ERFs, and then investigate the classification rate at single electrodes and at groups of selective electrodes by using machine learning algorithms trained on the time course of the signal. We then continue by analyzing the distributed activity over the whole array and apply ROC analysis to identify the most informative response features, time and time-frequency windows, and electrodes. Finally, we isolate the most informative data based on the results of the ROC analysis and show that these allow us to draw spatial information from single EFP trials with extremely high reliability.

5.5.1 ERF Coverage of the Epidural Multielectrode Array

To estimate the coverage of the visual field by the microelectrode array, we analyzed the location and size of areas with significant activation by using an automated bar-mapping procedure. The bar-mapping procedure elicited the strongest, and spatially most selective, responses in the broad gamma-frequency range (60-150 Hz, BGP). Accordingly, ERFs were defined by their mean activation in the BGP range (Z score > 1) and a minimum size (> 1 deg²). All analyses that follow were carried out on this set of electrodes with a significant ERF (88, 174, and 137 recording sites in *M1*, *M2*, and *M3*, respectively).

At some electrodes, responses to visual stimuli had a high SBR and ERFs were of rather limited size (Fig. 2A). At others, ERFs were larger and frequently covered the location of several of the stimuli intended for later visual stimulation (Fig. 2B). Based on the size and location of ERFs, we constructed activation maps quantifying the number of ERFs covering each location within the visually stimulated field. These maps show dense sampling at some locations and sparse sampling at others (Fig. 2, C and D, data from *M1* and *M3*), likely due to cortical magnification at fovea, actual coverage of the cortical surface by the array, and regular arrangement of array electrodes. As a consequence, the representation of the nine letter stimuli is expected to vary significantly over the array, not only with respect to location but also with regard to the number of electrodes carrying the signal and the separability of their representation from the representation of neighboring stimuli. This is illustrated in Fig. 2E, showing putative ERF activation maps for individual letter stimuli (data from *M2*). Maps were built by considering all ERFs with a center within 2° from the center of the respective letter stimulus. Based on the results of the bar-mapping procedure, these maps predict that some stimuli will be represented by a large number of electrodes (e.g., letters E and O),

5.5 Results

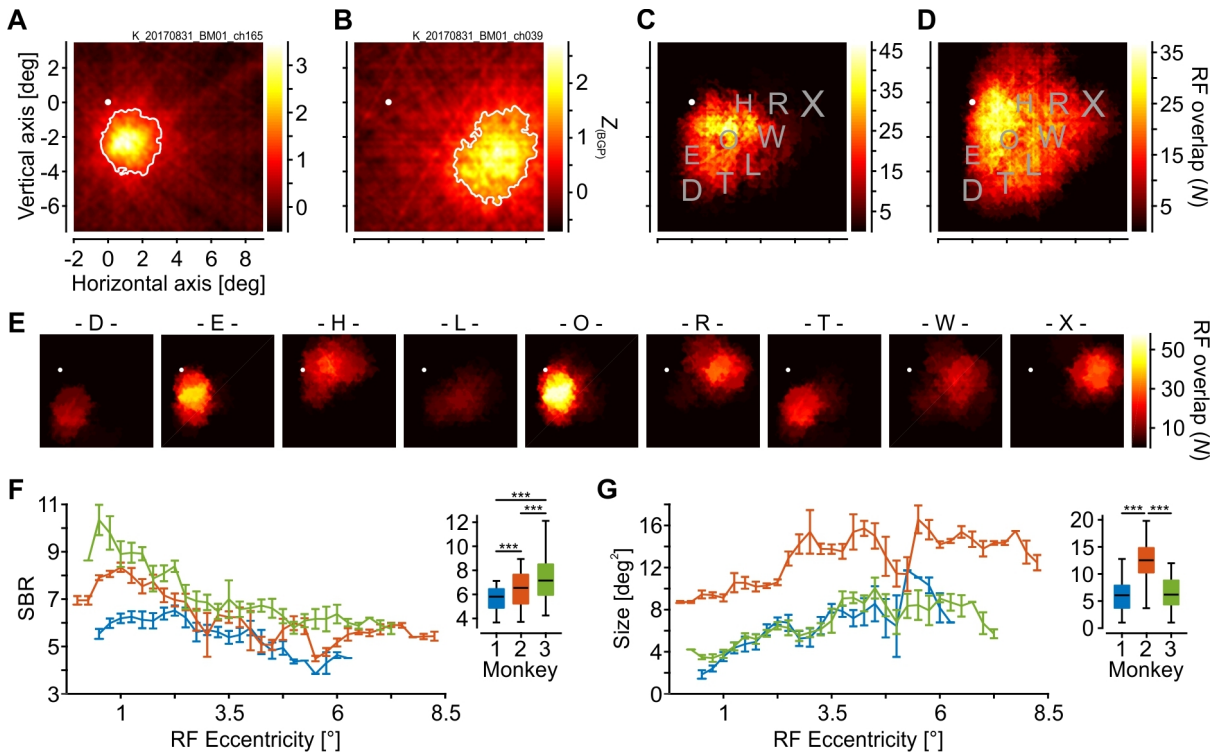


Fig. 2: Epidural field potential receptive field (ERF) coverage of visual fields and basic ERF characteristics. *A*: visual response map of one example electrode in *monkey 2* showing well-defined area with significant evoked response (ERF; white border) obtained from an automated bar-mapping procedure. *B*: single, rather large ERF mapped from another electrode in *monkey 2*. *C* and *D*: map of merged ERFs from *monkey 1* (*C*) and *monkey 3* (*D*). Color code indicates the number of overlapping ERFs at each position. Letter stimuli are shown for reference only and were not used for mapping ERFs. *E*: same as *C* and *D*, but referenced to the location of individual letter stimuli, as used in subsequent procedures. For each letter position, all ERFs with center coordinates within 2° from the stimulus center were considered. Color axis is identical for all maps. White spots in *A-E* indicate fixation point. Scaling of x - and y -axes is indicated in *A-E*. *F* and *G*: signal-to-background ratio (SBR; *F*) and size (*G*) as a function of ERF center eccentricity (line plots) and averaged over all electrodes per animal (box plots). Error bars in line plots are SE. Horizontal black lines in box plots indicate median, boxes indicate 25th and 75th percentiles, and whiskers show full range of data. *** $P < 10^{-3}$, significant differences. Z_{BGP} , Z -transformed broadband gamma power.

whereas others will be represented by a few electrodes only (e.g., letters D and L), due to the size of ERFs or location of a stimulus at the edge of the visual field covered by the array. The results also predict that some stimuli are likely to activate electrodes with strongly overlapping ERFs or to activate the same electrodes (e.g., letters D and T). Thus size and distribution of ERFs indicate that some letters are likely to yield better classification results than others. Additionally, we analyzed SBR and size of ERFs as a function of ERF eccentricity (using a sliding boxcar window of 2° in width, shifted in steps of 0.25°). For each array, SBR was significantly larger at more foveal locations and decreased toward the periphery [least-square linear regression, slope = $(-0.09 -0.08 -0.1.4)$, all $F > 51.8$, $P < 10^{-7}$, adjusted $R^2 > 0.61$; Fig. 2*F*]. Between arrays, SBR was significantly different (Kruskal-

Wallis, $\chi^2 = 55.41$, $P < 10^{-12}$, $df = 2$, $\omega^2 = 0.135$), with SBR being larger in *M3* than in both *M1* and *M2* (both $P < 10^{-3}$), and also being larger in *M2* compared with *M1* ($P < 10^{-4}$). For ERF size, we found a significant increase toward the periphery for *M1* and *M2* [slope = (0.29 0.17), $F > 33.1$, $P < 10^{-5}$, adjusted $R^2 > 0.49$], whereas the fit for *M3* was too poor (adjusted $R^2 = 0.09$) to draw a conclusion (Fig. 2*G*). Median ERF size over all electrodes of the arrays was 6.1, 12.5, and 6.2 deg² in *M1*, *M2*, and *M3*, respectively. Statistically, this was a significant difference between arrays (Kruskal-Wallis, $\chi^2 = 217.45$, $P < 10^{-47}$, $df = 2$, $\omega^2 = 0.543$), and ERF size was larger at array electrodes in *M2* than in *M1* and *M3* (both $P < 10^{-9}$), whereas it was not different between *M1* and *M3* ($P = 0.686$). Thus, for the 3×9 stimulus conditions in the experiments that follow, analysis of ERF parameters suggests considerable differences for the representation of the letter stimuli across individual arrays as well as between monkeys. The variance in ERF parameters probably reflects differences in the distance between electrodes and cortical tissue, either due to technical reasons, such as imperfect fitting of the array to the dural surface, or due to variances in dura thickness or volume of subdural space. High variability in ERF size, SBR, and coverage is likely influencing the reliability by which single-trial information can be read out from individual electrodes and (regarding the general usability of EFPs for basic and clinical science) addresses the question whether it is possible to find a robust approach to deal with this.

5.5.2 Time Course-Based Classification of Single Trials

To investigate stimulus specificity of single-trial signals recorded with epidural electrodes, we flashed visual letter stimuli at nine closely adjacent locations in the lower right quadrant of the visual field. Stimuli at each location were shown for 150 ms, separated by a blank screen of 100 ms in length (Fig. 1, *C* and *E*). They were isoluminant but differed in color and shape. For two example electrodes and three letters each, Fig. 3*A* shows the EFP between 25 and 175 ms after onset of 10 randomly drawn trials per condition, and the corresponding ERF. Note that ERFs were recorded in a separate session. The electrode in Fig. 3*A*, *top* (from *M1*), represents a class of recording sites with rather unspecific and strongly fluctuating responses, with no clear differences between responses to stimuli covering the ERF and stimuli outside the ERF. In contrast, the electrode in Fig. 3*A*, *bottom* (from *M2*), represents a class of recording sites with clearly modulated EFP traces in response to the stimulus covering the ERF. Yet, trials with a similar time course were acquired also in response to

5.5 Results

close-by stimuli. Figure 3B shows two more examples using wavelet-transformed derivatives of the EFP. Time-frequency plots averaged over all trials per condition reveal that most of the signal's modulation occurs at gamma frequencies > 60 Hz, as covered by the BGP range used

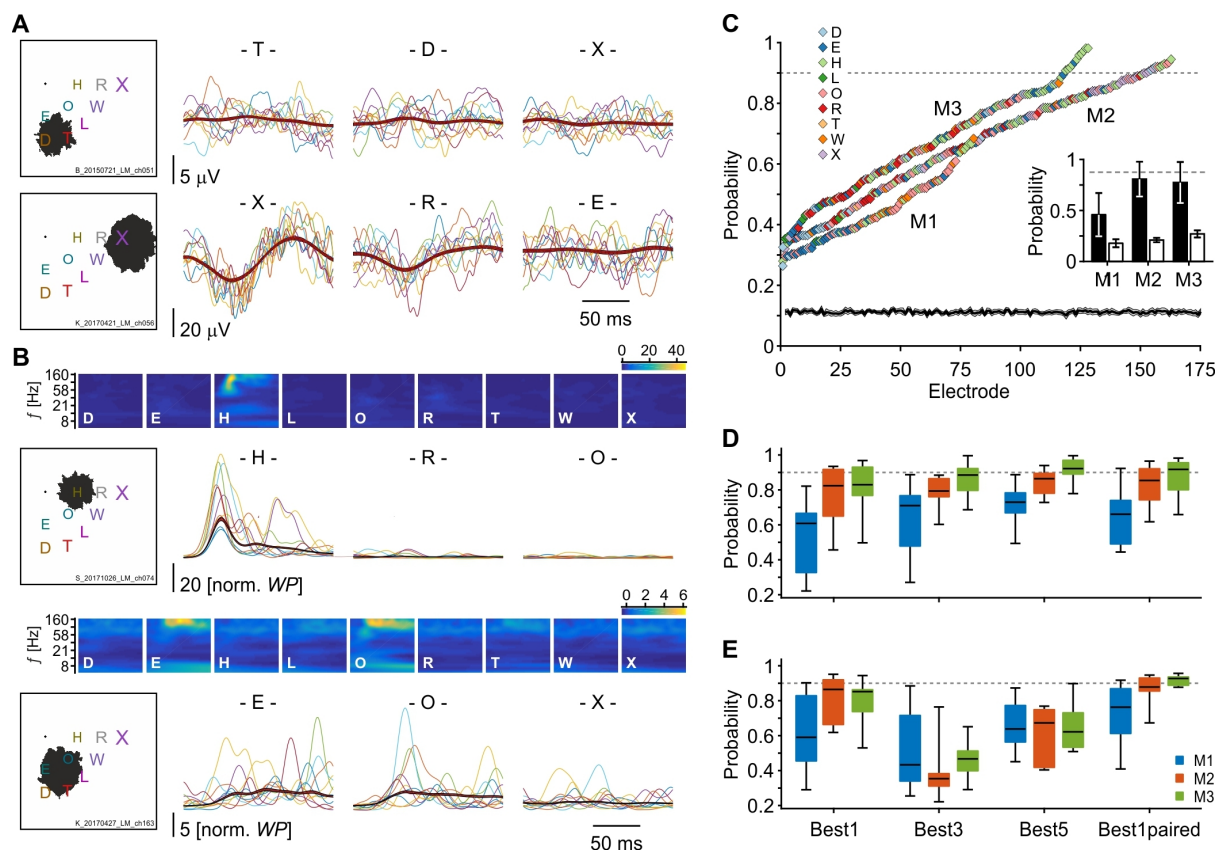


Fig. 3: Single-trial classification performance at single electrodes. *A*: stimulus location and epidural field potential (EFP) receptive field (ERF; black areas) for 2 example electrodes (*left*), taken from *monkey 1* (*M1*; *top*) and *monkey 2* (*M2*; *bottom*). For each electrode, the EFP signal of 10 randomly drawn trials for 3 of the 9 stimuli are shown (*right*). Thick red lines indicate mean \pm SE over all trials of the respective condition. *B*: same as *A*, except the broad gamma power (BGP) signal of 10 randomly drawn trials are shown (*right*) for 2 more example electrodes, taken from *monkey 3* (*M3*; *top*) and *M2* (*bottom*). Color images (*top* panel for each monkey) show the time-frequency plot of the same 2 electrodes in response to each of the 9 stimuli, averaged over all trials, during the time period 25-175 ms after stimulus onset. Note the strong stimulus-induced modulation in the BGP range and the absence of modulation in other frequency (f) ranges. Color code indicates normalized power. *C*: EFP-based single-trial support vector machine (SVM) classification performance for all individual electrodes. Electrodes are sorted by probability for getting the true stimulus identity, individually for each animal. Colors indicate the identity of the stimulus that was most often correctly classified. *Inset*: closed bars indicate mean (\pm SD) classification performance when the best letter stimulus of each electrode was considered, for each individual array; open bars indicate mean (\pm SD) performance for all other stimuli at the same electrodes. Solid line and shading at *bottom* indicate mean (\pm SE) chance level, estimated by classifying *M2* single trials with shuffled labels. *D* and *E*: mean SVM classification performance for each of the 3 animals with optimized parameters C and γ (see Materials and Methods, *Data Analysis, Support machine vectors*), summarizing the results for both EFP (*D*) and BGP (*E*). SVMs were trained using either only the electrode with the highest performance for each of the 9 letters (Best1), the concatenated responses of the best three (Best3) or best five (Best5) electrodes for each of the letters, or the concatenated responses of the 9 best electrodes from the Best1 comparison (Best1paired). Horizontal black lines in box plots indicate median, boxes indicate 25th and 75th percentiles, and whiskers show full range of data. Dashed lines in *C-E* indicate 90% performance level. norm. *WP*, normalized wavelet power.

for ERF analysis. At some electrodes where the ERF covered a single stimulus, the BGP response was highly selective (Fig. 3B, *top*). At other electrodes, however, single-trial responses were more variable in strength and timing, and very similar responses were elicited by neighboring stimuli and occasionally also by stimuli presented at clearly distant locations (Fig. 3B, *bottom*).

To investigate the information content of these signals, we trained SVMs on the time course from 25 to 175 ms of both the EFP and its wavelet-transformed BGP derivative, and tested SVM performance for each electrode separately. We classified a total of 6,552 trials (2,763, 1,800, and 1,989 trials from *M1*, *M2*, and *M3*, respectively). For the EFP (Fig. 3C), we found 13 (7.5%) and 11 (8%) electrodes in *M2* and *M3*, respectively, performing at 90% or higher (see Materials and Methods). Yet, these electrodes only represented 4 (*M2*) and 2 (*M3*) different stimuli, whereas maximal performance for 4 of the 12 remaining stimuli of these two monkeys, and for all the stimuli of *M1*, stayed below 75%. Performance averaged over the best electrodes per letter stimulus was 46.1, 81.1, and 77.7% in *M1*, *M2*, and *M3*, respectively. In comparison, mean performance of the same electrodes in response to all other letters was 17.9, 21.1, and 27.1% (Fig. 3C, *inset*). Use of the BGP time course instead of the EFP trace improved the classification rates such that now five (*M2*) and four (*M3*) stimuli were correctly classified at a performance level of 90% or higher. Yet, performance for half the stimuli of *M2* and *M3*, and for all stimuli of *M1*, still remained below that level.

Because intracortical V1 signals are spatially highly specific, we considered a detection rate of 90% or better as the wished-for classification performance for EFPs. To achieve better classification performance, we therefore selected the best electrode for each of the nine stimuli and retrained SVMs with optimized parameters C and γ . We also estimated classification rates using the Best3 and Best5 electrodes of each stimulus, as well as the concatenated responses of the best single electrodes per stimulus (see Materials and Methods; Fig. 3, *D* and *E*). Statistical analysis revealed that the latter delivered the highest classification rate for both EFP (mean: 78.6%) and BGP (mean: 85.6%) and that BGP allowed for significantly better performance than the EFP (Wilcoxon signed rank, $Z = 6.13$, $P < 10^{-9}$, $R = 0.217$, $N = 399$). Yet, 48% of the stimulus locations did not reach the 90% performance level, and 18.5% stayed below 75% correct. Thus, given the high variability of

the signal, using the time course at single electrodes does not allow sufficient classification of single-trial information.

5.5.2.1 Representation of single trials by patterns of distributed activity

As an alternative to single electrode-based classification, individual trials may be described as distinct patterns of distributed activity, due to the large cortical surface covered by the electrode arrays. Figure 4A, *top* and *bottom*, shows the mean EFP and BGP amplitude, respectively, in response to stimuli at three different locations, averaged over ~100 trials of *M1* (EFP) and *M3* (BGP). It is obvious from these examples that the distinct, stimulus-specific spatial distribution of activity constitutes a valid source of information for classifying different stimulus conditions when averaged data are considered. If similarly distinct patterns were also present in single trials, they might establish a more robust stimulus representation than the signals' time course.

We therefore collapsed the signals' time course at each electrode to a single value (e.g., mean EFP amplitude, negativity, mean power in a certain frequency range, etc.) and used the distribution of this feature over the entire array as the representation of a single trial (Fig. 4B). This way, each trial is described by a vector of length N , where N corresponds to the number of electrodes. We first visually explored different response features using t-SNE [Van Der Maaten & Hinton 2008]. t-SNE is a nonlinear, nonsupervised machine learning algorithm for embedding high-dimensional data in low-dimensional space, providing a visual means to investigate whether data contain sufficient structure to distinguish different stimuli with some reliability. For the majority of features, there was no or very weak clustering (Fig. 4C, *left* and *middle*), whereas for some we found distinct, well-separated clusters (Fig. 4C, *right*). Thus expressing a single trial as a pattern of distribution of a given response feature over the array may allow higher classification reliability to be achieved. At the same time, however, a significant number of trials was assigned to the wrong cluster even for overall well-clustering features, or clusters had considerable overlap. A possible reason for this is the inclusion of time periods containing random signal fluctuations rather than stimulus-specific information when the whole time course of the signal was considered for feature extraction. Therefore, a more distinct representation of each stimulus might be achieved by getting rid of such noninformative trial periods.

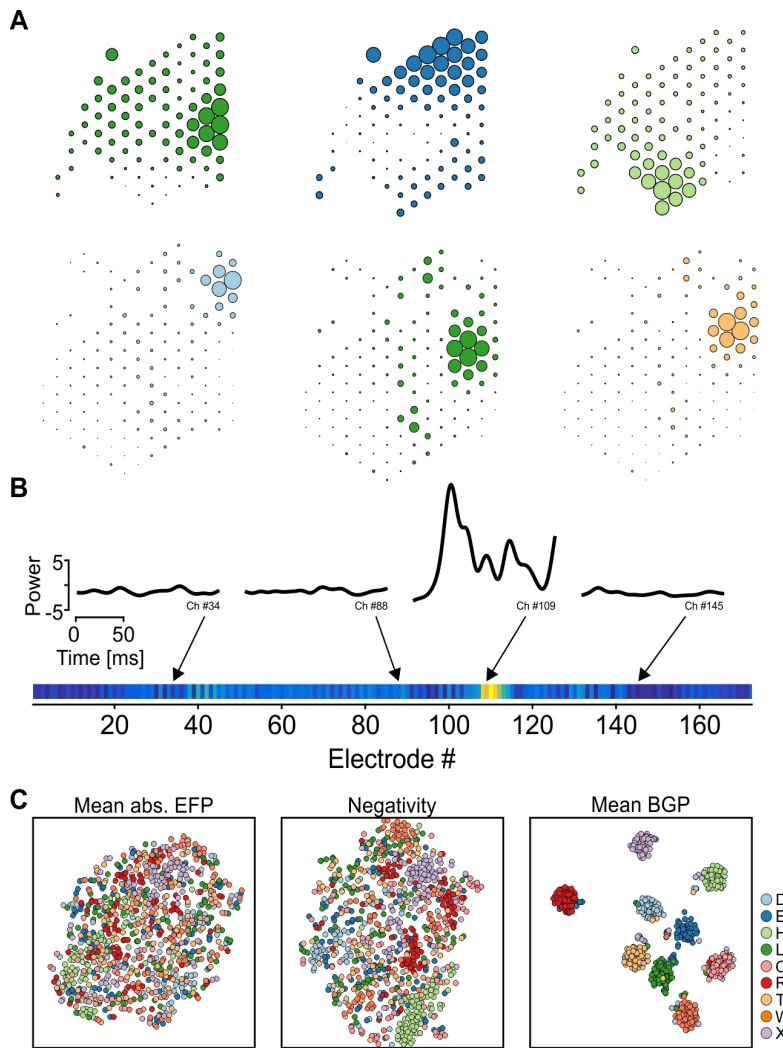


Fig. 4: Spatial distribution of response features. *A*: example plots of the spatial distribution of relative mean epidural field potential (EFP) over the array of *monkey 1* (*M1*; top) and relative broad gamma power (BGP) over the array of *monkey 3* (*M3*; bottom), averaged over the time period 25-175 ms after onset of all trials of the respective stimulus. All values were squared for illustration purposes. Color code is indicated in *C*. *B*: example for construction of trial vectors representing the distributed activity over the array (distributed activity vectors). For each electrode, the time course of the signal was collapsed to a single value [e.g., mean absolute (abs.) EFP or mean BGP] or, alternatively, only a single value was taken from the response (e.g., negativity). *C*: *t*-distributed stochastic neighborhood embedding (t-SNE) plots for 3 different response features (data taken from *M3*), each represented as the distributed activity of a given stimulus feature over the entire array, as shown in *B*. Each circle represents a single trial. Well-defined clusters indicate good separability. Ch., channel.

5.5.3 Identification of Most Informative Features and Time Bins Across the Entire Array

To determine the stimulus selectivity of individual time bins, we performed a time-resolved ROC analysis to find the most informative time periods to be used for stimulus classification. This was done separately for the EFP, the different frequency ranges of the wavelet-transformed data, phase angles, and both the real and imaginary parts of the wavelet transformation, $\text{Re}\{W\}$ and $\text{Im}\{W\}$. Before ROC, each signal's time course was averaged into bins of 5 ms. Subsequently, for each feature, electrode, and time bin, we calculated the AUC. Figure 5A provides an example for the EFP at one example channel of *M2*, averaged over all trials per stimulus condition, and the ROC curves for three 5-ms time bins, taken from the early, middle, and late response at that electrode. For the early and late time bins, the ROC curve for any of the nine stimuli was close to the diagonal, resulting in very similar

5.5 Results

AUC values around 0.5 and indicating poor separability of the stimuli. Yet, for the time bin around 55 ms, the EFP signal showed a strong negative deflection in response to one of the nine stimuli, providing a rather large AUC value, whereas AUC values for all other stimuli remained around 0.5. The resultant distribution of AUC values possesses a higher variance than did the AUC distribution of the other two time bins (cf. *insets* in Fig. 5A). We used this AUC variance to distinguish putatively informative from noninformative time bins, with high variance indicating stronger and potentially more stimulus-specific signal deflections than low variance. Following ROC analysis of all time bins and electrodes, we calculated the time-resolved grand average of AUC variance over all electrodes and finally Z-transformed this average to allow for better comparability across features and monkeys.

For the EFP, the resultant time course of AUC variance shows a strong positive peak around 80 ms after stimulus onset. Applying a threshold of 1.5 labels a time window of ~25 ms as the putatively most informative epoch (Fig. 5B). Likewise, the AUC variance for different frequency bands of the wavelet-transformed data indicates a period of ~60 ms in the high-gamma frequency range (> 100 Hz) and another, rather long period in the alpha frequency

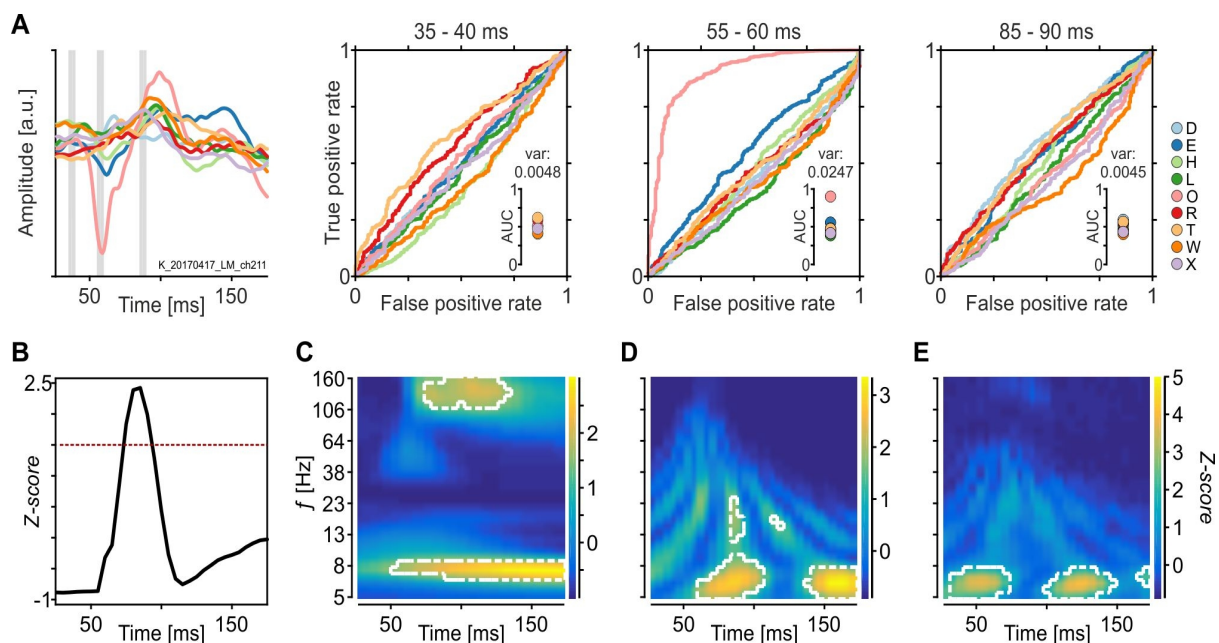


Fig. 5: Identification of most informative time epochs. *A*: mean epidural field potential (EFP) traces for each of the 9 stimuli at 1 example electrode from *monkey 2* (*M2*; left) and receiver operating characteristic (ROC) analysis of three 5-ms time bins, indicated by shaded areas in plot at left. *Insets* in ROC plots show distribution and variance (var.) of area-under-the-curve (AUC) values. *B*: Z-transformed grand mean of the variance over AUC values for *M2*, with all electrodes considered, after binwise ROC analysis of EFP amplitudes. *C-E*: same as in *B* but for time-resolved variance in power (*C*), real part of the wavelet coefficient (*D*), and phase angles (*E*) at 35 different frequency (f) bands. Dashed lines in *B-E* indicate threshold at $Z = 1.5$. a.u., Arbitrary units.

range as candidate time-frequency windows of high sensitivity (Fig. 5C). Corresponding analyses were done for the wavelet terms $\text{Re}\{W\}$ (Fig. 5D) and $\text{Im}\{W\}$, and phase angles (Fig. 5E). The selected epochs and frequencies were then used to trialwise calculate the feature values across the array for various candidate features of both the EFP signal and its wavelet-transformed derivatives, as illustrated in Fig. 4B.

5.5.4 Classification Performance for ROC-Based Feature Selection

For each of the nine letter stimuli, Fig. 6A shows the resultant high gamma power (HGP) distribution over all the electrodes of *M2* for each of 10 example trials per stimulus. Each electrode's value represents power in a single trial, averaged over the most informative time-frequency bins estimated by the ROC analysis. Although some electrodes were generally providing higher HGP than others, the specific pattern in response to each of the nine letters was quite distinct. Training the SVM with these feature vectors yielded a mean single-trial classification performance of 87.2% based on the EFP and 93.4% based on HGP, averaged over all stimulus conditions and monkeys. This was a significant improvement for HGP (Wilcoxon signed rank, both $Z = 4.35$, $P < 10^{-4}$, $R = 0.081$, $N = 27$) compared with SVM performance based on the signals' time course (cf. Fig. 3E, using the best electrode combinations per animal), and a corresponding statistical trend for the EFP (cf. Fig. 3D; $Z = 1.73$, $P = 0.084$). Additionally, ROC-based selection of specific time and time-frequency windows for extracting the values used in the distributed feature vectors outperformed whole trial-based value extraction for most of the response features we tested (Fig. 6B). HGP turned out to be very informative even when estimated by averaging all time bins of a trial, whereas all other features strongly benefited from reducing the noise by discarding noninformative time bins. Thus, using the spatial distribution of signal features and ROC-based selection of time bins allowed us to identify five response features with correct classification of more than 80% of single trials, averaged over all stimuli and arrays. Among these were three features derived from the wavelet-transformation (HGP, $\text{Re}\{W\}$, and $\text{Im}\{W\}$) and two features from the EFP (mean amplitude and maximum negativity).

The response to each of the stimuli, however, was carried by only a small group of electrodes, whereas many electrodes did not respond, as expected due to the limited size of ERFs (Fig. 6A). Therefore, in analogy to selection of the most informative time bins, we next

5.5 Results

isolated the most informative electrodes for representation of distributed feature vectors and discarded all others. To this end, we first chose the three features that allowed for best classification (HGP, $\text{Re}\{W\}$, and EFP amplitude). For classification, we started with the full set of electrodes and, per letter stimulus, used either a concatenated vector constructed from

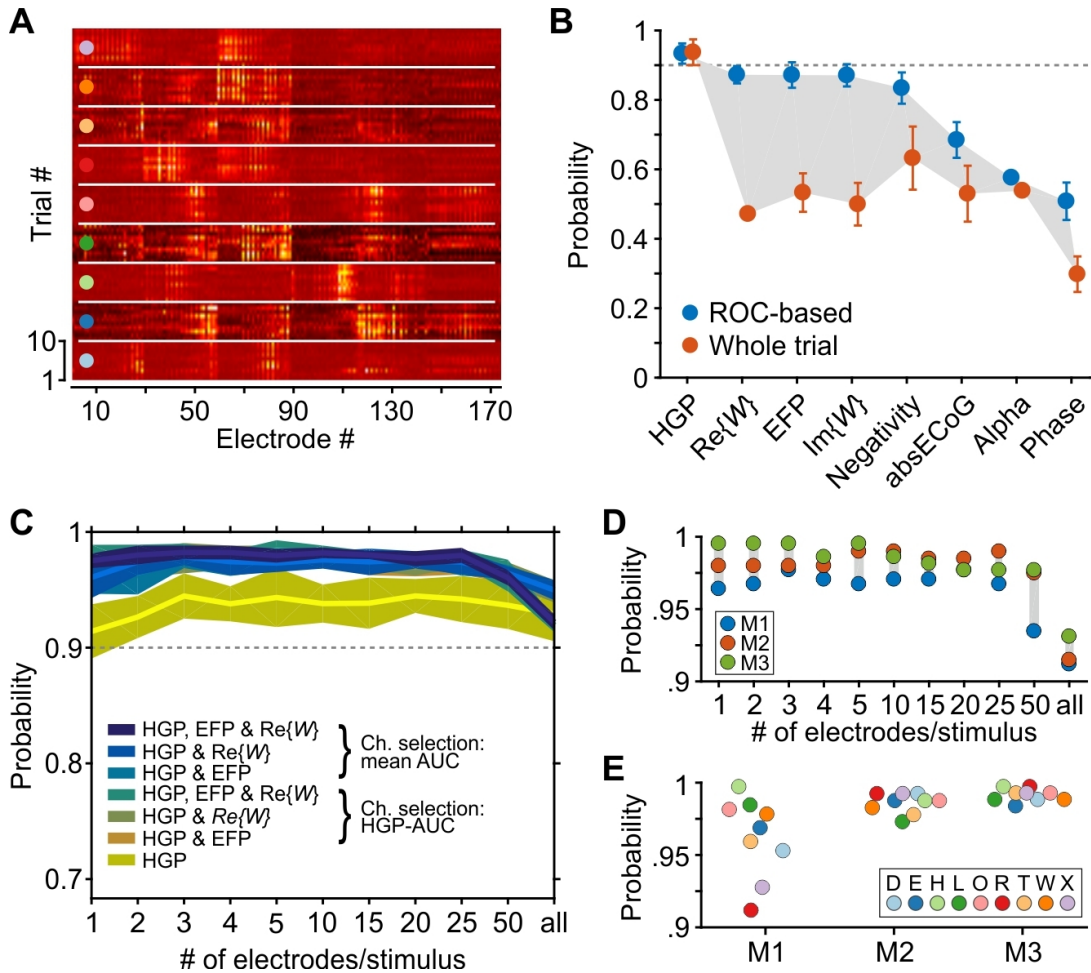


Fig. 6: Identification of most informative response features and electrodes. *A*: example trials from *monkey 2* (*M2*), represented as the distributed activity of high gamma power (HGP) over all electrodes of the array, sorted by stimulus condition. Only threshold-surpassing time-frequency bins as derived from preceding receiver operating characteristic (ROC) analysis were considered for construction of the distributed activity vectors. *B*: classification results for 8 candidate features using the distributed activity vectors constructed from ROC-based selection of time (or time-frequency) windows, compared with classification using vectors constructed from all time bins of the trial (of the same frequency range, where applicable). *C*: classification results for different combinations of the best response features, as derived from *B*, for different numbers of electrodes used to construct the distributed activity vectors. Electrodes were selected on the basis of either area-under-the-curve (AUC) variance for HGP or the mean AUC variance of the combined features. *D*: classification rates for the numerically best feature combination [HGP, real part of the wavelet coefficient ($\text{Re}\{W\}$), and epidural field potential (EFP) amplitude; electrodes selected by mean AUC] as a function of the number of electrodes used to construct the distributed activity vectors, individually for each animal. Each circle indicates median performance over the 9 stimulus conditions. *E*: classification rates for individual stimulus conditions based on the best selection of electrodes per animal. Note that in *D* and *E*, the *y*-scale for probability is limited to the range of 0.9 to 1. absECoG, absolute electrocorticography; Ch., channel; $\text{Im}\{W\}$, imaginary part of the wavelet coefficient

the mean HGP of each electrode or, alternatively, a concatenated vector using HGP plus either one or both of the other two features. Second, to reduce the number of electrodes, for each of the stimuli we stepwise excluded electrodes with the lowest AUC values and performed stimulus classification on vectors constructed from a decreasing number of electrodes with $N = (50, 25, 20, 15, 10, 5, 4, 3, 2, \text{ and } 1)$. Third, to select the most informative electrodes, we used two different procedures by sorting electrodes either by their HGP-AUC values only or, alternatively, by the mean AUC values across the two or three combined features. In summary, we tested different feature combinations on different sizes of electrode pools and used different procedures to select the electrodes that remain in the pool. We thus ended up with 77 different data sets of feature values constructed from ROC-based selection of time and time-frequency windows, all of which were then tested for classification of single trials. The results are summarized in Fig. 6C, showing the mean over the median performance per animal.

This analysis provided several insights. First, for nearly all of the data sets, mean performance was clearly above our criterion level of 90% (Fig. 6C). When only HGP was used as a response feature, minimum median performance was 87.3% (*M1* for electrode pool size of 1 per stimulus) and maximum median performance was 97.25% (*M3* for electrode pool size of 5 per stimulus). Interestingly, adding information from at least one of the other two features (EFP and/or $\text{Re}\{W\}$) increased classification performance significantly (Kruskal-Wallis, $\chi^2 = 51.17$, $P < 10^{-8}$, $\omega^2 = 0.2$, $\text{df} = 6$). Post hoc tests showed that HGP alone was worse than any other feature group (all $P < 10^{-3}$), whereas none of the remaining groups was different from another (all $P > 0.45$). Second, there was no significant difference between the two procedures to select the most informative electrodes (Wilcoxon signed rank, $Z = 1.404$, $P = 0.16$, $R = 0.007$, $N = 99$). Both methods (selection on either HGP-AUC values or mean AUC values of the concatenated features) worked equally well. Third, the number of electrodes used for classification made a significant difference (Kruskal-Wallis, $\chi^2 = 45.23$, $P < 10^{-5}$, $\omega^2 = 0.16$, $\text{df} = 10$). Post hoc tests revealed that using all electrodes to build the distributed activity vectors for each of the stimuli resulted in a significantly worse classification performance than using a limited number of more informative electrodes per stimulus (all $P < 0.044$ for ≤ 25 electrodes). All other performance comparisons regarding the number of electrodes used for classification were not significantly different. Numerically, however, performance was poorest for the extreme groups ($N \leq 2$ and $N \geq 50$ electrodes per

stimulus) and was higher and almost identical for pool sizes in between ($N = 3, 4, 5, 10, 15, 20$, or 25 electrodes per stimulus; largest median performance difference: $< 0.35\%$). Figure 6D provides a corresponding example for the numerically best feature combination (concatenated vectors of HGP, $\text{Re}\{W\}$, and EFP amplitude per electrode, and channel selection via HGP-AUC). Fourth, the high classification performance was true for each of the nine stimulus conditions in each of the three animals. When the numerically best number of electrodes per animal was selected, each individual stimulus condition was correctly classified in $> 90\%$ of the trials. For 25 of the 27 stimuli, classification reached the 95% performance level, and for 13 stimuli it even reached the 99% performance level (Fig. 6E). This was a highly significant performance increase compared with the concatenated time course of the best-performing electrodes (cf. Fig. 3E, Best1paired condition; Wilcoxon signed rank, $Z = 4.54$, $P < 10^{-5}$, $R = 0.084$, $N = 27$). Thus the strong performance difference for the arrays of the three monkeys as seen when the entire time course of the signal was used (cf. Fig. 3, D and E) disappeared almost completely, and classification performance for the three arrays was statistically not different anymore (Kruskal-Wallis, $\chi^2 = 3.75$, $P = 0.15$, $\text{df} = 2$).

In summary, limiting the data to the most informative time (time-frequency) windows and electrodes by, in our case, simple ROC analysis, and combination of two or three response features allowed for superb classification rates of the EFP signal, proving that extremely short data fragments of visually driven, single-trial, epidurally recorded potentials convey highly localized information and represent the underlying functional architecture with high selectivity.

5.5.5 Learning-Free Decoding and Implications for Future Development of Epidural Arrays

Because selectivity and reliability of signal features are of outstanding importance for any scientific, technical, and clinical application using epi- or subdurally implanted arrays, we finally investigated the question to what extent design factors of the arrays influence decoding performance. For visually evoked signals, decoding performance will be directly related to 1) sufficient activation of ERFs by the stimulus, 2) robustness against small spatial displacements of the stimulus relative to the center of gaze, and 3) robustness against signal variations. All of these factors place constraints for the electrode density of the array. This is illustrated by Fig. 7A, showing ERFs with a peak sensitivity within 1° of visual angle of the

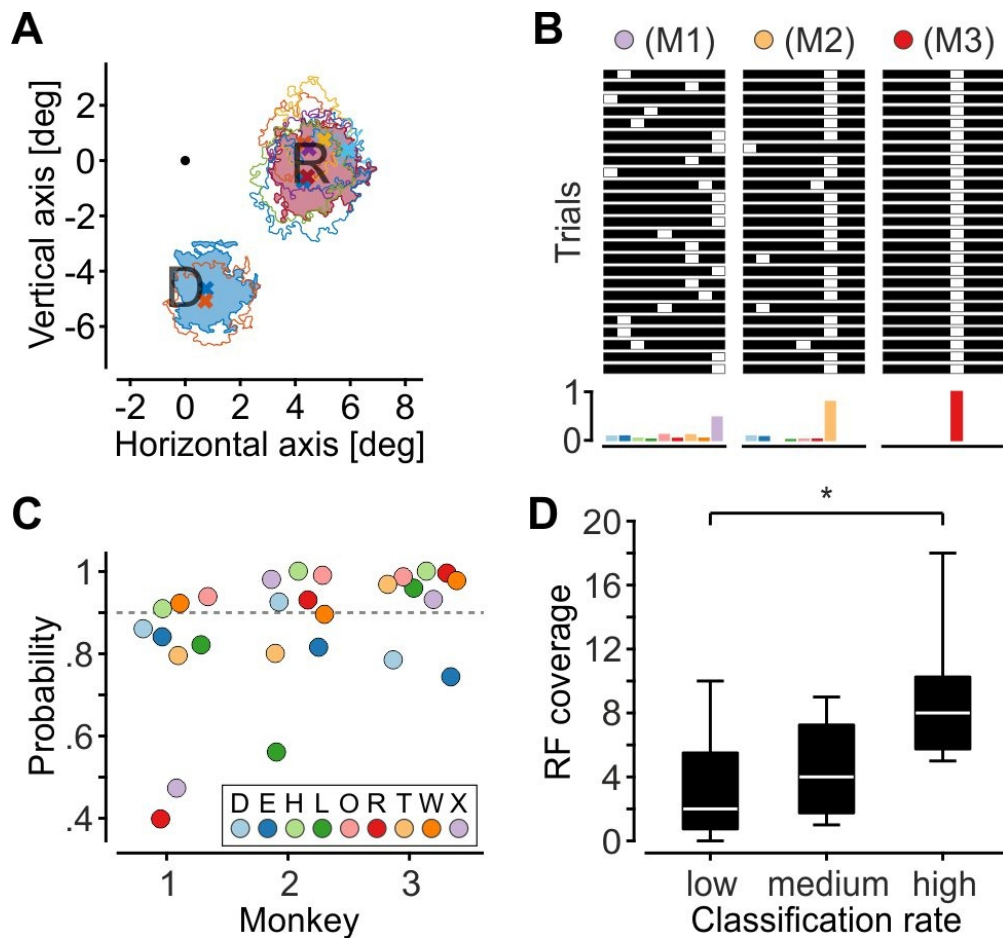


Fig. 7: Relation between classification performance and epidural field potential receptive field (ERF) coverage. *A*: ERFs covering the location of 2 example stimuli, with ERF centers located within 1° radius of the letter center. Crosses indicate ERF centers. Filled areas indicate ERFs used for classification. Colors are randomly drawn and do not relate to stimulus conditions. *B*: results of a binary classifier for 25 randomly drawn trials for 3 example stimuli (*top*). Each bar consists of 9 elements, each representing the mean high gamma power (HGP) of the best electrode per stimulus. The classifier assigns the value 1 to the element with the highest feature value (white square) and the value 0 to all other elements. Histograms (*bottom*) show the classification result for all trials of the stimuli. Color scheme is indicated in *C*. *C*: single-trial classification results for each of the 3×9 stimulus conditions using the binary classifier. *D*: ERF coverage at stimulus locations as a function of classification rates (lower, middle, and upper third of ranks). Boxes indicate 25th and 75th quartiles, whiskers indicate full range of data, and white bars indicate medians. *Significant difference at $\alpha = 5\%$ level. M1, M2, and M3, *monkeys 1, 2, and 3*, respectively.

corresponding stimulus center for two example stimuli (data from *M3*). For *stimulus R*, the visual space around the letter was covered by a total of eight electrodes. This is expected to increase the probability to significantly activate one of these electrodes, regardless of the exact coordinates of the stimulus. Moreover, small displacements of the stimulus (e.g., caused by small eye movements) would not shift the stimulus out of the area covered by the electrodes but toward a neighboring ERF center, and the denser ERF coverage provides some redundancy to compensate for electrodes with weaker signal-to-noise ratio. In contrast,

stimulus D was covered by ERFs of only two electrodes such that its neuronal representation is supposed to more strongly depend on the exact stimulus coordinates and is likely more vulnerable against displacements of the stimulus and signal fluctuations.

As shown in the preceding examples, combining advanced machine learning algorithms and careful selection of informative data can compensate for some ambiguity in the neuronal representation of the stimuli. In fact, even the absence of a visual response may serve as a unique pattern to allow reliable classification of a stimulus. For lasting functionality and reliability, however, good coverage of the visual field and high density of ERFs is likely to be most critical. This is illustrated by a reclassification of the 3×9 stimulus conditions with a simple binary classifier. For each array, the classifier was fed with a nine-element vector, where each element represented the single-trial HGP response averaged over the previously estimated most informative time-frequency bins of the best electrode per letter stimulus. The element with the highest activation was set to 1, whereas all others were set to 0 (Fig. 7B), i.e., the decoding was based on a simple max function and independent of training a classifier. As expected, the overall classification performance of this extremely simple procedure significantly decreased compared with the previous SVM-based classification (Wilcoxon signed rank, $Z=4.29$, $P < 10^{-5}$, $R = 0.58$, $N = 27$), yet single trials for 15 of the 27 stimulus conditions were still classified with 90% or more correct, and 2 conditions reached the 100% performance level (Fig. 7C). When all stimulus conditions were divided into three equally large fractions associated with low, medium, and high classification performance, it was found that classification performance significantly (Kruskal-Wallis, $\chi^2 = 8.01$, $P = 0.018$, $\omega^2 = 0.24$, $df = 2$) increased as a function of ERF coverage (Fig. 7D). Because only one electrode per stimulus was used for decoding, this result is likely due to the fact that the array provides a raster of slightly shifted ERFs in regions of high electrode coverage, and consequently, a higher likelihood of good center-to-center alignment between stimulus and ERF. The results of the binary classifier show that under such conditions, a very simple decoding strategy on an extremely small amount of data allows for close to, or literally perfect, readout of single-trial EFPs, proving that EFPs convey cortical signals with high spatial resolution and precisely reflect the underlying functional architecture of the cortex.

5.6 Discussion

Recording of EFPs, sometimes also termed micro-EEG or epidural ECoG, has become an important technique for analysis of neuronal data at the mesoscopic level and offers promising options for future research on both basic and clinical neuroscience [Engel et al. 2005; Slutzky & Flint 2017]. Because electrodes are placed on top of the dura, EFP recordings are less invasive than subdural ECoG and intracortical recordings. This has the general advantage of a reduced risk of infection both during and after surgery [Van Gompel et al. 2008] and circumvention of other possible complications associated with opening the dura. On the other hand, the barrier of the dura may have an effect on spatial selectivity and signal quality, particularly when electrodes with small diameter are used [Bundy et al. 2014]. Both factors potentially constrain the usability of epidural signals for applications and research relying on clearly localized and/or single-trial information. We have shown that despite these apparent drawbacks, single-trial EFPs from three different arrays were classified in all 27 stimulus conditions with a performance $> 90\%$. For single trials from 25 of the 27 conditions, the performance level was $> 95\%$, and for 13 conditions it was $> 99\%$ of all trials. Hence, epidurally recorded EFP signals constitute a highly specific, local signal. Because we recorded in an area with high spatial resolution, the reliable classification of single trials suggests that the EFP is integrated over a clearly limited volume of cortical tissue, for otherwise spatial information would get blurred and errors in assigning the spatial condition would significantly rise. Importantly, reliable classification was not primarily dependent on advanced machine learning algorithms but could be achieved even with a binary classifier applying a simple max function. The latter result correlated with the electrode coverage of the cortical surface, indicating that a proper stimulus-ERF alignment is critical for the information content of the EFP.

5.6.1 Methodological and technical considerations

Although we dedicated a good extent of the work to increase the classifier's overall performance as a proxy for both the selectivity and reliability of the EFP signal, it is important to note that it was not the goal of the study to find, or suggest, the optimal procedure. Particularly for somatosensory cortex, much emphasis has been put on the

optimization of classifiers and procedures, selection of signals, and choice of features, mostly using subdural or intracortical signals [Krusienski et al. 2011; Slutzky & Flint 2017; Tankus et al. 2014]. Yet, although some studies showed that also the EFP conveys sufficient information to be candidate as a source for BCI [Flint et al. 2012], the specific procedures that were applied, the experimental and clinical conditions, or the area delivering the neural signals usually did not allow the functional specificity of the EFP to be assessed. Epidural placement of electrodes introduces some additional variability, due to differences in dura thickness and volume of subdural space, slow changes in tissue impedance, and other factors. In the present study, this is exemplified by significant differences of both the size and SBR of ERFs between the arrays of the three monkeys and across individual arrays. Together with differences in ERF coverage at different stimulus positions and strong trialwise signal fluctuations, this variability predicts different probabilities for decoding stimulus information at the single-trial level, which constrains the use of EFPs. The goal of the present study, therefore, was to investigate the reliability by which these signals can be decoded. We have shown that whereas a difference between the arrays of the three monkeys and between individual stimuli was highly significant when decoding was based on the time course of the signal, an ROC-based approach for selecting the most informative time bins and electrodes allowed these limitations to be overcome, and single trials for all of 27 conditions could be classified with 90% correctness, at the least. Because this analysis was performed in an area with highly resolved retinotopic representation, our results prove that EFP recordings provide a strongly localized signal that can be directly related to the functional architecture of the underlying tissue, even when information is limited to single trials. This has important implications not only for the analysis of EFPs but also for the interpretability of subdurally recorded ECoG data derived from cortical areas having a less clear, or more dynamic, functional organization than V1.

Even though optimization of the classification procedure was not the primary focus of the study, our results allow, nevertheless, for some general methodological and technical conclusions. First, as reported before [Gunduz et al. 2012; Kapeller et al. 2018; Martin et al. 2019; Rotermund et al. 2009], visual gamma activity was found to be an excellent feature for distinguishing between different stimulus conditions, yet combining gamma with one or two other highly informative response features allowed for significant improvement of classification performance. Similar conclusions were drawn by other authors using

combinations of different response features [Li et al. 2017; Miller et al. 2016; Nourski et al. 2015; Wei et al. 2007; Zhang et al. 2013]. This finding is likely indicating that, if they are sufficiently independent, ambiguity in the information of one feature might be compensated by disambiguity in another. Second, excluding weakly or noninformative data by using only the most informative time (time-frequency) windows and electrodes not only reduced the computational load by orders of magnitude but also significantly improved classification performance. In line with our findings in visual cortex, studies in somatosensory cortex reported improved, or equally well, decoding performance by reducing the number of electrodes to some lower limit [Pan et al. 2018; Wei et al. 2010] and by referring to only a few time bins [Kaiju et al. 2017]. We performed selection of most informative electrodes and time-frequency bins by ROC, but other procedures for distinguishing between distributions of data from different conditions may work equally well. Third, classification performance correlated with ERF coverage of the cortical surface. This is likely due to the fact that a larger number of candidate electrodes significantly increases the likelihood to identify one or a few highly selective channels, whereas low coverage of the cortical surface induces a strong dependence on the signal quality of a limited number of available channels. In line with this, studies in somatosensory cortex reported high classification rates when high-density ECoG arrays were used to decode hand and finger gestures on the basis of information from a single channel per condition [Kaiju et al. 2017].

5.6.2 Functional Specificity of EFPs

Many of the studies recording signals from top of the brain have been performed using subdural arrays with large electrodes [Crone et al. 2006; Slutzky & Flint 2017]. Epidural arrays, however, offer a less traumatic access to intracranial brain signals, and commercially available arrays have recently been used, for example, in diagnosis of the cognitive state in locked-in syndrome [Bensch et al. 2014; Martens et al. 2014] and rehabilitation of patients after stroke [Gharabaghi et al. 2014a, 2014b]. In the motor system, recent studies in nonhuman primates showed that EFPs allow successful decoding of hand and finger gestures [Choi et al. 2018]. In the visual domain, monkey EFPs were used to study gamma-band responses [Grothe et al. 2012; Rotermund et al. 2009; Taylor et al. 2005], to predict allocation of attention between two close-by locations [Rotermund et al. 2013], and to predict saccade directions [Lee et al. 2017]. Yet, probably because of the large number of neurons

contributing to the EFP/ECoG signal [Miller et al. 2009], the additional attenuation of the signal by the dura makes epidural recordings a still rare case, despite its obvious clinical advantages. Two recent studies in monkey somatosensory cortex indeed indicated weaker decoding performance for epidural compared with subdural signals [Bundy et al. 2014; Farrokhi & Erfanian 2018]. On the other hand, a rodent study on forelimb movements concluded that EFPs allow for the same decoding performance as intracortical local field potentials (LFPs; [Slutzky et al. 2011]). In fact, in vivo measurements of signal attenuation by human dura indicated no detrimental effects on signal feature detection [Torres Valderrama et al. 2010]. A more significant factor determining the specificity of EFP/ECoG signals, therefore, might be given by the size and density of the recording electrodes. Only a few studies have compared signal quality and decoding performance for the different types of subdural and intracortical arrays used in clinical and basic neuroscience research [Flint et al. 2017; Kellis et al. 2016; Wang et al. 2017], yet it appears that many of the results indicating high signal specificity were obtained with high-density arrays and rather small electrodes [Branco et al. 2017; Hu et al. 2018; Kaiju et al. 2017; Ramsey et al. 2018]. The findings of the present study showing that EFPs possess high spatial selectivity are clearly in line with this: with the small electrodes of our array, we estimated mean ERF sizes of $\sim 2.7^\circ$ and 2.8° in diameter (recalculated from ERF areas by assuming circular ERFs) in *M1* and *M3*, respectively, and 4.0° in *M2*, which is around a factor of 1.6 to 2.3 of the receptive field size of intracortical LFPs measured with the same mapping paradigm [Drebitz et al. 2019]. A recent study using large, subdural electrodes reported about the same factor for comparison of ECoG and LFP ERFs [Dubey & Ray 2019]. Two other studies using subdural electrodes estimated V1 receptive fields of slightly smaller size [Yoshor et al. 2007a] or about the same size [Takaura et al. 2016] as we report here for epidural electrodes. Thus, with regard to selectivity of the signal, subdural or epidural placement of electrodes may not be the most limiting factor. In fact, because we achieved very good single-trial classification of many stimulus locations even without training advanced classifiers, the use of multielectrode arrays with small electrode diameter and high electrode density seems critical for improving the reliability by which single-trial information can be read out from both subdural and epidural recordings. This is also supported by a recent study in ferrets [Bockhorst et al. 2018], in which the authors used high-density arrays with electrodes of even smaller diameter than ours. The authors compared epicortical recordings with intracortical laminar probe recordings

and found well-preserved receptive field properties in epicortical recordings, probably due to the fact that epicortical signals reflect the highly synchronized cortical activity. Although epidural placement of electrodes increases the distance between electrodes and cortical sources, and likely reduces the correlations between epi- and intracortical signals, small electrodes will compensate for the larger distance by integrating over a smaller volume of tissue, thus providing selective estimates of cortical activity.

Taken together, our present results show that despite strong trial-by-trial fluctuations and signal attenuation by the dura, epidurally recorded signals convey a very high degree of spatial selectivity that is reliably available at the single-trial level. This offers new and exciting options for both clinical and basic neuroscience and for the use of EFPs as the source of information in brain-computer interfacing.

Authors contribution

B.F., A.S., A.K.K., W.L., and D.W. conceived and designed research; B.F. performed experiments; B.F. and D.W. analyzed data; B.F. and D.W. interpreted results of experiments; B.F. and D.W. prepared figures; B.F. and D.W. drafted manuscript; D.W. edited and revised manuscript; B.F., A.S., A.K.K., W.L., and D.W. approved final version of manuscript.

Grants

The work was funded by Deutsche Forschungsgemeinschaft Grant WE 5469/3-1, Tönjes-Vagt Foundation (Project XXXI), University of Bremen (ZF grant and Creative Unit I-See), and a scholarship from the German Academic Scholarship Foundation.

Acknowledgments

We thank Udo Ernst for helpful comments on an earlier draft and Peter Bujotzek, Katja Taylor, Serge Stokov, Ramazani Hakizimani, and Katrin Thoß for technical support.

Disclosures

No conflicts of interest, financial or otherwise, are declared by the authors.

6. Modulation of epidural field potentials from macaque V1 evoked by stimulus size, shape and color

Declaration of the contribution of the candidate to a multi-author manuscript which is included as a chapter in the submitted doctoral thesis.

Task	Contribution [%]
Experimental concept and design:	ca. 75
Data acquisition:	ca. 100
Data analysis and interpretation:	ca. 80
Preparation of figures and tables:	ca. 100
Drafting the manuscript:	ca. 80

Date:

Signature:

This chapter is a draft of a paper manuscript.

Authors: Benjamin Fischer & Detlef Wegener

Affiliation: Brain Research Institute, Center for Cognitive Sciences, University of Bremen, Bremen, Germany.

6.1 Abstract

Superficial extracortical recording techniques enable simultaneous electrocortical signal acquisition from multiple cortical areas with a dense electrode coverage. Among these, epidural electrodes placed on top of the dura mater constitute a promising technique for long-term application because of their lesser invasiveness compared to subdural recordings. The lower degree of invasiveness leads to a lower signal quality of epidural in comparison to subdural recordings. A previous study, however, demonstrated that signals recorded epidurally, with high-density electrode arrays from macaque primary visual cortex (V1), enable a precise decoding of the location of a stimulus from single trials. Apart from that, little is known about the extractability of local stimulus attributes of small visual stimuli from high-density epidural field potentials (EFPs) recorded from V1. In order to investigate its information content, we recorded EFPs with high-density electrode arrays from V1 of macaque monkeys performing a simple fixation task while stimulating the visual periphery with stimuli differing in position, size, shape and color. We found that the EFP gamma-band (γ -band) activity from macaque V1 is significantly modulated by stimulus size and shape. Interestingly, the γ -band response to equally shaped stimuli that were rotated differently was similar. The results demonstrate that the EFP reflects V1 activity elicited by local stimulus attributes. Hence, epidural recordings promise less-invasive signals that represent local changes in the cortical activity for brain research and clinical applications.

6.2 Introduction

Superficial extracortical recordings have become a frequently used tool in research and clinical applications like Brain-Computer Interfaces (BCIs) [Schalk & Leuthardt 2011]. These recordings can be performed subdurally or epidurally. Epidural electrodes are less invasive than subdural electrodes which is beneficial regarding the health of patients with a need for a long-term application of invasive neurophysiological recordings. In comparison to subdural electrodes, epidural electrodes are located more distant from the signal source, which potentially leads to less specific signals. While some comparative studies

demonstrated a better signal quality of subdural signals [Bundy et al. 2014; Torres Valderrama et al. 2010], others have shown that the quality of both epi- and subdural signals is similar [John et al. 2018; Slutzky et al. 2010]. In addition, some studies found that also the decoding performance based on epi- or subdural signals is similar [Flint et al. 2017; John et al. 2018; Torres Valderrama et al. 2010]. Flint and colleagues [2017], for example, achieved similar performances using either epi- or subdural signals from predominantly the primary motor cortex to decode three different grasp behaviors in humans. These findings indicate that epidural recordings could serve as a promising and less invasive alternative for recording extracortical signals, despite of their potentially lower signal quality.

In order to investigate the properties of epidural signals, recent studies recorded epidural field potentials (EFPs) utilizing high-density electrode arrays (inter-electrode distance < 5 mm, high-density EFP) (e.g., [Choi et al. 2018; Farrokhi & Erfanian 2018; Fischer et al. 2019; Flint et al. 2017; Lee et al. 2017; Marathe & Taylor 2013; Rotermund et al. 2009, 2013; Rouse et al. 2016; Shimoda et al. 2012]). Apart from delivering a higher spatial resolution, high-density arrays also allow for a better decoding of cortical activity patterns in comparison to arrays with lower electrode density in the subdural space [Wang et al. 2016]. So far, high-density EFPs were often recorded from motor-related cortices and/or during motor-tasks to decode movement-related information from EFPs (e.g., [Choi et al. 2018; Farrokhi & Erfanian 2018; Flint et al. 2017; Lee et al. 2017; Marathe & Taylor 2013; Shimoda et al. 2012]). Other cortical areas were less targeted for epidural recordings in order to investigate the information content of EFPs. A suitable cortical area to investigate the degree of cortical information that can be extracted from EFPs is the primary visual cortex (V1) because, firstly, large parts of it are superficially exposed in macaques [Blasdel & Campbell 2001] enabling a dense coverage with many epidural electrodes, and secondly, it processes different kinds of visual and cognitive information (for a review, see [Ng et al. 2007; Roelfsema & De Lange 2016]).

Previously, a few studies have investigated the performance of decoding sensory information from EFPs of macaque V1. High-density EFPs recorded from V1 enabled high-accuracy single-trial decoding of the visually stimulated position [Fischer et al. 2019]. In addition, the identity of multiple large complex stimuli presented at the same spatial position was decoded with classification rates $> 80\%$ using three epidural electrodes over V1 [Rotermund et al.

2009]. Up to now, it remains unclear whether high-density EFPs from V1 are modulated by local stimulus attributes of small stimuli.

In order to investigate the extent of visual stimulus properties being reflected in EFPs, we used custom-made high-density multi-electrode arrays to record epidurally over V1 of the left hemisphere from two macaque monkeys. We visually stimulated with small static stimuli which varied in position, size, shape and color and investigated the modulation of EFPs evoked by local stimulus attributes. The EFP γ -power response was significantly modulated by stimulus size and shape. In addition, objects which were constructed as a differently rotated version of the same shape evoked similar EFP modulations. These findings show that the high-density EFP represents small changes in the visual stimulation and is therefore well suited to investigate local cortical activity patterns.

6.3 Materials and Methods

6.3.1 Subjects

The surgeries and experiments followed the Regulation for the Welfare of Experimental Animals issued by the Federal Government of Germany and were approved by the local authorities. Two male macaque monkeys (*Macaca mulatta*), *M1* (13 yr., 12 kg) and *M2* (14 yr., 11.5 kg), were implanted with an epidural multi-electrode array over the left hemisphere. The arrays were placed posterior to the lunate sulcus and covered the dorsal part of left V1. The implantation procedure is described elsewhere [Fischer et al. 2019]. *M1* was housed in an indoor facility where he had auditory and visual contact to other macaques. *M2* was housed with another monkey in a facility which had an indoor and outdoor section. Facilities were enriched with animal toys and climbing opportunities. During days of training or recording, monkeys were rewarded with water or diluted fruit juice in the experiments. On all other days, free fruit and water was provided in the facilities of the monkeys. Daily checks of the behavior and regular veterinarian visits, as well as body weight documentation on training/recording days ensured the well-being of the monkeys.

6.3.2 Data acquisition

Technical details of the multi-electrode array are given elsewhere [Schander et al. 2019; Stokov et al. 2017]. In brief, the array consisted of 202 hexagonally arranged recording electrodes (electrode diameter: 560 μm), with a spacing of 1.8 mm, and a reference electrode on top of the array, which was oriented towards the skull.

The monkeys sat head fixated ~ 70 cm in front of a CRT monitor (resolution $1,152 \times 864$ pixels, refresh rate: 100 Hz). The gaze direction of the monkey was monitored by a custom-made eye tracker. The EFP of the multi-electrode array was recorded at 25 kHz sampling rate using devices from Multichannel Systems (Reutlingen, Germany; recording chain: MPA 32, Sc2x32, PGA64, USB-ME256). The amplified signal (total amplification $\times 50,000$), gaze-direction signals and a 50 Hz socket signal were fed via the USB-ME256 device into a windows PC.

6.3.3 Visual stimulation

The monkeys were trained to fixate a gray central fixation square (FS, $0.2^\circ \times 0.2^\circ$) and respond to its dimming. Following the presentation of the FS for 750 ms post trial start, three different objects were presented sequentially in the visual field, each for 800 ms and separated by 250 ms blank periods. After the offset of the third object, the monkey had to hold fixation until the FS dimmed (maximal 1,100 and 1,000 ms for *M1* and *M2* respectively). The monkey was rewarded if he responded between 200 and 950 ms post dimming onset. Provided that the monkey released the lever too early or too late, the trial was canceled without a reward. In addition, the trial was aborted without a reward, when the monkey directed its gaze for more than 100-170 ms (depending on monkey and session) more than $\sim 1^\circ$ away from the FS.

Objects differed in position, size, shape and color (as shown in Fig. 8A and B). Five positions were chosen to cover the lower right visual field (Fig. 8A). The different stimulus sizes were 1° , 1.2° and 1.4° . Objects were shaped either as a circle, a diamond, a rectangle, a pyramid or a triangle. The diameter of the circle was defined by the three different sizes. All other shapes were defined to fit into the borders of the circle (see Fig. 8B). Same sized objects were matched in the number of pixels. Objects were colored in either blue, brown, gray, green or

red (~ 10 cd/m²) and were presented onto a black background. In total 375 objects were defined.

6.3.4 Data preprocessing

Preprocessing and data analysis were carried out using custom written Matlab scripts (Matlab, TheMathWorks, Natick, USA). The data was low-pass filtered (< 300 Hz, finite impulse response filter in forward and backward direction, cutoff at 150 Hz) and down-sampled to 1 kHz. The 50 Hz socket signal was used to remove 50 Hz noise from the EFP. The low-pass filtered single-trial EFP was baseline normalized by subtracting the preceding mean baseline EFP activity (averaged over 201-700 ms post trial start) from the EFP.

6.3.5 Wavelet transformation

The wavelet transform was performed on the filtered non-normalized EFP in order to analyze the activity of the EFP in different frequency bands. Morlet wavelets were used which are defined as [Torrence & Compo 1998]:

$$\psi_0(\eta) = \pi^{-\frac{1}{4}} e^{i\omega_0\eta} e^{-\frac{\eta^2}{2}}$$

where ω_0 (set to six) is the non-dimensional frequency and η is the non-dimensional time parameter. 35 Morlet wavelets with logarithmic increasing center frequency from 5 to 160 Hz were used. Wavelet transformation was calculated as [Torrence & Compo 1998]:

$$W_n(s) = \sum_{n'=0}^{N-1} x_{n'} \psi^* \left[\frac{(n' - n) \delta t}{s} \right]$$

where $*$ is a complex conjugation, s is the scale of the wavelet, x_n is the discrete time series and δt is the time step. The wavelet power at each frequency/time bin was calculated as:

$$W_{power} = (2|W_n(s)|)^2.$$

The single-trial wavelet power was baseline normalized by subtracting the frequency-wise mean power during the preceding baseline period (averaged over 201-700 ms post trial start) from W_{power} and subsequently dividing through the same mean baseline value.

In the following, broadband γ -power (BGP) is referring to the mean power in the frequency range of 30-160 Hz.

6.3.6 Electrode selection

For analysis purposes, only electrodes recording visually modulated EFPs originating from neuronal populations in V1 were used. Therefore, the electrode selection was performed in two steps. Firstly, all electrodes which were located anterior to the lunate sulcus (identified by pictures from array placement in the surgery) were rejected to exclude electrodes which were not located in V1/V2. Secondly, a retinotopic mapping using an automated RF-mapping procedure was carried out shortly after array implantation to identify electrodes that show modulation in their EFP caused by visual stimulation. A detailed description of the automated procedure is given elsewhere [Drebitz et al. 2019]. Briefly, bars (size: $0.24^\circ \times 24^\circ$) were defined to move in one out of 12 different directions (separated by 30°) for 3 s (trajectory length: 19°). The crossing point of all trajectories was centered at $2.4^\circ/-3.6^\circ$. The overlapping area of the trajectories was covering a large part of the lower right visual field. At least ten trials per trajectory were recorded. The electrode-wise trial-averaged γ -power response (60-150 Hz) to each bar trajectory was z-normalized. In order to identify the RF of an electrode, the electrode-wise activity in the visual field was defined as the geometric mean of the z-normalized γ -power response of the 12 bars that crossed at each location. A delay of 80 ms was considered to compensate for the response latency of EFPs from V1. The RF of an electrode was determined as the largest area of connected spatial locations having a geometric mean of ≥ 1 z-score. Electrodes with an RF size of < 1 dva² (squared degree of visual angle) and electrodes that did not show an RF were rejected from the analysis. Finally, 137 and 178 electrodes for *M1* and *M2* respectively were available after electrode selection.

6.3.7 Trial rejection

In the following, the term trial denotes the presentation time of a single object in the object-presentation task. Trials with potentially artifactual high EFP activity were excluded. For each electrode and condition, the mean (μ) and the standard deviation (σ) over the mean EFP activity of all trials was calculated for the object presentation period (26-175 ms post stimulus onset) and the preceding baseline period separately. A trial was rejected provided that its mean activity was higher than $\mu + 4 \times \sigma$ or lower than $\mu - 4 \times \sigma$ in the object

presentation period and/or baseline period. In order to exclude trials with correlated and extraordinarily high BGP activity over multiple electrodes, a correlation analysis was performed. The mean BGP over time was calculated for all trials of a condition and for each electrode separately. Subsequently, trials with highest mean BGP (above the 80th percentile) were selected for each condition and electrode. When a trial of a condition was selected for \geq half of the electrodes (rounded down in the case of an odd number of electrodes), the pair-wise correlation of the BGP activity of the trial (26-175 ms post stimulus onset) between these electrodes was tested using Pearson correlation. A trial would be rejected for all electrodes, if the mean over all pair-wise correlation coefficients was ≥ 0.6 . Trials with extraordinary high BGP which survived the automatic trial rejection were rejected by visual inspection.

The trial rejection led to different amounts of trials for the conditions between electrodes. The amount of trials was balanced between conditions of all electrodes by random under-sampling. For each condition, trials were randomly drawn. The number of drawn trials was defined as the number of trials available for the condition with the lowest number of trials.

6.3.8 Statistics

For statistical testing, Kruskal-Wallis tests were used. In order to correct for multiple comparisons, *Tukey's Honestly Significant Difference Procedure* was performed. Statistical significance of a test was defined as $p < 0.05$. In addition, effect size ω^2 [Hays 1963; Lakens 2013; Okada 2013] was calculated as:

$$\omega^2 = \frac{SS_b - df_b MS_w}{SS_t + SS_w}$$

where SS_b , SS_t , SS_w , df_b and MS_w are the sum of squares between groups, the total sum of squares, the sum of squares within groups, the degrees of freedom between groups and the mean sum of squares within groups from the Kruskal-Wallis test, respectively. ω^2 is a bias corrected version of the better known effect size η^2 [Okada 2013]. It should be noted that the difference between these two effect size measures is small [Lakens 2013]. Therefore, small, medium and large ω^2 was defined as provided by Cohen [1988] for η^2 (small ≥ 0.01 , medium ≥ 0.06 , large ≥ 0.14).

6.3.9 Selection of most-informative signal features and position-selective electrodes

For the SVM classification (see below), only position-selective electrodes were used. The electrode selection was done by utilizing a Receiver-Operator Characteristics (ROC)-based method, as described in [Fischer et al. 2019]. The purpose of the procedure was to determine electrodes which record signals that enable a differentiation between a single stimulus position and all other stimulus positions. In order to select these electrodes, signal features were extracted for each electrode that enable the identification of a certain stimulus position. Signal features were extracted from the time/frequency space spanning 26-175 ms post stimulus onset (down-sampled by a factor of 0.2) and 5-160 Hz. The following procedure was done for each electrode separately. The single-trial activity of each single time/frequency bin was divided into two groups: single-trial activity belonging to a certain stimulus position and single-trial activity belonging to all other stimulus positions. These two distributions were compared using the Receiver-Operator Characteristic (ROC). The ROC provides an area-under-the-curve (AUC) value, which is a measure of discriminability between the two distributions. All time/frequency bins were analyzed. This procedure was repeated for each stimulus position, leading to one AUC value per stimulus position and time/frequency bin for each electrode. The AUC values of all electrodes and positions were pooled, leading to a data matrix with the size of [Dimension 1: frequency, Dimension 2: time, Dimension 3: [electrodes \times stimulus position]]. The variance over the third dimension was calculated to obtain the grand variance matrix. The z-normalized grand variance matrix was used to identify bins in the time-frequency space of the signal which hold most information about the stimulus position. A high AUC variance value reflects a large signal difference between electrodes and conditions which potentially indicates the ability to differentiate between stimulus conditions using the signal of that bin (for further detail, see [Fischer et al. 2019]). A threshold of 1.5 z-score was applied to find areas in time/frequency space with high variance (i.e., which hold much information about the stimulated position). In the case of finding multiple areas in the analyzed time/frequency space, the area with highest mean z-score was selected for further analysis.

In order to rank the electrodes by their position-selectivity, the AUC values of time/frequency bins located inside the previously defined area were averaged. Afterwards, the absolute mean

AUC (absolute deviation of the AUC value from 0.5) was calculated. This procedure resulted in one mean value for each electrode and position. These means were sorted for each position to obtain a position-wise electrode ranking. The rank of each electrode reflects the ability to differentiate a certain position using its recorded signal. The best position-selective electrodes were chosen from this ranking for the position-wise SVM classification of local stimulus attributes.

For statistical testing and SVM classification, the most-informative values (signal features) based on stimulus size, shape and color were calculated by repeating the above described feature extraction procedure for each stimulus attribute. The resulting area within the grand-variance matrix for each attribute (Fig. 9) was used to calculate the signal feature for each trial by averaging over the activity within the selected time-frequency area.

6.3.10 Support Vector Machine-based classification

SVM classification was performed to investigate whether different stimulus attributes could be distinguished from single-trial or trial-averaged EFPs. SVM classification was based on the libsvm toolbox [Chang & Lin 2011] using a radial basis function kernel and a “leave-one-out” design. For a given data set, each available trial was chosen once for testing.

For each classification round, the data set contained signal features of 51 random trials for each attribute category (i.e., for each class) drawn from all available trials. The data set was z-normalized for each feature before classification. The training set contained 50 trials per class while the test set contained one trial per class. None of the test trials were included in the training trial set. Before training the SVMs, SVM hyperparameters were optimized for the training set by grid search using cross-validation. Afterwards, one SVM was trained for each class. During testing, each SVM calculated the probability of the trials in the test set to have its trained class identity. Afterwards, the probability values were compared between the SVMs for each trial. The SVM with the highest probability determined the class identity of the tested trial. This procedure was repeated until all trials were tested once (in total 51 classification rounds per data set). Afterwards, a new data set of 51 random trials for each class was drawn. This procedure was repeated until ten data sets were used for classification.

Classification performance was defined as the ratio of correctly classified trials divided by the number of total classified trials. The mean classification performance was calculated over the ten repetitions and all positions. The chance level was calculated as $1/(\text{number of classes})$.

6.4 Results

For the investigation of EFP response modulations evoked by different stimulus attributes, the peripheral visual field of fixating macaque monkeys was stimulated with objects that differed in position, size, shape and color (Fig. 8A and B), while recording with high-density epidural multi-electrode arrays from V1. After preprocessing, 21 (*M1*) and 24 (*M2*) trials of each object presentation (375 different conditions) were available for the analysis. Data analysis was performed as follows: For each electrode, the BGP activity of all conditions was grouped by stimulus attribute categories and averaged to investigate EFP modulations evoked by the categories of each stimulus attribute. Afterwards, the mean BGP was used to quantify how many electrodes show significant differences between the categories of a stimulus attribute. The statistical test was repeated using attribute-specific signal features. We further investigated the difference in the EFP modulation between the categories of a stimulus attribute using only electrodes that showed significant differences for that attribute. Finally, we used SVMs to investigate whether the found EFP modulations enable the decoding of visual information from single-trial and trial-averaged EFPs.

6.4.1 EFP responses evoked by stimulus size, shape and color

For the initial investigation of the EFP modulation caused by different stimulus attributes, the activity of the EFP in the broadband γ -frequency band was focused because different frequency bands within the γ -frequency-range were found to reflect distinct information about different stimulus features (e.g. [Bartoli et al. 2019; Murty et al. 2018]). The condition-wise mean BGP (averaged over 30-160 Hz, 26-175 ms post stimulus onset and all trials) was calculated for each electrode and is shown for three example electrodes in Fig. 8C, *H* and *M*. The matrix in Fig. 8C, *H* and *M* is arranged in such a manner that the response to a certain stimulus attribute can be differentiated. The y-axis indicates both stimulus position and stimulus shape, while the x-axis indicates stimulus size and color. For an example electrode

6.4 Results

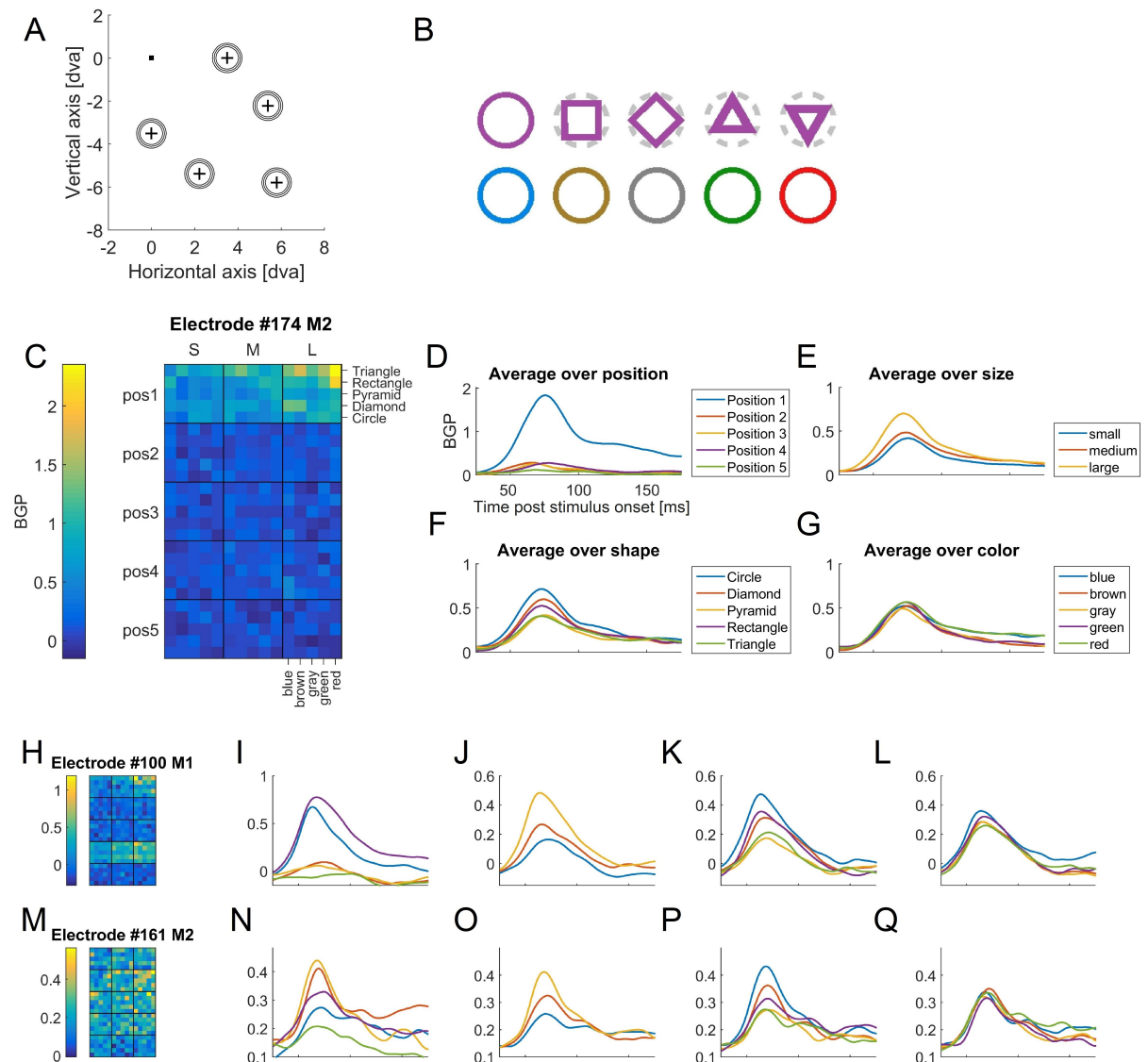


Fig. 8: Visual stimulation and BGP response to stimulus position, size, shape and color. *A*: Stimulus locations and stimulus sizes of the visual stimulation are shown in the visual field. The black square is the FS and black crosses the center of the stimulus positions. The three rings show the extent of the circle stimulus for the three used sizes (dva = degree of visual angle). *B*: Stimulus shape and color are illustrated. In the first row the used stimulus shapes are shown. The gray dashed circle around the shapes indicates the size of the circle stimulus. The second row shows the used stimulus colors *C*: Trial-averaged mean BGP response (averaged over 26-175 ms post stimulus onset and 30-160 Hz) over all trials for an example electrode of *M2*. The matrix is sorted by the four different stimulus attributes (y-axis: position and shape, x-axis: size and color; sizes are denoted as S = small, M = medium, L = large). *D-G*: Time-resolved mean BGP, averaged over all stimulus conditions grouped by stimulus position (*D*), size (*E*), shape (*F*) and color (*G*) for the example electrode of *M2*. *H-L*: Same as *C-G* for an example electrode of *M1*. *M-Q*: Same as *C-G* for another example electrode of *M2*.

of *M2* (Fig. 8C), most objects that were shown at position 1 elicited a higher mean BGP response in comparison to objects shown at all other positions. This is also visualized in Fig. 8D: The time-resolved, position-wise mean BGP response demonstrates that objects shown at position 1 elicited a transient peak, while the mean BGP response was barely modulated by

the presentation of objects at all other positions. Thus, this example electrode recorded signals that reflect the presentation of a stimulus at position 1. Furthermore, Fig. 8C reveals that with increasing stimulus size the BGP amplitude of many conditions at position 1 increased as well. The time-resolved BGP response averaged over all conditions that included the presentation of objects of a certain size (Fig. 8E) demonstrates that the mean BGP response modulation was highest for conditions that presented objects of the largest stimulus size, while the modulation was lowest for conditions that showed an object of the smallest size. By averaging the signal of all conditions where an object with a certain shape was presented (Fig. 8F), the highest BGP peak was revealed for the presentation of the circular shape. Intermediate BGP peaks were evoked by conditions that showed diamond or rectangular shaped objects, while smallest BGP peaks were evoked by objects that were shaped as triangle or pyramid. Interestingly, shapes that evoked a similar response consisted of the same but differently rotated geometrical shape: Diamond and rectangle were both rectangular shapes while triangle and pyramid were both triangular shapes (Fig. 8B). In contrast, only small differences were revealed between the averaged BGP transient response evoked by differently colored objects (Fig. 8G). After 100 ms post stimulus onset, red and blue colored objects showed higher BGP in comparison to differently colored objects. The described differences between stimulus attribute categories were also present at other electrodes: Similar findings were visible for an example electrode of *M1*, which was responsive to the presentation of objects at two positions (Fig. 8H-L). Additionally, Fig. 8M-Q illustrate the same analysis for an electrode of *M2* that showed a low BGP response modulation caused by the stimulation at multiple positions. Despite these properties, the previously found specific modulation of the BGP response caused by stimulus size and shape was visible for the signal recorded by this electrode (Fig. 8O and P). Highest mean BGP response was evoked by large stimuli, intermediate response by medium sized stimuli and lowest response by small stimuli (Fig. 8O). Fig. 8P shows that the circle shape evoked the highest response peak, while diamond and rectangular shaped stimuli evoked intermediate, and triangular and pyramid shaped stimuli evoked smallest response peaks. Regarding the stimulus color, there were only small differences in the transient response amplitude between conditions. After around 100 ms post stimulus onset, however, the blue and red stimulus condition showed higher BGP activity in comparison to the other colors (Fig. 8Q). Thus, not only high responsive electrodes that recorded signals that are selectively modulated by the

stimulation at a single position, but also signals from electrodes that showed small response amplitudes and/or from electrodes which were modulated by the presentation of objects at multiple positions show similar systematic modulation of the BGP response regarding stimulus size, shape and color.

In order to quantify the found difference in the BGP response modulation, we focus on stimulus size, shape and color because position selectivity of EFPs from V1 was already intensively investigated in a previous study [Fischer et al. 2019]. For each electrode, the condition-wise mean BGP (averaged over 30-160 Hz, 26-175 ms post stimulus onset and all trials) was grouped by the categories of each stimulus attribute separately. These grouped values were then used for statistical testing. An electrode with $p < 0.05$ was defined as being selective for the tested stimulus attribute.

The statistical test revealed that 54.01% (*M1*) and 57.87% (*M2*) of all electrodes showed significant differences in the mean BGP response between stimulus size groups. Regarding stimulus shape, 24.09% (*M1*) and 24.16% (*M2*) of all electrodes showed a significant difference between stimulus shape groups. 11.68% (*M1*) and 34.83% (*M2*) of all electrodes showed significant differences in the mean BGP response between the categories of stimulus color. Whereas more than half of the electrodes of both monkeys recorded signals that were selectively modulated by stimulus size, the signal modulation evoked by stimuli with different shapes or colors was not significantly different at most electrodes.

6.4.1.1 Using specific response features

Until now, the mean BGP response was averaged over a large time-course and a strictly defined frequency range. Using more specific signal features that reflect the response modulation caused by a single stimulus attribute is more suitable to investigate whether EFPs contain stimulus attribute-specific information. Therefore, we repeated the statistical analysis from the previous section using specific signal features which represent the part of the EFP response in time-frequency space that is particularly modulated by a certain stimulus attribute. We used a previously established ROC-based method [Fischer et al. 2019] to extract most-informative time/frequency bins from the wavelet-transformed EFP which best distinguish between the categories of each stimulus attribute. The method uses the variability of the area-under-the-curve (AUC) value provided by the ROC to identify time-frequency bins that are highly modulated by the categories of a stimulus attribute (for details, see

Materials and Methods). Fig. 9 displays the location of the extracted features in the time-frequency space. The color code displays the z-normalized variability of AUCs which indicates the information content about the specific stimulus attribute. For stimulus position, shape and size, most-informative signals were located in the γ -frequency range. However, patches of highest mean AUC variance were located in lower γ -frequency bands for stimulus size and shape in comparison to stimulus position. In contrast, most-informative signals were located in the low frequency range of ~ 8 -10 Hz (*M1*) and ~ 15 -21 Hz (*M2*) for stimulus color.

The mean activity within these areas was calculated to obtain one feature value for each trial and stimulus attribute of an electrode (referred to as ROC-feature from here on). The trial-averaged ROC-features were grouped by stimulus attribute categories and were used to perform statistical tests. For each stimulus attribute a statistical test was done for each electrode to quantify the number of attribute-selective electrodes. Selective electrodes ($p < 0.05$) were used for an additional statistical analysis: The electrode-wise feature activity averaged over each attribute category of all selective electrodes was pooled and tested statistically.

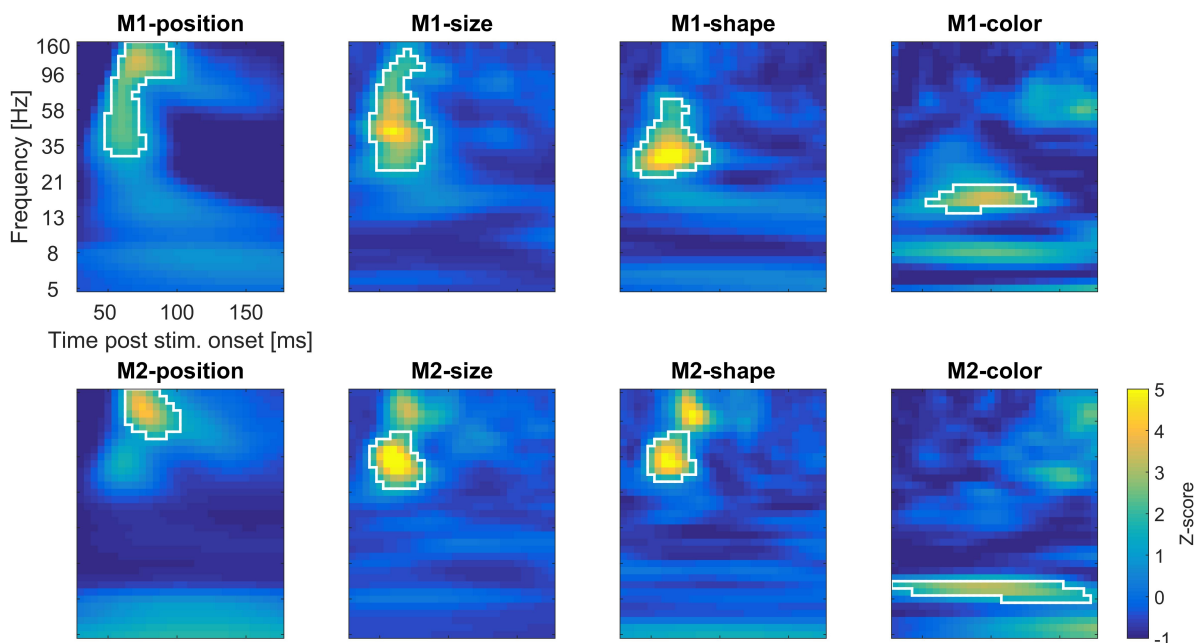


Fig. 9: Results of the ROC-based signal-feature selection. Each plot shows the tested time-frequency bins. Each bin is colored according to its z-normalized grand-variance AUC value which was calculated over attribute categories and electrodes. The white border indicates the area that was selected as most-informative area.

Stimulus size

The ROC-size-feature activity differed significantly between size groups for 83.21% (*M1*) and 84.27% (*M2*) of electrodes. Statistical analysis using mean ROC-size-features from all size-selective electrodes revealed significant differences between size groups (*M1*: $\chi^2 = 53.99$, $p < 10^{-11}$, $df = 2$, $\omega^2 = 0.08$; *M2*: $\chi^2 = 69.34$, $p < 10^{-15}$, $df = 2$, $\omega^2 = 0.08$). The post hoc test showed that all pairs of stimulus size categories differed significantly from each other (Fig. 10A). The median ROC-feature activity of each group is increasing with size (Fig. 10A): It was lowest for the small size group and highest for the large size group.

As for the statistical results using the mean BGP response, most electrodes recorded signals that differed in their ROC-size-feature in accordance to stimulus size: With increasing size, the ROC-size-feature activation rises.

Stimulus shape

The statistical test for each electrode using the ROC-shape-feature revealed that 72.99% (*M1*) and 65.73% (*M2*) of the electrodes show a significant difference between shape groups. The statistical test over all shape-selective electrodes revealed a statistical difference between shape groups (*M1*: $\chi^2 = 107.63$, $p < 10^{-21}$, $df = 4$, $\omega^2 = 0.12$; *M2*: $\chi^2 = 89.29$, $p < 10^{-17}$, $df = 4$, $\omega^2 = 0.08$). The post hoc test showed that most pairs of shape groups differed significantly. None-significant pairs of groups were rectangle and diamond (*M1* and *M2*), pyramid and triangle (*M1* and *M2*), and diamond and pyramid (*M2*) (Fig. 10B). The circle shape group elicited highest median feature activity, while lowest median feature activity was elicited by the triangle and pyramid shape group (Fig. 10B).

Due to the fact that pairs of shapes which were constructed as differently rotated versions of the same geometrical shape showed no significant differences (Fig. 10B), statistical analysis was repeated by grouping the ROC-shape-features by shape-classes (circles = circle shape, rectangles = diamond and rectangle shape, triangles = triangle and pyramid shape). For *M2*, no statistical difference was found between an additional pair of shapes. In order to test whether the third non-significant pair has an influence onto the categorization of shapes into groups, the statistical analysis of *M2* was done for each possible combination of grouping the diamond, pyramid, rectangle and triangle shape into two groups. A significant difference between all three shape-class groups was found only when grouping the data of *M2* into shape-classes as described above. Therefore, only the statistical test using these groups is

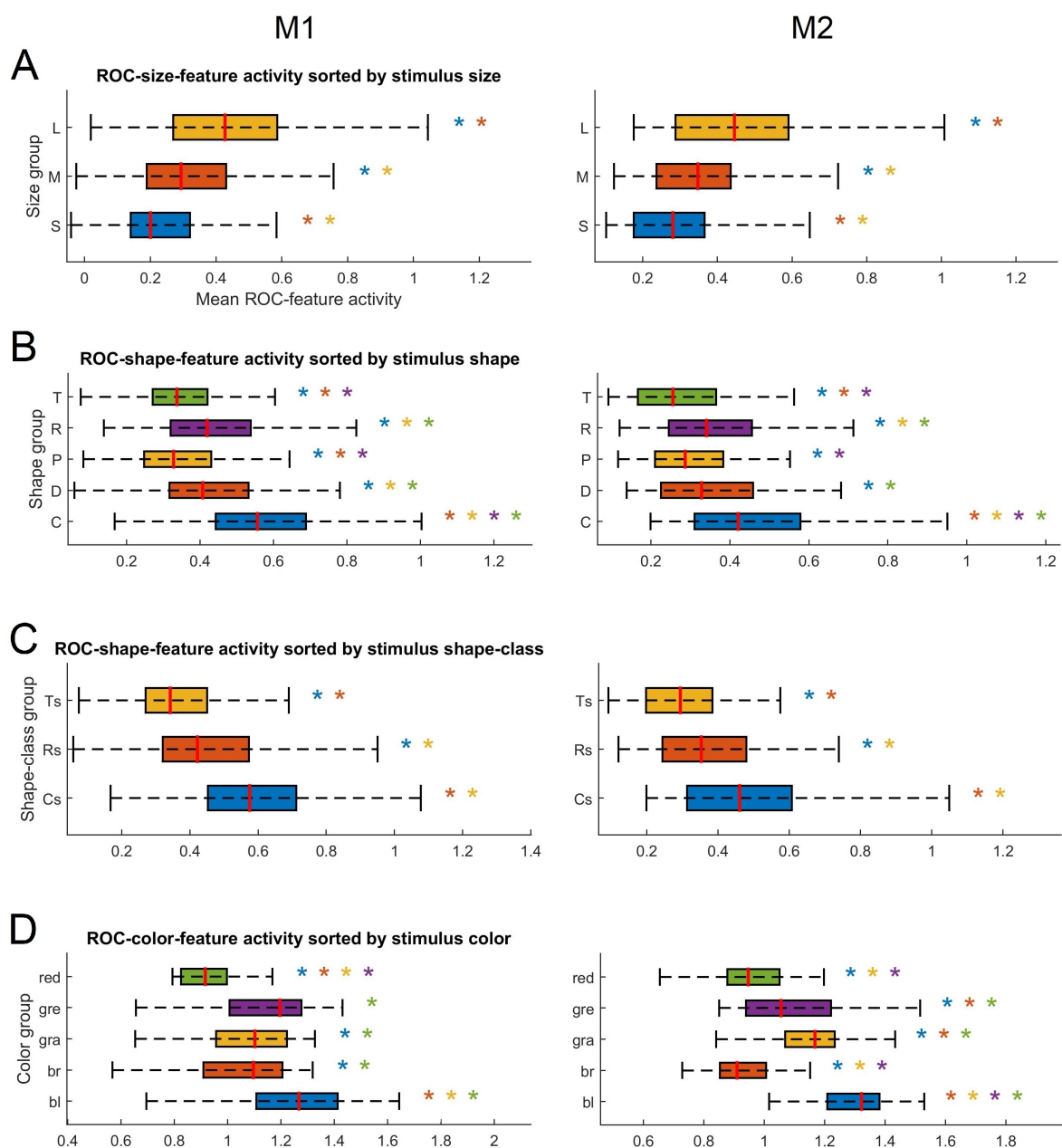


Fig. 10: Statistical analysis of the ROC-feature response modulation evoked by stimulus size, shape, shape-class and color. *A*: The size-grouped mean ROC-size-feature activity over all conditions for all significant electrodes is plotted (*left M1*, *right M2*). The red line in the middle of each bar indicates the median activity. Borders of the boxes indicate the 25th (*left*) and 75th (*right*) percentile. Whiskers indicate the minimum value within [25th percentile – 1.5 × inter-quantile range] (IQR, *left*) and maximum value within [75th percentile + 1.5 × IQR] (*right*). IQR is defined as the range between the 25th and the 75th percentile. Outliers are not shown to ensure readability. Stars on the right indicate significant differences between groups. The color of the star indicates the group which the size group is significant different to. (S = small, M = medium, L = large size). *B*: Same as *A* for the ROC-shape-feature, shape-selective electrodes and grouped by shapes (C = circle, D = diamond, P = pyramid, R = rectangle, T = triangle). *C*: Same as *B* for shape-classes (Cs = circles, Rs = rectangles, Ts = triangles). *D*: Same as *A* for the ROC-color-feature, color-selective electrodes and data grouped by colors. (gre = green, gra = gray, br = brown, bl = blue).

reported. 87.59% (*M1*) and 75.84% (*M2*) of the electrodes showed significant differences between shape-class groups. The test over all shape-class-selective electrodes showed significant differences between groups of shape-classes (*M1*: $\chi^2 = 107.17$, $p < 10^{-23}$, $df = 2$, $\omega^2 = 0.1$; *M2*: $\chi^2 = 85.91$, $p < 10^{-18}$, $df = 2$, $\omega^2 = 0.07$). The post hoc test revealed that all groups were significantly different (Fig. 10C). Lowest median ROC-feature activity was evoked by the shape-class triangles and highest median activity was evoked by the shape-class circles.

In contrast to the mean BGP response, the ROC-shape-feature shows a significant difference in the modulation caused by different stimulus shapes for the majority of electrodes. Furthermore, the modulation evoked by the shape-pairs diamond and rectangle, and pyramid and triangle was statistically not significant for both monkeys which is in line with the observation that these shapes evoke a similar BGP response (see Fig. 8F, K and P). The shape-class of the object modulated the ROC-shape-feature activity of most electrodes significantly and matched the ROC-shape-feature modulation comparing groups of stimulus shape.

Stimulus color

23.36% (*M1*) and 30.90% (*M2*) of the electrodes showed significant differences between color groups when the ROC-color-feature of single electrodes was used for statistical testing. Thus, the specific ROC-color-feature activity was not significantly different between differently colored objects for most electrodes. Using the color-wise grouped ROC-color-features over all electrodes for statistical testing resulted in a significant difference between groups (*M1*: $\chi^2 = 40.12$, $p < 10^{-17}$, $df = 4$, $\omega^2 = 0.13$; *M2*: $\chi^2 = 140.35$, $p < 10^{-28}$, $df = 4$, $\omega^2 = 0.34$). For both monkeys the post hoc test revealed that all pairs including the blue or the red color category except the blue-green pair in *M1* and the red-brown pair in *M2* were significantly different from each other (Fig. 10D). For both monkeys, the median ROC-color-feature activity of the blue group was highest, and the median ROC-color-feature activity of the red group (*M1*) or the brown group (*M2*) was lowest in comparison to all other color groups (Fig. 10D).

6.4.2 Classification of stimulus attributes from single-trial and trial-averaged EFP features

After analyzing the modulation of the EFP response, we investigated whether the modulations caused by stimulus size, shape and shape-class are decodable from single-trial and trial-averaged EFPs. Therefore we used ROC-features for a stimulus attribute-wise SVM classification of the attribute category (see Materials and Methods for further details). Due to the large influence of the stimulated position onto the EFP response, the classification was performed on data sets of each position separately. We used two ROC-features per electrode, extracted from the broadband EFP time course and from the time-frequency space of the wavelet-transformed EFP, because combining features from different EFP signal components increases classification performance of the stimulated position [Fischer et al. 2019]. Features of the five most position-selective electrodes were used for the classification of the data from each stimulus position. These were selected by ranking the AUC value of the ROC-position-feature of all electrodes for each stimulus position (for details, see Materials and Methods). As a result, two features of five electrodes were used to represent the activity of single-trial or trial-averaged features (averaged over $n = 2, 3, 4$ or 5 single-trial features).

We randomly drew 51 trials per attribute category and performed a “leave-one-out” classification using “one vs. rest” SVMs. The classification was repeated ten times for each stimulus attribute and each trial condition (i.e., single-trial or trial-averaged ROC-features). The reported mean performance was calculated over the SVM performance of all stimulus positions and classification repetitions.

Fig. 11 summarizes the results from the SVM classification. Mean SVM performance increased for all classification approaches with the number of trials that were averaged. This result is likely to be caused by averaging over trials because it reduces fluctuations within a single trial and keeps the information that is contained in multiple trials. In line with this assumption, the common information from multiple trials has led to an increase the classification performance (e.g., [Kaufmann et al. 2013; Parvar et al. 2015]). In general, best mean performance was reached using features that were averaged over five trials while the worst mean performance was reached using single-trial features. In the following, the performance of these classification conditions is denoted as min mean performance (single

6.4 Results

trial features) and max mean performance (features averaged over five trials) for each stimulus attribute.

When classifying the size of an object from ROC-size-features, max mean performance was 56.43 and 52.5%, and min mean performance was 42.82 and 40.12% for *M1* and *M2* respectively (Fig. 11A). The classification performance was higher for large and small size

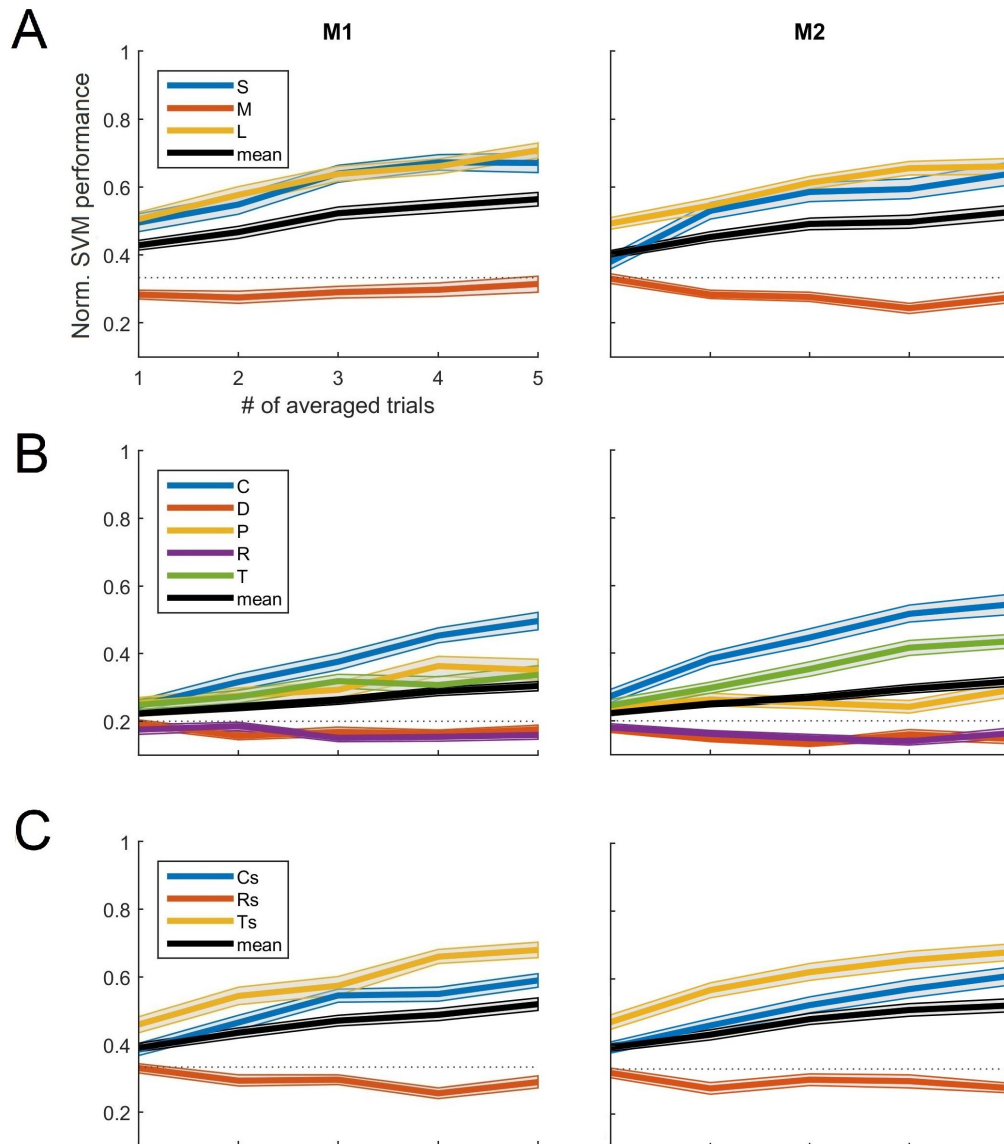


Fig. 11: Classification performance of decoding stimulus size, shape and shape-class. *A*: Normalized mean SVM performance for the classification of stimulus size with an increasing number of averaged single-trial ROC-features (*left plot M1, right plot M2*). The black line demonstrate the mean performance over all categories. Colored lines demonstrate the mean performance for each size separately (S = small, M = medium, L = large). Standard error of the mean is provided for each mean performance value. The thin dotted line indicates the chance level. *B*: As *A* for stimulus shape (C = circle, D = diamond, P = pyramid, R = rectangle, T = triangle). *C*: As *A* for stimulus shape-class (Cs = circles, Rs = rectangles, Ts = triangles).

categories in comparison to the medium size category. While the classification of the medium size category reached SVM performances worse than chance level (33.33%), large and small size had classification performances above chance level (Fig. 11A).

Fig. 11B shows the mean SVM performance classifying the shape identity of objects from ROC-shape-features. Max mean performance was 30.41 and 31.54%, and min mean performance was 22.31 and 22.24% for *M1* and *M2* respectively. In every condition, rectangular and diamond shape classification reached mean performances below chance level (20%) while all other shapes (circle, pyramid, triangle) reached performances higher than change level. Usually, highest mean performance was reached for classifying the circle shape while intermediate performances were reached for classifying the pyramid and triangle shape. The similar SVM performance for pyramid and triangle, or diamond and rectangle shaped objects is comparable to the found similarity of EFP responses evoked by shapes belonging to the same shape-class (see, Fig. 8F, K and P).

Repeating the classification to decode shape-classes (Fig. 11C) revealed max mean performance of 51.93 and 53.1%, and a min mean performance of 39.1 and 39.67% for *M1* and *M2* respectively. Circles and triangles were classified with performances over chance level (33.33%), while rectangles were classified with performances lower than chance level.

These results show that the information about certain stimulus sizes, shapes and shape-classes can be differentiated moderately from the attribute-specific trial-averaged ROC-feature activity of EFPs.

6.5 Discussion

The modulation of EFPs originating from neurons in V1 caused by different stimulus attributes was investigated by presenting stimuli that differed in position, size, shape and color to macaques performing a fixation task. Significant differences between attribute categories of stimulus size, shape and shape-classes were found for the signal recorded by the majority of electrodes using stimulus attribute-specific ROC-features. In addition, some categories of stimulus size, shape and shape-classes were decoded with a moderate classification performance from trial-averaged ROC-features.

6.5.1 Stimulus size

A larger stimulus evoked higher activity of the EFP ROC-size-feature which was predominantly located in the γ -frequency-band. In agreement with this finding, the intracortical LFP γ -power in V1 was found to increase with increasing stimulus size [Jia et al. 2013]. In addition, EEG activity shows higher stimulus induced power [Duszyk et al. 2014] and larger event-related amplitudes [DeVoe et al. 1968; Gebodh et al. 2017] when using larger stimuli. The increase in the ROC-size-feature activity (i.e., γ -band activity) is also in line with a study which showed that the γ -band activity (30-65 Hz) increases in both ECoG and the intracortical LFP with stimulus size [Dubey & Ray 2020]. Small and large objects were classified from trial-averaged ROC-signal-features with a performance of $> 50\%$, while intermediately sized objects were classified with a performance close or below chance level. This finding demonstrates that trial-averaged EFPs evoked by the intermediate size are too similar to the EFPs evoked by large and sized objects to be distinguished. Nevertheless, the present study demonstrates, that high-density EFPs are modulated by the size of a stimulus.

6.5.2 Stimulus shape and shape-class

Besides the identification of differently sized stimuli, we found significant modulations of EFP ROC-features based on stimulus shape and shape-class differences. In particular, we found that stimuli having the same but differently rotated shape elicited responses that were not significantly different from each other. Therefore, the EFP displays the shape-class rather than the shape of the objects. This observation could be explained by the orientation selectivity of V1 cells. The used shapes consisted of differently oriented bars. V1 cells are highly orientation selective and are organized in local columns which process all different orientations of a small area in the visual field in nearby neuronal populations [Hubel & Wiesel 1962, 1968, 1974a, 1977]. Differently rotated versions of a shape should activate a different set of orientation-tuned neurons, however, the amount and the response magnitude of the activated set of neuronal populations could be similar. Alternatively, the extend of the stimuli might have caused the found EFP response properties. The size of the triangles and rectangles were chosen to fit into the circle. As a result of their geometry and the matched number of pixels, they consisted of thicker lines and covered more of the inner area in

comparison to the circle. This explanation, however, would consider that covering different parts of the area surrounded by the circle would lead to a differentiated response. Due to the fact that we found very similar EFP responses for shapes with the same but differently rotated geometrical shape, the first assumption is more likely to explain the present findings.

Apart from that, we found the SVM classification performance of shapes and shape-classes to increase with the amount of averaged trials. We also found a rather low decoding performance using single-trial EFPs. In contrast, Rotermund and colleagues [2009] successfully classified complex shape stimuli (> 80% classification performance) with a line thickness of 0.3° , covering a visual area of $4^\circ \times 4^\circ$ with a center distance of $\sim 3^\circ$ eccentricity from the FS using single-trial signals of three epidural electrodes located above V1. In comparison to the present stimulation, the stimuli covered a larger area and were located more closely to the foveal region. In order to increase the EFP-based classification of small stimulus shapes, like the ones used in the present study, the placement of objects in the foveal part of the visual field could be considered. With increasing distance from the fovea, the visual field is represented by less cortical volume [Daniel & Whitteridge 1961; Hubel & Wiesel 1974b]. As a result, the part of the cortex which processes stimulation closer to or at the fovea is larger. Therefore, the foveal region is more densely covered by the equally spaced electrodes of the epidural array in comparison to cortical areas processing the peripheral visual space. This denser sampling could enable a more precise prediction of local changes in V1 activity. In addition, using larger objects could also lead to an increase in classification performance. The larger number of pixels activates more neuronal populations which potentially leads to the recording of shape-evoked signals at more electrodes. This approach could lead to more differentiated assemblies of electrodes that are activated by the presentation of certain shapes. Due to the fact that the objective of this study was to investigate whether EFPs are modulated by local stimulus attributes rather than decoding them with high accuracy, these suggestions could be realized in future work which is more focused on high-accuracy decoding of stimulus attributes from V1 EFPs.

6.5.3 Stimulus color

In general, stimulus color-evoked EFP modulations are not self-evident considering the spatial resolution of the used multi-electrode array. Previously, Xiao and colleagues [2007]

measured the cortical representation of a hue map in V1 (not to be confused with a color-blob) to be $\sim 160 \mu\text{m}$ in diameter. Within such a map, patches which process different hue levels overlap massively. Thus, the non-overlapping space which is needed to be activated for the formation of different spatial activity patterns is small. The used electrodes had a surface diameter of $560 \mu\text{m}$, ~ 3.5 times larger than the local hue map. Assuming that the spatial spread of EFPs and ECoG is similar, the finding that the cortical spread of ECoG is slightly larger than the electrode diameter [Dubey & Ray 2019] would indicate that the integrated area is far larger than a local hue map, impeding the recording of differentiated signals evoked by stimulus color.

Previous intracortical and ECoG studies found a higher γ -band activity caused by red stimuli in comparison to differently colored stimuli [Bartoli et al. 2019; Peter et al. 2019; Rols et al. 2001; Shirhatti & Ray 2018]. In addition, Peter and colleagues [2019] found that either a blue stimulus evokes higher LFP response γ -power than a green stimulus or vice versa, depending on the luminance of the isoluminant stimuli. In the present study, ROC-color-features, located in the low frequency range, did predominantly show a significant difference between pairs of colors including blue and/or red stimulus color. Due to the fact that the exact hue value of the used colors is not matched between the present and previous studies, it is difficult to draw conclusions regarding the comparison of the outcomes of these studies. In addition, Peter and colleagues [2019] found that differences in intracortical V1 γ -band oscillations, evoked by surface stimuli with different hue values, disappeared when these stimuli were shown on a black instead of a gray background. A repetition of the current experiment using a gray background and objects with the same color but different luminances could enable further insight into the EFP modulation evoked by stimulus color.

6.5.4 Outlook

Our results demonstrate that EFPs recorded from V1 are representing local properties of the visual stimulation, especially stimulus size and shape. Due to its lower level of invasiveness and high information content, epidural recordings provide specific signals for future neuroscientific research. The beneficial properties of signals recorded from high-density epidural electrode arrays could also enable a precise epidural mapping of cortical activity in

other sensory areas, providing promising possibilities for the development of EFP-based BCIs and other meso-invasive clinical applications.

7. Preliminary results: Modulation of EFPs from macaque V1 evoked by stimulus contrast.

7.1 Motivation

The previous chapter has given insight into the modulation of EFPs recorded from V1 caused by different stimulus sizes, shapes and colors. Besides these stimulus parameters, stimulus brightness and contrast influence the neuronal processing in V1 as well [Dai & Wang 2012]. This chapter documents investigations of EFP responses from V1 evoked by rapid flashes of stimuli with different contrasts.

7.2 Materials and Methods

7.2.1 Subjects

Two macaque monkeys (*Macaca mulatta*), *M1* (13 yr., 12 kg) and *M2* (14 yr., 11.5 kg), were chosen for the experiments. *M1* was single-housed and *M2* was housed pair-wise (for details, see General Materials and Methods). Surgeries and recordings were done as described in General Materials and Methods.

7.2.2 Visual stimulation

The visual stimulation consisted of nine different letters (D, E, H, L, O, R, T, W and X). They were composed of horizontal and vertical bars exclusively to ensure defined orientations of the edges (Fig. 12). Each letter was colored in a unique color. Each color was adjusted to 18 different luminance levels that were used to evoke a differentiated neuronal response in V1.

These were defined on a logarithmic scale from 0.25 to 50.58 cd/m². Due to the fact that the background color of the monitor was black, the contrast of each stimulus was defined by its luminance. The highest stimulus luminance was defined as 100% contrast. Each letter was placed at a specific position in the lower right quadrant of the visual field with eccentricities of 3°, 5° or 7° from the central FS (Fig. 12). Stimuli with the same distance to the FS had a height of 0.8°, 1.1° and 1.4° for 3°, 5° and 7° eccentricity respectively. The number of pixels was kept constant for stimuli with the same eccentricity.

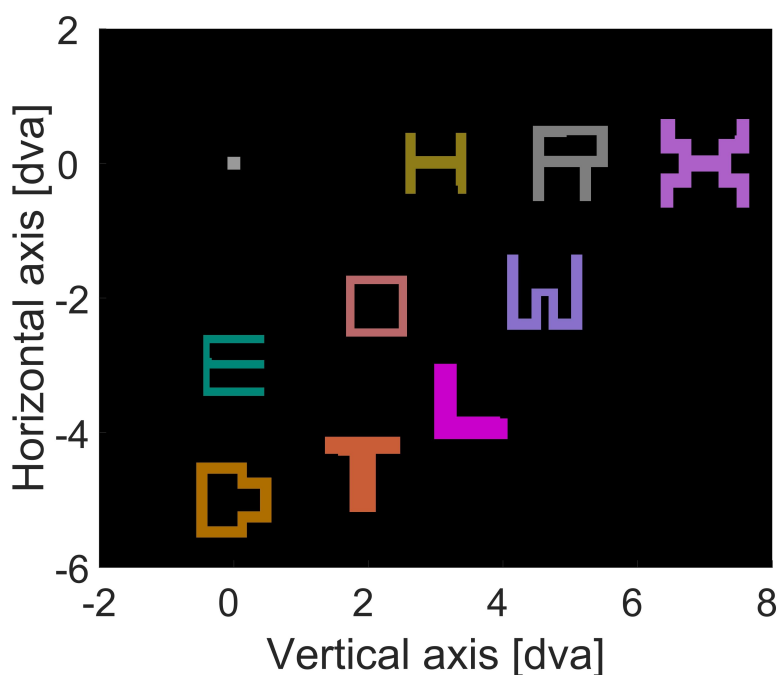


Fig. 12: The arrangement of letter stimuli in the lower right quadrant of the visual field. The arrangement was the same in experiment 1 and 2. Stimuli were centered on rings of eccentricity from the central fixation square and increased in size with increasing eccentricity (for details, see Materials and Methods). dva = degree of visual angle

7.2.3 Experiment 1 – Large area stimulation

The first experiment was done to study whether different levels of stimulus contrast affect the evoked EFP response recorded from V1. Therefore, all nine stimuli were flashed at once with the same contrast, while the monkey's task was to detect an FS dimming. The monkey started a trial by fixating a gray central FS (size: 0.2° × 0.2°) and pressing a lever. After trial start, a baseline period was initiated for 750 ms, where only the FS was visible. Next, nine equiluminant letter stimuli were shown for 1,000 ms. After their offset, only the FS was shown for a pseudo-randomized time window of minimally 700-1,000 ms (depending on

monkey and session) until the FS luminance was lowered. A response of the monkey up to 950 ms after FS dimming was rewarded. Provided that the animal responded before 200 ms post FS dimming or after 950 ms post FS dimming, the trial was aborted without reward. During trial execution, animals had to fixate within a window of $\sim 1^\circ$ radius around the FS.

The trials were shown block-wise. In each block, one trial per stimulus contrast had to be successfully executed including a trial where no stimuli were flashed (0% contrast condition). For *M1*, the three highest contrasts were presented only in the last recording session. In order to compensate for the number of trials recorded in the previous three sessions, trials of these higher contrast conditions occurred more often per block for *M1* in the last session.

7.2.4 Experiment 2 – Rapid local stimulation

In experiment 2, stimulus contrast changes (CC) of different magnitudes occurred at single stimulus positions sequentially while the animals did an FS dimming task. The monkey started a trial by fixating the FS and pressing the lever. Starting interval, trial abortion and FS specifications were equal to experiment 1. After trial start, a baseline period was initiated where the FS and nine stimuli with the same contrast (as arranged in Fig. 12) were shown for 1,000 (*M1*) or 750 (*M2*) ms. Afterwards, the contrast of the letters changed sequentially in a pseudo-random order for 150 ms and went back to the previous contrast. A blank period of 150 ms where no changes happened was set between the CC offset of the current stimulus and the CC onset of the next stimulus. The magnitude of the CC was equal for all nine stimuli within a trial. After the CC offset of the last stimulus, a pseudo-randomized time window followed, where the display did not change for 400-1,000 ms. After FS dimming, the monkey had to respond within 950 (*M1*) or 1,000 (*M2*) ms. Each level of CC was presented in a block.

The data of experiment 1 and 2 was recorded in multiple sessions for both monkeys.

7.2.5 Data preprocessing and wavelet transformation

The preprocessing and wavelet transformation of the data was done as described in General Materials and Methods for each single trial. The time window for the baseline normalization was defined as 201-700 ms post trial start. In the following, the frequency range of the broadband γ -band is defined as 30-160 Hz.

7.2.6 Removal of electrodes and trials with artifactual high γ -activity

The selection of visually driven electrodes was done as described in General Materials and Methods using RFs from an RF mapping which was carried out shortly after array implantation. Moreover, to exclude electrodes showing high artifactual γ -activity throughout many trials, an additional electrode rejection was performed. Electrodes showing ≥ 10 z-score activity in the mean broadband γ -power (BGP), calculated for the first 250 ms post stimulus display onset and offset (experiment 1) or the first 300 ms post CC onset (experiment 2), were rejected. The mean and the standard deviation for the z-normalization were calculated over electrodes for each condition separately.

To exclude single trials that were corrupted or featured artifactual γ -activity, a trial rejection was performed. Initially, trials were rejected that missed bins in the continuous time course. In addition, trials showing ≥ 5 z-score activity in the mean BGP, calculated for the time window of 1-250 ms post stimulus display onset and offset (experiment 1) or 1-300 ms post CC onset (experiment 2), were rejected. The mean and the standard deviation for the z-normalization were calculated over trials for each condition separately.

The same number of trials was chosen for all conditions in each experiment by using random under-sampling to balance the data sets for statistical testing and fitting in the result section. Therefore, the condition with the lowest number of trials was identified. For each condition in an experiment, the number of trials was reduced by randomly drawing as many trials as available for the previous identified condition. After this procedure, at least 35 trials were available for each condition and for each monkey.

7.2.7 Data analysis

7.2.7.1 *Broadband EFP and BGP signal features*

The analysis aimed to quantify the response modulation of EFPs in dependence of the stimulus contrast (experiment 1). In order to investigate the changes in the broadband EFP and BGP, different signal features for each electrode were calculated: the maximal absolute amplitude, the mean amplitude and the onset latency. These were calculated from trial-averaged signals in the following time windows (post stimulus onset): 1-175 ms for the BGP, 51-75 ms for the first negative peak in the broadband EFP (N1) and 61-150 ms for the

positive peak following the N1 in the broadband EFP (P1) (for further explanation, see Chapter 7.3.1). EFPs can contain multiple maxima in one response peak which makes a peak latency measure inappropriate. For this reason, the 50% fractional area latency [Kiesel et al. 2008] was calculated. The 50% fractional area latency calculates the latency as the time point before 50% of the area under the curve (i.e., under the time course) is filled. To enable this kind of measurement, a threshold needs to be defined on the y-axis [Kiesel et al. 2008]. For the present calculations, a threshold of $\mu + 0.5 \times \sigma$ was chosen, where μ is the mean and σ the standard deviation of the z-normalized signal time course. For the calculation of the N1 latency in experiment 1, the signal was multiplied by -1.

In order to quantify whether the response measures (max, mean and latency) change with an increasing stimulus contrast, they were averaged over electrodes and fit to different distributions. Mean vectors for each measure (size $1 \times N$ size, where N is the number of stimulus contrasts) were normalized by subtracting the minimal value and subsequently dividing by the maximum value. Normalized vectors were fit to a linear ($ax+b$), a sigmoidal ($1 \div (1 + e^{-a(x-c)})$), a power (ax^b), a polynomial (degree of three, ax^3+bx^2+cx+d) and a rectangular hyperbolic function ($a+(b \div x+c)$, referred to as hyperbolic function), where x denotes the normalized vector, and a , b , c and d are the variables that are changed for finding the optimal fit (fitting method: nonlinear least squares, using the fit function of Matlab). Fitting was repeated multiple times. The fit that most often reached the highest mean goodness of fit (R^2) over both monkeys was defined as the best fit and is reported in the result section. R^2 ranges from 0 to 1, with 1 indicating perfect fit of the data vector and the function.

7.2.7.2 Defining stimulus contrast changes for experiment 2

For defining the CCs of experiment 2, the objective was to find stimulus contrasts that evoke the lowest and highest EFP response (referred to as C_{Min} and C_{Max} respectively), as well as contrasts that evoke ~25% and ~50% of the highest EFP response in experiment 1 (referred to as C_{25} and C_{50} respectively). In order to find the desired contrasts, the mean BGP response (calculated over 1-175 ms post stimulus onset) was averaged over all available trials for each stimulus contrast and the vector was fit to a polynomial function (degree of three, using the polyfit function of Matlab). A polynomial function was used because it is able to fit the BGP response modulation of the highest contrasts. C_{25} and C_{50} were chosen as the closest stimulus contrast below 25 and 50% of the maximum fit response. Afterwards, CCs were defined as

contrast increase from C_{Min} to either C_{25} , C_{50} or C_{Max} (referred to as CC of 25, 50 and 100% respectively) and as contrast decrease from C_{Max} to either C_{50} , C_{25} or C_{Min} (referred to as CC of -50, -75 and -100% respectively).

7.2.7.3 Selection of best position-selective electrodes

In comparison to the stimulation in experiment 1, changes in the visual stimulation occurred locally in experiment 2. For studying the local cortical V1 activity modulation, only electrodes that were best-selective for a stimulus position were chosen for the analysis. The previously established ROC-based electrode selection was used (Chapter 5). Briefly, time bins of the EFP signal between 26-150 ms post initial 100% CC onset were identified which separate best between the stimulated positions. The time course of the broadband EFP and the BGP response was down-sampled by dividing it into bins of 5 ms and calculating the average of each bin. For each time bin, electrode and stimulated position, the broadband EFP or BGP values of all trials were grouped into trials where a certain position was stimulated and into trials where all other positions were stimulated. An ROC was performed using the distributions of these two groups resulting in one area-under-the-curve (AUC) value. The AUC variance was calculated over electrodes and positions for each time bin. The resulting variance vector was z-normalized. Time bins having > 1 z-score were selected. Afterwards, AUC values over the selected time bins were averaged for each electrode and position and were normalized by calculating the mean absolute AUC, i.e., the absolute deviation of the mean AUC from 0.5. These values were sorted to create an electrode ranking for each position. The five electrodes with the highest AUC values were chosen as best-selective electrode for each position. This procedure was done separately for the broadband EFP and the BGP time course. For the subsequent analysis, only the signal of the selected electrodes was used.

For the further investigation, the trial-averaged mean and the 50% fractional area latency of the broadband EFP and the BGP between 26 and 150 ms post stimulation onset was calculated for all selected electrodes and CC conditions. For the latency calculation (performed as described in Chapter 7.2.7.1), the z-normalized signal was multiplied by -1 provided that the most negative peak of the signal was higher in amplitude in comparison to the most positive peak.

7.2.8 Statistics and measurement of correlation

Kruskal-Wallis tests were performed ($\alpha = 0.05$) to test for statistical differences between groups. *Tukey's honest significant difference criterion* was applied to correct for multiple comparison. In addition, the effect size ω^2 was calculated as described in Chapter 6.3.8.

Pearson correlation was used for the investigation of correlations between signals. The coefficient ρ ranges from -1 to 1 . Positive values were interpreted as follows: above 0.7 as high, between 0.5 and 0.69 as intermediate, between 0.3 and 0.49 as small and from 0 to 0.29 as no positive correlation.

7.3 Results

Two different experiments were performed to investigate the response modulation of EFPs from V1 to changes in stimulus contrast. In the first experiment, the lower right quadrant of the visual field was stimulated with multiple stimuli at the same time while the monkeys were fixating a central FS. The task was repeated with stimulus sets of different stimulus contrast. The influence of stimulus contrast onto the broadband EFP and BGP was investigated by studying the difference in the latency, the mean and the peak activity over all electrodes. In the second experiment, the contrast of single stimuli within the previously used multi-stimulus display changed sequentially with contrast changes of different magnitudes. The data was used to investigate the signal modulation of a small set of electrodes evoked by local changes in stimulus contrast.

7.3.1 Experiment 1

The objective of the analysis of experiment 1 was to investigate signal modulations due to stimulus contrast over all electrodes ($n = 137$ and 172 , for *M1* and *M2* respectively). The mean broadband EFP activity over all electrodes and trials was analyzed for each condition (i.e., each stimulus contrast, Fig. 13A). Reported peak latencies were calculated for the highest stimulus contrast. The mean broadband EFP signal was similarly modulated for both monkeys (Fig. 13A): After a small positive deflection peaking at 43 and 52 ms, an initial negative deflection (N1) peaking at 53 and 57 ms post stimulation onset occurred which was

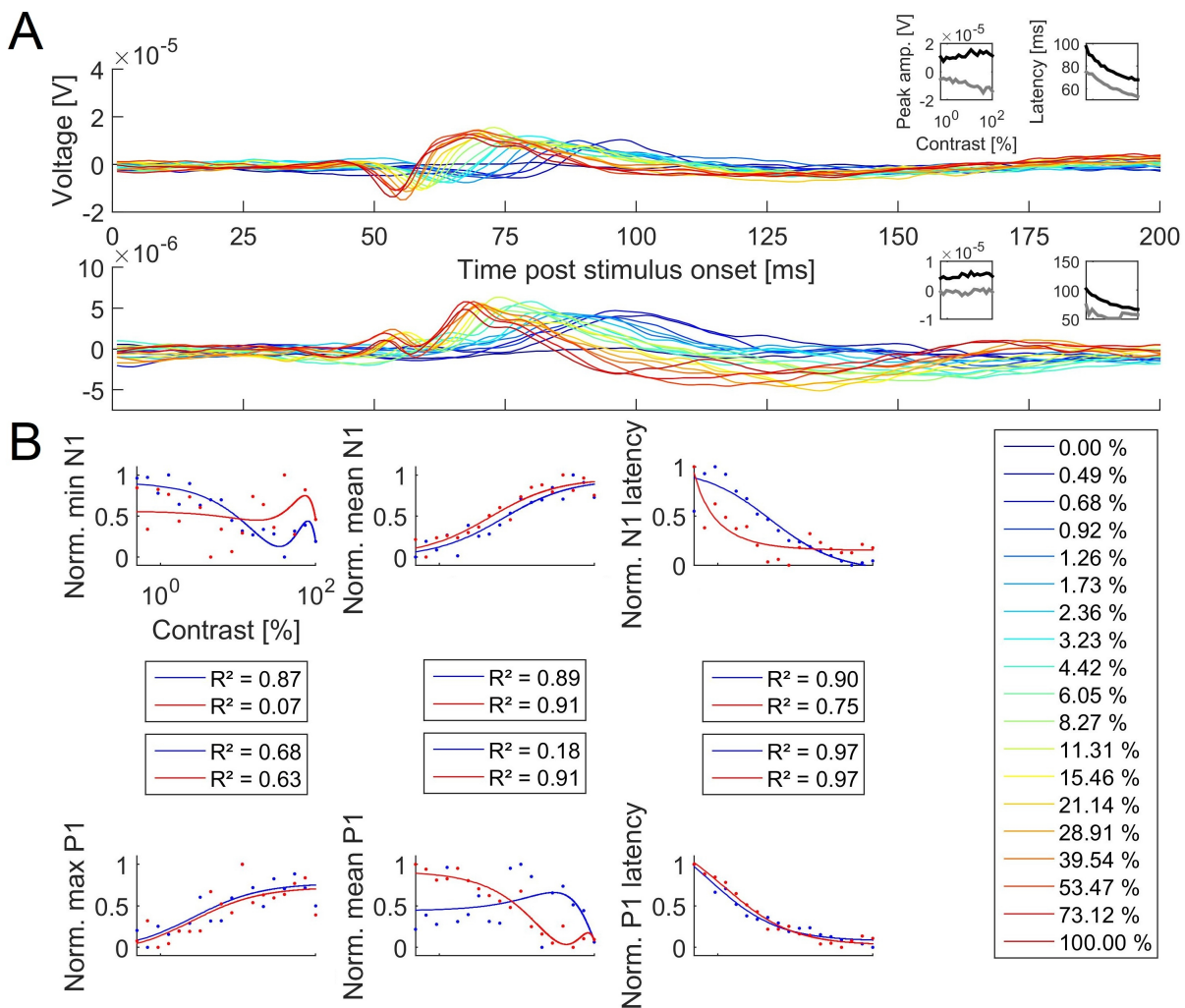


Fig. 13: Mean EFP response post stimulus display onset. *A*: The mean EFP response over all electrodes and trials evoked by the display onset is shown (*top M1*, *bottom M2*). Each line represents the stimulus contrast of each condition. The peak amplitude and peak latency of N1 (measured 51-75 ms post onset) and P1 (measured 61-150 ms post onset) is shown in the *inset* sorted by contrast (black line = P1, gray line = N1). The x-axis of the *inset* is logarithmically scaled. *B*: Shows the max absolute amplitude, the mean amplitude and the 50% fractal area latency averaged over all electrodes for each stimulus contrast (dots). These measures were calculated for N1 and P1, and for each monkey (blue = *M1*, red = *M2*). The means were fit to different functions. Best function is plotted (lines) and R^2 documents the goodness of fit. The x-axis is logarithmically scaled.

followed by a positive deflection (P1) peaking at 68 and 67 ms for *M1* and *M2* respectively. A second negative deflection (N2) peaked at 138 and 97 ms. For *M2*, N2 was divided into two peaks for the highest stimulus contrast (at 97 and 136 ms post stimulus onset) but fused into one for lower contrasts. For the investigation of N1 and P1 of the EFP, the time window for the analysis of N1 and P1 was chosen according to their occurrence (N1: 51-75 ms post onset, P1: 61-150 ms post onset). Within this time window, P1 and N1 absolute amplitude increased and P1 and N1 peak latency decreased with decreasing stimulus contrast for *M1*

(*insets* Fig. 13A *top*). The same held true for the P1 peak latency of *M2*. In contrast to *M1*, the N1 peak latency, and the N1 and P1 absolute amplitude of *M2* changed less uniform with increasing contrast (*insets* Fig. 13A *bottom*).

In order to quantify the observed modulation of the broadband EFP, the maximum absolute (max abs.) activity, the mean activity and the 50% fractal area latency was calculated for each single electrode (for details, see Materials and Methods). These measures were averaged over all electrodes. The averaged measures were fit to different functions (see Materials and Methods for all used functions; only the best-fitting function is reported here, Fig. 13B). The goodness of fit is denoted by R^2 . With increasing contrast, the N1 latency and the max absolute amplitude decreased (N1 latency, hyperbolic fit, *M1*: $R^2 = 0.90$, *M2*: $R^2 = 0.75$; N1 max abs., polynomial fit, *M1*: $R^2 = 0.87$, *M2*: $R^2 = 0.07$), while the N1 mean amplitude increased (hyperbolic fit, *M1*: $R^2 = 0.89$, *M2*: $R^2 = 0.91$). In comparison, the increase in stimulus contrast led to a decrease of the P1 latency and the mean amplitude (P1 latency, hyperbolic fit, *M1*: $R^2 = 0.97$, *M2*: $R^2 = 0.97$; P1 mean, polynomial fit, *M1*: $R^2 = 0.18$, *M2*: $R^2 = 0.91$) while the P1 max amplitude increased (hyperbolic fit, *M1*: $R^2 = 0.68$, *M2*: $R^2 = 0.63$).

In general, the fit of the P1 max amplitude, the N1 mean amplitude and the P1 latency reached highest mean R^2 over both monkeys. In contrast, the N1 maximal absolute peak of *M2* and the P1 mean amplitude for *M1* showed very low R^2 for the chosen fits. This observation could be explained by the missing N1 peak for lower stimulus contrasts in the signal of *M2* (Fig. 13A *bottom*). Furthermore, a long time window was chosen for the P1 analysis to include the elongated P1 response of *M2*, which could have made the measure for *M1* less accurate. When using a time window of 61-110 ms instead of 61-150 ms for the calculation of the P1 mean amplitude of *M1*, R^2 increased from 0.18 to 0.59 for the polynomial fit which confirms the previous assumption.

Apart from the broadband EFP, EFP γ -power activity was analyzed because it reliably indicated differences in the visual stimulation in the previous chapter (Chapter 6). The BGP was analyzed in the same manner as the broadband EFP by treating the mean BGP time course like the broadband EFP time course for the calculations. The grand BGP mean for each condition over electrodes and trials was calculated for both monkeys (Fig. 14A). The BGP increased in a single peak after stimulus onset. The peak of the response to the highest contrast occurred at 57 ms and 62 ms post stimulus onset for each monkey respectively. The

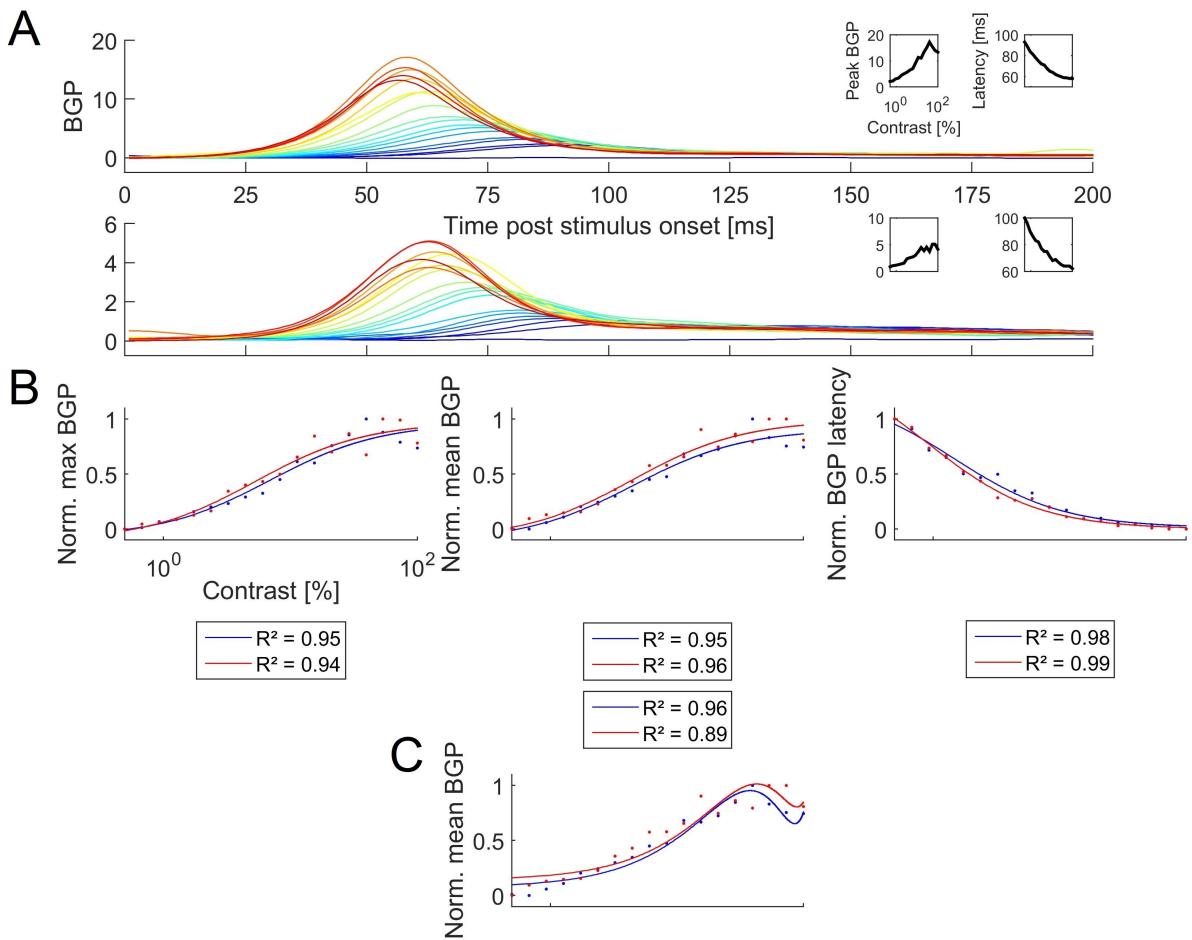


Fig. 14: Mean BGP response post stimulus display onset. *A*: The mean BGP response over all electrodes and trials evoked by the display onset is shown (*top M1, bottom M2*). Each line represents the response evoked by stimuli with a certain contrast (color labels for stimulus contrast as in Fig. 13). The onset peak amplitude and peak latency is shown in the *inset* sorted by the contrast level. The x-axis of the *inset* is logarithmically scaled. *B*: Shows the max absolute amplitude, the mean amplitude and the 50% fractal area latency averaged over all electrodes (dots). Measures were calculated for each monkey (blue = *M1*, red = *M2*). Means were fit to different functions. The best-fitting function is plotted (lines) and R^2 values document the goodness of fit. The x-axis is logarithmically scaled. *C*: As *B* for the mean BGP fit to another function (polynomial) which has a lower R^2 for *M2* value but fits better for highest contrast levels.

peak power increased with increasing stimulus contrast but was largest at lower than highest contrasts (*M1*: 40% stimulus contrast; *M2*: 73% stimulus contrast), decreasing afterwards for higher stimulus contrasts. The peak latency decreased with increasing contrast for both monkeys (Fig. 14*A insets*). As for the broadband EFP, the maximum activity, the mean activity and the latency of the BGP was calculated and fit to different functions using the BGP activity in the time window of 1-175 ms post stimulus onset. Means and fits are shown in Fig. 14*B*. The mean and the maximum peak power increased with increasing contrast (BGP max, hyperbolic fit, *M1*: $R^2 = 0.95$, *M2*: $R^2 = 0.94$; BGP mean, hyperbolic fit, *M1*: $R^2 =$

0.95, $M2$: $R^2 = 0.96$) while the BGP latency decreased (hyperbolic fit, $M1$: $R^2 = 0.98$, $M2$: $R^2 = 0.99$). The numerically one ($M2$) or three ($M1$) highest stimulus contrasts, however, evoked a lower mean BGP than the response to lower contrasts. Nevertheless, the polynomial fit, which fits better to the mean BGP for highest contrasts (Fig. 14C), was lower in R^2 for $M2$ (polynomial fit, $M1$: $R^2 = 0.96$, $M2$: $R^2 = 0.89$).

The investigation of EFP responses evoked by a sudden stimulus display onset revealed, that EFPs recorded from V1 were modulated by stimulus contrast. The measures that received best R^2 were the broadband EFP P1 latency and the BGP latency. These latencies decreased in a hyperbolic fashion with increasing stimulus contrast. The maximum and the mean BGP response also reached high R^2 for both monkeys. They increased with increasing stimulus contrast but peaked at stimulus contrasts lower than the highest contrast. Thus, the latency of EFP P1 and BGP onset indicated the magnitude of stimulus contrast, while the mean BGP response was highest for lower than highest contrasts.

7.3.1.1 Broadband EFP and BGP responses evoked by stimulus display on- and offset

In experiment 1, the onset of the stimulus display was followed by an offset to the black background color. This stimulation design enables the comparison of signal modulations evoked by display on- and offset. For the comparison, the mean over trials and electrodes 1-250 ms post onset and offset for each contrast was calculated for both broadband EFP and BGP. In order to quantify the similarity between on- and offset response, two-dimensional maps $N \times M$ (N = stimulus contrasts, M = the time course averaged over all trials and electrodes) were compared using Pearson correlation.

Both stimulus on- and offset evoked a response in the broadband EFP and the BGP (Fig. 15 and 16). The offset of the stimulus display evoked responses with a smaller amplitude in comparison to the response evoked by the onset of the stimulus display. For $M2$, the broadband EFP modulation was intermediately correlated between on- and offset response ($\rho = 0.56$). For $M1$ there was no correlation between on- and offset response ($\rho = 0.23$). In contrast, the correlation between onset EFP maps of $M1$ and $M2$ was intermediate ($\rho = 0.7$). For both monkeys, the display onset-evoked BGP was intermediately correlated to the offset evoked BGP ($M1$: $\rho = 0.51$, $M2$: $\rho = 0.63$). In comparison, the correlation between the onset evoked BGP of $M1$ and $M2$ was high ($\rho = 0.93$).

7.3 Results

Thus, EFPs also capture the neuronal activity evoked by a stimulus display offset. The offset evoked BGP response modulation to different stimulus contrasts is similar to the response modulation evoked by a display onset. Nevertheless, a stimulus display offset elicited lower BGP amplitudes in comparison to a stimulus display onset.

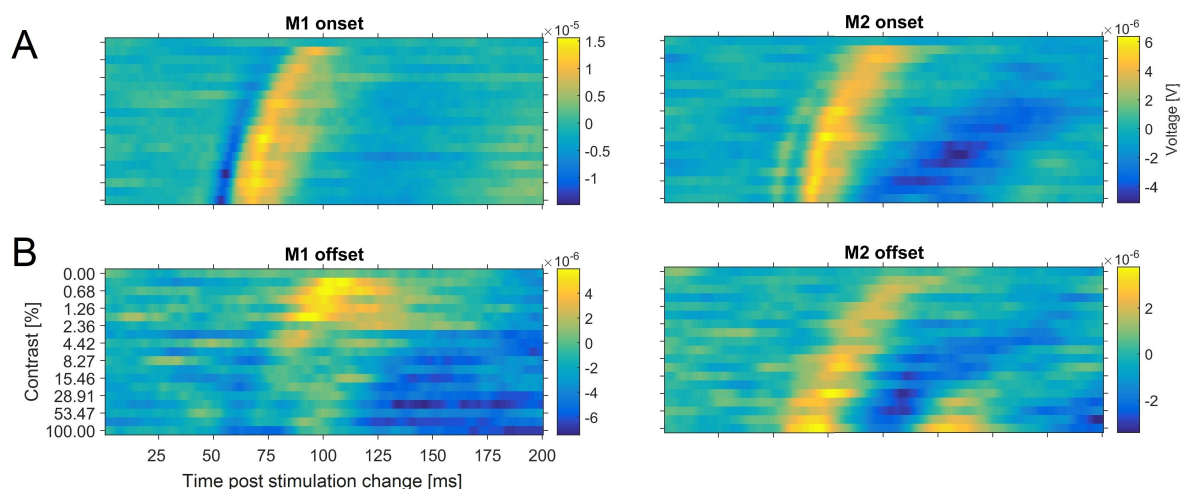


Fig. 15: The EFP response to the onset and the offset of the stimulus display. *A*: Same data as colored traces in Fig. 13A (left M1, right M2). *B*: Same as *A* for the EFP response to the stimulus display offset.

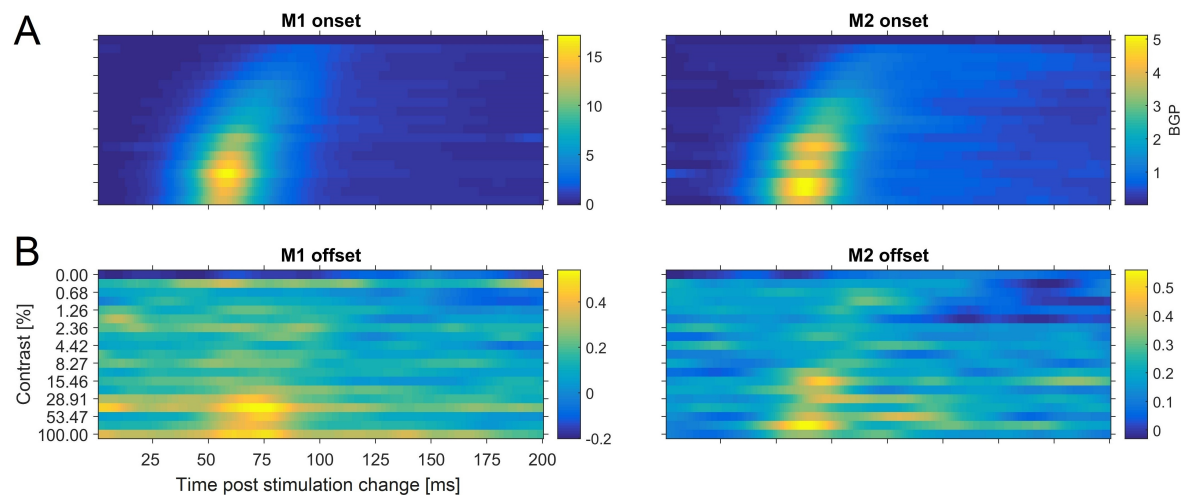


Fig. 16: The BGP response to the onset and the offset of the stimulus display. *A*: Same EFP data as colored traces in Fig. 14A (left M1, right M2). *B*: Same as *A* for the BGP response to the stimulus display offset.

7.3.2 Experiment 2

After the investigation of the multi-electrode response to a whole-field stimulus display presentation, locally evoked responses to CCs of different magnitudes were investigated at single electrodes using data from experiment 2. CCs were defined as 25, 50 and 100% increase from the contrast evoking lowest BGP response and as a change of -50, -75 and

7.3 Results

–100% from the contrast evoking highest BGP response (for details, see Materials and Methods). For each stimulus (i.e., spatial location of the stimulation), the five best position-selective electrodes were chosen for both broadband EFP and BGP as described in Materials and Methods. The selection was based on a previous established ROC-based method which ranks the electrodes by the ability to discriminate a single position from all other positions (see, Chapter 5). Due to their good fit in experiment 1, mean BGP and both EFP and BGP latency were calculated for each electrode and CC within 26-150 ms post CC onset to investigate modulations caused by different CC conditions. These values were grouped by the CC magnitude and tested for significant difference between groups. Mean values, latencies and post hoc results are shown in Fig. 17 and 18 for positive and negative CCs respectively.

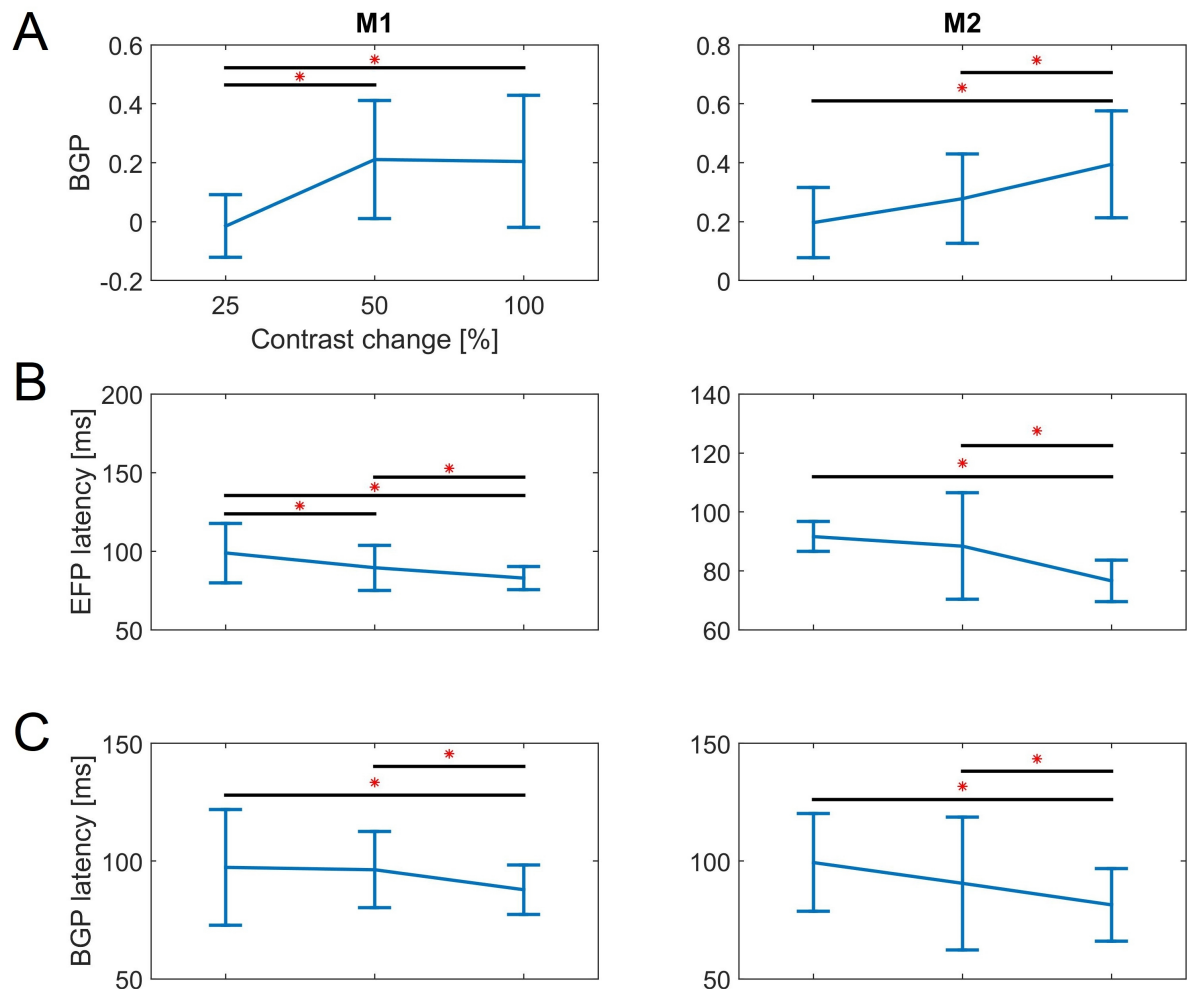


Fig. 17: Mean response and latency of best position-selective electrodes to a suddenly increasing stimulus contrast. *A*: The mean BGP over best position-selective electrodes evoked by different magnitudes of CCs for both monkeys is shown. The significant difference ($p < 0.05$) between pairs is indicated by black bars and red stars. SD is provided by error bars. *B*: Same as *A* for the broadband EFP onset latency. *C*: Same as *A* for the BGP onset latency.

7.3 Results

As illustrated in Fig. 17, the mean BGP, the BGP latency and the EFP latency differed significantly between groups of positive CC magnitudes (BGP mean: *M1*: $\chi^2 = 39.48$, $p < 10^{-8}$, $df = 2$, $\omega^2 = 0.17$; *M2*: $\chi^2 = 26.29$, $p < 10^{-5}$, $df = 2$, $\omega^2 = 0.1$. BGP latency: *M1*: $\chi^2 = 28.36$, $p < 10^{-6}$, $df = 2$, $\omega^2 = 0.11$; *M2*: $\chi^2 = 18.68$, $p < 10^{-4}$, $df = 2$, $\omega^2 = 0.07$. EFP latency: *M1*: $\chi^2 = 32.69$, $p < 10^{-7}$, $df = 2$, $\omega^2 = 0.13$; *M2*: $\chi^2 = 44.62$, $p < 10^{-9}$, $df = 2$, $\omega^2 = 0.19$). Post hoc tests revealed a significant decrease in the latency between the 25% and 100%, and the 50% and 100% CC condition for both broadband EFP and BGP, and for both monkeys. The increase in mean BGP was significantly different between the 25 and 100% CC condition for both monkeys. The increase in the mean BGP and decrease in the BGP and the EFP latency at single electrodes due to an CC of increasing magnitude is similar to the modulation which

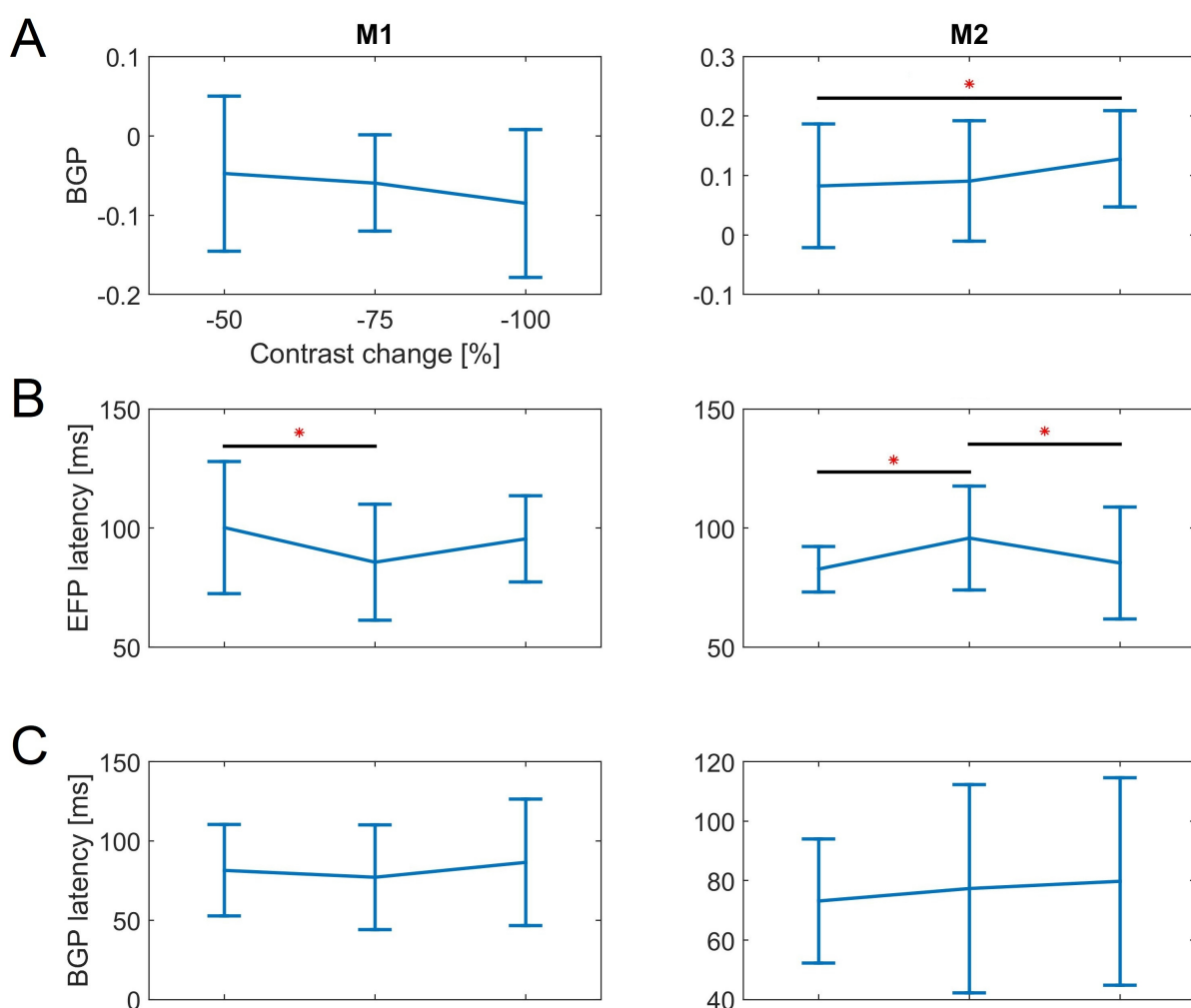


Fig. 18: Mean response and mean latency of best position-selective electrodes to a sudden decrease in stimulus contrast. *A*: The mean BGP over best-selective electrodes evoked by different magnitudes of contrast decrease for both monkeys is shown. The significant difference ($p < 0.05$) between pairs is indicated by black bars and red stars. SD is provided by error bars. *B*: Same as *A* for the broadband EFP onset latency. *C*: Same as *A* for the BGP onset latency.

was found over all electrodes for an increasing stimulus contrast in experiment 1. Thus, the mean BGP, the BGP latency and the EFP latency measured at single electrodes reflect differences in the neuronal activity evoked by local positive CCs of different magnitudes.

The investigation of the mean activity for negative CC conditions (Fig. 18) revealed that the EFP latency showed significant differences between CC groups (*M1*: $\chi^2 = 7.3$, $df = 2$, $p = 0.026$, $\omega^2 = 0.02$; *M2*: $\chi^2 = 14.35$, $p < 10^{-3}$, $df = 2$, $\omega^2 = 0.05$). In contrast, the mean BGP differed only for *M2* between CC groups and the BGP latency did not show significant differences between CC groups (BGP mean: *M1*: $\chi^2 = 2.83$, $df = 2$, $p = 0.24$; *M2*: $\chi^2 = 7.93$, $p = 0.019$, $df = 2$, $\omega^2 = 0.02$; BGP latency: *M1*: $\chi^2 = 0.96$, $p = 0.62$, $df = 2$; *M2*: $\chi^2 = 0.25$, $p = 0.89$, $df = 2$). Nevertheless, *M1* showed a significant decrease in EFP latency from -50 to -75% while *M2* showed a significant increase in EFP latency from -50 to -75% CC and a significant decrease from -75 to -100% CC. Hence, these results demonstrate no consistent significant signal modulation caused by an increase in the magnitude of a contrast decrease for both monkeys.

7.4 Discussion

The investigation of EFP responses to a sudden flash of multiple stimuli at once revealed that EFPs are modulated by stimulus contrast. In particular, the broadband EFP P1 latency, the BGP latency and the BGP amplitude were systematically modulated. While the broadband EFP and the BGP onset latency decreased in a hyperbolic fashion with increasing stimulus contrast, the BGP amplitude increased in response to increasing contrast but peaked at a lower than highest stimulus contrast. Furthermore, the BGP response evoked by the stimulus offset was intermediately correlated to the response evoked by the stimulus onset, and showed lower amplitudes. The analysis of EFP responses to local CCs revealed decreasing onset latencies of the broadband EFP and the BGP, and increasing absolute amplitudes of the BGP caused by an increasing magnitude of the positive CC.

7.4.1 Evoked broadband EFP modulations

The broadband EFP modulation evoked by a whole-field stimulus display presentation in experiment 1 was similar to the VEP evoked by large checkerboards in a ECoG study [Dagnelie et al. 1989], even though the present latencies of the EFP occurred earlier. N1, P1 and N2 peaked at 53 to 57 ms, 67 to 68 ms and 97 to 138 ms post stimulus onset for the highest stimulus contrast while Dagnelie and colleagues found these peaks to occur at 75, 100 and 135 ms post stimulus onset. These differences could be caused by the difference in the visual stimulation: While the present stimulation was based on small static stimuli, Dagnelie and colleagues used large checkerboard stimuli. Furthermore, both the findings of Dagnelie and colleagues [1989] and the present findings demonstrate that the peak latency of ECoG/EFPs is influenced by stimulus contrast. The luminance of the stimuli and the background was not matched between the present and the previous study, which could have caused the differences between the peak onset latencies.

7.4.2 The influence of stimulus contrast and luminance onto the EFP

The visual stimulation used different levels of stimulus contrast to evoke changes in the activity of V1 to investigate whether EFPs record changes in the neuronal activity of V1 caused by this stimulus attribute. The parameter stimulus luminance was changed to create different stimulus contrasts while the background was kept black. Depending on the RF properties of V1 neurons that were recorded, both stimulus contrast and luminance could have influenced the EFP modulation evoked by the visual stimulation. The epidural array was placed to cover the part of V1 containing neurons that process stimuli within $\sim 2\text{-}8^\circ$ eccentricity from fixation center in the bottom right quarter of the visual field. According to Hubel and Wiesel [1974b], these neurons should have RF sizes between $\sim 0.3\text{-}0.7^\circ$. The used stimuli were larger than these RF sizes. Therefore, most neurons should be activated by only a part of a stimulus. Due to the fact that the letter stimuli were composed out of lines, the probability to drive contrast responsive cells is increased because of the high probability of an RF to cover a border of a letter instead of the surface of a line. Many neurons in V1 are responsive to stimulus contrast or both stimulus contrast and luminance, while a minority of neurons are responsive to stimulus luminance but not to stimulus contrast [Dai & Wang 2012]. Due to the fact that the EFP is a signal that integrates over the activity of neuronal

populations, it potentially reflects the activity of neurons that were activated by contrast and/or luminance. Therefore, the following sections discuss results from previous studies regarding both stimulus contrast and luminance.

7.4.3 Increased γ -power response with increasing stimulus contrast/luminance

The analysis of experiment 1 revealed an increase in the amplitude of BGP with increasing stimulus contrast. V1 neurons are known to respond to stimulus luminance and/or contrast [Dai & Wang 2012]. The response of neurons in V1 increases as a hyperbolic function when contrast is increased [Albrecht & Hamilton 1982]. The response of surface luminance responsive V1 neurons was found to be modulated in different ways by an increasing luminance: monotonically increasing, monotonically decreasing or in a v-shaped fashion where the trough of the response curve is reached when the stimulus luminance is equal to the background luminance [Kinoshita & Komatsu 2001]. In addition, the intracranial LFP of multiple frequency bands from V1 was found to increase with increasing contrast, fitting to a hyperbolic function [Lashgari et al. 2012]. Rols and colleagues [2001] showed that ECoG γ -power (46-90 Hz) recorded in V1 increases with increasing stimulus luminance. Similar to this study, the present results show an increase in BGP (30-160 Hz) of the EFP with increasing stimulus contrast. In addition, the decrease in BGP for highest contrast in the present study is in line with intracortical studies. Some V1 neurons were found to respond highest to medium luminances [Peng & Van Essen 2005] and intracortical LFP γ -power increased with increasing stimulus contrast but decreased for the highest contrast [Jia et al. 2013]. Another study found ECoG and LFP γ -power (20-75 Hz) activity to reach a plateau for highest stimulus contrasts [Dubey & Ray 2020]. Taken together, the EFP γ -power was similarly modulated by stimulus contrast in comparison to ECoG and the intracortical LFP.

The BGP amplitude elicited by a stimulus display onset was found to be higher than the BGP amplitude elicited by a stimulus display offset. Due to the fact that the stimuli were flashed on a black background, this finding could also be explained by results of a study investigating intracortical signals. Xing and colleagues [2014] found the intracortical LFP transient response of V1 to be higher to rapid stimulus luminance changes from black to white than from white to black.

In summary, the present findings indicate that epidural signals are similarly modulated by stimulus contrast (and luminance) compared to intracortical and subdural recordings.

7.4.4 Shorter response latencies with increasing stimulus contrast/luminance

Higher stimulus contrasts evoked shorter transient response latencies in the broadband EFP and the BGP in the present study. This finding is in line with single cell, ECoG and EEG studies. Stimulating with objects having higher stimulus luminance/contrast led to a shorter onset latency of the firing rate of many V1 neurons [Gawne et al. 1996; Geisler et al. 2007]. An ECoG study used checkerboards to evoke VEPs and found that an increasing checkerboard contrast led to a decrease in the latency of the first negative peak post stimulus onset [Dagnelie et al. 1989]. In addition, the latency of the C1 and N1 component of EEG recorded by central occipital electrodes was found to decrease with increasing contrast [Gebodh et al. 2017; Jones & Keck 1978]. Furthermore, EEG N1 latency decreased at occipital electrodes for stimuli with higher luminance [Johannes et al. 1995]. In summary, the decreasing response latency evoked by an increasing stimulus contrast/luminance is similarly modulated at the level of intracortical, subdural, epidural and scalp electrodes.

7.4.5 Conclusion and outlook

The present findings demonstrate that the EFP is modulated by stimulus contrast. The found modulation is similar to the contrast- and/or luminance-evoked modulation of the intracortical LFP and ECoG. The similarities in the response modulation indicate that EFPs are similarly well suited to record neuronal activity in comparison to more invasive methods like ECoG which emphasizes the usage of epidural recordings in neuroscientific investigations and clinical applications.

8. Preliminary results: Attentional modulation of EFPs from V1, and correlation of EFPs and response time

8.1 Motivation

As stated in Chapter 3.2, many visual BCIs rely on eye movements. Therefore, tLIS patients are excluded from the usage of these BCIs. Hence, the main targeted group of BCI users is unable to control them. To provide a solution, recent studies used covert attentional shifts for gaze-independent EEG-based BCI control (e.g., [Aloise et al. 2012a; Marchetti et al. 2013; Treder et al. 2011b]). A lower classification accuracy, however, was found for BCIs based on covert attention in comparison to BCIs based on overt attention [Aricò et al. 2014]. Utilizing subdural or epidural electrodes instead of EEG could be favorable for covert attention-based BCIs because the performance of decoding the locus of spatial attention is comparable or better based on ECoG in comparison to EEG (for a tabular comparison between studies using EEG or ECoG, see [Astrand et al. 2014]). In addition, some ECoG-based BCI studies have suggested the inclusion of electrodes located over visual cortical areas in the analysis to enable a higher accuracy [Brunner et al. 2011; Speier et al. 2013]. Therefore, the usage of ECoG/EFPs for BCIs could balance the decrease in accuracy of gaze-independent covert-attention-based BCIs provided that they enable a reliable decoding of the spatial location of covert attention from visual cortices. Especially V1 could serve as a target region for such a BCI design because it has a precise retinotopic architecture [Tootell et al. 1988] which could enable the differentiation of small differences in the location of the covert attentional focus. There are, however, controversial findings regarding the magnitude of the attentional modulation of ECoG activity from V1: Both a modest modulation [Yoshor et al. 2007b] and a moderate modulation of V1 ECoG activity evoked by attention [Davidesco et al. 2013; Martin et al. 2019] was found.

EFPs would be preferable for a long-term usage of covert-attention-based BCIs because these signals are recorded with less-invasive electrodes in comparison to ECoG (as reviewed in Chapter 3.2.1). Previously, the locus of attention was decoded using EFPs from V1 and V4 from macaque monkeys (two attentional locations, performance: > 90%, [Rotermund et al. 2013]). Human ECoG was used to decode the locus of spatial attention based on electrodes covering parietal and occipital areas (three attentional locations, performance: 70%, [Andersson et al. 2011]) or based on electrodes covering non-occipital areas (three attentional locations, performance: 48%, [Gunduz et al. 2012]). Two to three selectable commands for BCI control enable a simple communication like a yes/no communication. Nevertheless, when considering a BCI speller that provides word-spelling, the limited number of commands decreases the speed of communication. To implement high-speed spelling, multiple locations should be targetable by shifts of covert attention for a free spelling of words. In this section, high-density EFP was recorded to investigate the possibility of decoding multiple closely arranged covert attentional loci. A monkey was trained to covertly attend 1 out of 15 spatially separated target letters while the EFP was recorded from V1. The preliminary results show a small attentional modulation in the broadband γ -band activity for electrodes with an RF near to the attentional target when averaging over all target letters. In addition, the same data was analyzed for signal features that predict the behavioral performance of the monkey. The single-trial EFP response latency evoked by the change of the target stimulus was found to correlate with the response time.

8.2 Materials and Methods

8.2.1 Subject

A male macaque monkey (*Macaca mulatta*) M1 (15 yr., 12.5 kg) was trained and used for the recordings. The monkey was housed pair-wise (see General Materials and Methods). Surgeries and recordings were done as described in General Materials and Methods.

8.2.2 Visual stimulation

Stimuli consisted of all 26 letters of the Latin alphabet. They were exclusively composed out of lines (Fig. 19). Each letter had a unique color which was chosen isoluminant for the whole set of letters (~ 13 cd/m²). They were arranged in three rings of eccentricity around the fixation spot (3° , 5° and 7°). The spacing of letters on each ring was equidistant. Each letter was always shown at the same position. The letter size increased with the eccentricity from the FS to cope with the cortical magnification factor [Hubel & Wiesel 1974b]. The letters had a height of 1° , 1.2° and 1.4° for the inner, the middle and the outer ring, respectively. Letters located on the same ring of eccentricity were matched in the number of pixels. Out of the 26 letters, 15 were chosen as targets for the task. A small gray square was placed on the surface of each target ($0.14^\circ/0.20^\circ/0.22^\circ$ height and width for each eccentricity respectively, ~ 36 cd/m², referred to as luminance change area, LCA). The dimming of one of the LCAs had to be

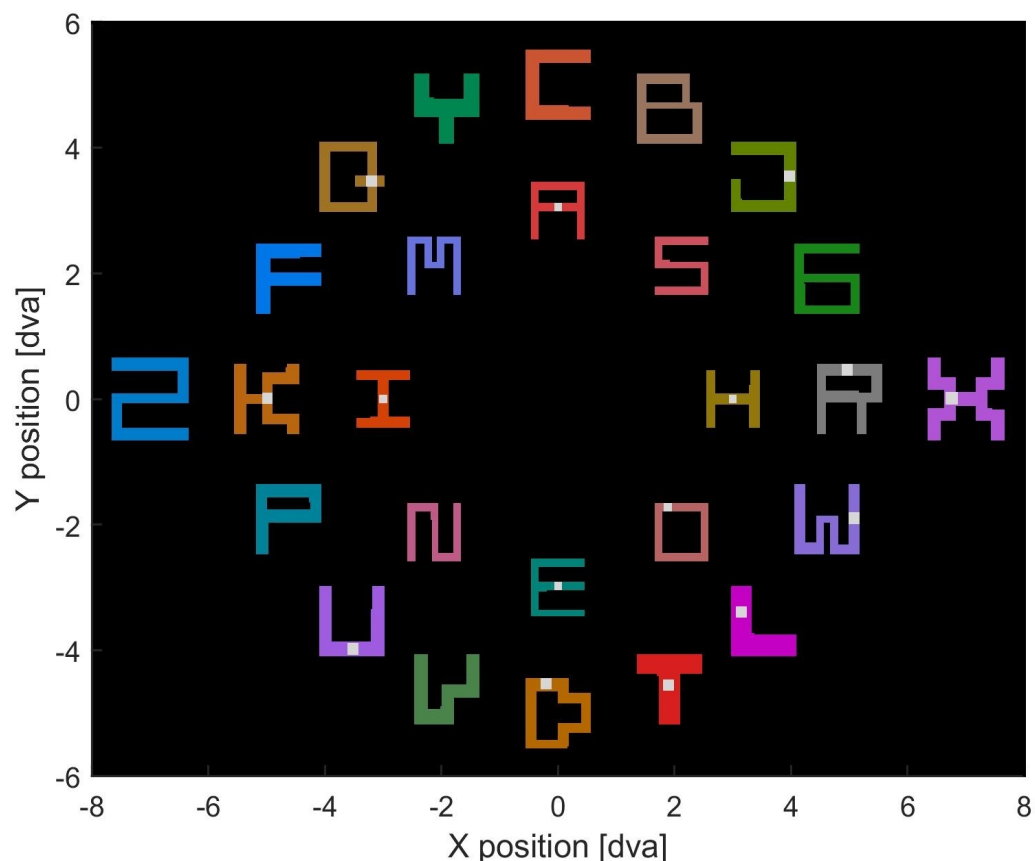


Fig. 19: Multi-stimulus display. 26 letter stimuli were arranged on rings of eccentricity from the FS (3° , 5° and 7°). Each letter was colored in an individual color. Colors were chosen isoluminant. Letter size and number of pixels was matched for each ring of eccentricity. Gray squares on 15 of the 26 letters are the luminance change areas (LCAs) of the target letters. dva = degree of visual angle.

detected in each trial. A blurred version of the target letter (not matched in the amount of pixels) with a height and width of $\sim 0.8^\circ$ without the gray square was used as a cue. The cue was placed behind the central FS. The background color was black.

8.2.3 Task

The monkey was trained to covertly shift its attentional focus to a cued letter and to respond to the luminance change of the LCA of the cued letter. After the ITI, the FS ($0.18^\circ \times 0.18^\circ$) was shown for 2,000 ms. The monkey could start a trial within this period by fixating the FS and pressing a lever. Fixation needed to be maintained throughout the trial. The stimulus display was presented 250 ms after successful trial start. After 750 ms, a symbolic cue was shown behind the FS, indicating the target letter of the current trial. After a pseudo-randomized time window of 1,500-3,500 ms, the LCA on the target letter dimmed with a luminance decrease of $\sim 16 \text{ cd/m}^2$ (deviating for each target). The monkey was rewarded for a response within 760 ms post luminance decrease. If the monkey responded too early (before 140-160 ms, depending on session; false alarm) or too late (miss) or if the signal of the gaze direction was not located inside an area of $\sim 1^\circ$ around the FS for more than 120-150 ms (eye error, depending on session), the trial would be aborted without a reward. After a successful trial termination or an error, an ITI of 1,000 ms was started where nothing but the black background was presented. The provided amount of reward was dependent on the monkey's reaction time (RT). Three different kinds of reward were defined: a large amount ($\sim 50 \text{ mL}/100\text{Hits}$) for fast ($\sim 150\text{-}250 \text{ ms}$), a medium amount ($\sim 25 \text{ mL}/100\text{Hits}$) for medium ($\sim 260\text{-}290 \text{ ms}$) and a small amount ($\sim 12 \text{ mL}/100\text{Hits}$) for slow ($> 290 \text{ ms}$) RTs. Reward amounts and time interval borders for the response were adjusted according to the performance of the monkey. Between sessions, luminance decrease of the LCA was adjusted to reach similar behavioral performance for each individual target letter (max increase or decrease throughout sessions $< 3 \text{ cd/m}^2$).

In 20% of the trials, a dimming of a non-cued target (distractor) occurred before the target dimming (referred to as catch trials). A distractor stimulus dimmed 1,500-2,500 ms post cue onset and previous to the target. A distractor was always one of the other targets and usually placed on the same ring of eccentricity. In 50% of the catch trials, the distractor was an opposite stimulus ($135\text{-}180^\circ$). In the other 50% of the catch trials, the distractor was placed

closer to the target (27.5-135°). The monkey was allowed to respond to the distractor dimming. The response window was the same as for the target letter in normal trials. The monkey was rewarded with a very small reward (~3 mL/100Hits) for a response to the distractor dimming. Otherwise, the target dimmed 750-1,050 ms afterwards. A response of the monkey between distractor and target dimming terminated the trial without a reward. For a fast or a medium RT following the target dimming, the monkey was rewarded with a large amount and for a slow RT with a small amount of reward (as defined above).

8.2.4 Behavioral analysis

The RT was normalized to compensate the behavioral differences between sessions, or sessions and conditions by:

$$RT_{norm} = \frac{RT_i}{RT_{median}}$$

where RT_i is the RT of a single trial and RT_{median} the median RT calculated over all RTs from either the same session, or the same session and condition as RT_i . The hit rate was calculated by dividing the sum of successful trials by the sum of successful trials, misses and false alarms.

8.2.5 Preprocessing of EFPs

Data preprocessing was done as described in General Materials and Methods. Due to the large effect of the display onset onto the EFP signal (see Fig. 23), the signals were normalized using the time period between cue onset and target change. The mean activity in the time window of 100-600 ms pre-luminance decrease was used to normalize the data of each electrode separately by subtracting the mean activity and subsequently dividing by the SD of the mean activity within the pre-luminance decrease time window. This procedure was done for each frequency band separately for the normalization of the wavelet-transformed EFP.

8.2.6 Electrode and trial rejection

The selection of visually driven V1 electrodes was done using an RF mapping procedure as described in General Materials and Methods. For the analysis of the attentional modulation in

V1, trials and electrodes with artifactual high γ -band activity were rejected as described in Chapter 7.2.6 using the time window of 100-600 ms pre target change and the frequency range of 30-160 Hz. In addition, the number of the remaining trials was adjusted to an equal number for all conditions as described in Chapter 7.2.6.

8.2.7 Analysis of attention

8.2.7.1 **Calculating the RF eccentricity of electrodes to the target letter**

Spatial attention modulates the activity of neurons that process visual information from the attended spatial location (for further detail, see Chapter 3.1.6). Epidural electrodes that record from neuronal populations processing spatial locations within the attentional focus should be stronger modulated in comparison to electrodes recording from neurons that process non-attended spatial locations. Therefore, the influence of attention onto EFP γ -band activity was investigated with regard to the distance from each electrodes RF to the attended letter. The RF eccentricity from each electrode to a target letter was defined as the rounded eccentricity of each electrodes RF max activity peak to the center of the target letter. The RF activity center was taken from a single previously performed RF mapping (see General Materials and Methods). This procedure resulted in RF eccentricity values ranging from 0° to the rounded maximum eccentricity in steps of 1° .

8.2.7.2 **Data normalization**

For statistical testing of differences between attentional conditions, mean broadband γ -power (30-160 Hz, BGP) from 100-600 ms pre-dimming onset was calculated for each target letter, electrode and trial. These values were normalized into a range from 0 to 1 by calculating

$$x_{range01} = \frac{x_{tr} - \min(x)}{\max(x) - \min(x)}$$

where x_{tr} is the single-trial mean BGP and x are all other trials. Afterwards, these values were averaged over all trials per target letter and electrode.

8.2.7.3 **Attention index**

The attention index (AI) was calculated as

$$AI = \frac{Att_{In} - Att_{Out}}{Att_{Out} + Att_{In}}$$

where Att_{In} is the normalized mean BGP of the attend-in and Att_{Out} the normalized mean BGP of the attend-out condition.

8.2.8 Statistics

Statistical tests and the effect size calculation were done as described in Chapter 6.3.8. Statistical significance was defined when $p < 0.05$ was reached. In addition, the ex-Gaussian fit was used to fit the RT distributions of different conditions (<https://github.com/bramzandbelt/exgauss>). Details are described in Chapter 9.4.3. Briefly, RT distributions are usually non-normally distributed. Therefore, the ex-Gaussian fit divides the distribution into different parts, to extract measures which describe the normally distributed part (μ and σ for mean and variability) and the exponential part (τ) of the distribution [Heathcote et al. 1991]. For the investigation of fast responses, μ was analyzed, while τ was analyzed to investigate slow responses.

8.3 Results

A monkey was trained to allocate its attentional focus to one out of 15 letters within a multi-stimulus display. In a first step, the behavioral performance was investigated. In a second step, the modulation of the EFP γ -activity of V1 caused by spatial attention was studied. Finally, the correlation between transient EFP responses evoked by an LCA dimming and RT was investigated.

8.3.1 Behavioral results

The monkey reached a hit rate of 75.74% over seven sessions. The RT of all available trials was divided into three groups: responses to target stimuli in normal trials (2,936 trials), responses to target stimuli in catch trials (304 trials) and responses to distractor stimuli in catch trials (468 trials). The raw RT was analyzed as well as the session-wise normalized RT (for details, see Materials and Methods). The median raw RT difference between the

conditions was 10 ms: The fastest median RT was reached for target responses in catch trials (260 ms), an intermediate median for target responses in normal trials (270 ms) and the slowest median for distractor responses in catch trials (280 ms). The normalized RT was investigated by fitting the distributions with an ex-Gaussian fit. The fit of each of the RT distributions is illustrated in Fig. 20. The parameter μ of the Gaussian fit, describing the left side of the distribution, was lowest for responses to the target in catch trials (0.84), intermediate to target responses in normal trials (0.85) and highest for distractor responses in catch trials (0.86). Ex-Gauss parameter τ derived from the exponentially distributed right part of the RT distribution was lowest for target responses in catch trials (0.22), intermediate for target responses in normal trials (0.27) and largest for catch responses in catch trials (0.3). Thus, RTs to target changes, especially in catch trials, were faster in comparison to RTs to distractor changes.

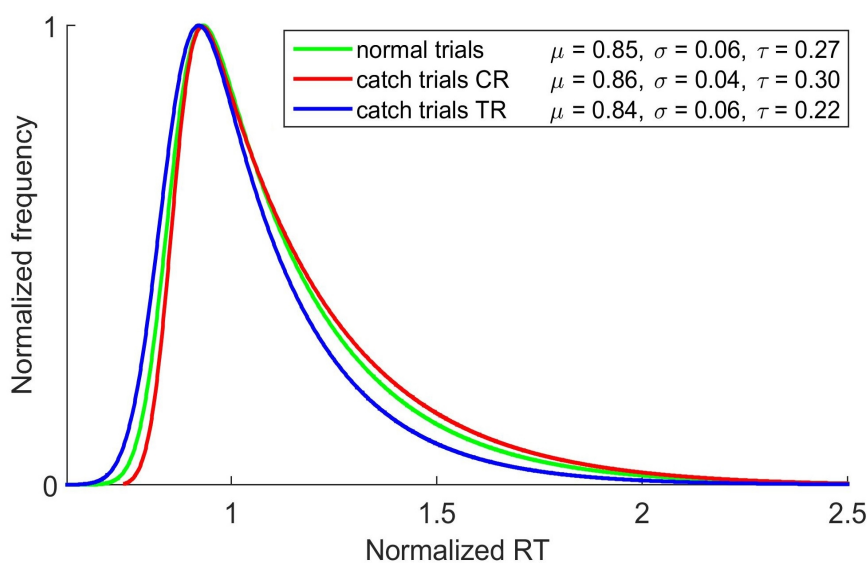


Fig. 20: RT distribution for three different types of responses. Session-wise normalized RTs were separated into three groups: responses in normal trials (green), responses to distractor LCA dimming in catch trials (red) and responses to target LCA dimming in catch trials (blue). Groups of RTs were fit (ex-Gaussian fit). Fitting parameters are noted in the legend. (CR = catch response, TR = target response)

8.3.2 Attentional modulation of EFPs

The present difference in the RT distributions between the response to target and distractor letters indicates a slightly better behavioral performance when the target letter was attended. Therefore, it was investigated whether the EFP activity from V1 was modulated by attention.

In principle, an electrode with an RF that covers the visual space of a certain target letter should show a differentiated attentionally evoked γ -activity during the allocation of attention to the target letter in comparison to the allocation to a distractor letter (for details, see Chapter 3.1.6). In order to test this assumption, a far located “distractor letter” was chosen for each target letter to serve as attend-out condition (135-180° circular distance). In addition, the mean BGP recorded by electrodes that had the same distance to the target letter were pooled in order to be able to relate the distance between electrodes and the attentional target with the attentional modulation. Therefore, the distance of each electrodes RF to the target letter was calculated (see Materials and Methods). Electrodes were grouped according to their RF distance to the target letter in steps of 1° (see Materials and Methods). For each electrode, the trial-averaged normalized BGP activity (see Materials and Methods) during trials in which the chosen letter was the target (attend-in condition) was calculated. For the same groups of electrodes, the trial-averaged normalized BGP activity during trials in which the distractor letter was the target (attend-out condition) was pooled. This procedure resulted in groups of trial-averaged BGP activity for each RF eccentricity group and for both attentional conditions. This was done for each of the 15 target letters. The mean over each RF eccentricity and attentional condition is shown in Fig. 21 for each target separately. Only RF eccentricity groups were included that contained data of more than nine electrodes. The mean BGP response was differently modulated in the attend-in and attend-out conditions regarding different locations (Fig. 21). Nevertheless, there is no general trend visible comparing the BGP activity of different attentional conditions between targets. In order to quantify whether a general tendency of the BGP response modulation for the attend-in and -out condition exists, groups of the same RF eccentricity and attentional condition over all target letters were pooled. This resulted in two groups for each RF eccentricity for all target letters. A Kruskal-Wallis test was done to test whether the BGP activity of the attend-in and -out group of each RF eccentricity differed significantly. In the following, significant comparisons were only documented when at least a small effect size was evident. Only groups of 1 to 12° RF eccentricity were analyzed because other groups covered only a small proportion of electrodes (< 40 electrodes). Besides the statistical analysis, an attention index (AI) was calculated for each eccentricity group (see Materials and Methods).

The statistical analysis revealed that electrodes with an RF distance of 1° to 3° recorded significantly higher BGP in the attend-in compared to the attend-out condition (Fig. 22A).

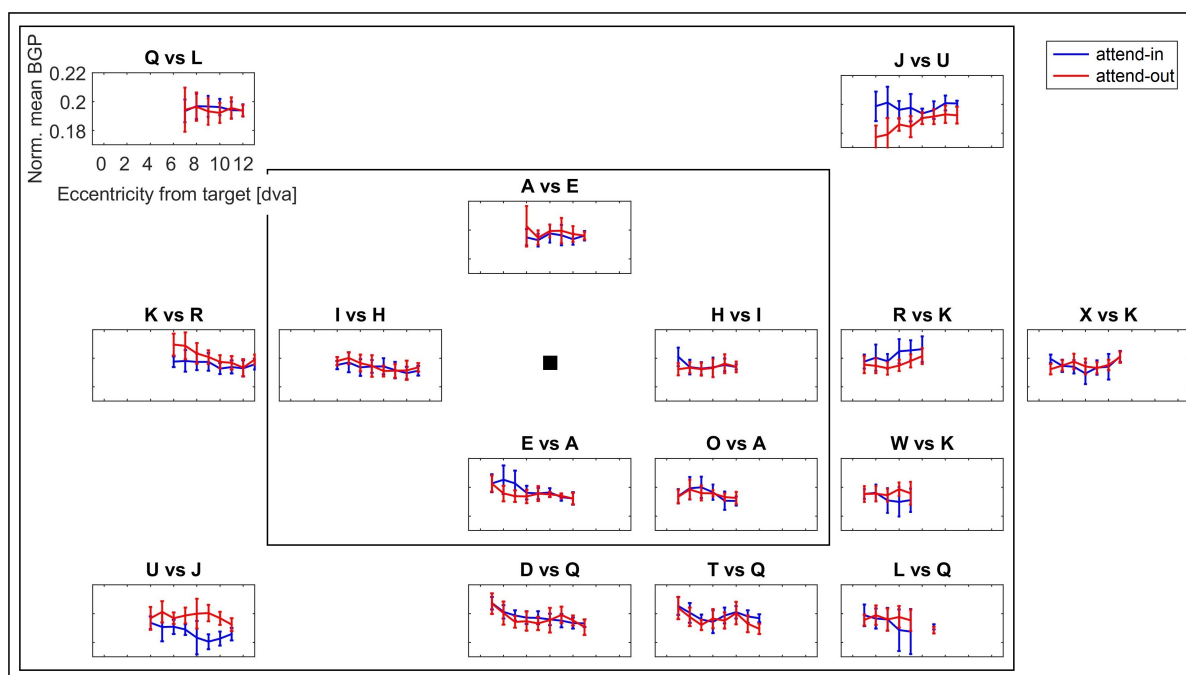


Fig. 21: BGP in accordance to the RF eccentricity from electrodes to target letters in the attend-in and attend-out condition. Each plot represents the BGP during the allocation of attention to a target against its opposite distractor (attend-in vs. -out condition). Averaged normalized BGP and SD are plotted for each pool of electrodes in an RF eccentricity bin. The position of the plot reflects its position on the visual display. Plots in a square correspond to targets placed on one ring of eccentricity to the FS. The location of the FS is indicated by the small black square. In each title, the target and distractor is noted.

Numerically, but only significant for the 10° and 11° eccentricity group, intermediate and far recorded signals showed higher BGP in the attend-out condition. The AI value of significant RF eccentricity groups was 0.008, 0.007, 0.006, -0.006 and -0.009 (for 1°, 2°, 3°, 10° and 11° respectively). The AI was most positive at electrodes that were closely located to the target and usually negative for electrodes that were located far from the target (Fig. 22F).

The attentional modulation should be higher in trials where the monkey responded fast because the animal needs to be focused to achieve fast RTs. In order to test this assumption, the above described analysis was repeated using only trials which resulted in RTs that were faster than the median RT (RT normalized by the session- and condition-wise median RT, see Materials and Methods). Differences between attend-in and -out were present throughout the span of RF eccentricities (Fig. 22C). Attentional conditions differed significantly for 1° to 3° (higher BGP for attend-in) and 10° to 12° RF eccentricity (higher BGP for attend-out). AI values of significant groups with RF eccentricities near to the target letter ranged between 0.009 to 0.015 while AI was -0.009 to -0.021 for the far eccentricity groups. The AI was

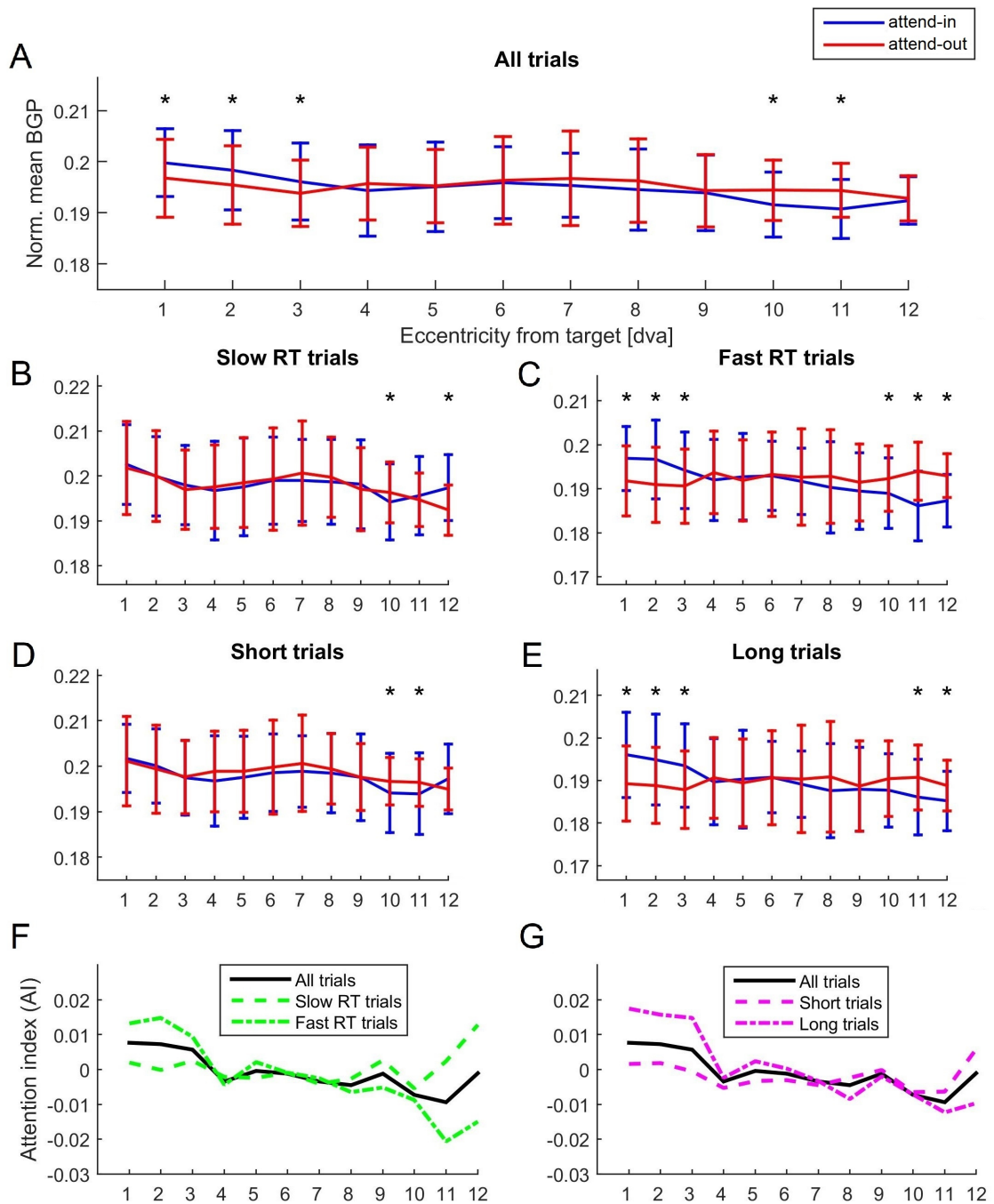


Fig. 22: BGP modulation caused by covert spatial attention. *A*: The averaged normalized BGP of each group of electrodes having the same RF eccentricity to the target is shown for trials where the target was attended (attend-in, blue) or where a far located distractor was attended (attend-out, red). Errorbars indicate the SD. Stars indicate significant difference between attend-in vs. -out ($p < 0.05$, $\omega^2 \geq 0.01$). Norm. mean BGP = normalized mean broadband γ -power. *B*: same as *A* using only trials which resulted in RT slower than and equal to the median RT of normal trials. *C*: the same as *B* for trials resulting in trials faster than the median RT of normal trials. *D*: same as *C* using trials with a waiting time shorter than median time between cue onset and target LCA dimming onset over all normal trials. *E*: same as *D* for trials with waiting times longer or equal to median waiting time over all normal trials. *F*: Attention index calculated from data shown in *A-C*. *G*: same as *F* for data shown in *A, D* and *E*. dva = degree of visual angle.

high for close and low or negative for intermediate to far electrode eccentricities (Fig. 22F). The repetition of the analysis with all trials resulting in slower than or equal to median RT is summarized in Fig. 22B. The RF eccentricity groups 10° and 12° showed significant differences between attentional conditions (AI: -0.06 and 0.013 respectively, Fig. 22F).

The AI was previously shown to be influenced by the duration of a trial [Sharma et al. 2015]. Therefore, the trials were split by the duration between cue and target LCA dimming onset into short (< median trial length) and long trials (\geq median trial length) to test whether the trial duration influences the attentional modulation. Using only long trials, RF eccentricity groups of 1° to 3° showed significantly higher BGP for the attend-in condition (Fig. 22E, AI between 0.015 and 0.018). RF eccentricity groups of 11° and 12° showed significantly higher BGP for the attend-out condition (AI between -0.01 and -0.012). Utilizing only short trials for the analysis revealed significantly higher BGP activity for the 10° and 11° groups for the attend-in condition (AI -0.007 and -0.006, Fig. 22D and G).

Taken together, the BGP activity of electrodes with RFs near to (< 4°) and far from (> 9°) the attentional target was significantly influenced by covert attention. For fast RT and long trials, AI was positive for nearby and negative for far located electrodes. The attentional modulation disappears for groups with RF eccentricities near to the target when short or slow RT trials were used for the analysis, while a significant difference remained for electrodes with far distance to the target letter. Electrode groups with RFs of intermediate distance to the target letter showed no significant modulation between the attend-in and -out condition.

8.3.3 Visual evoked EFP latencies correlate with RT

After the investigation of the attentional modulation of the BGP, the transient EFP signal evoked by the stimulus display, the cue and the dimming onset was investigated. The mean over all normal trials, target letters and electrodes was calculated to illustrate the mean EFP activity over the electrode array during a trial. The mean (which will be denoted as event-related potential, ERP) is displayed in Fig. 23. In general, all onset events had an influence onto the EFP time course. The ERP evoked by the display onset is similar to the ERP found at occipital-temporal EEG electrodes (for an example, see Figure 1 in [Woodman 2010]). There were five peaks starting with a positive peak (54 ms post display onset), followed by a negative (63 ms), a positive (74 ms), a negative (144 ms) and a slow-rising low-amplitude

positive deflection with a small negative bump (345 ms). After the onset of the cue, a positive peak with a plateau (from 74-110 ms post cue onset) was evoked, followed by a negative peak (142 ms). The onset of the target LCA dimming evoked a small negative (68 ms post LCA dimming onset) and a positive deflection (134 ms).

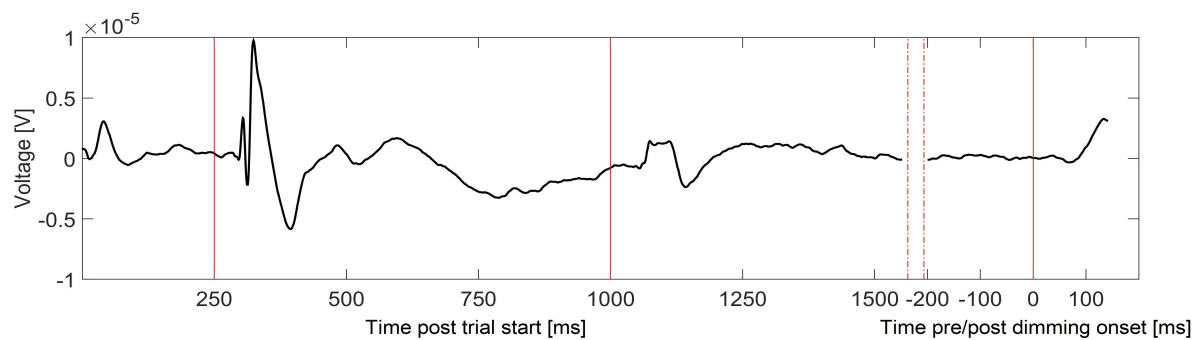


Fig. 23: Grand average ERP of the EFP over electrodes and normal trials. Single red lines indicate a change in the stimulation (1. stimuli display onset, 2. cue onset and 3. target LCA dimming onset). The space between the broken-dotted red lines represents a pseudo-random time interval which was cut out because of the trial-alignment.

The amplitude and latency of the stimulus-induced VEP of the occipital cortex recorded with EEG is correlated with the subsequent RT [Donchin & Lindsley 1966; Eason et al. 1967; Hartwell & Cowan 1994]. In order to test whether this holds true for EFPs from V1, a possible correlation between the EFP response peaks evoked by the LCA dimming of the target letter and the RT was investigated.

For each target letter, an electrode was selected that was highly modulated by the luminance change of the LCA (most stimulus-selective electrodes). For each electrode and target letter the mean over the trial-averaged EFP signal in between ± 25 ms from 68 ms post LCA dimming onset was calculated. The time window was chosen to cover the negative peak response that was evident in the ERP post LCA dimming. The electrode which had lowest mean EFP response for a target letter was chosen as the stimulus-selective electrode for that letter. Due to the fact that only the lower right quadrant of the visual field was covered by the RFs of the electrodes, some letters did cause no or only a modest modulation of the EFP. Thus, target letters were rejected from further analysis whose selected electrode showed a negative peak amplitude in the trial-averaged EFP higher than -0.5×10^{-5} V. Five out of 15 target letters were rejected. For the remaining most stimulus-selective electrodes, all available trials were sorted by the normalized RT (normalized by the condition- and session-wise RT

8.3 Results

median, see Materials and Methods). An example of an electrode is shown in Fig. 24A right. Additionally, the EFP activity averaged over the first, intermediate and last 50 trials (non overlapping, sorted by RT) was plotted (Fig. 24B right). The same was done for the time post stimulus display and post cue onset (see Fig. 24A left and middle, and Fig. 24B left and middle). The latency of the EFP activity evoked by the target dimming was shortest for fast RT and longest for slow RT, while the latency of the display onset was more or less constant between RT groups. The cue onset did not evoke a clear negative peak in this example.

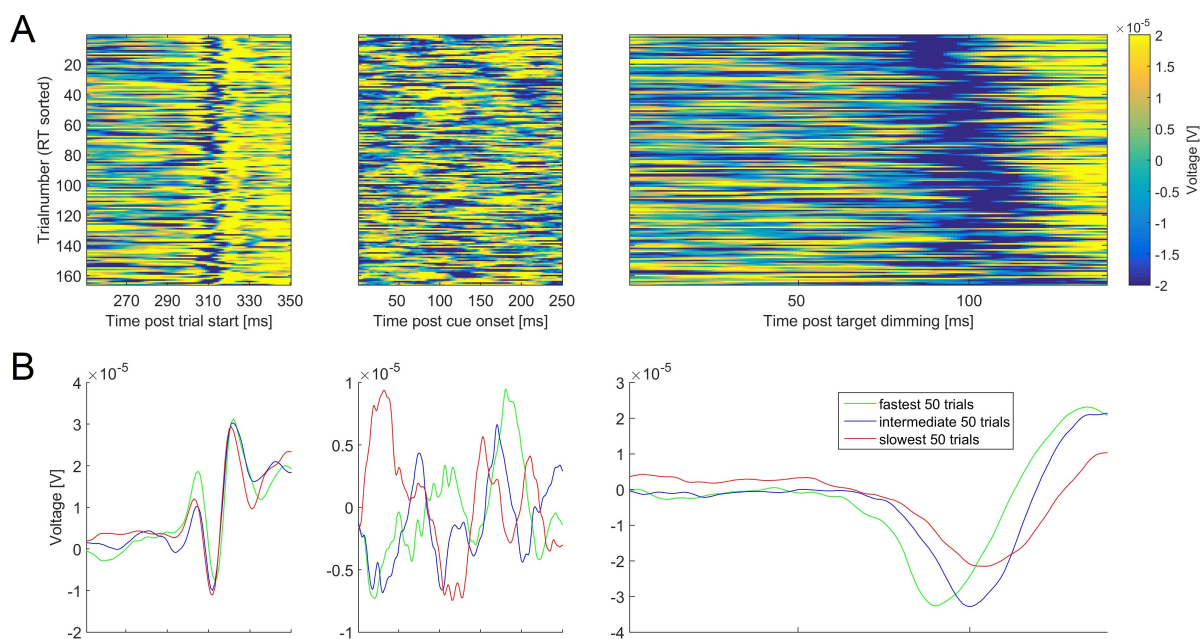


Fig. 24: Analysis of the correlation between evoked EFP responses and RTs. Data of the best-selective electrode of the target letter R is used in this figure. *A*: Single trials were sorted by normalized RT from fastest to slowest and plotted for the different onsets. *B*: From the sorted trials the first, intermediate and last 50 trials (non-overlapping) were averaged for three different stimulation onsets. The onset latency evoked by the target dimming is shifted to the right for slower RTs.

In order to quantify the observed latency shift, the 50% fractal area latency of the negative response from 51 to 140 ms post LCA dimming onset with a threshold of 0 z-score was calculated for all single trials of the selected electrode (for details, see Chapter 7.2.7.1). Single-trial RTs were divided into thirds to sort the latencies into three groups: fast, medium and slow RT trials. These groups of single-trial latencies were tested for statistical differences between them. Five out of ten of the selected electrodes showed significant differences between the grouped latencies (mean ω^2 : 0.024; $p < 0.05$). The post hoc test revealed a

significant difference between slow and fast RT for all of the five electrodes. All other pairwise comparisons were only significant for ≤ 1 electrodes.

The previous analysis was repeated, but this time, RT groups were defined by shuffling RT values and by dividing these into thirds to serve as control. Using shuffled RT groups did not result in significant differences between any groups.

The analysis of the attentional modulation of EFPs from V1 revealed that the attentional modulation was higher in long lasting trials in comparison to shorter trials. In order to investigate whether the trial duration has an influence onto the EFP response latency, the EFP latency analysis was repeated with trials sorted by the time between cue onset and target LCA dimming (groups: short, medium and long trials). This analysis revealed a significant latency difference between the medium and the short trials group for only two electrodes ($p < 0.025$) and between the fast and the short trials group for a single electrode ($p = 0.04$).

8.4 Discussion

In the present study, the allocation of covert attention caused a modulation of the EFP γ -power recorded from macaque V1. An increased BGP activity due to attention was found for electrodes with an RF maximum activity center that had a distance of 1° to 3° to the target in comparison to a distant distractor letter. The AI decreased with RF eccentricity from the target letter. The AI was usually < 0.01 , highest using only long trials (max AI: 0.018) and most negative using only fast RT trials (min AI: -0.021). Intracortical studies investigating the effect of spatial attention in V1 have found similar or higher AI in comparison to the present study, ranging from 0.02 to 0.23 [Buffalo et al. 2010; Chen et al. 2008; Hembrook-Short et al. 2017; Sharma et al. 2015]. In line with the previously found AI, the present enhancement of the γ -power could be caused by attention. Different factors, however, could have caused the low AI:

1. At the behavioral level, one could argue that the monkey has not shifted its attention properly. While the presence of (near) distractors increases the attentional modulation [Motter 1993; Rotermund et al. 2013], the multi-stimulus display could also have made the task very difficult for the monkey. While the AI was found to be higher in

difficult tasks [Chen et al. 2008], only a low AI was found in the present study. Despite the moderate hit rate, the RT median difference between the response in normal and catch trials was low. This could indicate two issues. Firstly, the task could have been too easy making a covert shift of attention unnecessary for the monkey. The moderate hit rate of the monkey, however, indicates that the task was demanding. Secondly, the low AI could have been caused by the monkey doing the task in a different than the desired way. The monkey could have found other strategies like broadening the attentional focus to cover large parts of the visual field. This behavior could be caused by the difficulty of the task. To encompass this issue, the number of objects needs to be reduced or the salience of the target change needs to be increased. In the event of a too easy task, however, the monkey does not need to shift its attentional focus. In addition, a lower task demand in visual tasks increases the extent of the attentional focus [Handy et al. 1996]. A careful adaption of the task is necessary for future experiments. Higher RT differences between the target and the distractor response are preferable to be achieved in further investigations to ensure that the monkey does the task as desired.

2. Attentional effects are usually small in V1 compared to higher visual areas like V2 and V4 when investigated with intracortical electrodes (e.g., [Buffalo et al. 2010; Luck et al. 1997; Mehta et al. 2000]). In addition, the signal amplitude of high-density ECoG was found to be higher in comparison to high-density EFPs [Bundy et al. 2014]. Therefore, the dura mater attenuates the signal recorded by high-density epidural electrodes which in turn leads to smaller signal differences between attend-in and attend-out, and thereby to a lower AI. To cope with the attenuation, other visual areas showing higher AI like V4 could be targeted. EFPs from V1 but predominantly V4 have been used for the decoding of the covert spatial attentional focus previously [Rotermund et al. 2013]. Keeping the task unchanged and recording from cortical areas that show a stronger attentional modulation in comparison to V1, could therefore enable a successful decoding of multiple spatial locations of the attentional focus from EFPs.
3. Some studies which found an attentional effect in V1 used visual stimulation which elicited γ -activity over a prolonged period of time (e.g., [Rotermund et al. 2009,

2013]). A sustained γ -activity was absent in the present study due to the task design. The task evoked predominantly transient γ -responses. Using an alternative visual stimulation that evokes a sustained neuronal activity could enhance the attentional effects in the EFP recorded from V1.

So far, the present attentional modulation is found in only one monkey. To verify the findings, this study needs to be repeated with additional monkeys.

A higher AI was found for trials in which the monkey scored faster RT and for trials with a longer time period between cue onset and target dimming. These findings are in line with a previous intracortical study in V1 showing a higher AI for longer delays of the target change [Sharma et al. 2015]. In addition, attentional modulation was shown to be higher in the visual area MT for trials in which the subject responded fast [Galashan et al. 2013].

The BGP activity was usually significantly modulated for electrodes belonging to the near and far RF eccentricity groups. The highest BGP activity in the attend-in condition was found for electrodes nearest to the target letter and BGP activity was decreasing with the distance from the target letter. Electrodes with an intermediate RF eccentricity did not show significant differences between the attend-in and -out condition. The AI was decreasing from positive values to negative values from near to far RF eccentricities analyzing all trials (Fig. 22). For all repetitions of the analysis, the negative AI of the most distant RF eccentricity (12°) increased to a less negative or even positive value. When ignoring the last finding, the attentional modulation of the γ -activity over eccentricities would support the gradient attention model [Mangun & Hillyard 1988; Shulman et al. 1986], which describes the modulation of spatial attention as a smooth decreasing function from the focus of attention to the surrounding area. The change in the sign of the AI comparing near and far RF eccentricities could be explained by the arrangement of the visual stimulation. The median distance between target and distractor was 9.8° , in a range of 5.6° to 12° (mean 8.7°). Therefore, some far located electrodes from a target letter are potentially near to the distractor letter. Due to the fact that the attend-out condition for a target letter was an allocation of spatial attention to the distractor letter, the EFP of electrodes far from the target letter could have been modulated by the attentional focus onto the distractor. Furthermore, the less negative or positive AI for 12° RF eccentricity indicates less attentional modulation in comparison to groups with a lower RF eccentricity. This finding could be explained by the

fact that only one out of 15 target had a distance of 12° to the distractor letter. For the other targets, which were more closely located to their distractor, the majority of electrodes which have an RF distance of 12° to the target letter are potentially not located near to the distractor. In addition, only two target letters possessed more than nine electrodes with an RF eccentricity of 12° (see Fig. 21). Therefore, the reduced number of electrodes covering the spatial location of the attentional focus onto the distractor letters as well as the distance between targets and distractors may have caused the weaker negative or positive attentional modulation for the 12° RF eccentricity group.

The current analysis did not focus on the evoked transient amplitude in the EFP between normal and catch trials. In an EEG study where humans have been forced to attend a stimulus, the VEP amplitude increased [Groves & Eason 1969]. In a subsequent analysis, the transient response amplitude could be compared between EFP responses to targets in normal trials and the EFP response in catch trials where the catch was ignored. Furthermore, the comparison of the transient response amplitude between the target response in normal trials and the catch response in catch trials, provided that the catch and the target are the same letter, could reveal differences in the EFP response amplitude due to covert spatial attention. In order to study the differences between EFPs evoked in normal and catch trials, a large amount of catch trials is necessary for each target letter, which was not provided in the present data set.

In the present study, a shorter latency of EFP onset responses evoked by the LCA dimming was found for trials with faster RT. The significant effect only occurred at five out of ten electrodes. Nevertheless, this result shows that EFP onset transients and behavior correlate. The relationship between onset transients and RT was previously investigated using EEG and intracortical electrodes. The latency of the stimulus-induced VEP recorded with scalp electrodes from the occipital cortex was found to be shorter with increasing RT [Donchin & Lindsley 1966]. In line with the previous finding, an EEG study found that different peaks of the ERP show shorter latencies when the RT was faster [Kammer et al. 1999]. They conclude that the latency modulation occurs at many stages of visual processing which is conclusive considering that different peaks of the EFP of EEG reflect different cortical stages of signal processing (for a review, see [Woodman 2010]). Comparing VEPs, RT and stimulus intensity, Vaughan and colleagues [1966] concluded that the velocity of RTs is defined by retinal and

cortical processes, whereas cortical processes are represented by the VEP. Therefore, it is not surprising that another study showed that RT and VEPs both reflect the retinocortical processing time [Chakor et al. 2005]. Besides these interactions between RT and VEPs latency found in EEG, a few intracortical studies have investigated the relationship between onset latencies and RT. Amplitudes of pop-out responses were found to correlate to the behavioral performance, potentially reflecting the salience of the stimulus [Lee et al. 2002]. In addition, the amplitude of visually evoked responses in area MT was shown to correlate with RT [Galashan et al. 2013; Parto Dezfouli et al. 2018]. Due to the fact that RT and EFP onset latencies correlate, the present results show that the relationship between evoked transients and RTs found at the level of EEG and single cells in the visual cortex can also be concluded from EFPs recorded from V1.

Altogether, these findings suggest that attention and behavior can be correlated to the signal modulation of the EFP recorded from V1. This fact supports the findings of the previous chapters that emphasize the high information content which is represented in epidural signals. Further investigations are necessary to investigate whether these modulations can be accurately and reliably decoded for single targets and single trials. A reliable encoding of the attentional focus from epidural signals recorded from V1 could pave the way for the development of meso-invasive gaze-independent BCIs.

9. Emphasizing the “positive” in positive reinforcement: using nonbinary rewarding for training monkeys on cognitive tasks

Declaration of the contribution of the candidate to a multi-author article which is included as a chapter in the submitted doctoral thesis.

Task	Contribution [%]
Experimental concept and design:	ca. 15
Data acquisition:	ca. 40
Data analysis and interpretation:	ca. 20
Preparation of figures and tables:	ca. 10
Drafting the manuscript:	ca. 10

Date:

Signature:

This study was previously published. Citation: Fischer B & Wegener D (2018), “Emphasizing the “positive” in positive reinforcement: using nonbinary rewarding for training monkeys on cognitive tasks.” *J Neurophysiol.* 120(1):115-128, doi: 10.1152/jn.00572.2017

Link: <https://journals.physiology.org/doi/full/10.1152/jn.00572.2017>

Authors

Benjamin Fischer and Detlef Wegener

Affiliation

Brain Research Institute, Center for Cognitive Sciences, University of Bremen, Bremen, Germany.

9.1 Abstract

Nonhuman primates constitute an indispensable model system for studying higher brain functions at the neurophysiological level. Studies involving these animals elucidated the neuronal mechanisms of various cognitive and executive functions, such as visual attention, working memory, and decision-making. Positive reinforcement training (PRT) constitutes the gold standard for training animals on the cognitive tasks employed in these studies. In the laboratory, PRT is usually based on application of a liquid reward as the reinforcer to strengthen the desired behavior and absence of the reward if the animal's response is wrong. By trial and error, the monkey may adapt its behavior and successfully reduce the number of error trials, and eventually learn even very sophisticated tasks. However, progress and success of the training strongly depend on reasonable error rates. If errors get too frequent, they may cause a drop in the animal's motivation to cooperate or its adaptation to high error rates and poor overall performance. We introduce in this report an alternative training regime to minimize errors and base the critical information for learning on graded rewarding. For every new task rule, the feedback to the animal is provided by different amounts of reward to distinguish the desired, optimal behavior from less optimal behavior. We applied this regime in different situations during training of visual attention tasks and analyzed behavioral performance and reaction times to evaluate its effectiveness. For both simple and complex behaviors, graded rewarding was found to constitute a powerful technique allowing for effective training without trade-off in accessible task difficulty or task performance.

9.2 New & Noteworthy

Laboratory training of monkeys usually builds on providing a fixed amount of reward for the desired behavior, and no reward otherwise. We present a nonbinary, graded reward schedule to emphasize the positive, desired behavior and to keep errors on a moderate level. Using data from typical training situations, we demonstrate that graded rewards help to effectively guide the animal by success rather than errors and provide a powerful new tool for positive reinforcement training.

9.3 Introduction

Nonhuman primates are capable to learn sophisticated behavioral tasks. During the last few decades and since, insights into the neuronal mechanisms of cognitive control and executive functions were gained by physiological experiments requiring animals to perform specific cognitive operations while neuronal activity was recorded in the cortical area of interest. The behavioral tasks used in these studies are often complex and highly demanding. They frequently require the animals to follow intricate selection and response rules [Herrington & Assad 2009; Schledde et al. 2017; Shichinohe et al. 2009; Watanabe & Sakagami 2007] and may include storage of numerous items in working memory [Barone & Joseph 1989; Inoue & Mikami 2006; Miller et al. 1996], sustained covert attention to peripheral stimuli [Hafed et al. 2011; Wegener et al. 2004], multiple-object tracking in space [Matsushima & Tanaka 2014; Mitchell et al. 2007b], identification of a target shape in a morphing object [Grothe et al. 2012; Taylor et al. 2005], basic arithmetic [Cantlon & Brannon 2007], and even video gambling with another monkey [Hosokawa & Watanabe 2012]. Training of such tasks (and, likewise, the training of much simpler forms of cognitive tasks) is usually acquired by a succession of many discrete steps, with each step requiring adaptation of the learned behavior to a slightly changed task rule (successive approximation).

Positive reinforcement training (PRT) constitutes the gold standard for animal training procedures. A substantial body of literature is available describing the benefits of PRT for scientific, veterinary, and husbandry purposes (for a tabulated overview, see [Prescott et al. 2005]), but only a few papers deal with the specifics of training procedures for cognitive tasks in the laboratory [Mitchell et al. 2007a; Remington et al. 2012; Scott et al. 2003; Watanabe & Funahashi 2015]. The usual procedure, however, consists of reward delivery in response to the desired behavior (e.g., a fast lever release following the onset of a target stimulus) and withholding of reward for the wrong behavior (e.g., a lever release that comes too soon or too late), typically accompanied by trial termination [Newsome & Stein-Aviles 1999]. We will call this form of feedback a “binary” reward schedule in the remainder of the article, because it consists of either delivering or not delivering the reinforcer to the animal.

The overall time needed to train an animal on a demanding cognitive task in the laboratory is influenced by many factors, among those 1) the overall willingness of the animal to

cooperate, 2) the effective number of trials the monkey can learn on, and 3) the information provided by the feedback. In some critical phase during training, the learning progress of an animal might slow down, often because of problems with one of these factors, or their interaction. First, regarding the willingness to cooperate, consider that monkeys have no insight into the structure and the requirement of a new task (or task rule) and depend on learning by trial and error. Necessarily, many trials will terminate with the undesired response and the monkey will not be rewarded. Because the animal may have spent some effort to perform the trial correctly, withholding a reward potentially counteracts the intrinsic motivation to perform the task, thus reducing the absolute number of training trials and potential progress. Second, despite this possibly negative influence of errors, they constitute the most important source of information during learning. Only if a trial does not end with the expected reward is there a need for the animal to adapt its behavior. Yet, high error rates bear the risk that the animal will end a training session early and/or get used to errors in the long term, whereas small error rates will reduce the amount of information the monkey can build on for adapting to a new task rule. Both cases potentially constitute a limitation for fast learning progress. Third, withholding the reward and termination of a trial in response to an error signals the animal that its response was wrong but does not provide information about the desired behavior. Due to multiple behaviors causing an error, the feedback gets ambiguous, slowing down learning of the new task rule and potentially also affecting the animal's behavior regarding previously learned rules.

We propose an alternative, nonbinary reward scheme that emphasizes successful behavior (nonbinary positive reinforcement training, NB-PRT). For training both simple and complex tasks, we demonstrate that NB-PRT provides a valuable additional tool for positive reinforcement training. NB-PRT builds on the principle that a new task rule is trained by associating the to-be-learned behavior (e.g., precisely gazing at the fixation spot) with a high amount of reward, whereas other behavior (e.g., small saccades during fixation) may receive lesser, graded reward. We argue that this reward regime potentially helps to refine training procedures by 1) providing a differentiated feedback in successful trials, 2) potentially increasing the efficient number of trials the monkey can learn on, 3) keeping the animal's willingness to cooperate by reducing the number of unrewarded trials, and 4) providing potentially more information for the trainer to find the best-suited training schedule. This article explains the details of this approach and provides four examples for its efficiency,

including situations where it may seem to be counterproductive at first view. The article is thought to serve the community with the experiences gathered with this approach but does not attempt to present a quantitative comparison of NB-PRT with the normal, binary PRT. This is mainly because careful planning of the training schedule mandatorily needs to consider a variety of factors before a specific protocol is decided, including but not limited to previous training experience, age, and rank of the animals. NBPRT is introduced as a new tool to be considered within the framework of PRT, but explicitly not as a replacement of previously established techniques that proved to be successful for a given condition or requirement.

9.4 Material and Methods

9.4.1 Subjects

All surgical and experimental procedures followed the Regulation for the Welfare of Experimental Animals issued by the Federal Government of Germany and were approved by the local authorities. Training procedures were carried out with 3 male macaque monkeys (*Macaca mulatta*) with body weight of ~11 (*M1*, *M2*) and 13 kg (*M3*), implanted with a headpost. Surgical procedures followed previously published protocols [Schledde et al. 2017; Wegener et al. 2004]. All animals had been used in other projects before. They were familiar with the laboratory conditions and with a dimming task at fixation (see below) but were naive to the specific stimulus and task conditions reported here. Out of training sessions, animals were kept in a species-appropriate, environmentally enriched husbandry. *M1* and *M2* were each pair-housed and had daily access to an outdoor compartment; *M3* lived in an indoor compartment with visual and auditory contact with other monkeys. The animals received free fruits and water on Friday afternoon and during the weekend as well as during nontraining periods. Health and well-being were checked by daily monitoring of behavior and body weight and regular checks by veterinarians.

9.4.2 Visual stimulation, reward schedule, and behavioral paradigms

Training sessions were performed in a lightly dimmed room. Animals sat in a primate chair 80 cm in front of a 22-in. cathode ray tube monitor (1152 × 864 pixels, 100-Hz refresh rate). Eye movements were measured at a spatial resolution of 0.2° visual angle, using a custom-made remote video-oculography system. Reward consisted of water or diluted red grape juice, applied by a simple, valve-controlled gravity liquid dispenser. A “high reward” consisted of ~25-30 ml/100 correct responses, a “medium reward” of ~15-20 ml/100 corrects, a “small reward” of ~10-15 ml/100 corrects, and a “very small reward” of ~5-10 ml/100 corrects. “Zero reward” refers to trials that were not rewarded but neither terminated. Details about the reward schedule in different training situations are given in Results. Training sessions were not terminated before the monkey showed no further interest in performing the task. During training days, monkeys usually did not receive additional liquid in their home compartment.

Visual stimulation was carried out with custom-made software, run on a Pentium computer. The computer software chose the amount of reward depending on the monkeys’ behavior (e.g., precision of fixation or reaction time) and saved all stimulation and behavioral data in a trial-description file. We applied NB-PRT during four different early and late periods of training attention tasks, as well as investigating its effectiveness regarding fixation accuracy and reaction time (RT) acceleration in simple fixation tasks. For better traceability, the general task requirements are explained in the corresponding Results.

Trial timing in the different experiments and conditions is summarized in Table 1. Common to all examples reported in this article, monkeys were required to initiate a trial by gazing at a fixation point (FP; 0.11°- 0.18° side length) at the center of the screen and pressing a lever. With the exception of *example 1*, they had to keep fixation within a maximally 1.5° radius throughout the trial. For the experiments described in *example 1*, the fixation window was divided into two zones of different radius. Trials during which the eyes did not leave the inner fixation zone received a higher reward than trials during which eyes entered the outer zone. Leaving the outer zone resulted in termination of the trial without reward. In all experiments, monkeys were required to respond to a change in a stimulus (described below for each example separately) by releasing the lever within a time window of 150-750 ms after this

event. If not stated differently, providing the response in the appropriate time window had been trained before and was considered a well-established behavior. As such, releasing the lever too soon (false alarm) or too late (miss) resulted in immediate trial termination without reward. Intertrial intervals in all examples had a length of maximally 1,000 ms, followed by an interval of maximally 3,000 ms for trial initiation. Not initiating the trial during this time resulted in a reset of the trial clock. In any case, monkeys performed as many trials as they wanted. When they showed no further interest in performing the task, they were carried back to their home compartment.

Experiments were performed using either a simple fixation task or two different tasks requiring covert attention to either a moving Gabor stimulus (speed change task) or a static object (object dimming task). Simple fixation tasks (*example 1, M2*; and *example 2, M2 and M3*) were carried out with no other objects on the screen. The FP was shown on a dark background at the center of the display. Dimming occurred at a pseudorandom time after FP onset (cf. Table 1 for details). For all experiments, dimming was clearly above threshold. The speed change task (*examples 1-3, M1*) required detection of an instantaneous speed increment of a Gabor element (2 cycles/° spatial frequency, enveloped by a Gaussian with 0.75° at half height, 10 cd/m² mean luminance) placed 8° away from the FP. The Gabor inherently drifted with 2.17°/s and increased speed by 100% (*examples 1 and 2*) or 80% (*example 3*) at a pseudorandom point in time 1,360-3,520 ms after trial initiation. If cued, Gabor onset was preceded by displaying a 3° × 3° rectangular frame at the upcoming target position for 500 ms. When the Gabor was shown together with another Gabor, both objects were displayed at opposite positions across the FP (Fig. 25E). In the object dimming task (*example 4, M3 and M1*), visual stimulation consisted of 26 isoluminant objects, each of which was unique in shape and color. Objects were arranged on three imaginary, circular rings around the FP, centered at 3, 5, and 7° eccentricity. Object size on the inner ring was ~0.9° width and ~0.9° height, and increased by a factor of ~1.2 and ~1.5 on the middle and outer ring, respectively, to account for larger receptive fields in the periphery. Objects had a luminance of 10 cd/m² and were presented on a dark background. Thirteen (*M3*) and 15 (*M1*) of all objects were possible targets, distributed over the inner and middle rings (*M3*) or over all rings (*M1*). The monkeys' task was to covertly attend to one of these targets and to indicate a dimming of this object (*M3*) or of a small spot (0.15°, 0.22°, or 0.23° side length on inner, middle, or outer ring, respectively) on the object (*M1*). The target in each upcoming trial was cued by a

9.4 Material and Methods

smaller (factor 0.75), slightly blurred version of the respective object, located at the center of the screen, behind the FP (see Fig. 29A). Object locations were kept constant during all training sessions. On 0-20% of the trials, the cued change was preceded by an uncued change in another, randomly chosen distractor object (catch trial). Unless stated differently, monkeys were allowed to respond to both the cued and uncued change within 150-750 ms after the change. Dimming of cued and uncued objects was separated by at least 750 ms. For the first five sessions of the training to introduce catch trials, however, the minimal temporal separation between changes at uncued and cued objects was allowed to be as short as 250 ms. In such cases, when the temporal separation between two changes was too short to allow a definite assignment of the response, we considered responses below 750 ms after the first change as a response to the first, uncued change and responses occurring later as a response to the second, cued change.

Tab 1: Trial timing and cue validity. Values for cue onset, stimulus onset, and first and second change event refer to time of trial start (lever press). SCD, speed change detection task; FPD, fixation point dimming task; OBD, object dimming task; NT, normal trials; CT, catch trials.

Monkey	Task	Session	Cue Validity, %	Cue Onset, ms	Stimulus Onset, ms	First Change, ms	Second Change, ms
				<i>Example 1</i>			
M1	SCD	1-5			200	860-3020	
		6-13	100	200	500	1,360-3,520	
M2	FPD	All				1,500-4,000	
				<i>Example 2</i>			
M1	SCD	All	100	200	500	1,360-3,520	
M2, M3	FPD	All				1,500-4,000	
				<i>Example 3</i>			
M1	SCD	All	90-75	200	500	1,360-3,520	
				<i>Example 4</i>			
M3	OBD	1-5	100	1,000	250	1,700-4,700	
		6-45, NT	90	1,000	250	1,700-4,700	
		6-45, CT	90	1,000	250	1,700-2,700	1,950-5,150
M1	OBD	All, NT	80	1,000	250	2,500-4,500	
		All, CT	80	1,000	250	2,500-3,500	4,000-5,300

9.4.3 Data analysis

Data were analyzed using MATLAB (The MathWorks, Natick, MA). Data analysis was based on the amount of correct and error responses (false alarms, misses, eye errors) and RT distributions. RT distributions were fit by an ex-Gaussian probability density function (<https://github.com/bramzandbelt/exgauss>), which is a convolution of a Gaussian and an exponential distribution. The ex-Gaussian fit provides the parameters μ and σ to describe the mean and the variability, respectively, of the normally distributed component of the distribution, and parameter τ to describe the exponential part, which accounts for the skew of the distribution [Heathcote et al. 1991; Tarantino et al. 2013].

For some analyses, training sessions with a low number of trials were disregarded to allow conclusive statistics. Such sessions occurred on Mondays only, as a result of ad libitum supply of water and fruits during the weekend. Exclusion of sessions is reported in the corresponding Results. Statistical testing was done using nonparametric tests throughout. P levels are reported for two-tailed testing. Significance is reported at the $\alpha = 5\%$ level. Statistical details are reported separately for each comparison. If only Z and P values are reported, they were obtained using the same statistical test and the same sample size as in the directly preceding comparison. The effect size R for Mann-Whitney's U -test to test whether two independent, unpaired samples come from the same distribution was calculated as

$$R = \frac{Z}{\sqrt{N_1 + N_2}}$$

where Z is drawn from the Mann-Whitney test statistics and N_1 and N_2 correspond to the number of elements in each of the samples. The estimated probability EP to randomly draw a value from one data group that is larger (smaller) than a randomly drawn value from a second data group was calculated as

$$EP = \frac{U}{N_1 \times N_2}$$

where U is the smaller (larger) of the two U values derived from the Mann-Whitney test statistics.

9.5 Results

In the following, we provide four examples for nonbinary rewarding during training of different tasks and/or task rules. Inspired by studies of reward-based decision-making [Amiez et al. 2006; Feng et al. 2009], our approach builds on the assumption that monkeys will effectively adapt their behavior to maximize the reward amount delivered in a single trial, and across a series of trials. This will be investigated in more detail in *example 2* (see below). In *example 1*, we will consider a relatively simple requirement for precise fixation, first during training of a covert attention task and second for an animal with very low error tolerance. We will show that NB-PRT allows to effectively train the desired behavior independent of error rates. In *examples 3* and *4*, we will deal with teaching abstract cues to allocate selective attention during progressively more complex task conditions. We will show how NB-PRT can be used to increase the number of trials the monkey can learn on, to more directly guide the animal toward the desired behavior. For each example, we give a brief overview about stimulus and task requirements. Details about stimulus timing are summarized in Table 1.

9.5.1 Example 1: Preventing high error rates

Consider a monkey having learned to properly gaze at a central fixation point (FP) and press a lever to initiate a trial, keep its gaze at the FP, and release the lever in response to the dimming of the FP after a pseudorandom interval of up to several seconds. Now assume this monkey shall be trained to attend a peripheral target while keeping proper fixation and to detect a sudden feature change of this target. Compared with what was learned previously, this task has two new components that are likely to cause errors: first, keeping fixation while covertly attending to a distant location, and second, detecting a feature change of a distant stimulus instead of the FP dimming. Based on binary feedback (distinguishing only between correct and incorrect responses), both types of errors get the same feedback (usually termination of the trial without reward) but do not provide information to the monkey as to which behavior caused the error. To prevent unfavorably high error rates, the training must be split into many small steps, e.g., by slowly approaching the final target position over the course of several training sessions.

NB-PRT provides additional options by allowing association of different behaviors with different amounts of reward. For the example outlined above, the desired behavior (keeping fixation and detecting a peripheral feature change) would get the highest reward, a suboptimal behavior (detecting the feature change but making small eye movements due to the new, to-be-trained behavior of covertly attending a distant stimulus) would get a clearly smaller reward, and undesired behavior (noncompliance to previously learned task rules, e.g., a large saccade toward the stimulus, and responding too soon or too late) would cause immediate trial termination without reward. On the basis of reports from human subjects performing the same task [Wegener et al. 2008], we considered the monkey to be aware of large saccades, whereas small fixation errors during initial training of a covert attention task may occur without the monkey being aware of these. Thus acceptance of such small saccades helps to keep the error rate on a moderate level and allows the monkey to learn the new requirement of feature change detection, while better rewarding of trials with precise fixation indexes the most beneficial (desired) behavior.

We tested this approach by training one monkey (*MI*) on the new task rule (detect a speed change of an inherently moving Gabor grating at 3° eccentricity) during one session and then placed the Gabor directly at its desired, final eccentricity of 8° in the first session following this training (Fig. 25A). The fixation window was divided into two zones: an inner fixation window with a radius of 1° (as already used in previous training) and an outer fixation window with a radius of 2° . For successful trials with precise fixation, the monkey obtained a medium reward, and for successful trials with unprecise fixation, it obtained a small reward (see Material and Methods for nomenclature of rewards and associated amounts). Saccades leaving the outer fixation window were treated as errors and resulted in trial termination. Thus, like binary rewarding, the three-level reward scheme provided clear feedback when previously learned rules were disregarded, but additionally allowed the monkey to distinguish the desired behavior from suboptimal behavior by graded reward.

The following training was performed within a total of 17 sessions. Four Monday sessions were disregarded for analysis, due to a small number of trials (< 50 hits). In the first and second training session with the nonbinary schedule, *MI* released the lever too soon (false alarm) or too late (miss) in less than 1% of all trials. In 53% and 58% of the trials, respectively, the monkey kept its eyes within the inner fixation window, and in 25% and

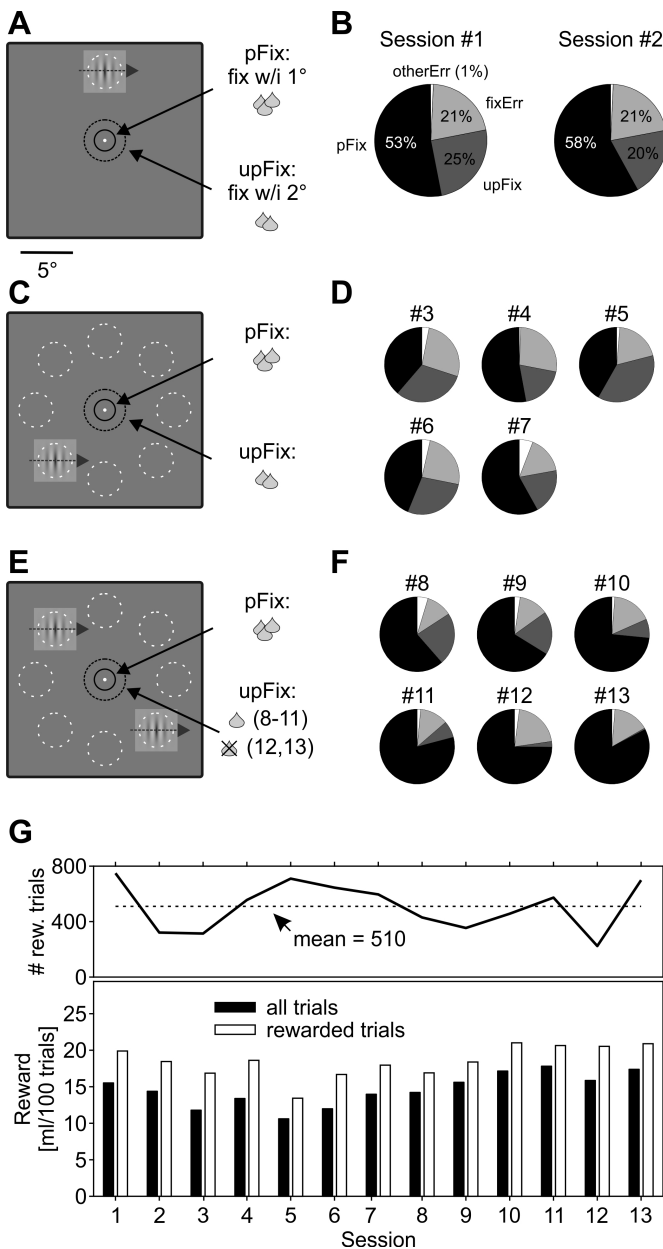


Fig. 25: Nonbinary reward scheme during training of a covert attention task. *A*: stimulus display, fixation windows, and reward associations (pFix, precise fixation; upFix, unprecise fixation) during training *sessions 1* and *2* after the animal had learned to release the lever in response to the speed change of a Gabor stimulus with inherent motion. w/i, within. *B*: mean behavioral performance [fixErr, fixation errors; otherErr, errors not related to fixation (false alarms and misses)]. *C* and *E*: visual display and possible target positions during *sessions 3-7* (*C*) and *sessions 8-13* (*E*). *D* and *F*: behavioral performance during *sessions 3-7* (*D*) and *sessions 8-13* (*F*). Pie shading corresponds to *B*. *G*: number of correct responses during all training sessions (*top*) and reward obtained per 100 hits in relation to all trials performed and to all rewarded trials (*bottom*). Dashed horizontal line indicates mean. Solid black circles in display diagrams indicate pFix zone (2° diameter), dashed black circles indicate upFix zone (4° diameter), and dashed gray circles indicate possible target positions. Circles are shown for illustration purposes only; they were not displayed. Drop symbols: 3 drops, medium reward; 2 drops, small reward; 1 drop, very small reward (see Materials and Methods for nomenclature of rewards and associated amounts).

20%, within the outer fixation window. About 21% of all trials were terminated due to a fixation error (Fig. 25B). Thus the overall success rate was kept close to 80%, though only trials with precise fixation received the full reward.

Starting with *session 3*, we placed the target at 8 different positions, each at a distance of 8° from the FP (Fig. 25C). In *session 6*, we also introduced a cue to indicate the upcoming target location at trial beginning (low contrast first and then gradually increased to final contrast). During *sessions 3-7*, the monkey made a moderate number of fixation errors (16%-27%) and a small number of errors not related to fixation (0.01%-6%). The ratio of successful trials

varied between 70% and 79%, and 39%-58% of all trials were performed with precise fixation (Fig. 25D). During *sessions 8-13*, we additionally presented a second stimulus opposite to the target (low contrast first and gradually increased during *session 8*) and reduced the amount of reward for unprecise fixation to “very small” in *sessions 8-11* (Fig. 25E). Because the number of trials with unprecise fixation decreased continuously during these sessions, such trials were not rewarded anymore in *sessions 12 and 13*, but neither were they terminated (“zero reward” condition). At this stage, we considered the new task rules as fairly well established, and withholding of reward for trials with unprecise fixation was used to finally shape the desired behavior. In line with this, during *sessions 12 and 13*, the number of hits with precise fixation reached 75% and 83% of all trials, and the number of eye errors did not exceed 21% and 15%, respectively (Fig. 25F). Taking these findings together shows the monkey learned to covertly attend to one of several peripheral locations with good fixation performance and to reliably indicate a speed change of a peripheral target stimulus in the presence of a distracting second stimulus within 13 training sessions. The nonbinary reward regime allowed us to constrain errors to previously established rules (e.g., suppression of large saccades) and to prevent an unfavorably strong increase in the overall number of errors. Providing more reward for trials with precise fixation than for trials with small fixation errors allowed us to shape the desired behavior without daily changes of the task rule (e.g., by stepwise decreases of the fixation window size), based on the hypothesis that the monkey would aim to maximize reward per trial. In line with this, analysis of the average amount of reward per trial showed an almost continuous increase starting with *session 5* (i.e., after the 8 peripheral target positions had been introduced), whereas the absolute number of successful trials was fluctuating (mean: 510; range: 224-749) but uncorrelated to the average amount of reward the monkey managed to obtain (correlation coefficient for reward relative to number of all trials: $R = -0.07$, $P = 0.811$; for reward relative to number of rewarded trials: $R = -0.14$, $P = 0.654$, $n = 13$; Fig. 25G).

NB-PRT may be particularly useful as an alternative to standard binary reward schedules for animals with low error tolerance. Figure 26 provides an example for another fixation training, carried out with a different monkey (*M2*). This monkey was previously trained on a fixation task for a technical research study [Galashan et al. 2011] but was then used for another project not considering eye movements, because of a strong tendency to make a lot of saccades out of the fixation window and to quickly stop cooperating when errors got too

9.5 Results

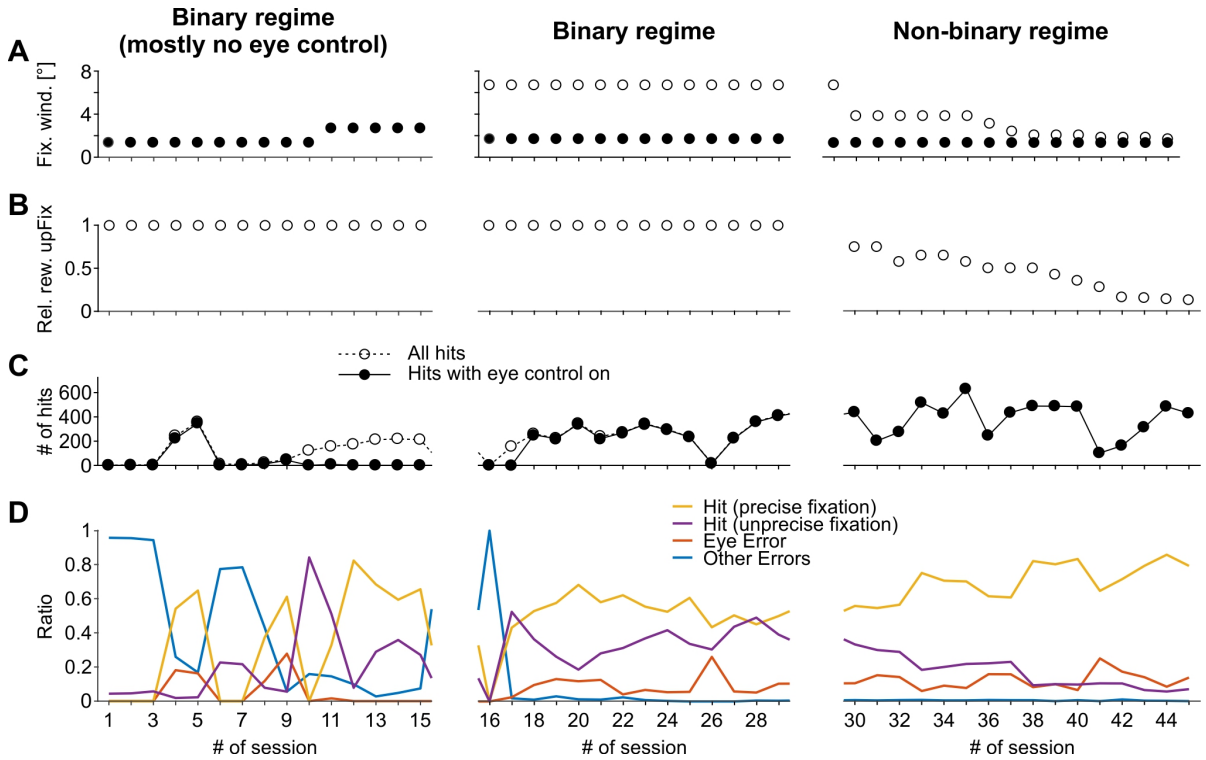


Fig. 26: Nonbinary positive reinforcement training for an animal with low error tolerance. *A*: diameter of inner (solid circles) and outer (open circles) fixation window during sessions 1-45. In sessions 1-15 (left), the eyes had to stay within a fixation window of maximally 2.7° radius, but eye control was switched off in most trials due to poor performance. Reward regime was binary. In sessions 16-29 (middle), eyes had to stay within a 6.7° radius from the fixation point (radius of outer fixation window), and the reward regime was kept binary. In sessions 30-45 (right), nonbinary rewarding was applied and the size of the outer fixation window was slowly decreased to 1.7° radius. Fix. wind., fixation window. *B*: relative reward for correct responses in trials with unprecise fixation (Rel. rew. upFix). The reward is represented as the fraction of reward given in a trial with precise fixation, with a value of 1 indicating the same reward and values below 1 indicating smaller reward in trials with unprecise fixation. During sessions 1-15 (with no outer fixation window but inactive eye control), the relative reward of 1 indicates that the monkey received the same amount of liquid for all correctly indicated target events (fixation point dimming), independent of eye movements. *C*: number of correct trials (hits) with no regard to eye control (dashed line, open circles) and number of correct trials with eye control (solid line, solid circles). *D*: ratio of hits with precise and unprecise fixation, eye errors, and other errors (false alarms, misses).

frequent. *M2* went back to fixation training 6 yr after initial training and after a general break from training of 10 mo. The task was to fixate a fixation spot at the center of the screen for up to 4 s and to indicate a (clearly visible) dimming of this point. No other objects were presented. The first 15 sessions were carried out with a binary reward regime, with eye control switched off most of the time. In sessions 4 and 5, the monkey reached 222 and 347 correct responses (out of a total of 372 and 505 performed trials), respectively, demonstrating that he was basically able to do the task (Fig. 26C, left). Yet, in all other sessions, *M2* made a lot of eye errors, false alarms, and misses (Fig. 26D, left) and stopped working on the task quickly after eye control was switched on, even when allowing the eyes to stay within a

fixation window of 2.7° radius (Fig. 26A, *left*). Starting with *session 16*, we introduced an outer fixation window of 6.7° radius, to reestablish proper performance by reducing the overall number of errors. The monkey received the same amount of reward as for staying within the inner fixation window such that the effective reward scheme was still binary (Fig. 26B, *middle*). With these very moderate requirements, the monkey performed more reliably and significantly increased its number of hits per session (Fig. 26, C and D, *middle*). In $\sim 60\%$ of the trials, he managed to stay within the inner fixation window. However, with the uniform task requirements during *sessions 16-29*, M2 did not improve fixation accuracy and still made a lot of saccades, although no distracting objects were presented. Because of its very low error tolerance, we used NB-PRT to avoid an increase in eye errors following more rigid requirements for fixation accuracy and started to differentiate the amount of reward the monkey was given for successful trials with either precise or unprecise fixation (Fig. 26, A and B, *right*). This reward-based guidance toward precise fixation improved fixation accuracy quickly and allowed us to slowly decrease the outer fixation window, yet without affecting the monkey's error rate (Fig. 26D, *right*). At the end of the training block, the monkey performed more than 80% of all trials with precise fixation.

9.5.2 Example 2: Improving feedback and increasing alertness

Training progress critically depends on the effective number of trials on which the monkey can learn. In a binary reward scheme, a rewarded trial teaches the monkey that its behavior was appropriate, whereas unrewarded trials teach it to adapt behavior. Yet, a sole distinction between “correct” and “incorrect” does not easily provide information about the direction the monkey should go to increase its ratio of rewarded trials. NB-PRT can be used to provide additional information in successful trials (i.e., independent from the number of error trials) and thus helps to increase the effective learning rate. This is shown in the next example, continuing the training of M1 described in *example 1* (cf. Fig. 25E). As mentioned earlier, we switched back to binary rewarding when the monkey was good at performing the task in the desired manner during *sessions 12 and 13*, to reset the reward regime before the next training step. During these sessions, the monkey obtained a fixed, medium reward for detecting the target's speed change within 150-750 ms without leaving the inner fixation window. The monkey reached a performance of 81% correct responses and a median RT of 380 ms (Fig. 27A). The next step was to force the monkey to focus its attention on the target object by

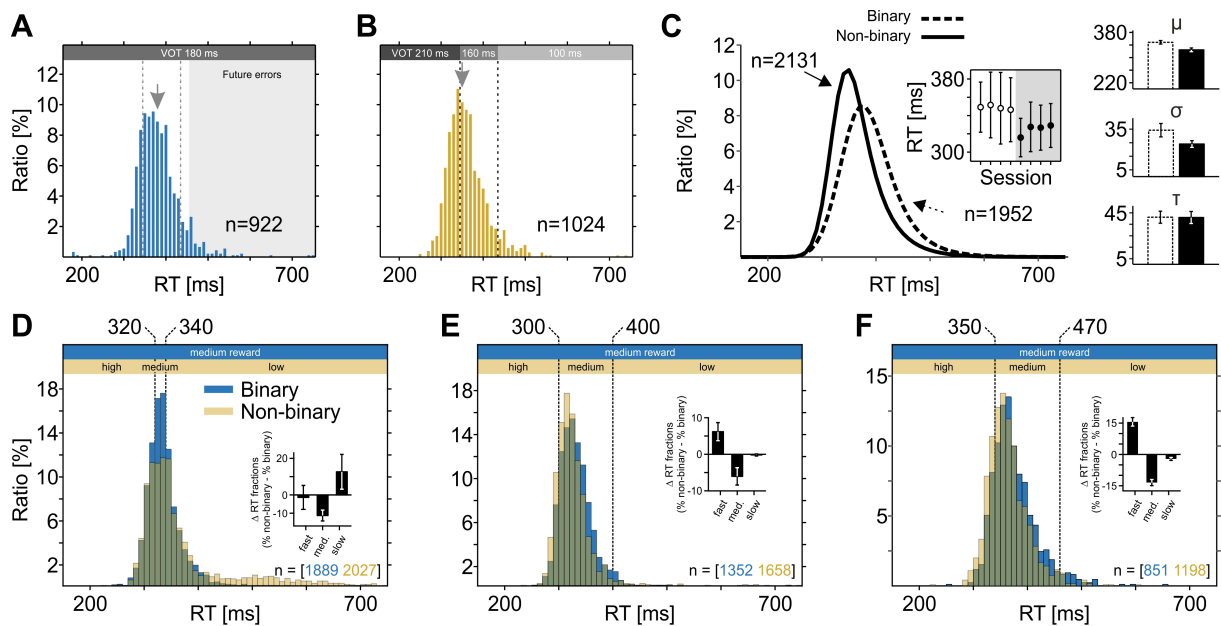


Fig. 27: Reaction time (RT)-dependent rewarding. *A*: empirical RT distribution for speed-change detection with binary reward, averaged over 2 days before introduction of RT-dependent rewarding. Shaded horizontal bar indicates future errors if the response window is limited to 450 ms. Dashed gray lines indicate response time windows as chosen in *B*. VOT, valve opening time (reward amount); gray arrow, median RT. *B*: empirical RT distribution averaged over 2 days following a 1-session introduction of RT-dependent rewarding. Shaded horizontal bars indicate VOT for fast, medium, and slow RTs. *C*: ex-Gaussian fits of RT distributions from 4 sessions before introduction of RT-dependent rewarding and 4 sessions afterward. *Inset* shows μ (mean) and σ (variability) values of single sessions. Bar plots at *right* show the mean μ and σ values of the Gaussian component and the mean τ (skew) of the exponential component before (open bars) and after (solid bars) introduction of RT-dependent rewarding. *D-F*: RT distributions during binary and nonbinary reward regimes. In *D*, the nonbinary schedule was chosen to label around one-third of all trials as fast, medium, and slow and associate them with high, medium, and low reward, respectively. The schedule was calculated to provide the same amount of reward per 100 trials as during the binary schedule if the monkey kept its RT distribution the same. In *E* and *F*, edges to define RT fractions were chosen to better separate fast from slow trials, to allow the monkeys to associate different behavior with different reward amount. *Insets* show the difference in the percentage of trials in each of the 3 RT fractions for the nonbinary compared with the binary schedule. Data in *A-C* were derived from *M1*, data in *D* and *E* from *M3*, and data in *F* from *M2*. All errors bars are SD.

requiring him to respond as fast as possible. With a binary reward scheme, this would be achieved by reducing the length of the response time window. Consequently, a fraction of previously successful responses will become future errors. In the example shown in Fig. 27*A*, reducing the maximal response time from 750 to 450 ms would label ~9% of the trials as misses. Hence, the monkey must perform many trials to arrive at one “teacher trial,” i.e., a trial with a previously rewarded but now unrewarded behavior that provides essential information for the animal to adapt its responses. Increasing the number of teacher trials for faster learning (by requiring responses within even shorter time) is obligatorily linked to a

higher number of errors. For animals with low error tolerance, this strategy may counteract the monkey's willingness to perform the task if errors exceed a critical number.

As already shown in *example 1*, NB-PRT allows emphasis on the positive, to-be-facilitated behavior, the fast response. Rather than relying on the failure to respond in time, providing a large reward for every fast response results in a considerably higher number of teacher trials. For example, 25% of all trials shown in Fig. 27A had an RT of < 350 ms. To speed up response times, we associated such trials with a high reward, whereas trials with an RT of > 440 ms received a small reward. Trials with an RT in between received a medium reward, yet slightly less than in previous training sessions, to make the reward difference between fast and medium RTs clearly distinguishable. This new regime was highly effective and caused a decrease in the median RT from 380 to 350 ms within a single training session. Figure 27B shows the RT distribution of the following 2 sessions, revealing a total of 45% successful responses being faster than 350 ms. Because we did not shorten the absolute length of the response period, the rate of misses stayed at 0% during all sessions, including the one during which RT-dependent reward was introduced. For statistical analysis, we compared the RT distributions from before and after the new reward regime by using a Mann-Whitney U -test. We found a significant shift toward faster RT within the RT-dependent reward regime ($Z = 11.028$; $P < 10^{-27}$, $n = [922, 1024]$), with an effect size of $R = 0.25$. Based on U values, the Mann-Whitney statistics indicate an estimated probability of 64.4% for getting a faster response when applying RT-dependent rewarding.

Additionally, we fitted ex-Gaussian probability density functions [Heathcote et al. 1991] to the RT distributions of four sessions each before and after the RT-dependent reward was introduced. Ex-Gaussians constitute a convolution of a Gaussian and an exponential distribution to separately fit the Gaussian part (with parameters μ and σ) and the exponential part (with parameter τ) of the skewed RT distribution, and allowed us to investigate which parameters of the distributions were affected by the change in reward regime. Pooled over all RTs, these fits illustrate a clear, leftward shift of the RT distribution after introduction of the RT-dependent reward (Fig. 27C). The mean of the Gaussian component [fitting the *left* (fast) part of the skewed RT distribution] decreased from 348 to 324 ms (Wilcoxon rank sum test, $Z = 2.16$, $P = 0.03$, $n = 4$), whereas the mean of the exponential component [fitting the *right* (slow) part of the skewed distribution] was unchanged (τ_{binary} : 41 ms; $\tau_{\text{nonbinary}}$: 41 ms; $Z = 0$, P

= 1). Thus emphasizing the desired, fast response by RT-dependent rewarding as an alternative to training down the undesired, slow response by reward rejection caused an essentially instantaneous and lasting acceleration of response times. To be effective, NB-PRT depends on a well-justified reward regime. It should allow the animal to associate different amounts of reward with clearly different behaviors. To illustrate this more directly, we performed a simple fixation task with monkey *M3* under two different nonbinary regimes. *M3* had a long expertise with the task as well as with NB-PRT. Each condition consisted of five sessions (Monday to Friday), where *sessions 1* and *2* were used to make the monkey familiar with the current schedule, and *sessions 3-5* were used for data analysis. Both conditions were preceded by a block of sessions with a binary schedule, following the same outline, to provide reference RT distributions.

We first tested a NB-PRT regime in which about one-third of trials each were associated with high, medium, and low reward. To this end, we first gathered the reference RT distribution using a binary schedule. The monkey was given a medium reward for every correct response, whereas error trials resulted in immediate trial termination. With the binary regime, *M3* yielded 98% correct responses (including eye errors) and responded faster than 400 ms in 96% of the trials (Fig. 27D). For the following NB-PRT block, we divided the RT distribution into three fractions of ~33% of trials with fast, medium, and slow RT, and calculated the reward schedule as to provide the same amount of reward per 100 trials as during binary rewarding. Yet, because of the skewed RT distribution, the fraction of trials with medium RT consisted of only 2 bins, separating fast from slow responses by just 20 ms. This makes it hard (if not impossible) to associate behavior and reward, and leaves many trials with a reasonably quick response with low reward. As a consequence, with this schedule *M3* performed significantly worse. The ratio of fast trials did not change, but many more trials were performed with slow RT (Fig. 27D). Thus, instead of keeping its previous RT distribution (and thus keeping the same amount of reward per 100 trials) or compensating for the low-reward trials by increasing the ratio of fast trials (and thus increasing the absolute reward amount), the monkey responded very slow in many trials and obtained fewer reward per 100 trials than under the binary schedule.

We then tested the effect of NB-PRT when RT fractions were chosen more purposefully. We first switched back to binary rewarding and reestablished the previous RT distribution (Fig.

27E). We then applied an NB-PRT regime that only provided a low reward for RTs longer than 400 ms. Trials with RTs faster than 300 ms received a high reward, and all other RTs were rewarded as during the preceding block of binary rewarding. This regime is much more likely to allow the monkey to distinguish the association between different behaviors and different reward amounts. Note, however, that only 15.1% of trials were treated differently than during the preceding session with binary rewarding, whereas all other trials received exactly the same reward as before. Nevertheless, this NB-PRT regime had a strong effect on the monkey's performance and caused a clear leftward shift of the entire RT distribution (Fig. 27E). Based on Mann-Whitney statistics ($Z = 7.32$; $P < 10^{-12}$, $n = [1,352, 1,658]$, $R = 0.13$), the estimated probability EP for getting a faster response in the NB-PRT regime was 0.58. We applied a similar regime to $M2$ (Fig. 26F) after it had finished fixation training and obtained essentially the same result ($Z = 6.77$; $P < 10^{-10}$, $n = [851, 1,198]$, $R = 0.15$, $EP = 0.59$). Thus, even with a simple fixation paradigm, graded rewarding exerted clear effects on RT distributions, indicating that the trial-wise reward outcome has a direct impact on an animal's performance. If properly chosen, graded rewarding can support the willingness of the animal to spent effort and provides a useful tool to guide the animal toward the desired behavior.

9.5.3 Example 3: Teaching abstract cues.

Because of its influence on performance and its capability for guiding the animal more directly, nonbinary, graded rewarding also may be used to support training of more sophisticated tasks. Many behavioral paradigms to investigate higher cognitive functions rely on abstract cues to indicate the required behavior. For example, spatial, colored, or symbolic cues may be used to indicate the identity of an object to be kept in memory [Chelazzi et al. 1998; Inoue & Mikami 2006], the type of a desired motor action [Everling & Munoz 2000; Snyder et al. 2000], or the task rule [Asaad et al. 2000; Schledde et al. 2017]. For the example given above for $M1$, a spatial cue was used to direct the monkey's attention to the location of one of the two simultaneously presented stimuli (Fig. 28A). Under experimental conditions, the cue may directs attention either to the stimulus over the receptive field of the recorded neuron or away from it, thus allowing analysis of neuronal activity under identical physical stimulation but different loci of covert attention. Yet, to test whether the monkey follows the cue instructions and in fact selectively attends the cued item, it is necessary to

9.5 Results

introduce target events (change in color, motion direction, orientation, or the like) at uncued items, which have to be ignored by the animal. With binary rewarding, responses to such uncued events are considered errors, resulting in the termination of the trial [Galashan et al. 2013; Reynolds et al. 1999; Treue & Maunsell 1996; Wegener et al. 2004].

Teaching the animal the meaning of such abstract cues frequently is a matter of patience. From the perspective of the trainer, the task rule might be straightforward because reward is only provided for responses to the cued item, yet, from the perspective of the animal, the situation is less clear. Even with selective attention directed to the cued item, a target event occurring at the uncued item usually is not out of sight but may be well perceived [Braun & Sagi 1990; Wegener et al. 2008]. Responding to this event is exactly what has been trained before; for the example in Fig. 28A, the monkey would be perfectly in line with the previously learned task rules if it indicated a speed change of any of the two stimuli, independently of the cue. With a binary reward, there is no clear alternative to guide the animal toward the desired behavior other than adjusting the number of errors by some means,

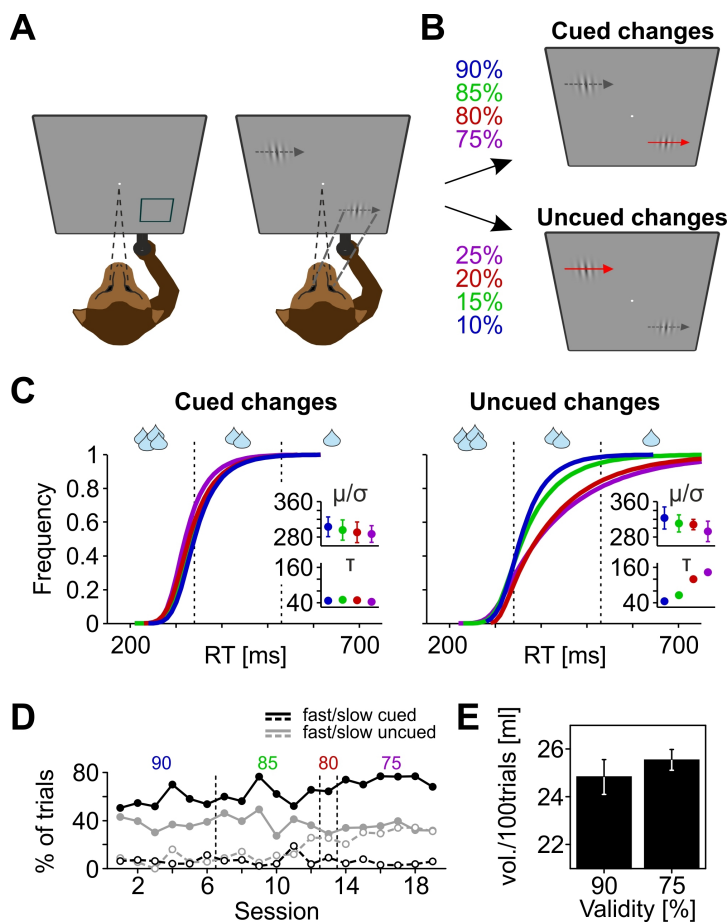


Fig. 28: Training of abstract cues. *A*: visual display. The monkey was required to gaze at the fixation point (FP) in the center of the display. A rectangular frame indicated the mutual position of the object to undergo the to-be-detected speed-change event (*left*). Gabor stimuli appeared subsequently at 2 FP-mirrored locations (*right*). The desired behavior was to use the cue information for allocating spatial attention (bold dashed lines). *B*: in valid trials, the speed change occurred at the cued object, whereas it occurred at the uncued object in invalid trials. Validity (indicated as color-coded percentages) was changed over the course of training sessions. *C*: empirical reaction-time (RT) distributions for cued and uncued changes. *Insets* depict the mean parameters (μ , mean; σ , variability) of ex-Gaussian fits to each of the RT distributions, depending on cue validity. Color code is same as in *B*. *D*: relative amount of reward obtained in response to cued and uncued changes, depending on cue validity. Trials with medium reward are disregarded for simplicity. *E*: average reward amount (vol./100 trials) per 100 trials during early (90% validity) and late (75% validity) training sessions. Error bars are SD.

assuming that at some point the animal makes the association between cue appearance at one of the stimulus locations and reward delivery following a correct response to that stimulus. NB-PRT, in contrast, provides additional options for shaping the monkey's behavior, relying on the monkey's natural expertise: getting the highest reward. In this and the following example, we show how NB-PRT can be used to teach abstract cues within a few sessions.

The first example continues the training situation of monkey *MI*, described above (Figs. 25 and 27, *A-C*). The spatial cue indicating the position of the upcoming target had been introduced when the second stimulus was added to the display, as mentioned previously. Yet, the cue had no obvious meaning with respect to uncued events, because such events were not present in earlier sessions. To use nonbinary rewarding for teaching the meaning of the cue, we chose a Posner paradigmlike design [Petersen et al. 1987; Posner 1980] and presented speed changes at the uncued location in a fraction of trials. We rewarded responses to such uncued events in the same way as responses to cued events, with high, medium, and small reward for fast, medium, and slow RTs, respectively. The rationale of this scheme was to test whether the monkey would distribute attention over the whole display (likely resulting in RTs of medium length and a relatively safe amount of medium reward) or, alternatively, use the information provided by the cue and direct attention to one stimulus selectively (increasing the chance of a high reward for fast RTs, at the risk of getting a small reward for slow RTs if changes occur outside the attentional focus). If the monkey mainly relies on maximizing reward in the short term (i.e., in single trials) and/or the reward regime is chosen to provide a higher mean reward per trial in the long term (i.e., over the entire session), choosing the second of the two options is beneficial.

We started with a cue validity of 90% and then reduced it to 85%, 80%, and 75% (Fig. 28*B*). Stepwise decreasing cue validity was chosen to slowly accustom the animal to uncued changes. Each validity was kept for six sessions, with the exception of the 80% condition, which was applied in only one session. To foster selective attention, the speed-change magnitude was reduced from 100% to 80% for all sessions. For different cue validities, RTs were analyzed by fitting ex-Gaussians to their distributions (Fig. 28*C*). With reduced validity, RTs to cued changes became increasingly faster [$\mu(\sigma)_{[90\ 85\ 80\ 75]}$: 303 (22), 295 (23), 291 (23), 287 (19) ms; Wilcoxon rank sum test_(val90, val75), $Z = 2.8$, $P = 0.0051$, $n = 6$], whereas RTs to uncued changes became increasingly slower due to an increase in the exponential component

of the distribution ($\tau_{[90\ 85\ 80\ 75]}$: 45, 66, 120, 143 ms; $Z = 2.8$, $P = 0.0051$). Based on Mann-Whitney statistics, the estimated probability EP of getting a faster response for cued changes was 59.6% in the 90% validity condition and increased to 77% in the 75% validity condition. This shows that the training by RT-dependent rewarding was highly effective, even though responses to uncued changes were not treated as errors. At the end of the training, the median RT difference between cued and uncued changes was as large as 50 ms. This is about the same magnitude as observed in human psychophysical experiments using the same stimuli and paradigm, after verbal instructions [Wegener et al. 2008].

If reward amount is not considered, this significant, cue validity-associated RT effect may seem surprising at first glance, because a higher number of uncued changes is expected to promote distributed rather than spatially selective attention. However, a closer look at the reward schedule helps to explain the behavior of the monkey: the nonbinary rewarding allowed it to select a 50% reward benefit for fast RTs and a 33% loss for slow RTs, compared with medium RTs. With decreasing cue validity, considering the cue information and allocating attention to the cued object not only helps the monkey to get a high reward more often in a single trial but, at the same time, compensates a probable loss in average reward amount in the long run. In fact, for cued changes, the monkey significantly increased its ratio of high-reward trials from 0.57 in the 90% validity condition to 0.74 in the 75% validity condition (Wilcoxon rank sum test, $Z = 2.48$, $P = 0.013$, $n = 6$; Fig. 28D). This was at the expense of reward for uncued changes, which showed an increase in the ratio of low-reward trials from 0.07 to 0.3 ($Z = 2.81$, $P = 0.005$). Thus, despite reduced cue validity and higher uncertainty of target location, focusing on the cued targets allowed the monkey to not only keep the same amount of reward obtained per trial but even to achieve a slight (although insignificant) increase in the average amount of reward per trial ($Z = 1.52$, $P = 0.128$; Fig. 28E).

9.5.4 Example 4: Fine-shaping of behavior

Providing meaningful feedback and keeping error rates on a moderate level gets more and more important with increasing task and stimulus demands. We finally tested NB-PRT in a change detection task requiring monkey *M3* to select 1 of 26 objects displayed in parallel (Fig. 29A; for simplicity, only 8 arbitrary objects are shown). The monkey was required to

9.5 Results

indicate a contrast change of the cued object, occurring at a random point in time between 1,450 and 4,450 ms after stimulus onset. It was trained using a nonbinary reward scheme emphasizing fast RTs, similar to the approach described in the previous example. The monkey had just learned to deal with the high number of objects during the preceding training step, and the contrast change was kept easy to recognize. The next training step was to include changes at uncued objects; however, unlike the approach described in *example 3*, any uncued change would be followed by a change of the cued object later in the trial. As before, our question was whether rewarding of responses at uncued objects helps (or rather

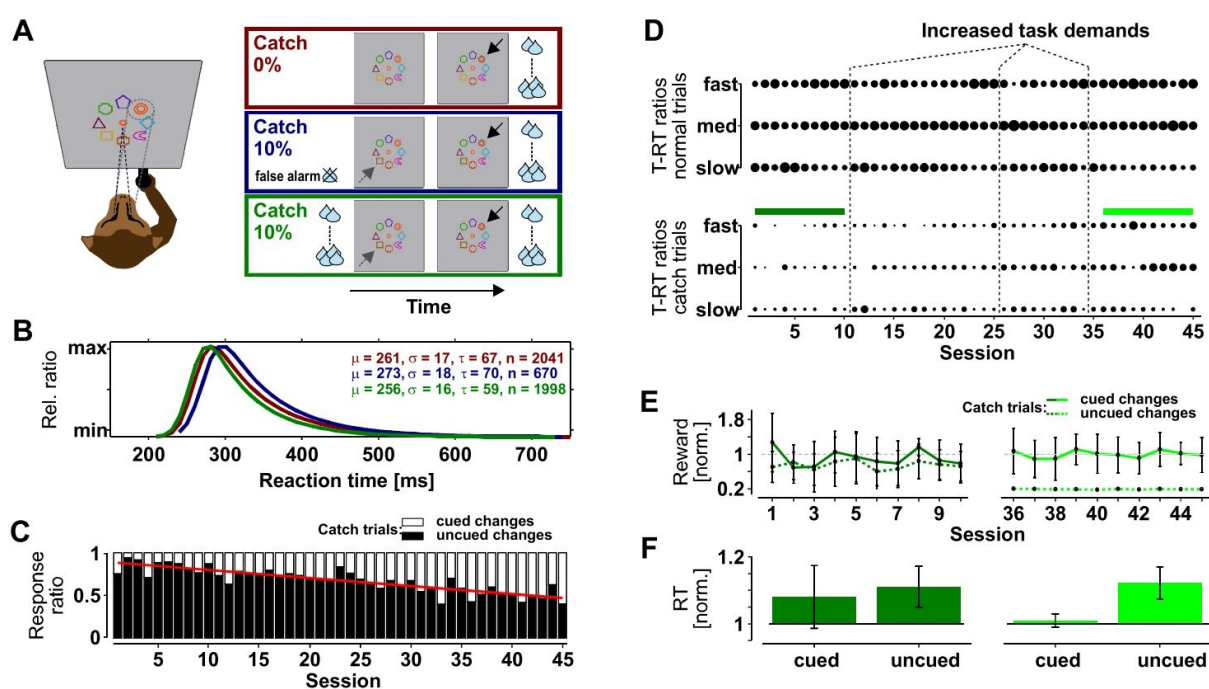


Fig. 29: Reward-associated shaping of behavior. *A*: simplified visual display, showing 8 arbitrary representatives for 26 simultaneously displayed objects of different shape and color. The monkey's task was to detect a luminance change at the cued object (cue displayed at the fixation point). In either 0% (red frame) or 10% of the trials, the luminance change at the cued object (solid arrows) was preceded by a luminance change at an uncued object (dashed arrows). Detection of such uncued changes was either treated as a false alarm and resulted in unrewarded trial termination (blue frame) or rewarded as a cued change (green frame). Drop symbols indicate reaction time (RT)-dependent amount of reward. *B*: ex-Gaussian fits of RT distributions and corresponding fit parameters (μ , mean; σ , variability). Color code is same as in *A*; Rel., relative. *C*: ratio of responses to the cued and uncued change in catch trials during the course of 45 training sessions. Red line indicates a linear fit to the data. *D*: ratio of fast, medium, and slow responses to the cued change in normal trials (*top*) and in catch trials (*bottom*). Size of dots represents their relative number compared with all correct responses in normal trials and in catch trials, respectively. Responses to uncued changes were considered for calculating catch trial ratios but are not shown for simplicity. *E*: reward amount obtained in catch trials during sessions 1-10 (*left*) and during sessions 36-45 (*right*) after task demands were slowly increased and reward decreased for responses to uncued changes. Reward amount is normalized to the mean reward amount obtained in normal trials during the same session. *F*: mean RT in response to cued and uncued changes in catch trials, normalized to median RT during normal trials. Color coding is same as in *E*. Error bars are SD. Rel., relative; T-RT ratio, target-reaction time ratio; norm., normalized.

counteracts) training of the desired behavior and, furthermore, to what extent fine adjustments of reward amounts can be used to gradually shape behavior under this much more complex condition of visual stimulation.

We measured RTs during five sessions before the introduction of uncued changes. High, medium, and small rewards were provided for fast, medium, and slow RTs, respectively. Following these sessions, we introduced uncued changes in 10% of the trials (“catch trials”) and treated responses to these changes (UC responses) as false alarms, resulting in the termination of the trial without reward (as in the classic, binary approach). Ignoring these uncued changes and responding to the change of the cued object (C responses) later in the trial was rewarded as before. After two sessions with this feedback scheme, we switched to rewarding UC responses in the same way as C responses. The results of these two different approaches show two interesting features. First, in the two sessions during which UC responses resulted in the termination of the trial (binary regime), the number of error trials (excluding fixation errors) increased by 50% compared with the average performance in the five sessions without catch trials. Many of these errors were the consequence of a UC response, but even when catch trials were disregarded, errors increased by 21%. Second, responses to correctly cued objects (disregarding catch trials) were slower than before. Fitting ex-Gaussians to the RT distributions before and after the introduction of catch trials revealed a rightward shift of the RT distribution by ~10 ms (Fig. 29B). The data suggest that even with a catch trial ratio of only 10%, the animal’s overall confidence with the task requirements was significantly attenuated when trials were terminated after UC responses. In contrast, switching to rewarding UC responses (nonbinary regime) helped to quickly reestablish the previous performance, and the animal returned to about the same RT distribution as observed before the introduction of catch trials (Fig. 29B).

The key question is, however, whether this reward scheme supports the selective allocation of attention to the cued object (the desired behavior) or rather supports distributing attention over the entire stimulus array (the undesired behavior). With the exception of the very first training sessions introducing catch trials, a cued change occurred 750 ms after the uncued change at the earliest. For the monkey, waiting for the cued change bears the risk of a fixation error due to the longer trial time. Hence, because even slow UC responses would provide a safe reward, our reward scheme potentially facilitates the undesired behavior, a distributed

rather than selective spatial attention. On the other hand, assuming that the monkey would aim to maximize its reward per trial, selective attention to the cued item increases the chance to respond with a fast RT (i.e., getting a high reward). To obtain a detailed insight into the behavioral strategy of the animal, we introduced the following training steps rather slowly. For 10 sessions, we left the task parameters unchanged and kept reward equal for UC and C responses. During the 24 sessions thereafter, we stepwise increased the task demands (reduction of contrast change, alignment of objects, double the number of catch trials) and reduced the amount of reward for UC responses, until finally UC responses received a very small reward only, independent of RT. Task demands and reward scheme were then kept unchanged for the last 11 sessions. Three Monday sessions were disregarded for analysis due to a small number of catch trials (< 10).

During the first sessions of this training period, in catch trials the monkey had a high ratio of UC responses (mean_{S1-S10}: $84.13 \pm 7.84\%$). Within this interval, there was no strong need for the animal to allocate attention selectively to one stimulus because the contrast change was relatively easy to recognize and responses to both cued and uncued changes often resulted in a high reward. Yet, with the adjustment of task demands and reward amounts, there was an increasingly larger benefit for selectively attending to the cued stimulus, and the monkey started to respond more and more frequently to the cued change later in a catch trial (Fig. 29C). Comparison of the first and the last 10 sessions of the training shows this change in behavior was highly significant (Wilcoxon rank sum test: $Z = 3.74$, $P < 10^{-3}$).

A detailed analysis of RTs and obtained reward provides a deeper insight into the factors likely responsible for this behavioral adaptation. Figure 29D shows the performance of the animal in each of the sessions, in terms of relative fractions of fast, medium, and slow C responses (resulting in high, medium, and low reward, respectively), separately for normal and catch trials. During the first 10 training sessions, in normal trials the monkey responded more and more frequently with a fast RT and reduced the number of trials with slow RT (Fig. 29D, *top*). After the task demands were increased, each time performance dropped initially and then rose again during subsequent sessions, until the monkey eventually managed a high ratio of fast, high-reward responses with the final task demands.

Obviously, use of the information provided by the cue got more and more beneficial to reach a high-reward regime. This increased attention to the cued item is mirrored by the

performance level in catch trials. At the beginning of the training, *M3* only rarely responded to the cued item in catch trials, and if so, managed only a small or medium reward in the majority of trials, suggesting a more distributed rather than selective attention. With increasing task demands, however, *M3* responded more often to the contrast change at the cued object later in a catch trial and frequently achieved a fast, high-reward RT (Fig. 29D, *bottom*). From the perspective of the animal, this behavior was highly rational, as shown by the analysis of obtained reward (Fig. 29E). With low task demands and a more distributed attention, the monkey managed to get about equal amounts of reward for both UC and C responses in catch trials. Yet, compared with normal trials, the amount was significantly less after UC responses (73% of mean per-trial reward in normal trials; Wilcoxon signed rank test, $P = 0.002$, $n = 10$) and slightly but not significantly less after C responses (90%; $P = 0.16$). In accordance with this, RTs to both cued and uncued changes were significantly slower in catch trials than in normal trials ($P < 0.013$ for both; Fig. 29F, *left*), indicating that uncued events captured some attention such that the monkey was generally slower during catch trials. In contrast, at the end of the training, when task demands were higher and UC responses received a small to very small reward, the monkey strongly focused its attention on the cued item. In catch trials, the monkey achieved responses to the cued change as fast as in normal trials ($P = 0.127$) and managed the same reward amount ($P = 0.922$; Fig. 29, *E and F, right*). UC responses were significantly slower ($P = 0.002$) than C responses and were delayed by 37 ms, on average. Thus, even though NB-PRT was used for rewarding basically undesired behavior (responses to uncued events), it was highly efficient to train the animal on selecting the cued target. With this approach, we could prevent the animal from switching to other, undesired strategies potentially resulting from the multitude of possible error causes in a multiple-object task design. Careful association of behavior with different reward amounts allowed us to shape the desired behavior and provided the trainer with meaningful information during the training procedure. We confirmed these conclusions by using NB-PRT to train *M1* on essentially the same task (to detect the dimming of a small area in 1 of 26 objects, using a cue validity of 80%). As *M3* did, *M1* also used the cue information to selectively allocate attention, as indicated by significantly shorter RTs for cued stimuli, tested during 10 sessions after the final of 15 possible target objects had been introduced (Wilcoxon signed rank test, $Z = 3.35$, $P < 10^{-3}$).

9.6 Discussion

PRT is a widely used tool for training animals to cooperate for husbandry or scientific purposes. It was successfully applied to train animals on entering a compartment, presenting an arm or leg for blood sampling, moderate aggressive or affiliative behavior among individuals, and as environmental enrichment (for review: [Coleman & Maier 2010; Laule et al. 2003; Prescott & Buchanan-Smith 2003; Rogge et al. 2013; Schapiro et al. 2003; Westlund 2015]). PRT has also been successfully used for automated procedures to assess cognitive abilities before training in a laboratory environment [Fagot & Paleressompoulle 2009] and for automated, voluntarily performed training procedures inside the animal facility [Calapai et al. 2017; Tulip et al. 2017]. It is based on the simple technique that a reward (or otherwise positively reinforcing feedback) is given whenever the animal shows the desired behavior, and no reward else. For laboratory purposes involving awake, behaving nonhuman primates, PRT has been successfully used since the early years of neurophysiological recordings [Evarts 1968; Goldberg & Wurtz 1972; Lemon & Porter 1976; Mountcastle et al. 1975; Wurtz 1969].

Even under largely identical conditions, however, success and progress during training may differ significantly from animal to animal and are subject to the animal's individual behavioral needs [Berger et al. 2018; Coleman 2012]. Training of the behavioral tasks used in cognitive neuroscientific faces specific challenges: first, animals are outside the familiar environment of their home compartment, in a laboratory environment; second, they need to be restrained by means of a primate chair and usually a head holder; third, the desired behavior frequently relies on interpretation of rather abstract sensory cues; fourth, tasks are often highly demanding; and fifth, animals are required to perform many (usually several hundred) consecutive trials to allow meaningful data analysis. Given these particularities, successful training in reasonable time depends on generally accepted guidelines on the one hand, such as rigid planning of training steps and prudent handling of the animal in the laboratory [Smith et al. 2006; Tardif et al. 2006]. On the other, it requires specific approaches to ensure the animal's cooperation to perform the behavioral task. With increasingly more sophisticated and demanding tasks to study higher cognitive functions and complex motor

behaviors, training procedures get more difficult and time consuming and may face unforeseen pitfalls, potentially causing additional delays.

The method we describe is a modification of the traditional reward schedule used for PRT. It was partly motivated by recent studies showing that monkeys integrate information about reward probabilities to bias their choices in free-choice paradigms [Feng et al. 2009; Kubanek & Snyder 2015; Rorie et al. 2010] and quickly learn selection rules based on stimulus-reward associations [Gaffan et al. 2002; Lennert & Martinez-Trujillo 2011]. NB-PRT relies on this natural expertise and uses it for interacting with the animal. NB-PRT can be applied both for training a new task and for maintaining high performance levels when learning has finished. The present study reports the potential of this approach for different training situations, ranging from simple to complex, in three individuals. This report attempts to share the experiences gathered with this approach but does not provide a systematic comparison of the pros and cons of binary vs. nonbinary reward schedules. Because of the many factors influencing success and progress in training (trainer's experience, animal's experience, temperament, age, social rank, task requirements, etc.), a systematic comparison needs a large cohort of animals to average out such differences, which is beyond the resources of our laboratory. However, this is also beyond the conclusions we want to draw: because of the many factors influencing the training of an individual, there is not just one and only true approach to train an animal, but rather the requirement to design the training schedule to optimally meet the individual needs of the animal. NB-PRT, therefore, should be thought of as an additional instrument in the PRT toolbox that might be considered in addition to established protocols to allow for optimal training progress.

9.6.1 Potential and benefits of NB-PRT

On the basis of the experience reported in this article, we identified three general hallmarks of NB-PRT for laboratory training of both simple and complex cognitive tasks. The first is that NB-PRT provides more differentiated feedback to the monkey. During trial-and-error learning, monkeys learn how not to behave for preventing trial termination and rejection of reward. This learning of behavioral errors is critical for the progression of the training and its overall success [Sutton & Barto 1998]. Yet, training of complex tasks involves introduction of new error sources at some critical steps. For the animal, such unfamiliar errors easily cause

confusion with the current task rules, not only with regard to the new task component but also with respect to already established behaviors (cf. Fig. 29B). NB-PRT provides the opportunity to introduce such new error sources in a soft way and to keep the animal's confidence with the general task rules. Instead of trial termination and rejection of reward, undesired behavior related to a new task rule is rewarded, but much less than the desired behavior (e.g., Results, *Example 1: Preventing high error rates*). This makes the feedback more distinct: previously learned error sources still cause trial termination, but the new error source is systematically “taught” to the animal based on small rewards. After the animal learns the desired behavior (by figuring out how to get the most reward), the reward scheme can eventually be reset by fully rejecting reward for the undesired behavior first, and subsequently associating it with trial termination, such that new reward-behavior associations may be defined for the next training step. The more informative feedback provided by NB-PRT may be exemplified by a metal detector when searching for a coin on a beach. With a binary device, a tone signal may indicate that the coin is somewhat close, but no signal provides no hint about where the coin is. A graded feedback provides this hint: the higher the tone, the closer the coin. It allows the target zone to be enlarged such that less time is spent outside of it, and within the target zone, the signal provides information about its center.

The second hallmark is an increase in the learning rate. Because, in the laboratory, trial-and-error learning with binary feedback cannot signal more than “right” and “wrong,” unsuccessful trials will make the difference for the animal to adapt its behavior. Yet, their relative number must not exceed a critical ratio, to prevent a loss in task confidence and in the overall willingness to cooperate. This causes a conflict, because keeping the number of errors within a critical range also limits the number of trials for learning. With a graded reward, it is possible to put emphasis on correctly performed trials. By a careful choice of criteria to obtain, e.g., high, medium, and low reward, NB-PRT provides the animal with a larger number of informative trials (*example 2*) and guides it toward the desired behavior more purposefully than error-based learning.

The third hallmark is the introduction of a “gambling factor” for tasks of otherwise uniform structure that helps to increase the animal's overall alertness (e.g., Fig. 27, *E* and *F*). As mentioned previously, in neuroscience research, monkeys are usually required to perform hundreds of consecutive trials. Even when the focus is on individuals that are very good

performers in the laboratory, there is not much reason to believe that performing the same task again and again is constantly thrilling. NB-PRT provides the opportunity for the monkey to “win” a trial by rewarding very good performance better than medium performance. Associating the task outcome with the animal’s performance makes the reward more unpredictable and, as such, provides a lasting incentive for the animal to stay focused even when learning has finished.

9.6.2 Limitations and side aspects of NB-PRT

It is worth mentioning, however, that NB-PRT has limits and side aspects that need to be taken into account. First, depending on the research question, during neuronal data acquisition, variable reward amounts may impair the interpretability of neuronal responses. For example, neurons may be modulated by cognitive processes and reward value or reward expectancy at the same time [Gottlieb 2007; Leon & Shadlen 1999; Stănişor et al. 2013]. For meaningful data analysis, investigating the response of such neurons usually requires all factors but the one under examination to be fixed, making variable rewards an unfavorable condition. Second, animals may get saturated more quickly if they receive higher reward for the desired behavior, yielding fewer trials overall. Albeit in the current study we observed no such effect, or even the opposite compared with the animal’s performance in a binary regime, we cannot exclude this possibility because of the small number of animals tested. Third, combination, adaptation, and gradation of reward amounts entails possible pitfalls. For example, if a reward bonus for precise fixation is combined with an RT-dependent reward schedule, fast RTs in trials with unprecise fixation potentially yield a similar reward than medium RTs in trials with precise fixation. This makes the feedback ambiguous again. Furthermore, frequent adaption of criteria for high, medium, and low reward in an RT-dependent reward schedule to fix the ratio of high-reward trials likely constitutes a punishment for focused performance, because achieving higher rewards gets more and more difficult. Under such circumstances, monkeys may easily learn that mediocre performance makes a high reward more easily accessible than good performance. Similarly, if the choice of criteria for different reward amounts makes it hard or even impossible for the animal to associate them with different behaviors, NB-PRT may exert undesired effects (Fig. 27D).

Thus, like any other training approach, successful application of NB-PRT requires careful planning of the individual training steps and taking the perspective of the animal. When based on careful choice of parameters and daily data inspection, NB-PRT constitutes a powerful technique that provides additional options to guide the animal's behavior. Because it is based on success rather than failure, it adds an additional motivating factor, helps to prevent animals from developing a very low or very high error tolerance, and constitutes a promising approach for refining laboratory methods for nonhuman primates.

Author contribution

D.W. conceived and designed research; B.F. and D.W. performed experiments; B.F. and D.W. analyzed data; B.F. and D.W. interpreted results of experiments; B.F. and D.W. prepared figures; D.W. drafted manuscript; B.F. and D.W. edited and revised manuscript; B.F. and D.W. approved final version of manuscript.

Grants

This work was supported by Deutsche *Forschungsgemeinschaft* Grants WE 5469/2-1 and WE 5469/3-1, a Zentrale Forschungsförderung grant from the University of Bremen, and a scholarship from the German Academic Scholarship Foundation.

Acknowledgments

We acknowledge support by Constantin Neagu, Sally Lott, Miriam Schillner, Peter Bujotzek, Ramazani Hakizimani, and Katrin Thoss regarding various aspects of the study. We thank Eric Drebitz and Malte Persike for comments on an earlier draft.

Disclosures

No conflicts of interest, financial or otherwise, are declared by the authors.

10. General conclusion and outlook

10.1 The specificity of EFPs

The majority of studies documented in this thesis characterized the specificity of high-density EFPs by investigating whether information about sensory processing in V1 is reflected in the epidural signal. The present results demonstrate that the differentiated V1 neuronal activity evoked by various stimulus features is represented in EFPs:

- The spatial location of closely arranged small visual stimuli has been classified from single-trial EFPs.
- The properties stimulus size, shape and contrast evoked systematic modulations in the BGP activity of the EFP. In addition, stimulus size and shape were decoded above chance level from trial-averaged EFP features. Large and small sized objects as well as circular and triangular shaped objects have been best distinguishable.
- The findings about the systematic EFP modulation caused by shape-classes imply that EFPs reflect the shape of a stimulus regardless of its rotation, potentially reflecting the functional organization of orientation-selective neurons in V1.

Many of the results indicate a similarity between epidural and intracortical signal modulations especially regarding the γ -band activity. Therefore, despite the integration over neuronal populations and the potential dampening of the signal caused by the dura mater (as described in Chapter 3.2.1), high-density EFP is an accurate meso-scale measure of cortical activity evoked by visual stimulation.

10.2 EFP modulation is correlated to behavior and spatial attention

The results of Chapter 8 revealed a modest attentional modulation of the trial-averaged broadband γ -activity and a correlation between RT and the latency of evoked EFP responses. Differences between fast and slow RT were found for both the EFP latency and the attentional modulation of the EFP. Behavioral choices and neuronal responses in V1 covariate [Palmer et al. 2007]. The present findings emphasize the potential usage of EFPs for the prediction of perception and behavioral performance from meso-scale recordings. The found attentional modulation, however, was small and the experiment was performed with only one monkey. The experiment needs to be repeated with additional subjects to verify the present results. Furthermore, for future investigations of the attentional modulation of EFPs recorded from V1, it is necessary to use an alternative task design which potentially leads to higher attentional effects (as discussed in Chapter 8.4). This could enable a precise decoding of the focus of covert spatial attention using EFPs from V1. Fortunately, for the repetition of the current and the execution of future experiments, the non-binary positive reinforcement training, described in Chapter 9, will be helpful for a fast and reliable training of macaques. Using this training strategy, the time between the start of the monkey training and the first signal recording from task-performing monkeys can be shortened, while the motivation and the task confidence of the monkeys is kept high.

10.3 Optimization of information decoding

To further improve the decoding performance, the placement of stimuli into areas of dense electrode coverage is suggested by Chapters 5 and 6. Stimulation in foveal and close-to-foveal regions paired with high-density recordings in corresponding V1 areas could further increase stimulus differentiation because of the large cortical area representing the central part of the visual field [Tootell et al. 1988]. Within the analysis of most electrophysiological studies in this thesis, optimal-selective electrodes were selected for a given stimulus to decode visual information. Alternatively, the visual stimulation could have been adapted to fit

optimally into the RFs of single or multiple electrodes. This optimization of the visual stimulation for a pre-defined set of electrodes could lead to an improvement in the decoding of visual information and should therefore be tested in future studies that are focused on investigating the benchmarks of information decoding from EFPs originating from V1.

10.4 Transfer to the human brain

An important field of research that uses superficial extracortical recordings is the reestablishment of communication and motor control of severely paralyzed patients via BCIs. A direct transfer of the present findings to human BCI applications is, however, beyond the scope of this thesis. Three major reasons challenge the direct translation of the present results to clinical applications.

1. The location of V1 on the brain's surface is different in humans compared to macaques [Van Essen et al. 2001]. Only a small part of V1 representing the fovea, the central degrees and the vertical meridian of the visual field is exposed to the cortical surface [Horton & Hoyt 1991]. The rest of V1 and therefore the representation of the largest part of the visual field is concealed in the calcarine sulcus [Horton & Hoyt 1991]. Due to the restricted epidural access to predominantly the foveal parts of the visual field in human V1, investigations need to be expanded by studying EFPs recorded from regions in V1 that represent the foveal region.
2. The size of the brain, the cortical surface area and the cortical magnification differs between humans and non-human primates [Hubel & Wiesel 1974b; Schira et al. 2007; Van Essen et al. 2001]. As a result, the spatial resolution of the same array differs between humans and non-human primates. Due to the fact that the size of the human brain is larger compared to the macaque brain, using the same array as in the present studies for human EFP recordings should lead to a denser sampling of the cortical surface. Nevertheless, investigations on humans are needed to enable an evaluation of the functional spatial resolution of the used electrode density in humans.
3. Patients, in contrast to the monkeys in the present studies, are usually not head fixated in clinical applications. Due to the retinotopic organization of V1, slight head and eye

movements could decrease the decoding performance because the cortical activity is changed by the displacement of the visual scene. In addition, the monkeys were highly motivated and trained. Patients are usually not in good health which could lead to a non-optimal performance and issues that are not present in non-human primate studies. In the circumstance that, for example, cLIS patients use visual BCIs, issues could arise from the moistination of the eyes which needs to be artificially maintained because these patients are unable to make eye blinks [Bauer et al. 1979].

Despite these challenges that impede a direct translation of the present findings to the human brain, they demonstrate that EFPs represent the differentiated neuronal activity evoked by stimulus attributes in high resolution and that EFPs can be correlated to attention and behavior. Even though the dura mater attenuates the neuronal signal recorded with high-density arrays [Bundy et al. 2014], the attentional modulation of neuronal populations from V1 was found to be represented in EFPs. According to the similarity of the macaque and the human visual system [Newsome & Stein-Aviles 1999], these findings provide evidence for the applicability of EFPs for future BCIs. In case that further investigations fail to precisely decode the spatial location of covert visual attention from V1, the usage of high-density EFPs from visual areas that have shown a stronger attentional modulation in comparison to V1, for example from V2 or V4 [Buffalo et al. 2010; Luck et al. 1997; Mehta et al. 2000], could enable this decoding approach. Due to the beneficial properties of EFPs, the present findings suggest further investigations of EFPs with regard to their application in BCIs.

10.5 Outlook

Altogether, high-density epidural recordings from V1 reflect the cortical activity beneath the electrodes accurately and therefore visual information can be precisely extracted from high-density EFPs. Visual BCIs could benefit from epidural recording from V1 because of V1's richness of extractable information. V1 was, however, targeted because of its beneficial properties for the objective of this thesis. Due to the high specificity of EFPs, the present findings indicate that high-density epidural arrays promise meso-scale mildly-invasive superficial extracortical recordings not only from V1 but also from other cortical areas. Unfortunately, EFPs are rarely used (for a detailed tabular list of studies based on high-

density ECoG and high-density EFP, see [Wang et al. 2017]). Until now, subdural recordings dominate in clinical application [Jayakar et al. 2016; Kovac et al. 2017; Reif et al. 2016; Sperling 1997] and BCI research [Slutzky & Flint 2017]. The lack of long-term studies investigating the stability of epidural recordings (as discussed in Chapter 3.2.1) as well as the limited knowledge about its specificity impedes a common usage of EFPs for long-term clinical applications. Thus, epidural recordings could be an equivalent alternative to subdural and intracortical recordings if the knowledge about epidural recordings is expanded. This thesis contributes to the literature which emphasizes the usage of epidural recordings because of its high specificity. Epidural recordings expand the variety of neurophysiological methods rather than replacing other options. My thesis demonstrates the beneficial properties of EFPs and constitutes reasons to consider epidural recordings as mildly-invasive, alternative neurophysiological method for research and also for clinical application.

11. References

- Abiri R, Borhani S, Sellers EW, Jiang Y, & Zhao X (2019) A Comprehensive Review of EEG-Based Brain-Computer Interface Paradigms. *J Neural Eng*, 16(1): 011001.
- Acqualagna L, & Blankertz B (2013) Gaze-Independent BCI-Spelling Using Rapid Serial Visual Presentation (RSVP). *Clin Neurophysiol*, 124(5): 901–908.
- Albrecht DG, & Hamilton DB (1982) Striate Cortex of Monkey and Cat: Contrast Response Function. *J Neurophysiol*, 48(1): 217–237.
- Allison BZ, Brunner C, Kaiser V, Müller-Putz GR, Neuper C, & Pfurtscheller G (2010) Toward a Hybrid Brain-Computer Interface Based on Imagined Movement and Visual Attention. *J Neural Eng*, 7(2): 026007.
- Aloise F, Aricò P, Schettini F, Riccio A, Salinari S, Mattia D, ... Cincotti F (2012a) A Covert Attention P300-Based Brain-Computer Interface: Geospell. *Ergonomics*, 55(5): 538–551.
- Aloise F, Schettini F, Aricò P, Salinari S, Babiloni F, & Cincotti F (2012b) A Comparison of Classification Techniques for a Gaze-Independent P300-Based Brain-Computer Interface. *J Neural Eng*, 9(4): 045012.
- Amiez C, Joseph JP, & Procyk E (2006) Reward Encoding in the Monkey Anterior Cingulate Cortex. *Cereb Cortex*, 16(7): 1040–1055.
- Andersson P, Plum JPW, Siero JCW, Klein S, Viergever MA, & Ramsey NF (2011) Real-Time Decoding of Brain Responses to Visuospatial Attention Using 7T fMRI. *PLoS One*, 6(11): e27638.
- Aricò P, Aloise F, Schettini F, Salinari S, Mattia D, & Cincotti F (2014) Influence of P300 Latency Jitter on Event Related Potential-Based Brain-Computer Interface Performance. *J Neural Eng*, 11(3): 035008.
- Aronov D, Reich DS, Mechler F, & Victor JD (2003) Neural Coding of Spatial Phase in V1 of the Macaque Monkey. *J Neurophysiol*, 89(6): 3304–3327.
- Asaad WF, Rainer G, & Miller EK (2000) Task-Specific Neural Activity in the Primate Prefrontal Cortex. *J Neurophysiol*, 84(1): 451–459.
- Astrand E, Wardak C, & Ben Hamed S (2014) Selective Visual Attention to Drive Cognitive Brain-Machine Interfaces: From Concepts to Neurofeedback and Rehabilitation Applications. *Front Syst Neurosci*, 8: 144.
- Bacher D, Jarosiewicz B, Masse NY, Stavisky SD, Simeral JD, Newell K, ... Hochberg LR (2015) Neural Point-And-Click Communication by a Person With Incomplete Locked-In Syndrome. *Neurorehabil Neural Repair*, 29(5): 462–471.
- Ball T, Kern M, Mutschler I, Aertsen A, & Schulze-Bonhage A (2009) Signal Quality of Simultaneously Recorded Invasive and Non-Invasive EEG. *Neuroimage*, 46(3): 708–716.
- Baluch F, & Itti L (2011) Mechanisms of Top-Down Attention. *Trends Neurosci*, 34(4): 210–224.
- Barlow HB (1981) The Ferrier Lecture, 1980. Critical Limiting Factors in the Design of the Eye and Visual Cortex. *Proc R Soc Lond B Biol Sci*, 212(1186): 1–34.
- Barone P, Batardiere A, Knoblauch K, & Kennedy H (2000) Laminar Distribution of Neurons in Extrastriate Areas Projecting to Visual Areas V1 and V4 Correlates With the Hierarchical Rank and Indicates the Operation of a Distance Rule. *J Neurosci*, 20(9): 3263–3281.
- Barone P, & Joseph JP (1989) Prefrontal Cortex and Spatial Sequencing in Macaque Monkey. *Exp Brain Res*, 78(3): 447–464.

11. References

- Bartfeld E, & Grinvald A (1992) Relationships Between Orientation-Preference Pinwheels, Cytochrome Oxidase Blobs, and Ocular-Dominance Columns in Primate Striate Cortex. *Proc Natl Acad Sci U S A*, 89(24): 11905–11909.
- Bartoli E, Bosking W, Chen Y, Li Y, Sheth SA, Beauchamp MS, ... Foster BL (2019) Functionally Distinct Gamma Range Activity Revealed by Stimulus Tuning in Human Visual Cortex. *Curr Biol*, 29(20): 3345–3358.
- Bauer G, Gerstenbrand F, & Rimpl E (1979) Varieties of the Locked-In Syndrome. *J Neurol*, 221(2): 77–91.
- Ben-Hur A, & Weston J (2010) *A User's Guide to Support Vector Machines*. Carugo O., Eisenhaber F. (eds) *Data Mining Techniques for the Life Sciences. Methods in Molecular Biology (Methods and Protocols)*, vol 609. New York: Humana Press.
- Benabid AL, Costecalde T, Eliseyev A, Charvet G, Verney A, Karakas S, ... Chabardes S (2019) An Exoskeleton Controlled by an Epidural Wireless Brain-Machine Interface in a Tetraplegic Patient: A Proof-Of-Concept Demonstration. *Lancet Neurol*, 18(12): 1112–1122.
- Bensch M, Martens S, Halder S, Hill J, Nijboer F, Ramos A, ... Gharabaghi A (2014) Assessing Attention and Cognitive Function in Completely Locked-In State With Event-Related Brain Potentials and Epidural Electroencephalography. *J Neural Eng*, 11(2): 026006.
- Berens P (2009) CircStat: A MATLAB Toolbox for Circular Statistics. *J Stat Softw*, 31(10).
- Berens P, Keliris GA, Ecker AS, Logothetis NK, & Tolias AS (2008) Comparing the Feature Selectivity of the Gamma-Band of the Local Field Potential and the Underlying Spiking Activity in Primate Visual Cortex. *Front Syst Neurosci*, 2: 2.
- Berger M, Calapai A, Stephan V, Niessing M, Burchardt L, Gail A, & Treue S (2018) Standardized Automated Training of Rhesus Monkeys for Neuroscience Research in Their Housing Environment. *J Neurophysiol*, 119(3): 796–807.
- Bergey GK, Morrell MJ, Mizrahi EM, Goldman A, King-Stephens D, Nair D, ... Seale CG (2015) Long-Term Treatment With Responsive Brain Stimulation in Adults With Refractory Partial Seizures. *Neurology*, 84(8): 810–817.
- Bin G, Gao X, Wang Y, Hong B, & Gao S (2009) VEP-Based Brain-Computer Interfaces: Time, Frequency, and Code Modulations [Research Frontier]. *IEEE Comput Intell Mag*, 4(4): 22–26.
- Birbaumer N (2006) Breaking the Silence: Brain-Computer Interfaces (BCI) for Communication and Motor Control. *Psychophysiology*, 43(6): 517–532.
- Birbaumer N, & Cohen LG (2007) Brain-Computer Interfaces: Communication and Restoration of Movement in Paralysis. *J Physiol*, 579(3): 621–636.
- Bisley JW (2011) The Neural Basis of Visual Attention. *J Physiol*, 589(1): 49–57.
- Blabe CH, Gilja V, Chestek CA, Shenoy K V., Anderson KD, & Henderson JM (2015) Assessment of Brain-Machine Interfaces From the Perspective of People With Paralysis. *J Neural Eng*, 12(4): 043002.
- Blankertz B, Lemm S, Treder M, Haufe S, & Müller K-R (2011) Single-Trial Analysis and Classification of ERP Components – A Tutorial. *Neuroimage*, 56(2): 814–825.
- Blankertz B, Tomioka R, Lemm S, Kawanabe M, & Müller K-R (2008) Optimizing Spatial Filters for Robust EEG Single-Trial Analysis. *IEEE Signal Process Mag*, 25(1): 41–56.
- Blasdel G, & Campbell D (2001) Functional Retinotopy of Monkey Visual Cortex. *J Neurosci*, 21(20): 8286–8301.
- Bockhorst T, Pieper F, Engler G, Stieglitz T, Galindo-Leon E, & Engel AK (2018) Synchrony Surfacing: Epicortical Recording of Correlated Action Potentials. *Eur J Neurosci*, 48(12): 3583–3596.
- Bonhoeffer T, & Grinvald A (1991) Iso-Orientation Domains in Cat Visual Cortex Are Arranged in Pinwheel-Like Patterns. *Nature*, 353(6343): 429–431.
- Bosman CA, Schoffelen J-M, Brunet N, Oostenveld R, Bastos AM, Womelsdorf T, ... Fries P (2012) Attentional Stimulus Selection Through Selective Synchronization Between Monkey Visual Areas. *Neuron*, 75(5): 875–888.

11. References

- Boynton GM (2011) Spikes, BOLD, Attention, and Awareness: A Comparison of Electrophysiological and fMRI Signals in V1. *J Vis*, 11(5): 12.
- Branco MP, Freudenburg Z V, Aarnoutse EJ, Bleichner MG, Vansteensel MJ, & Ramsey NF (2017) Decoding Hand Gestures From Primary Somatosensory Cortex Using High-Density ECoG. *Neuroimage*, 147: 130–142.
- Braun J, & Sagi D (1990) Vision Outside the Focus of Attention. *Percept Psychophys*, 48(1): 45–58.
- Bredfeldt CE, & Ringach DL (2002) Dynamics of Spatial Frequency Tuning in Macaque V1. *J Neurosci*, 22(5): 1976–1984.
- Brodmann K (1909) *Vergleichende Lokalisationslehre der Großhirnrinde in ihren Prinzipien dargestellt auf Grund des Zellenbaues*. Leipzig: Barth.
- Brunner P, Joshi S, Briskin S, Wolpaw JR, Bischof H, & Schalk G (2010) Does the “P300” Speller Depend on Eye Gaze? *J Neural Eng*, 7(5): 056013.
- Brunner P, Ritaccio AL, Emrich JF, Bischof H, & Schalk G (2011) Rapid Communication With a “P300” Matrix Speller Using Electrographic Signals (ECoG). *Front Neurosci*, 5: 5.
- Buffalo EA, Fries P, Landman R, Liang H, & Desimone R (2010) A Backward Progression of Attentional Effects in the Ventral Stream. *Proc Natl Acad Sci U S A*, 107(1): 361–365.
- Bundy DT, Zellmer E, Gaona CM, Sharma M, Szrama N, Hacker C, ... Leuthardt EC (2014) Characterization of the Effects of the Human Dura on Macro- and Micro-Electrocorticographic Recordings. *J Neural Eng*, 11(1): 016006.
- Burle B, Spieser L, Roger C, Casini L, Hasbroucq T, & Vidal F (2015) Spatial and Temporal Resolutions of EEG: Is It Really Black and White? A Scalp Current Density View. *Int J Psychophysiol*, 97(3): 210–220.
- Buzsáki G, Anastassiou CA, & Koch C (2012) The Origin of Extracellular Fields and Currents – EEG, ECoG, LFP and Spikes. *Nat Rev Neurosci*, 13(6): 407–420.
- Calapai A, Berger M, Niessing M, Heisig K, Brockhausen R, Treue S, & Gail A (2017) A Cage-Based Training, Cognitive Testing and Enrichment System Optimized for Rhesus Macaques in Neuroscience Research. *Behav Res Methods*, 49(1): 35–45.
- Callaway EM (2005) Structure and Function of Parallel Pathways in the Primate Early Visual System. *J Physiol*, 566(1): 13–19.
- Campbell A, & Wu C (2018) Chronically Implanted Intracranial Electrodes: Tissue Reaction and Electrical Changes. *Micromachines*, 9(9): 430.
- Cantlon JF, & Brannon EM (2007) Basic Math in Monkeys and College Students. *PLoS Biol*, 5(12): e328.
- Carandini M, Demb JB, Mante V, Tolhurst DJ, Dan Y, Olshausen BA, ... Rust NC (2005) Do We Know What the Early Visual System Does? *J Neurosci*, 25(46): 10577–10597.
- Carrasco M (2011) Visual Attention: The Past 25 Years. *Vision Res*, 51(13): 1484–1525.
- Chakor H, Bertone A, McKerral M, Faubert J, & Lachapelle P (2005) Visual Evoked Potentials and Reaction Time Measurements to Motion-Reversal Luminance- and Texture-Defined Stimuli. *Doc Ophthalmol*, 110(2–3): 163–172.
- Chalk M, Herrero JL, Gieselmann MA, Delicato LS, Gotthardt S, & Thiele A (2010) Attention Reduces Stimulus-Driven Gamma Frequency Oscillations and Spike Field Coherence in V1. *Neuron*, 66(1): 114–125.
- Chang C-C, & Lin C-J (2011) LIBSVM: A Library for Support Vector Machines. *ACM Trans Intell Syst Technol*, 2(3): 27.
- Chang E (2015) Towards Large-Scale Human-Based Mesoscale Neurotechnologies. *Neuron*, 86(1): 68–78.
- Chang MH, Lee JS, Heo J, & Park KS (2016) Eliciting Dual-Frequency SSVEP Using a Hybrid SSVEP-P300 BCI. *J Neurosci Methods*, 258: 104–113.
- Chao ZC, Nagasaka Y, & Fujii N (2010) Long-Term Asynchronous Decoding of Arm Motion Using Electrographic Signals in Monkeys. *Front Neuroeng*, 3: 3.

11. References

- Chelazzi L, Duncan J, Miller EK, & Desimone R (1998) Responses of Neurons in Inferior Temporal Cortex During Memory-Guided Visual Search. *J Neurophysiol*, 80(6): 2918–2940.
- Chen C, Zhang X, Wang Y, Zhou T, & Fang F (2016) Neural Activities in V1 Create the Bottom-Up Saliency Map of Natural Scenes. *Exp Brain Res*, 234(6): 1769–1780.
- Chen X, Wang Y, Nakanishi M, Gao X, Jung T-P, & Gao S (2015) High-Speed Spelling With a Noninvasive Brain-Computer Interface. *Proc Natl Acad Sci U S A*, 112(44): E6058–E6067.
- Chen Y, Martinez-Conde S, Macknik SL, Bereshpolova Y, Swadlow HA, & Alonso J-M (2008) Task Difficulty Modulates the Activity of Specific Neuronal Populations in Primary Visual Cortex. *Nat Neurosci*, 11(8): 974–982.
- Chen Z (2012) Object-Based Attention: A Tutorial Review. *Atten Percept Psychophys*, 74(5): 784–802.
- Chestek CA, Gilja V, Nuyujukian P, Foster JD, Fan JM, Kaufman MT, ... Shenoy K V (2011) Long-Term Stability of Neural Prosthetic Control Signals From Silicon Cortical Arrays in Rhesus Macaque Motor Cortex. *J Neural Eng*, 8(4): 045005.
- Chisholm N, & Gillett G (2005) The Patient's Journey: Living With Locked-In Syndrome. *BMJ*, 331(7508): 94–97.
- Choi H, Lee J, Park J, Lee S, Ahn KH, Kim IY, ... Jang DP (2018) Improved Prediction of Bimanual Movements by a Two-Stage (Effector-Then-Trajectory) Decoder With Epidural ECoG in Nonhuman Primates. *J Neural Eng*, 15(1): 016011.
- Chow K-L, Blum JS, & Blum RA (1950) Cell Ratios in the Thalamo-Cortical Visual System of *Macaca Mulatta*. *J Comp Neurol*, 92(2): 227–239.
- Cleland BG, & Lee BB (1985) A Comparison of Visual Responses of Cat Lateral Geniculate Nucleus Neurons With Those of Ganglion Cells Afferent to Them. *J Physiol*, 369(1): 249–268.
- Cohen J (1988) *Statistical Power Analysis for the Behavioral Science*. (2nd ed.). Hillsdale, NJ: Lawrence Erlbaum Associates.
- Coleman K (2012) Individual Differences in Temperament and Behavioral Management Practices for Nonhuman Primates. *Appl Anim Behav Sci*, 137(3–4): 106–113.
- Coleman K, & Maier A (2010) The Use of Positive Reinforcement Training to Reduce Stereotypic Behavior in Rhesus Macaques. *Appl Anim Behav Sci*, 124(3–4): 142–148.
- Collinger JL, Boninger ML, Bruns TM, Curley K, Wang W, & Weber DJ (2013a) Functional Priorities, Assistive Technology, and Brain-Computer Interfaces After Spinal Cord Injury. *J Rehabil Res Dev*, 50(2): 145–160.
- Collinger JL, Wodlinger B, Downey JE, Wang W, Tyler-Kabara EC, Weber DJ, ... Schwartz AB (2013b) High-Performance Neuroprosthetic Control by an Individual With Tetraplegia. *Lancet*, 381(9866): 557–564.
- Conway BR (2001) Spatial Structure of Cone Inputs to Color Cells in Alert Macaque Primary Visual Cortex (V-1). *J Neurosci*, 21(8): 2768–2783.
- Cook MJ, O'Brien TJ, Berkovic SF, Murphy M, Morokoff A, Fabinyi G, ... Himes D (2013) Prediction of Seizure Likelihood With a Long-Term, Implanted Seizure Advisory System in Patients With Drug-Resistant Epilepsy: A First-In-Man Study. *Lancet Neurol*, 12(6): 563–571.
- Crone NE, Korzeniewska A, & Franaszczuk PJ (2011) Cortical Gamma Responses: Searching High and Low. *Int J Psychophysiol*, 79(1): 9–15.
- Crone NE, Sinai A, & Korzeniewska A (2006) High-Frequency Gamma Oscillations and Human Brain Mapping With Electrocorticography. *Prog Brain Res*, 159: 275–295.
- Dacey DM (2000) Parallel Pathways for Spectral Coding in Primate Retina. *Annu Rev Neurosci*, 23(1): 743–775.
- Dacey DM, & Lee BB (1994) The “Blue-On” Opponent Pathway in Primate Retina Originates From a Distinct Bistratified Ganglion Cell Type. *Nature*, 367(6465): 731–735.

11. References

- Dacey DM, Peterson BB, Robinson FR, & Gamlin PD (2003) Fireworks in the Primate Retina: In Vitro Photodynamics Reveals Diverse LGN-Projecting Ganglion Cell Types. *Neuron*, 37(1): 15–27.
- Dagnelie G, Spekreijse H, & Van Dijk B (1989) Topography and Homogeneity Of Monkey V1 Studied Through Subdurally Recorded Pattern-Evoked Potentials. *Vis Neurosci*, 3(6): 509–525.
- Dai J, & Wang Y (2012) Representation of Surface Luminance and Contrast in Primary Visual Cortex. *Cereb Cortex*, 22(4): 776–787.
- Daniel PM, & Whitteridge D (1961) The Representation of the Visual Field on the Cerebral Cortex in Monkeys. *J Physiol*, 159(2): 203–221.
- Das A, & Ray S (2018) Effect of Stimulus Contrast and Visual Attention on Spike-Gamma Phase Relationship in Macaque Primary Visual Cortex. *Front Comput Neurosci*, 12: 66.
- Davidesco I, Harel M, Ramot M, Kramer U, Kipervasser S, Andelman F, ... Malach R (2013) Spatial and Object-Based Attention Modulates Broadband High-Frequency Responses Across the Human Visual Cortical Hierarchy. *J Neurosci*, 33(3): 1228–1240.
- De Valois RL, Albrecht DG, & Thorell LG (1982) Spatial Frequency Selectivity of Cells in Macaque Visual Cortex. *Vision Res*, 22(5): 545–559.
- DeAngelis GC, Ghose GM, Ohzawa I, & Freeman RD (1999) Functional Micro-Organization of Primary Visual Cortex: Receptive Field Analysis of Nearby Neurons. *J Neurosci*, 19(10): 4046–4064.
- Degenhart AD, Eles J, Dum R, Mischel JL, Smalianchuk I, Endler B, ... Cui XT (2016) Histological Evaluation of a Chronically-Implanted Electrocorticographic Electrode Grid in a Non-Human Primate. *J Neural Eng*, 13(4): 046019.
- DeVoe RC, Ripps H, & Vaughan Jr. HG (1968) Cortical Responses to Stimulation of the Human Fovea. *Vision Res*, 8(2): 135–147.
- Donchin E, & Lindsley DB (1966) Average Evoked Potentials and Reaction Times to Visual Stimuli. *Electroencephalogr Clin Neurophysiol*, 20(3): 217–223.
- Dow BM (1974) Functional Classes of Cells and Their Laminar Distribution in Monkey Visual Cortex. *J Neurophysiol*, 37(5): 927–946.
- Drebitz E, Schledde B, Kreiter AK, & Wegener D (2019) Optimizing the Yield of Multi-Unit Activity by Including the Entire Spiking Activity. *Front Neurosci*, 13: 83.
- Dubey A, & Ray S (2016) Spatial Spread of Local Field Potential Is Band-Pass in the Primary Visual Cortex. *J Neurophysiol*, 116(4): 1986–1999.
- Dubey A, & Ray S (2019) Cortical Electrocorticogram (ECoG) Is a Local Signal. *J Neurosci*, 39(22): 4299–4311.
- Dubey A, & Ray S (2020) Comparison of Tuning Properties of Gamma and High-Gamma Power in Local Field Potential (LFP) Versus Electrocorticogram (ECoG) in Visual Cortex. *Sci Rep*, 10: 5422.
- Duszyk A, Bierzyńska M, Radzikowska Z, Milanowski P, Kuś R, Suffczyński P, ... Durka P (2014) Towards an Optimization of Stimulus Parameters for Brain-Computer Interfaces Based on Steady State Visual Evoked Potentials. *PLoS One*, 9(11): e112099.
- Eason RG, Oden D, & White CT (1967) Visually Evoked Cortical Potentials and Reaction Time in Relation to Site of Retinal Stimulation. *Electroencephalogr Clin Neurophysiol*, 22(4): 313–324.
- Egan JM, Loughnane GM, Fletcher H, Meade E, & Lalor EC (2017) A Gaze Independent Hybrid-BCI Based on Visual Spatial Attention. *J Neural Eng*, 14(4): 046006.
- Ekanayake J, Hutton C, Ridgway G, Scharnowski F, Weiskopf N, & Rees G (2018) Real-Time Decoding of Covert Attention in Higher-Order Visual Areas. *Neuroimage*, 169: 462–472.

11. References

- Enatsu R, & Mikuni N (2016) Invasive Evaluations for Epilepsy Surgery: A Review of the Literature. *Neurol Med Chir*, 56(5): 221–227.
- Engel AK, Moll CKE, Fried I, & Ojemann GA (2005) Invasive Recordings From the Human Brain: Clinical Insights and Beyond. *Nat Rev Neurosci*, 6(1): 35–47.
- Eriksson D, Valentiniene S, & Papaioannou S (2010) Relating Information, Encoding and Adaptation: Decoding the Population Firing Rate in Visual Areas 17/18 in Response to a Stimulus Transition. *PLoS One*, 5(4): e10327.
- Evarts E V (1968) Relation of Pyramidal Tract Activity to Force Exerted During Voluntary Movement. *J Neurophysiol*, 31(1): 14–27.
- Everling S, & Munoz DP (2000) Neuronal Correlates for Preparatory Set Associated With Pro-Saccades and Anti-Saccades in the Primate Frontal Eye Field. *J Neurosci*, 20(1): 387–400.
- Fagot J, & Paleressompouille D (2009) Automatic Testing of Cognitive Performance in Baboons Maintained in Social Groups. *Behav Res Methods*, 41(2): 396–404.
- Farrokhi B, & Erfanian A (2018) A Piecewise Probabilistic Regression Model to Decode Hand Movement Trajectories From Epidural and Subdural ECoG Signals. *J Neural Eng*, 15(3): 036020.
- Farwell LA, & Donchin E (1988) Talking Off the Top of Your Head: Toward a Mental Prosthesis Utilizing Event-Related Brain Potentials. *Electroencephalogr Clin Neurophysiol*, 70(6): 510–523.
- Fatourechi M, Bashashati A, Ward RK, & Birch GE (2007) EMG and EOG Artifacts in Brain Computer Interface Systems: A Survey. *Clin Neurophysiol*, 118(3): 480–494.
- Fazel-Rezai R, Allison BZ, Guger C, Sellers EW, Kleih SC, & Kübler A (2012) P300 Brain Computer Interface: Current Challenges and Emerging Trends. *Front Neuroeng*, 5: 14.
- Felleman DJ, & Van Essen DC (1991) Distributed Hierarchical Processing in the Primate Cerebral Cortex. *Cereb Cortex*, 1(1): 1–47.
- Feng S, Holmes P, Rorie A, & Newsome WT (2009) Can Monkeys Choose Optimally When Faced With Noisy Stimuli and Unequal Rewards? *PLoS Comput Biol*, 5(2): e1000284.
- Fernández E, Greger B, House PA, Aranda I, Botella C, Albusua J, ... Normann RA (2014) Acute Human Brain Responses to Intracortical Microelectrode Arrays: Challenges and Future Prospects. *Front Neuroeng*, 7: 24.
- Fiebelkorn IC, Pinsk MA, & Kastner S (2019) The Mediodorsal Pulvinar Coordinates the Macaque Fronto-Parietal Network During Rhythmic Spatial Attention. *Nat Commun*, 10: 215.
- Field A (2013) *Discovering Statistics Using IBM SPSS Statistics*. London: SAGE.
- Fiorani M, Azzi JCB, Soares JGM, & Gattass R (2014) Automatic Mapping of Visual Cortex Receptive Fields: A Fast and Precise Algorithm. *J Neurosci Methods*, 221: 112–126.
- Fischer B, Schander A, Kreiter AK, Lang W, & Wegener D (2019) Visual Epidural Field Potentials Possess High Functional Specificity in Single Trials. *J Neurophysiol*, 122(4): 1634–1648.
- Fischer B, & Wegener D (2018) Emphasizing the “Positive” in Positive Reinforcement: Using Nonbinary Rewarding for Training Monkeys on Cognitive Tasks. *J Neurophysiol*, 120(1): 115–128.
- Fiser J, Chiu C, & Weliky M (2004) Small Modulation of Ongoing Cortical Dynamics by Sensory Input During Natural Vision. *Nature*, 431(7008): 573–578.
- Flint RD, Lindberg EW, Jordan LR, Miller LE, & Slutzky MW (2012) Accurate Decoding of Reaching Movements From Field Potentials in the Absence of Spikes. *J Neural Eng*, 9(4): 046006.
- Flint RD, Rosenow JM, Tate MC, & Slutzky MW (2017) Continuous Decoding of Human Grasp Kinematics Using Epidural and Subdural Signals. *J Neural Eng*, 14(1): 016005.

11. References

- Flint RD, Scheid MR, Wright ZA, Solla SA, & Slutzky MW (2016) Long-Term Stability of Motor Cortical Activity: Implications for Brain Machine Interfaces and Optimal Feedback Control. *J Neurosci*, 36(12): 3623–3632.
- Forti A, Ambrosetto G, Amore M, De Maria R, Michelucci R, Omicini E, ... Tassinari CA (1982) Locked-In Syndrome in Multiple Sclerosis With Sparing of the Ventral Portion of the Pons. *Ann Neurol*, 12(4): 393–394.
- Fox MD, & Raichle ME (2007) Spontaneous Fluctuations in Brain Activity Observed With Functional Magnetic Resonance Imaging. *Nat Rev Neurosci*, 8(9): 700–711.
- Foxe JJ, & Simpson G V (2002) Flow of Activation From V1 to Frontal Cortex in Humans. A Framework for Defining “Early” Visual Processing. *Exp Brain Res*, 142(1): 139–150.
- Friedman HS, Zhou H, & Von Der Heydt R (2003) The Coding of Uniform Colour Figures in Monkey Visual Cortex. *J Physiol*, 548(2): 593–613.
- Fukushima M, Chao ZC, & Fujii N (2015) Studying Brain Functions With Mesoscopic Measurements: Advances in Electro-corticography for Non-Human Primates. *Curr Opin Neurobiol*, 32: 124–131.
- Fukushima M, Saunders RC, Mullarkey M, Doyle AM, Mishkin M, & Fujii N (2014) An Electro-corticographic Electrode Array for Simultaneous Recording From Medial, Lateral, and Intrasulcal Surface of the Cortex in Macaque Monkeys. *J Neurosci Methods*, 233: 155–165.
- Gaffan D, Easton A, & Parker A (2002) Interaction of Inferior Temporal Cortex With Frontal Cortex and Basal Forebrain: Double Dissociation in Strategy Implementation and Associative Learning. *J Neurosci*, 22(16): 7288–7296.
- Galashan FO, Rempel HC, Meyer A, Gruber-Dujardin E, Kreiter AK, & Wegener D (2011) A New Type of Recording Chamber With an Easy-To-Exchange Microdrive Array for Chronic Recordings in Macaque Monkeys. *J Neurophysiol*, 105(6): 3092–3105.
- Galashan FO, Saßen HC, Kreiter AK, & Wegener D (2013) Monkey Area MT Latencies to Speed Changes Depend on Attention and Correlate With Behavioral Reaction Times. *Neuron*, 78(4): 740–750.
- Gallegos-Alaya G, Furdea A, Takano K, Ruf CA, Flor H, & Birbaumer N (2014) Brain Communication in a Completely Locked-In Patient Using Bedside Near-Infrared Spectroscopy. *Neurology*, 82(21): 1930–1932.
- Gandhi SP, Heeger DJ, & Boynton GM (1999) Spatial Attention Affects Brain Activity in Human Primary Visual Cortex. *Proc Natl Acad Sci U S A*, 96(6): 3314–3319.
- Ganzini L, & Block S (2002) Physician-Assisted Death – A Last Resort? *N Engl J Med*, 346(21): 1663–1665.
- Gao S, Wang Y, Gao X, & Hong B (2014) Visual and Auditory Brain-Computer Interfaces. *IEEE Trans Biomed Eng*, 61(5): 1436–1447.
- Garrett DD, Samanez-Larkin GR, MacDonald SWS, Lindenberger U, McIntosh AR, & Grady CL (2013) Moment-To-Moment Brain Signal Variability: A Next Frontier in Human Brain Mapping? *Neurosci Biobehav Rev*, 37(4): 610–624.
- Gawne TJ, Kjaer TW, & Richmond BJ (1996) Latency: Another Potential Code for Feature Binding in Striate Cortex. *J Neurophysiol*, 76(2): 1356–1360.
- Gawne TJ, & Martin JM (2002) Responses of Primate Visual Cortical Neurons to Stimuli Presented by Flash, Saccade, Blink, and External Darkening. *J Neurophysiol*, 88(5): 2178–2186.
- Gebodh N, Vanegas MI, & Kelly SP (2017) Effects of Stimulus Size and Contrast on the Initial Primary Visual Cortical Response in Humans. *Brain Topogr*, 30(4): 450–460.
- Geisler WS, Albrecht DG, & Crane AM (2007) Responses of Neurons in Primary Visual Cortex to Transient Changes in Local Contrast and Luminance. *J Neurosci*, 27(19): 5063–5067.
- Gharabaghi A, Naros G, Khademi F, Jesser J, Spüler M, Walter A, ... Birbaumer N (2014a) Learned Self-Regulation of the Lesioned Brain With Epidural Electro-corticography. *Front Behav Neurosci*, 8: 429.

11. References

- Gharabaghi A, Naros G, Walter A, Grimm F, Schuermeyer M, Roth A, ... Birbaumer N (2014b) From Assistance Towards Restoration With Epidural Brain-Computer Interfacing. *Restor Neurol Neurosci*, 32(4): 517–525.
- Gieselmann MA, & Thiele A (2008) Comparison of Spatial Integration and Surround Suppression Characteristics in Spiking Activity and the Local Field Potential in Macaque V1. *Eur J Neurosci*, 28(3): 447–459.
- Gilbert CD, & Li W (2013) Top-Down Influences on Visual Processing. *Nat Rev Neurosci*, 14(5): 350–363.
- Goldberg ME, & Wurtz RH (1972) Activity of Superior Colliculus in Behaving Monkey. II. Effect of Attention on Neuronal Responses. *J Neurophysiol*, 35(4): 560–574.
- Gomez-Rodriguez M, Grosse-Wentrup M, Peters J, Naros G, Hill J, Schölkopf B, & Gharabaghi A (2010) Epidural ECoG Online Decoding of Arm Movement Intention in Hemiparesis. *2010 First Work Brain Decod Pattern Recognit Challenges Neuroimaging*, 36–39.
- Goodale MA, & Milner AD (1992) Separate Visual Pathways for Perception and Action. *Trends Neurosci*, 15(1): 20–25.
- Gottlieb J (2007) From Thought to Action: The Parietal Cortex as a Bridge Between Perception, Action, and Cognition. *Neuron*, 53(1): 9–16.
- Gouras P (1968) Identification of Cone Mechanisms in Monkey Ganglion Cells. *J Physiol*, 199(3): 533–547.
- Gouws AD, Alvarez I, Watson DM, Uesaki M, Rogers J, & Morland AB (2014) On the Role of Suppression in Spatial Attention: Evidence From Negative BOLD in Human Subcortical and Cortical Structures. *J Neurosci*, 34(31): 10347–10360.
- Graimann B, Townsend G, Huggins JE, Levine SP, & Pfurtscheller G (2005) A Comparison Between Using ECoG and EEG for Direct Brain Communication. *Conf IFMBS Proceedings, Eur Med Biol Eng Conf*, 11.
- Grech R, Cassar T, Muscat J, Camilleri KP, Fabri SG, Zervakis M, ... Vanrumste B (2008) Review on Solving the Inverse Problem in EEG Source Analysis. *J Neuroeng Rehabil*, 5: 25.
- Green JJ, Boehler CN, Roberts KC, Chen L-C, Krebs RM, Song AW, & Woldorff MG (2017) Cortical and Subcortical Coordination of Visual Spatial Attention Revealed by Simultaneous EEG-fMRI Recording. *J Neurosci*, 37(33): 7803–7810.
- Grill WM, Norman SE, & Bellamkonda R V (2009) Implanted Neural Interfaces: Biochallenges and Engineered Solutions. *Annu Rev Biomed Eng*, 11(1): 1–24.
- Groppe DM, Bickel S, Keller CJ, Jain SK, Hwang ST, Harden C, & Mehta AD (2013) Dominant Frequencies of Resting Human Brain Activity as Measured by the Electrocorticogram. *Neuroimage*, 79: 223–233.
- Grothe I, Neitzel SD, Mandon S, & Kreiter AK (2012) Switching Neuronal Inputs by Differential Modulations of Gamma-Band Phase-Coherence. *J Neurosci*, 32(46): 16172–16180.
- Groves PM, & Eason RG (1969) Effects of Attention and Activation on the Visual Evoked Cortical Potential and Reaction Time. *Psychophysiology*, 5(4): 394–398.
- Grunewald A, & Skoumbourdis EK (2004) The Integration of Multiple Stimulus Features by V1 Neurons. *J Neurosci*, 24(41): 9185–9194.
- Guger C, Spataro R, Allison BZ, Heilinger A, Ortner R, Cho W, & La Bella V (2017) Complete Locked-In and Locked-In Patients: Command Following Assessment and Communication With Vibro-Tactile P300 and Motor Imagery Brain-Computer Interface Tools. *Front Neurosci*, 11: 251.
- Gunduz A, Brunner P, Daitch A, Leuthardt EC, Ritaccio AL, Pesaran B, & Schalk G (2012) Decoding Covert Spatial Attention Using Electrocorticographic (ECoG) Signals in Humans. *Neuroimage*, 60(4): 2285–2293.
- Gutierrez C, Cola MG, Seltzer B, & Cusick C (2000) Neurochemical and Connectional Organization of the Dorsal Pulvinar Complex in Monkeys. *J Comp Neurol*, 419(1): 61–86.

11. References

- Haenny PE, & Schiller PH (1988) State Dependent Activity in Monkey Visual Cortex. I. Single Cell Activity in V1 and V4 on Visual Tasks. *Exp Brain Res*, 69(2): 225–244.
- Hafed ZM, Lovejoy LP, & Krauzlis RJ (2011) Modulation of Microsaccades in Monkey During a Covert Visual Attention Task. *J Neurosci*, 31(43): 15219–15230.
- Hahn B, Ross TJ, & Stein EA (2006) Neuroanatomical Dissociation Between Bottom-Up and Top-Down Processes of Visuospatial Selective Attention. *Neuroimage*, 32(2): 842–853.
- Hallez H, Vanrumste B, Grech R, Muscat J, De Clercq W, Vergult A, ... Lemahieu I (2007) Review on Solving the Forward Problem in EEG Source Analysis. *J Neuroeng Rehabil*, 4: 46.
- Handy TC, Kingstone A, & Mangun GR (1996) Spatial Distribution of Visual Attention: Perceptual Sensitivity and Response Latency. *Percept Psychophys*, 58(4): 613–627.
- Hartwell RC, & Cowan JD (1994) Covariability of Visually Evoked Potentials and Simple Motor Reaction Times. *Electroencephalogr Clin Neurophysiol*, 92(6): 487–490.
- Hayashi H, & Kato S (1989) Total Manifestations of Amyotrophic Lateral Sclerosis. ALS in the Totally Locked-In State. *J Neurol Sci*, 93(1): 19–35.
- Hays WL (1963) *Statistics for Psychologists*. New York: Holt, Rinehart, and Winston.
- Heathcote A, Popiel SJ, & Mewhort DJK (1991) Analysis of Response Time Distributions: An Example Using the Stroop Task. *Psychol Bull*, 109(2): 340–347.
- Hembrook-Short JR, Mock VL, & Briggs F (2017) Attentional Modulation of Neuronal Activity Depends on Neuronal Feature Selectivity. *Curr Biol*, 27(13): 1878–1887.E5.
- Henderickson AE, Wilson JR, & Ogren MP (1978) The Neuroanatomical Organization of Pathways Between the Dorsal Lateral Geniculate Nucleus and Visual Cortex in Old World and New World Primates. *J Comp Neurol*, 182(1): 123–136.
- Hendry SH, & Reid RC (2000) The Koniocellular Pathway in Primate Vision. *Annu Rev Neurosci*, 23(1): 127–153.
- Hendry SH, & Yoshioka T (1994) A Neurochemically Distinct Third Channel in the Macaque Dorsal Lateral Geniculate Nucleus. *Science*, 264(5158): 575–577.
- Henle C, Raab M, Cordeiro JG, Doostkam S, Schulze-Bonhage A, Stieglitz T, & Rickert J (2011) First Long Term in Vivo Study on Subdurally Implanted Micro-ECoG Electrodes, Manufactured With a Novel Laser Technology. *Biomed Microdevices*, 13(1): 59–68.
- Hermes D, Miller KJ, Wandell BA, & Winawer J (2015) Stimulus Dependence of Gamma Oscillations in Human Visual Cortex. *Cereb Cortex*, 25(9): 2951–2959.
- Hermiz J, Rogers N, Kaestner E, Ganji M, Cleary DR, Carter BS, ... Gilja V (2018) Sub-Millimeter ECoG Pitch in Human Enables Higher Fidelity Cognitive Neural State Estimation. *Neuroimage*, 176: 454–464.
- Herrington TM, & Assad JA (2009) Neural Activity in the Middle Temporal Area and Lateral Intraparietal Area During Endogenously Cued Shifts of Attention. *J Neurosci*, 29(45): 14160–14176.
- Hill NJ, Gupta D, Brunner P, Gunduz A, Adamo MA, Ritaccio A, & Schalk G (2012) Recording Human Electrocorticographic (ECoG) Signals for Neuroscientific Research and Real-Time Functional Cortical Mapping. *J Vis Exp*, (64): e3993.
- Hill NJ, Lal TN, Schröder M, Hinterberger T, Wilhelm B, Nijboer F, ... Birbaumer N (2006) Classifying EEG and ECoG Signals Without Subject Training for Fast BCI Implementation: Comparison of Nonparalyzed and Completely Paralyzed Subjects. *IEEE Trans Neural Syst Rehabil Eng*, 14(2): 183–186.
- Hinterberger T, Widman G, Lal TN, Hill J, Tangermann M, Rosenstiel W, ... Birbaumer N (2008) Voluntary Brain Regulation and Communication With Electrocorticogram Signals. *Epilepsy Behav*, 13(2): 300–306.

11. References

- Hochberg LR, Bacher D, Jarosiewicz B, Masse NY, Simeral JD, Vogel J, ... Donoghue JP (2012) Reach and Grasp by People With Tetraplegia Using a Neurally Controlled Robotic Arm. *Nature*, 485(7398): 372–375.
- Hollingsworth A, Maxcey-Richard AM, & Vecera SP (2012) The Spatial Distribution of Attention Within and Across Objects. *J Exp Psychol Hum Percept Perform*, 38(1): 135–151.
- Hopf J-M, Boehler CN, Luck SJ, Tsotsos JK, Heinze H-J, & Schoenfeld MA (2006) Direct Neurophysiological Evidence for Spatial Suppression Surrounding the Focus of Attention in Vision. *Proc Natl Acad Sci U S A*, 103(4): 1053–1058.
- Horton JC, & Adams DL (2005) The Cortical Column: A Structure Without a Function. *Philos Trans R Soc B Biol Sci*, 360(1456): 837–862.
- Horton JC, & Hoyt WF (1991) The Representation of the Visual Field in Human Striate Cortex: A Revision of the Classic Holmes Map. *Arch Ophthalmol*, 109(6): 816–824.
- Hosokawa T, & Watanabe M (2012) Prefrontal Neurons Represent Winning and Losing During Competitive Video Shooting Games Between Monkeys. *J Neurosci*, 32(22): 7662–7671.
- Hosseini M-P, Pompili D, Elisevich K, & Soltanian-Zadeh H (2017) Optimized Deep Learning for EEG Big Data and Seizure Prediction BCI via Internet of Things. *IEEE Trans Big Data*, 3(4): 392–404.
- Hu K, Jamali M, Moses ZB, Ortega CA, Friedman GN, Xu W, & Williams ZM (2018) Decoding Unconstrained Arm Movements in Primates Using High-Density Electrocorticography Signals for Brain-Machine Interface Use. *Sci Rep*, 8: 10583.
- Huang X, & Paradiso MA (2008) V1 Response Timing and Surface Filling-In. *J Neurophysiol*, 100(1): 539–547.
- Hubel DH, & Wiesel TN (1961) Integrative Action in the Cat's Lateral Geniculate Body. *J Physiol*, 155(2): 385–398.
- Hubel DH, & Wiesel TN (1962) Receptive Fields, Binocular Interaction and Functional Architecture in the Cat's Visual Cortex. *J Physiol*, 160: 106–154.
- Hubel DH, & Wiesel TN (1968) Receptive Fields and Functional Architecture of Monkey Striate Cortex. *J Physiol*, 195(1): 215–243.
- Hubel DH, & Wiesel TN (1972) Laminar and Columnar Distribution of Geniculate-Cortical Fibers in the Macaque Monkey. *J Comp Neurol*, 146(4): 421–450.
- Hubel DH, & Wiesel TN (1974a) Sequence Regularity and Geometry of Orientation Columns in the Monkey Striate Cortex. *J Comp Neurol*, 158(3): 267–293.
- Hubel DH, & Wiesel TN (1974b) Uniformity of Monkey Striate Cortex: A Parallel Relationship Between Field Size, Scatter, and Magnification Factor. *J Comp Neurol*, 158(3): 295–305.
- Hubel DH, & Wiesel TN (1977) Ferrier Lecture. Functional Architecture of Macaque Monkey Visual Cortex. *Proc R Soc Lond B Biol Sci*, 198(1130): 1–59.
- Hubel DH, Wiesel TN, & LeVay S (1977) Plasticity of Ocular Dominance Columns in Monkey Striate Cortex. *Philos Trans R Soc Lond B Biol Sci*, 278(961): 377–409.
- Huggins JE, Wren PA, & Gruis KL (2011) What Would Brain-Computer Interface Users Want? Opinions and Priorities of Potential Users With Amyotrophic Lateral Sclerosis. *Amyotrophic Lateral Scler*, 12(5): 318–324.
- Hwang H-J, Ferreria VY, Ulrich D, Kilic T, Chatziliadis X, Blankertz B, & Treder M (2015) A Gaze Independent Brain-Computer Interface Based on Visual Stimulation Through Closed Eyelids. *Sci Rep*, 5: 15890.
- Hwang H-J, Kim S, Choi S, & Im C-H (2013) EEG-Based Brain-Computer Interfaces: A Thorough Literature Survey. *Int J Hum Comput Interact*, 29(12): 814–826.
- Ibos G, & Freedman DJ (2016) Interaction Between Spatial and Feature Attention in Posterior Parietal Cortex. *Neuron*, 91(4): 931–943.

11. References

- Im C, & Seo J-M (2016) A Review of Electrodes for the Electrical Brain Signal Recording. *Biomed Eng Lett*, 6: 104–112.
- Inoue M, & Mikami A (2006) Prefrontal Activity During Serial Probe Reproduction Task: Encoding, Mnemonic, and Retrieval Processes. *J Neurophysiol*, 95(2): 1008–1041.
- Ito M, & Gilbert CD (1999) Attention Modulates Contextual Influences in the Primary Visual Cortex of Alert Monkeys. *Neuron*, 22(3): 593–604.
- Jacobs GH (2008) Primate Color Vision: A Comparative Perspective. *Vis Neurosci*, 25(5–6): 619–633.
- Jarosiewicz B, Sarma AA, Bacher D, Masse NY, Simeral JD, Sorice B, ... Hochberg LR (2015) Virtual Typing by People With Tetraplegia Using a Self-Calibrating Intracortical Brain-Computer Interface. *Sci Transl Med*, 7(313): 313ra179.
- Jayakar P, Gotman J, Harvey AS, Palmieri A, Tassi L, Schomer D, ... Kahane P (2016) Diagnostic Utility of Invasive EEG for Epilepsy Surgery: Indications, Modalities, and Techniques. *Epilepsia*, 57(11): 1735–1747.
- Jeffreys DA, & Axford JG (1972) Source Locations of Pattern-Specific Components of Human Visual Evoked Potentials. I. Component of Striate Cortical Origin. *Exp Brain Res*, 16(1): 1–21.
- Jeffries AM, Killian NJ, & Pezaris JS (2014) Mapping the Primate Lateral Geniculate Nucleus: A Review of Experiments and Methods. *J Physiol Paris*, 108(1): 3–10.
- Jia X, Xing D, & Kohn A (2013) No Consistent Relationship Between Gamma Power and Peak Frequency in Macaque Primary Visual Cortex. *J Neurosci*, 33(1): 17–25.
- Johannes S, Münte TF, Heinze HJ, & Mangun GR (1995) Luminance and Spatial Attention Effects on Early Visual Processing. *Cogn Brain Res*, 2(3): 189–205.
- John SE, Opie NL, Wong YT, Rind GS, Ronayne SM, Gerboni G, ... Oxley TJ (2018) Signal Quality of Simultaneously Recorded Endovascular, Subdural and Epidural Signals Are Comparable. *Sci Rep*, 8: 8427.
- Johnson EN, Hawken MJ, & Shapley R (2008) The Orientation Selectivity of Color-Responsive Neurons in Macaque V1. *J Neurosci*, 28(32): 8096–8106.
- Jones R, & Keck MJ (1978) Visual Evoked Response as a Function of Grating Spatial Frequency. *Investig Ophthalmol Vis Sci*, 17(7): 652–659.
- Kaas JH, Guillery RW, & Allman JM (1972) Some Principles of Organization in the Dorsal Lateral Geniculate Nucleus. *Brain Behav Evol*, 6(1): 253–299.
- Kaas JH, & Lyon DC (2007) Pulvinar Contributions to the Dorsal and Ventral Streams of Visual Processing in Primates. *Brain Res Rev*, 55(2): 285–296.
- Kaiju T, Doi K, Yokota M, Watanabe K, Inoue M, Ando H, ... Suzuki T (2017) High Spatiotemporal Resolution ECoG Recording of Somatosensory Evoked Potentials With Flexible Micro-Electrode Arrays. *Front Neural Circuits*, 11: 20.
- Kammer T, Lehr L, & Kirschfeld K (1999) Cortical Visual Processing Is Temporally Dispersed by Luminance in Human Subjects. *Neurosci Lett*, 263(2–3): 133–136.
- Kapeller C, Kamada K, Ogawa H, Prueckl R, Scharinger J, & Guger C (2014) An Electrographic BCI Using Code-Based VEP for Control in Video Applications: A Single-Subject Study. *Front Syst Neurosci*, 8: 139.
- Kapeller C, Ogawa H, Schalk G, Kunii N, Coon WG, Scharinger J, ... Kamada K (2018) Real-Time Detection and Discrimination of Visual Perception Using Electrographic Signals. *J Neural Eng*, 15(3): 036001.
- Kaplan E, & Shapley RM (1986) The Primate Retina Contains Two Types of Ganglion Cells, With High and Low Contrast Sensitivity. *Proc Natl Acad Sci U S A*, 83(8): 2755–2757.
- Käthner I, Kübler A, & Halder S (2015) Rapid P300 Brain-Computer Interface Communication With a Head-Mounted Display. *Front Neurosci*, 9: 207.

11. References

- Katsuki F, & Constantinidis C (2014) Bottom-Up and Top-Down Attention: Different Processes and Overlapping Neural Systems. *Neurosci*, 20(5): 509–521.
- Katzner S, Nauhaus I, Benucci A, Bonin V, Ringach DL, & Carandini M (2009) Local Origin of Field Potentials in Visual Cortex. *Neuron*, 61(1): 35–41.
- Kaufmann T, Holz EM, & Kübler A (2013) Comparison of Tactile, Auditory, and Visual Modality for Brain-Computer Interface Use: A Case Study With a Patient in the Locked-In State. *Front Neurosci*, 7: 129.
- Kellis S, Sorensen L, Darvas F, Sayres C, O’Neill III K, Brown RB, ... Greger B (2016) Multi-Scale Analysis of Neural Activity in Humans: Implications for Micro-Scale Electrocoricography. *Clin Neurophysiol*, 127(1): 591–601.
- Kelly SP, Gomez-Ramirez M, & Foxe JJ (2008) Spatial Attention Modulates Initial Afferent Activity in Human Primary Visual Cortex. *Cereb Cortex*, 18(11): 2629–2636.
- Khodagholy D, Gelineas JN, Thesen T, Doyle W, Devinsky O, Malliaras GG, & Buzsáki G (2015) NeuroGrid: Recording Action Potentials From the Surface of the Brain. *Nat Neurosci*, 18(2): 310–315.
- Kiesel A, Miller J, Jolicœur P, & Brisson B (2008) Measurement of ERP Latency Differences: A Comparison of Single-Participant and Jackknife-Based Scoring Methods. *Psychophysiology*, 45(2): 250–274.
- Kincade JM, Abrams RA, Astafiev S V, Shulman GL, & Corbetta M (2005) An Event-Related Functional Magnetic Resonance Imaging Study of Voluntary and Stimulus-Driven Orienting of Attention. *J Neurosci*, 25(18): 4593–4604.
- Kinoshita M, & Komatsu H (2001) Neural Representation of the Luminance and Brightness of a Uniform Surface in the Macaque Primary Visual Cortex. *J Neurophysiol*, 86(5): 2559–2570.
- Koch C, & Ullman S (1985) Shifts in Selective Visual Attention: Towards the Underlying Neural Circuitry. *Hum Neurobiol*, 4(4): 219–227.
- Kovac S, Vakharia VN, Scott C, & Diehl B (2017) Invasive Epilepsy Surgery Evaluation. *Seizure*, 44: 125–136.
- Kraut MA, Arezzo JC, & Vaughan Jr HG (1985) Intracortical Generators of the Flash VEP in Monkeys. *Electroencephalogr Clin Neurophysiol*, 62(4): 300–312.
- Kravitz DJ, & Behrmann M (2011) Space-, Object-, and Feature-Based Attention Interact to Organize Visual Scenes. *Atten Percept Psychophys*, 73(8): 2434–2447.
- Krüger J, Caruana F, Dalla Volta R, & Rizzolatti G (2010) Seven Years of Recording From Monkey Cortex With a Chronically Implanted Multiple Microelectrode. *Front Neuroeng*, 3: 6.
- Krusienski DJ, Grosse-Wentrup M, Galán F, Coyle D, Miller KJ, Forney E, & Anderson CW (2011) Critical Issues in State-Of-The-Art Brain-Computer Interface Signal Processing. *J Neural Eng*, 8(2): 025002.
- Kubaneck J, & Snyder LH (2015) Reward-Based Decision Signals in Parietal Cortex Are Partially Embodied. *J Neurosci*, 35(12): 4869–4881.
- Kübler A, & Birbaumer N (2008) Brain-Computer Interfaces and Communication in Paralysis: Extinction of Goal Directed Thinking in Completely Paralyzed Patients? *Clin Neurophysiol*, 119(11): 2658–2666.
- Lakens D (2013) Calculating and Reporting Effect Sizes to Facilitate Cumulative Science: A Practical Primer for t-Tests and ANOVAs. *Front Psychol*, 4: 863.
- Landisman CE, & Ts’o DY (2002) Color Processing in Macaque Striate Cortex: Relationships to Ocular Dominance, Cytochrome Oxidase, and Orientation. *J Neurophysiol*, 87(6): 3126–3137.
- Lashgari R, Li X, Chen Y, Kremkow J, Bereshpolova Y, Swadlow HA, & Alonso J-M (2012) Response Properties of Local Field Potentials and Neighboring Single Neurons in Awake Primary Visual Cortex. *J Neurosci*, 32(33): 11396–11413.
- Laule GE, Bloomsmith MA, & Schapiro SJ (2003) The Use of Positive Reinforcement Training Techniques to Enhance the Care, Management, and Welfare of Primates in the Laboratory. *J Appl Anim Welf Sci*, 6(3): 163–173.

11. References

- Laureys S, Pellas F, Van Eeckhout P, Ghorbel S, Schnakers C, Perrin F, ... Goldman S (2005) The Locked-In Syndrome: What Is It Like to Be Conscious but Paralyzed and Voiceless? *Prog Brain Res*, 150: 495–511.
- Lebedev MA, & Nicolelis MAL (2017) Brain-Machine Interfaces: From Basic Science to Neuroprostheses and Neurorehabilitation. *Physiol Rev*, 97(2): 767–837.
- Lee BB (1996) Receptive Field Structure in the Primate Retina. *Vision Res*, 36(5): 631–644.
- Lee J, Choi H, Lee S, Cho BH, Ahn K-H, Kim IY, ... Jang D-P (2017) Decoding Saccadic Directions Using Epidural ECoG in Non-Human Primates. *J Korean Med Sci*, 32(8): 1243–1250.
- Lee S, Park J, & Smirnakis SM (2019) Internal Gain Modulations, but Not Changes in Stimulus Contrast, Preserve the Neural Code. *J Neurosci*, 39(9): 1671–1687.
- Lee ST, Mumford D, Romero R, & Lamme VAF (1998) The Role of the Primary Visual Cortex in Higher Level Vision. *Vision Res*, 38(15–16): 2429–2454.
- Lee TS, Yang CF, Romero RD, & Mumford D (2002) Neural Activity in Early Visual Cortex Reflects Behavioral Experience and Higher-Order Perceptual Saliency. *Nat Neurosci*, 5(6): 589–597.
- Lemon RN, & Porter R (1976) Afferent Input to Movement-Related Precentral Neurones in Conscious Monkeys. *Proc R Soc Lond B Biol Sci*, 194(1116): 313–339.
- Lennert T, & Martinez-Trujillo J (2011) Strength of Response Suppression to Distracter Stimuli Determines Attentional-Filtering Performance in Primate Prefrontal Neurons. *Neuron*, 70(1): 141–152.
- Leon MI, & Shadlen MN (1999) Effect of Expected Reward Magnitude on the Response of Neurons in the Dorsolateral Prefrontal Cortex of the Macaque. *Neuron*, 24(2): 415–425.
- Lesenfants D, Habbal D, Lugo Z, Lebeau M, Horki P, Amico E, ... Noirhomme Q (2014) An Independent SSVEP-Based Brain-Computer Interface in Locked-In Syndrome. *J Neural Eng*, 11(3): 035002.
- Lesser RP, & Arroyo S (2005) Subdural Electrodes. In: E. Niedermeyer & F. Lopes Da Silva (Eds.), *Electroencephalography: Basic Principles, Clinical Applications, and Related Fields*. Baltimore: MD: Lippincott Williams & Wilkens.
- Lesser RP, Crone NE, & Webber WRS (2010) Subdural Electrodes. *Clin Neurophysiol*, 121(9): 1376–1392.
- Leuthardt EC, Schalk G, Wolpaw JR, Ojemann JG, & Moran DW (2004) A Brain-Computer Interface Using Electrocorticographic Signals in Humans. *J Neural Eng*, 1(2): 63–71.
- LeVay S, Connolly M, Houde J, & Van Essen DC (1985) The Complete Pattern of Ocular Dominance Stripes in the Striate Cortex and Visual Field of the Macaque Monkey. *J Neurosci*, 5(2): 486–501.
- LeVay S, Hubel DH, & Wiesel TN (1975) The Pattern of Ocular Dominance Columns in Macaque Visual Cortex Revealed by a Reduced Silver Stain. *J Comp Neurol*, 159(4): 559–576.
- Lewicki MS (1998) A Review of Methods for Spike Sorting: The Detection and Classification of Neural Action Potentials. *Network*, 9(4): R53–R78.
- Lewis CM, Bosman CA, & Fries P (2015) Recording of Brain Activity Across Spatial Scales. *Curr Opin Neurobiol*, 32: 68–77.
- Li W, Piëch V, & Gilbert CD (2008) Learning to Link Visual Contours. *Neuron*, 57(3): 442–451.
- Li Y, Bahn S, Nam CS, & Lee J (2014) Effects of Luminosity Contrast and Stimulus Duration on User Performance and Preference in a P300-Based Brain-Computer Interface. *Int J Hum Comput Interact*, 30(2): 151–163.
- Li Y, Zhang S, Jin Y, Cai B, Controzzi M, Zhu J, ... Zheng X (2017) Gesture Decoding Using ECoG Signals From Human Sensorimotor Cortex: A Pilot Study. *Behav Neurol*, 2017: 3435686.

11. References

- Lin Z, Zhang C, Zeng Y, Tong L, & Yan B (2018) A Novel P300 BCI Speller Based on the Triple RSVP Paradigm. *Sci Rep*, 8: 3350.
- Liu Y, Zhou Z, & Hu D (2011) Gaze Independent Brain-Computer Speller With Covert Visual Search Tasks. *Clin Neurophysiol*, 122(6): 1127–1136.
- Livingstone M, & Hubel D (1988) Segregation of Form, Color, Movement, and Depth: Anatomy, Physiology, and Perception. *Science*, 240(4853): 740–749.
- Livingstone MS, & Hubel DH (1984) Anatomy and Physiology of a Color System in the Primate Visual Cortex. *J Neurosci*, 4(1): 309–356.
- Logothetis NK (2003) The Underpinnings of the BOLD Functional Magnetic Resonance Imaging Signal. *J Neurosci*, 23(10): 3963–3971.
- Lu HD, Chen G, Tanigawa H, & Roe AW (2010) A Motion Direction Map in Macaque V2. *Neuron*, 68(5): 1002–1013.
- Luck SJ, Chelazzi L, Hillyard SA, & Desimone R (1997) Neural Mechanisms of Spatial Selective Attention in Areas V1, V2, and V4 of Macaque Visual Cortex. *J Neurophysiol*, 77(1): 24–42.
- Lulé D, Zickler C, Häcker S, Bruno MA, Demertzi A, Pellas F, ... Kübler A (2009) Life Can Be Worth Living in Locked-In Syndrome. *Prog Brain Res*, 177: 339–351.
- Lund JS (1988) Anatomical Organization of Macaque Monkey Striate Visual Cortex. *Annu Rev Neurosci*, 11(1): 253–288.
- Mangun GR, & Hillyard SA (1988) Spatial Gradients of Visual Attention: Behavioral and Electrophysiological Evidence. *Electroencephalogr Clin Neurophysiol*, 70(5): 417–428.
- Marathe AR, & Taylor DM (2013) Decoding Continuous Limb Movements From High-Density Epidural Electrode Arrays Using Custom Spatial Filters. *J Neural Eng*, 10(3): 036015.
- Marchesotti S, Bassolino M, Serino A, Bleuler H, & Blanke O (2016) Quantifying the Role of Motor Imagery in Brain-Machine Interfaces. *Sci Rep*, 6: 24076.
- Marchetti M, Piccione F, Silvoni S, Gamberini L, & Priftis K (2013) Covert Visuospatial Attention Orienting in a Brain-Computer Interface for Amyotrophic Lateral Sclerosis Patients. *Neurorehabil Neural Repair*, 27(5): 430–438.
- Marchetti M, Piccione F, Silvoni S, & Priftis K (2012) Exogenous and Endogenous Orienting of Visuospatial Attention in P300-Guided Brain Computer Interfaces: A Pilot Study on Healthy Participants. *Clin Neurophysiol*, 123(4): 774–779.
- Martens S, Bensch M, Halder S, Hill J, Nijboer F, Ramos-Murguialday A, ... Gharabaghi A (2014) Epidural Electrocorticography for Monitoring of Arousal in Locked-In State. *Front Hum Neurosci*, 8: 861.
- Martin AB, Yang X, Saalman YB, Wang L, Shestyuk A, Lin JJ, ... Kastner S (2019) Temporal Dynamics and Response Modulation Across the Human Visual System in a Spatial Attention Task: An ECoG Study. *J Neurosci*, 39(2): 333–352.
- Martin S, Iturrate I, Millán J del R, Knight RT, & Pasley BN (2018) Decoding Inner Speech Using Electrocorticography: Progress and Challenges Toward a Speech Prosthesis. *Front Neurosci*, 12: 422.
- Matsuo T, Kawasaki K, Osada T, Sawahata H, Suzuki T, Shibata M, ... Hasegawa I (2011) Intracal Electroencephalography in Macaque Monkeys With Minimally Invasive Neurosurgical Protocols. *Front Syst Neurosci*, 5: 34.
- Matsushima A, & Tanaka M (2014) Differential Neuronal Representation of Spatial Attention Dependent on Relative Target Locations During Multiple Object Tracking. *J Neurosci*, 34(30): 9963–9969.
- Maunsell JHR, & Gibson JR (1992) Visual Response Latencies in Striate Cortex of the Macaque Monkey. *J Neurophysiol*, 68(4): 1332–1344.
- Maunsell JHR, & Treue S (2006) Feature-Based Attention in Visual Cortex. *Trends Neurosci*, 29(6): 317–322.

11. References

- Mazer JA, Vinje WE, McDermott J, Schiller PH, & Gallant JL (2002) Spatial Frequency and Orientation Tuning Dynamics in Area V1. *Proc Natl Acad Sci U S A*, 99(3): 1645–1650.
- McAdams CJ, & Maunsell JHR (1999) Effects of Attention on Orientation-Tuning Functions of Single Neurons in Macaque Cortical Area V4. *J Neurosci*, 19(1): 431–441.
- McAdams CJ, & Reid RC (2005) Attention Modulates the Responses of Simple Cells in Monkey Primary Visual Cortex. *J Neurosci*, 25(47): 11023–11033.
- McAlonan K, Cavanaugh J, & Wurtz RH (2008) Guarding the Gateway to Cortex With Attention in Visual Thalamus. *Nature*, 456(7220): 391–394.
- McMains S, & Kastner S (2011) Interactions of Top-Down and Bottom-Up Mechanisms in Human Visual Cortex. *J Neurosci*, 31(2): 587–597.
- Mehta AD, Ulbert I, & Schroeder CE (2000) Intermodal Selective Attention in Monkeys. I: Distribution and Timing of Effects Across Visual Areas. *Cereb Cortex*, 10(4): 343–358.
- Merigan WH, & Maunsell JHR (1993) How Parallel Are the Primate Visual Pathways? *Annu Rev Neurosci*, 16(1): 369–402.
- Michael CR (1988) Retinal Afferent Arborization Patterns, Dendritic Field Orientations, and the Segregation of Function in the Lateral Geniculate Nucleus of the Monkey. *Proc Natl Acad Sci U S A*, 85(13): 4914–4918.
- Michel CM, Murray MM, Lantz G, Gonzalez S, Spinelli L, & Grave De Peralta R (2004) EEG Source Imaging. *Clin Neurophysiol*, 115(10): 2195–2222.
- Miller EK, Erickson CA, & Desimone R (1996) Neural Mechanisms of Visual Working Memory in Prefrontal Cortex of the Macaque. *J Neurosci*, 16(16): 5154–5167.
- Miller KJ, Schalk G, Hermes D, Ojemann JG, & Rao RPN (2016) Spontaneous Decoding of the Timing and Content of Human Object Perception From Cortical Surface Recordings Reveals Complementary Information in the Event-Related Potential and Broadband Spectral Change. *PLoS Comput Biol*, 12(1): e1004660.
- Miller KJ, Sorensen LB, Ojemann JG, & Den Nijs M (2009) Power-Law Scaling in the Brain Surface Electric Potential. *PLoS Comput Biol*, 5(12): e1000609.
- Mitchell AS, Baxter MG, & Gaffan D (2007a) Dissociable Performance on Scene Learning and Strategy Implementation After Lesions to Magnocellular Mediodorsal Thalamic Nucleus. *J Neurosci*, 27(44): 11888–11895.
- Mitchell JF, Sundberg KA, & Reynolds JH (2007b) Differential Attention-Dependent Response Modulation Across Cell Classes in Macaque Visual Area V4. *Neuron*, 55(1): 131–141.
- Miyawaki Y, Uchida H, Yamashita O, Sato M-A, Morito Y, Tanabe HC, ... Kamitani Y (2008) Visual Image Reconstruction From Human Brain Activity Using a Combination of Multiscale Local Image Decoders. *Neuron*, 60(5): 915–929.
- Moore T, & Armstrong KM (2003) Selective Gating of Visual Signals by Microstimulation of Frontal Cortex. *Nature*, 421(6921): 370–373.
- Moran D (2010) Evolution of Brain-Computer Interface: Action Potentials, Local Field Potentials and Electroencephalograms. *Curr Opin Neurobiol*, 20(6): 741–745.
- Motokawa K, Taira N, & Okuda J (1962) Spectral Responses of Single Units in the Primate Visual Cortex. *Tohoku J Exp Med*, 78(3): 320–337.
- Motter BC (1993) Focal Attention Produces Spatially Selective Processing in Visual Cortical Areas V1, V2, and V4 in the Presence of Competing Stimuli. *J Neurophysiol*, 70(3): 909–919.
- Mountcastle VB, Lynch JC, Georgopoulos A, Sakata H, & Acuna C (1975) Posterior Parietal Association Cortex of the Monkey: Command Functions for Operations Within Extrapersonal Space. *J Neurophysiol*, 38(4): 871–908.
- Müller NG, & Kleinschmidt A (2003) Dynamic Interaction of Object- and Space-Based Attention in Retinotopic Visual Areas. *J Neurosci*, 23(30): 9812–9816.

11. References

- Murguialday AR, Hill J, Bensch M, Martens S, Halder S, Nijboer F, ... Gharabaghi A (2011) Transition From the Locked in to the Completely Locked-In State: A Physiological Analysis. *Clin Neurophysiol*, 122(5): 925–933.
- Murphy MD, Guggenmos DJ, Bundy DT, & Nudo RJ (2016) Current Challenges Facing the Translation of Brain Computer Interfaces From Preclinical Trials to Use in Human Patients. *Front Cell Neurosci*, 9: 497.
- Murray SO (2008) The Effects of Spatial Attention in Early Human Visual Cortex Are Stimulus Independent. *J Vis*, 8(10): 2.
- Murray SO, Kersten D, Olshausen BA, Schrater P, & Woods DL (2002) Shape Perception Reduces Activity in Human Primary Visual Cortex. *Proc Natl Acad Sci U S A*, 99(23): 15164–15169.
- Murty DVPS, Shirhatti V, Ravishankar P, & Ray S (2018) Large Visual Stimuli Induce Two Distinct Gamma Oscillations in Primate Visual Cortex. *J Neurosci*, 38(11): 2730–2744.
- Nakanishi M, Wang Y, Wang Y-T, Mitsukura Y, & Jung T-P (2014) A High-Speed Brain Speller Using Steady-State Visual Evoked Potentials. *Int J Neural Syst*, 24(6): 1450019.
- Nassi JJ, & Callaway EM (2009) Parallel Processing Strategies of the Primate Visual System. *Nat Rev Neurosci*, 10(5): 360–372.
- Nauhaus I, Nielsen KJ, Disney AA, & Callaway EM (2012) Orthogonal Micro-Organization of Orientation and Spatial Frequency in Primate Primary Visual Cortex. *Nat Neurosci*, 15(12): 1683–1690.
- Newsome WT, & Stein-Aviles JA (1999) Nonhuman Primate Models of Visually Based Cognition. *ILAR J*, 40(2): 78–91.
- Ng J, Bharath AA, & Zhaoping L (2007) A Survey of Architecture and Function of the Primary Visual Cortex (V1). *EURASIP J Adv Signal Process*, 2007: 97961.
- Nicolas-Alonso LF, & Gomez-Gil J (2012) Brain Computer Interfaces, a Review. *Sensors*, 12(2): 1211–1279.
- Nicolelis MAL, Dimitrov D, Carmena JM, Crist R, Lehew G, Kralik JD, & Wise SP (2003) Chronic, Multisite, Multielectrode Recordings in Macaque Monkeys. *Proc Natl Acad Sci U S A*, 100(19): 11041–11046.
- Noudoost B, Chang MH, Steinmetz NA, & Moore T (2010) Top-Down Control of Visual Attention. *Curr Opin Neurobiol*, 20(2): 183–190.
- Nourski K V., Steinschneider M, Rhone AE, Oya H, Kawasaki H, Howard III MA, & McMurray B (2015) Sound Identification in Human Auditory Cortex: Differential Contribution of Local Field Potentials and High Gamma Power as Revealed by Direct Intracranial Recordings. *Brain Lang*, 148: 37–50.
- Nunez PL, Silberstein RB, Cadusch PJ, Wijesinghe RS, Westdorp AF, & Srinivasan R (1994) A Theoretical and Experimental Study of High Resolution EEG Based on Surface Laplacians and Cortical Imaging. *Electroencephalogr Clin Neurophysiol*, 90(1): 40–57.
- Nunez PL, & Srinivasan R (2006) *Electric Fields of the Brain. The Neurophysics of EEG*. (2nd ed.). Oxford, New York: Oxford University Press.
- Nurse ES, John SE, Freestone DR, Oxley TJ, Ung H, Berkovic SF, ... Grayden DB (2018) Consistency of Long-Term Subdural Electrocoricography in Humans. *IEEE Trans Biomed Eng*, 65(2): 344–352.
- Nuyujukian P, Sanabria JA, Saab J, Pandarinath C, Jarosiewicz B, Blabe CH, ... Henderson JM (2018) Cortical Control of a Tablet Computer by People With Paralysis. *PLoS One*, 13(11): e0204566.
- Okada K (2013) Is Omega Squared Less Biased? A Comparison of Three Major Effect Size Indices in One-Way Anova. *Behaviormetrika*, 40(2): 129–147.
- Okahara Y, Takano K, Nagao M, Kondo K, Iwadate Y, Birbaumer N, & Kansaku K (2018) Long-Term Use of a Neural Prosthesis in Progressive Paralysis. *Sci Rep*, 8: 16787.
- Ortner R, Aloise F, Prückl R, Schettini F, Putz V, Scharinger J, ... Guger C (2011) Accuracy of a P300 Speller for People With Motor Impairments: A Comparison. *Clin EEG Neurosci*, 42(4): 214–218.

11. References

- Palmer C, Cheng S-Y, & Seidemann E (2007) Linking Neuronal and Behavioral Performance in a Reaction-Time Visual Detection Task. *J Neurosci*, 27(30): 8122–8137.
- Palmini A (2006) The Concept of the Epileptogenic Zone: A Modern Look at Penfield and Jasper's Views on the Role of Interictal Spikes. *Epileptic Disord*, 8(Suppl. 2): S10–S15.
- Pan G, Li J-J, Qi Y, Yu H, Zhu J-M, Zheng X-X, ... Zhang S-M (2018) Rapid Decoding of Hand Gestures in Electrocorticography Using Recurrent Neural Networks. *Front Neurosci*, 12: 555.
- Pandarínath C, Nuyujukian P, Blabe CH, Sorice BL, Saab J, Willett FR, ... Henderson JM (2017) High Performance Communication by People With Paralysis Using an Intracortical Brain-Computer Interface. *Elife*, 6: e18554.
- Parkkonen L, Andersson J, Hämäläinen M, & Hari R (2008) Early Visual Brain Areas Reflect the Percept of an Ambiguous Scene. *Proc Natl Acad Sci U S A*, 105(51): 20500–20504.
- Parto Dezfouli M, Khamechian MB, Treue S, Esgehaei M, & Daliri MR (2018) Neural Activity Predicts Reaction in Primates Long Before a Behavioral Response. *Front Behav Neurosci*, 12: 207.
- Parvar H, Sculthorpe-Petley L, Satel J, Boshra R, D'Arcy RCN, & Trappenberg TP (2015) Detection of Event-Related Potentials in Individual Subjects Using Support Vector Machines. *Brain Informatics*, 2(1): 1–12.
- Parvizi J, & Kastner S (2018) Promises and Limitations of Human Intracranial Electroencephalography. *Nat Neurosci*, 21(4): 474–483.
- Patel SH, & Azzam PN (2005) Characterization of N200 and P300: Selected Studies of the Event-Related Potential. *Int J Med Sci*, 2(4): 147–154.
- Patterson JR, & Grabois M (1986) Locked-In Syndrome: A Review of 139 Cases. *Stroke*, 17(4): 758–764.
- Pels EGM, Aarnoutse EJ, Leinders S, Freudenburg Z V, Branco MP, Van Der Vijgh BH, ... Ramsey NF (2019) Stability of a Chronic Implanted Brain-Computer Interface in Late-Stage Amyotrophic Lateral Sclerosis. *Clin Neurophysiol*, 130(10): 1798–1803.
- Penfield W, & Jaspers H (1954) Electrocorticography. In: *Epilepsy and Functional Anatomy of the Human Brain*. Boston, MA: Little Brown.
- Peng X, & Van Essen DC (2005) Peaked Encoding of Relative Luminance in Macaque Areas V1 and V2. *J Neurophysiol*, 93(3): 1620–1632.
- Perry VH, Oehler R, & Cowey A (1984) Retinal Ganglion Cells That Project to the Dorsal Lateral Geniculate Nucleus in the Macaque Monkey. *Neuroscience*, 12(4): 1101–1123.
- Peter A, Uran C, Klon-Lipok J, Roese R, Van Stijn S, Barnes W, ... Vinck M (2019) Surface Color and Predictability Determine Contextual Modulation of V1 Firing and Gamma Oscillations. *Elife*, 8: e42101.
- Petersen SE, Robinson DL, & Morris JD (1987) Contributions of the Pulvinar to Visual Spatial Attention. *Neuropsychologia*, 25(1A): 97–105.
- Petro LS, Vizioli L, & Muckli L (2014) Contributions of Cortical Feedback to Sensory Processing in Primary Visual Cortex. *Front Psychol*, 5: 1223.
- Petroff OA, Spencer DD, Goncharova II, & Zaveri HP (2016) A Comparison of the Power Spectral Density of Scalp EEG and Subjacent Electrocorticograms. *Clin Neurophysiol*, 127(2): 1108–1112.
- Piccione F, Giorgi F, Tonin P, Priftis K, Giove S, Silvoni S, ... Beverina F (2006) P300-Based Brain Computer Interface: Reliability and Performance in Healthy and Paralyzed Participants. *Clin Neurophysiol*, 117(3): 531–537.
- Pinto Y, Van Der Leij AR, Sligte IG, Lamme VAF, & Scholte HS (2013) Bottom-Up and Top-Down Attention Are Independent. *J Vis*, 13(3): 16.
- Poggio GF, & Fischer B (1977) Binocular Interaction and Depth Sensitivity in Striate and Prestriate Cortex of Behaving Rhesus Monkey. *J Neurophysiol*, 40(6): 1392–1405.

11. References

- Polikov VS, Tresco PA, & Reichert WM (2005) Response of Brain Tissue to Chronically Implanted Neural Electrodes. *J Neurosci Methods*, 148(1): 1–18.
- Posner JB, Saper CB, Schiff ND, & Plum F (2007) *Diagnosis of Stupor and Coma*. (4th ed.). Oxford, New York: Oxford University Press.
- Posner MI (1980) Orienting of Attention. *Q J Exp Psychol*, 32(1): 3–25.
- Posner MI, & Gilbert CD (1999) Attention and Primary Visual Cortex. *Proc Natl Acad Sci U S A*, 96(6): 2585–2587.
- Pranti AS, Schander A, Bödecker A, & Lang W (2018) PEDOT: PSS Coating on Gold Microelectrodes With Excellent Stability and High Charge Injection Capacity for Chronic Neural Interfaces. *Sensors Actuators B Chem*, 275: 382–393.
- Prescott MJ, Howell VA, & Buchanan-Smith HM (2005) Training Laboratory-Housed Non-Human Primates, Part 2: Resources for Developing and Implementing Training Programmes. *Anim Technol Welf*, 4(3): 133–148.
- Prescott MJ, & Buchanan-Smith HM (2003) Training Nonhuman Primates Using Positive Reinforcement Techniques. *J Appl Anim Welf Sci*, 6(3): 157–161.
- Quian Quiroga R, & Panzeri S (2009) Extracting Information From Neuronal Populations: Information Theory and Decoding Approaches. *Nat Rev Neurosci*, 10(3): 173–185.
- Rabbani Q, Milsap G, & Crone NE (2019) The Potential for a Speech Brain–Computer Interface Using Chronic Electrooculography. *Neurotherapeutics*, 16(1): 144–165.
- Ragazzoni A, Grippo A, Tozzi F, & Zaccara G (2000) Event-Related Potentials in Patients With Total Locked-In State Due to Fulminant Guillain-Barré Syndrome. *Int J Psychophysiol*, 37(1): 99–109.
- Ramsey NF, Salari E, Aarnoutse EJ, Vansteensel MJ, Bleichner MG, & Freudenburg Z V (2018) Decoding Spoken Phonemes From Sensorimotor Cortex With High-Density ECoG Grids. *Neuroimage*, 180(Pt A): 301–311.
- Ray S, Crone NE, Niebur E, Franaszczuk PJ, & Hsiao SS (2008) Neural Correlates of High-Gamma Oscillations (60–200 Hz) in Macaque Local Field Potentials and Their Potential Implications in Electrooculography. *J Neurosci*, 28(45): 11526–11536.
- Reid RC, & Shapley RM (1992) Spatial Structure of Cone Inputs to Receptive Fields in Primate Lateral Geniculate Nucleus. *Nature*, 356(6371): 716–718.
- Reid RC, & Shapley RM (2002) Space and Time Maps of Cone Photoreceptor Signals in Macaque Lateral Geniculate Nucleus. *J Neurosci*, 22(14): 6158–6175.
- Reif PS, Strzelczyk A, & Rosenow F (2016) The History of Invasive EEG Evaluation in Epilepsy Patients. *Seizure*, 41: 191–195.
- Remington ED, Osmanski MS, & Wang X (2012) An Operant Conditioning Method for Studying Auditory Behaviors in Marmoset Monkeys. *PLoS One*, 7(10): e47895.
- Reynolds JH, Chelazzi L, & Desimone R (1999) Competitive Mechanisms Subserve Attention in Macaque Areas V2 and V4. *J Neurosci*, 19(5): 1736–1753.
- Rezeika A, Benda M, Stawicki P, Gemblar F, Saboor A, & Volosyak I (2018) Brain-Computer Interface Spellers: A Review. *Brain Sci*, 8(4): 57.
- Ringach DL, Shapley RM, & Hawken MJ (2002) Orientation Selectivity in Macaque V1: Diversity and Laminar Dependence. *J Neurosci*, 22(13): 5639–5651.
- Ritaccio AL, Brunner P, & Schalk G (2018) Electrical Stimulation Mapping of the Brain: Basic Principles and Emerging Alternatives. *J Clin Neurophysiol*, 35(2): 86–97.
- Rockland KS, & Pandya DN (1979) Laminar Origins and Terminations of Cortical Connections of the Occipital Lobe in the Rhesus Monkey. *Brain Res*, 179(1): 3–20.

11. References

- Roelfsema PR, & De Lange FP (2016) Early Visual Cortex as a Multiscale Cognitive Blackboard. *Annu Rev Vis Sci*, 2(1): 131–151.
- Roelfsema PR, Lamme VAF, & Spekreijse H (1998) Object-Based Attention in the Primary Visual Cortex of the Macaque Monkey. *Nature*, 395(6700): 376–381.
- Roelfsema PR, Tolboom M, & Khayat PS (2007) Different Processing Phases for Features, Figures, and Selective Attention in the Primary Visual Cortex. *Neuron*, 56(5): 785–792.
- Rogge J, Sherenco K, Malling R, Thiele E, Lambeth S, Schapiro S, & Williams L (2013) A Comparison of Positive Reinforcement Training Techniques in Owl and Squirrel Monkeys: Time Required to Train to Reliability. *J Appl Anim Welf Sci*, 16(3): 211–220.
- Rols G, Tallon-Baudry C, Girard P, Bertrand O, & Bullier J (2001) Cortical Mapping of Gamma Oscillations in Areas V1 and V4 of the Macaque Monkey. *Vis Neurosci*, 18(4): 527–540.
- Romanelli P, Piangerelli M, Ratel D, Gaude C, Costecalde T, Puttilli C, ... Torres N (2018) A Novel Neural Prosthesis Providing Long-Term Electroencephalography Recording and Cortical Stimulation for Epilepsy and Brain-Computer Interface. *J Neurosurg*, 130(4): 1166–1179.
- Romanski LM, Giguere M, Bates JF, & Goldman-Rakic PS (1997) Topographic Organization of Medial Pulvinar Connections With the Prefrontal Cortex in the Rhesus Monkey. *J Comp Neurol*, 379(3): 313–332.
- Rorie AE, Gao J, McClelland JL, & Newsome WT (2010) Integration of Sensory and Reward Information During Perceptual Decision-Making in Lateral Intraparietal Cortex (LIP) of the Macaque Monkey. *PLoS One*, 5(2): e9308.
- Rotermund D, Ernst UA, Mandon S, Taylor K, Smiyukha Y, Kreiter AK, & Pawelzik KR (2013) Toward High Performance, Weakly Invasive Brain Computer Interfaces Using Selective Visual Attention. *J Neurosci*, 33(14): 6001–6011.
- Rotermund D, Taylor K, Ernst UA, Kreiter AK, & Pawelzik KR (2009) Attention Improves Object Representation in Visual Cortical Field Potentials. *J Neurosci*, 29(32): 10120–10130.
- Rouse AG, Williams JJ, Wheeler JJ, & Moran DW (2016) Spatial Co-Adaptation of Cortical Control Columns in a Micro-ECoG Brain Computer Interface. *J Neural Eng*, 13(5): 056018.
- Rubehn B, Bosman C, Oostenveld R, Fries P, & Stieglitz T (2009) A MEMS-Based Flexible Multichannel ECoG-Electrode Array. *J Neural Eng*, 6(3): 036003.
- Saha S, Ahmed KI, Mostafa R, Khandoker AH, & Hadjileontiadis L (2017) Enhanced Inter-Subject Brain Computer Interface With Associative Sensorimotor Oscillations. *Health Technol Lett*, 4(1): 39–43.
- Saha S, & Baumert M (2020) Intra- and Inter-Subject Variability in EEG-Based Sensorimotor Brain Computer Interface: A Review. *Front Comput Neurosci*, 13: 87.
- Sauter-Starace F, Ratel D, Cretallaz C, Foerster M, Lambert A, Gaude C, ... Torres-Martinez N (2019) Long-Term Sheep Implantation of WIMAGINE®, a Wireless 64-Channel Electroencephalogram Recorder. *Front Neurosci*, 13: 847.
- Schalk G, & Leuthardt EC (2011) Brain-Computer Interfaces Using Electroencephalographic Signals. *IEEE Rev Biomed Eng*, 4: 140–154.
- Schalk G, Miller KJ, Anderson NR, Wilson JA, Smyth MD, Ojemann JG, ... Leuthardt EC (2008) Two-Dimensional Movement Control Using Electroencephalographic Signals in Humans. *J Neural Eng*, 5(1): 75–84.
- Schander A, Stokov S, Stemmann H, Teßmann T, Kreiter AK, & Lang W (2019) A Flexible 202-Channel Epidural ECoG Array With PEDOT: PSS Coated Electrodes for Chronic Recording of the Visual Cortex. *IEEE Sens J*, 19(3): 820–825.
- Schapiro SJ, Bloomsmith MA, & Laule GE (2003) Positive Reinforcement Training As a Technique to Alter Nonhuman Primate Behavior: Quantitative Assessments of Effectiveness *J Appl Anim Welf Sci*, 6(3): 175–187.

11. References

- Schendel AA, Nonte MW, Vokoun C, Richner TJ, Brodnick SK, Atry F, ... Williams JC (2014) The Effect of Micro-ECoG Substrate Footprint on the Meningeal Tissue Response. *J Neural Eng*, 11(4): 046011.
- Schendel AA, Thongpang S, Brodnick SK, Richner TJ, Lindevig BDB, Krugner-Higby L, & Williams JC (2013) A Cranial Window Imaging Method for Monitoring Vascular Growth Around Chronically Implanted Micro-ECoG Devices. *J Neurosci Methods*, 218(1): 121–130.
- Schiller PH (2010) Parallel Information Processing Channels Created in the Retina. *Proc Natl Acad Sci U S A*, 107(40): 17087–17094.
- Schira MM, Wade AR, & Tyler CW (2007) Two-Dimensional Mapping of the Central and Parafoveal Visual Field to Human Visual Cortex. *J Neurophysiol*, 97(6): 4284–4295.
- Schledde B, Galashan FO, Przybyla M, Kreiter AK, & Wegener D (2017) Task-Specific, Dimension-Based Attentional Shaping of Motion Processing in Monkey Area MT. *J Neurophysiol*, 118(3): 1542–1555.
- Schneider KA, & Kastner S (2009) Effects of Sustained Spatial Attention in the Human Lateral Geniculate Nucleus and Superior Colliculus. *J Neurosci*, 29(6): 1784–1795.
- Schroeder CE, Tenke CE, Givre SJ, Arezzo JC, & Vaughan Jr HG (1991) Striate Cortical Contribution to the Surface-Recorded Pattern-Reversal VEP in the Alert Monkey. *Vision Res*, 31(7–8): 1143–1157.
- Schwartz AB, Cui XT, Weber DJ, & Moran DW (2006) Brain-Controlled Interfaces: Movement Restoration With Neural Prosthetics. *Neuron*, 52(1): 205–220.
- Schwarz DA, Lebedev MA, Hanson TL, Dimitrov DF, Lehew G, Meloy J, ... Nicolelis MAL (2014) Chronic, Wireless Recordings of Large-Scale Brain Activity in Freely Moving Rhesus Monkeys. *Nat Methods*, 11(6): 670–676.
- Scott L, Pearce P, Fairhall S, Muggleton N, & Smith J (2003) Training Nonhuman Primates to Cooperate With Scientific Procedures in Applied Biomedical Research. *J Appl Anim Welf Sci*, 6(3): 199–207.
- Selemon LD, & Goldman-Rakic PS (1988) Common Cortical and Subcortical Targets of the Dorsolateral Prefrontal and Posterior Parietal Cortices in the Rhesus Monkey: Evidence for a Distributed Neural Network Subserving Spatially Guided Behavior. *J Neurosci*, 8(11): 4049–4068.
- Senden M, Emmerling TC, Van Hoof R, Frost MA, & Goebel R (2019) Reconstructing Imagined Letters From Early Visual Cortex Reveals Tight Topographic Correspondence Between Visual Mental Imagery and Perception. *Brain Struct Funct*, 224(3): 1167–1183.
- Shapley R, & Hawken MJ (2011) Color in the Cortex: Single- and Double-Oponent Cells. *Vision Res*, 51(7): 701–717.
- Sharma J, Sugihara H, Katz Y, Schummers J, Tenenbaum J, & Sur M (2015) Spatial Attention and Temporal Expectation Under Timed Uncertainty Predictably Modulate Neuronal Responses in Monkey V1. *Cereb Cortex*, 25(9): 2894–2906.
- Shichinohe N, Akao T, Kurkin S, Fukushima J, Kaneko CRS, & Fukushima K (2009) Memory and Decision Making in the Frontal Cortex During Visual Motion Processing for Smooth Pursuit Eye Movements. *Neuron*, 62(5): 717–732.
- Shimoda K, Nagasaka Y, Chao ZC, & Fujii N (2012) Decoding Continuous Three-Dimensional Hand Trajectories From Epidural Electrographic Signals in Japanese Macaques. *J Neural Eng*, 9(3): 036015.
- Shirhatti V, & Ray S (2018) Long-Wavelength (Reddish) Hues Induce Unusually Large Gamma Oscillations in the Primate Primary Visual Cortex. *Proc Natl Acad Sci U S A*, 115(17): 4489–4494.
- Shokouejad M, Park D-W, Jung YH, Brodnick SK, Novello J, Dingle A, ... Williams J (2019) Progress in the Field of Micro-Electrocorticography. *Micromachines*, 10(1): 62.
- Shulman GL, Sheehy JB, & Wilson J (1986) Gradients of Spatial Attention. *Acta Psychol*, 61(2): 167–181.
- Siegel M, Donner TH, & Engel AK (2012) Spectral Fingerprints of Large-Scale Neuronal Interactions. *Nat Rev Neurosci*, 13(2): 121–134.

11. References

- Sillay KA, Rutecki P, Cicora K, Worrell G, Drzakowski J, Shih JJ, ... Wingeier B (2013) Long-Term Measurement of Impedance in Chronically Implanted Depth and Subdural Electrodes During Responsive Neurostimulation in Humans. *Brain Stimul*, 6(5): 718–726.
- Silverman MS, Groszof DH, De Valois RL, & Elfar SD (1989) Spatial-Frequency Organization in Primate Striate Cortex. *Proc Natl Acad Sci U S A*, 86(2): 711–715.
- Sincich LC, & Horton JC (2005) The Circuitry of V1 and V2: Integration of Color, Form, and Motion. *Annu Rev Neurosci*, 28(1): 303–326.
- Slotnick SD (2013) The Nature of Attentional Modulation in V1. In: *Controversies in Cognitive Neuroscience*. Basingstoke, UK: Palgrave Macmillan.
- Slutzky MW, & Flint RD (2017) Physiological Properties of Brain-Machine Interface Input Signals. *J Neurophysiol*, 118(2): 1329–1343.
- Slutzky MW, Jordan LR, Krieg T, Chen M, Mogul DJ, & Miller LE (2010) Optimal Spacing of Surface Electrode Arrays for Brain-Machine Interface Applications. *J Neural Eng*, 7(2): 26004.
- Slutzky MW, Jordan LR, Lindberg EW, Lindsay KE, & Miller LE (2011) Decoding Rat Forelimb Movement Direction From Epidural and Intracortical Field Potentials. *J Neural Eng*, 8(3): 036013.
- Smith E, & Delargy M (2005) Locked-In Syndrome. *BMJ*, 330(7488): 406–409.
- Smith JJ, Hadzic V, Li X, Liu P, Day T, Utter A, ... Basso MA (2006) Objective Measures of Health and Well-Being in Laboratory Rhesus Monkeys (*Macaca mulatta*). *J Med Primatol*, 35(6): 388–396.
- Snyder LH, Batista AP, & Andersen RA (2000) Saccade-Related Activity in the Parietal Reach Region. *J Neurophysiol*, 83(2): 1099–1102.
- Somers DC, Dale AM, Seiffert AE, & Tootell RBH (1999) Functional MRI Reveals Spatially Specific Attentional Modulation in Human Primary Visual Cortex. *Proc Natl Acad Sci U S A*, 96(4): 1663–1668.
- Speier W, Fried I, & Pouratian N (2013) Improved P300 Speller Performance Using Electrocorticography, Spectral Features, and Natural Language Processing. *Clin Neurophysiol*, 124(7): 1321–1328.
- Sperling MR (1997) Clinical Challenges in Invasive Monitoring in Epilepsy Surgery. *Epilepsia*, 38(S4): S6–S12.
- Spillmann L (2014) Receptive Fields of Visual Neurons: The Early Years. *Perception*, 43(11): 1145–1176.
- Spillmann L, Dresch-Langley B, & Tseng C-H (2015) Beyond the Classical Receptive Field: The Effect of Contextual Stimuli. *J Vis*, 15(9): 7.
- Spüler M (2017) A High-Speed Brain-Computer Interface (BCI) Using Dry EEG Electrodes. *PLoS One*, 12(2): e0172400.
- Spüler M, Walter A, Ramos-Murguialday A, Naros G, Birbaumer N, Gharabaghi A, ... Bogdan M (2014) Decoding of Motor Intentions From Epidural ECoG Recordings in Severely Paralyzed Chronic Stroke Patients. *J Neural Eng*, 11(6): 066008.
- Spyropoulos G, Bosman CA, & Fries P (2018) A Theta Rhythm in Macaque Visual Cortex and Its Attentional Modulation. *Proc Natl Acad Sci U S A*, 115(24): E5614–E5623.
- Srinivasan R (1999) Methods to Improve Spatial Resolution of EEG. *Int J Bioelectromagn*, 1(1): 102–111.
- Staba RJ, Wilson CL, Bragin A, Fried I, & Engel Jr J (2002) Quantitative Analysis of High-Frequency Oscillations (80–500 Hz) Recorded in Human Epileptic Hippocampus and Entorhinal Cortex. *J Neurophysiol*, 88(4): 1743–1752.
- Stănişor L, Van Der Togt C, Pennartz CMA, & Roelfsema PR (2013) A Unified Selection Signal for Attention and Reward in Primary Visual Cortex. *Proc Natl Acad Sci U S A*, 110(22): 9136–9141.
- Strokov S, Schander A, Stemmann H, Teßmann T, Lang W, & Kreiter A (2017) A Flexible Multichannel ECoG Array With PEDOT-Coated Electrodes for Minimally Invasive Recording and Stimulation. *2017, IEEE SENSORS, Glasgow*, 1–3.

11. References

- Suner S, Fellows MR, Vargas-Irwin C, Nakata GK, & Donoghue JP (2005) Reliability of Signals From a Chronically Implanted, Silicon-Based Electrode Array in Non-Human Primate Primary Motor Cortex. *IEEE Trans Neural Syst Rehabil Eng*, 13(4): 524–541.
- Sung C-H, & Chuang J-Z (2010) The Cell Biology of Vision. *J Cell Biol*, 190(6): 953–963.
- Supèr H, & Roelfsema PR (2005) Chronic Multiunit Recordings in Behaving Animals: Advantages and Limitations. *Prog Brain Res*, 147: 263–282.
- Supèr H, Spekreijse H, & Lamme VAF (2001) A Neuronal Correlate of Working Memory in the Monkey Primary Visual Cortex. *Science*, 293(5527): 120–124.
- Sutton RS, & Barto AG (1998) *Reinforcement Learning*. Cambridge, MA: MIT Press.
- Szostak KM, Grand L, & Constantinou TG (2017) Neural Interfaces for Intracortical Recording: Requirements, Fabrication Methods, and Characteristics. *Front Neurosci*, 11: 665.
- Takaura K, Tsuchiya N, & Fujii N (2016) Frequency-Dependent Spatiotemporal Profiles of Visual Responses Recorded With Subdural ECoG Electrodes in Awake Monkeys: Differences Between High- and Low-Frequency Activity. *Neuroimage*, 124(Pt A): 557–572.
- Tankus A, Fried I, & Shoham S (2014) Cognitive-Motor Brain-Machine Interfaces. *J Physiol Paris*, 108(1): 38–44.
- Tarantino V, Cutini S, Mogentale C, & Bisiacchi PS (2013) Time-On-Task in Children With ADHD: An Ex-Gaussian Analysis. *J Int Neuropsychol Soc*, 19(7): 820–828.
- Tardif S, Bales K, Williams L, Moeller EL, Abbott D, Schultz-Darken N, ... Ruiz J (2006) Preparing New World Monkeys for Laboratory Research. *ILAR J*, 47(4): 307–315.
- Taylor K, Mandon S, Freiwald WA, & Kreiter AK (2005) Coherent Oscillatory Activity in Monkey Area V4 Predicts Successful Allocation of Attention. *Cereb Cortex*, 15(9): 1424–1437.
- Thiele A, Pooresmaeili A, Delicato LS, Herrero JL, & Roelfsema PR (2009) Additive Effects of Attention and Stimulus Contrast in Primary Visual Cortex. *Cereb Cortex*, 19(12): 2970–2981.
- Tolstosheeva E, Gordillo-González V, Biefeld V, Kempen L, Mandon S, Kreiter AK, & Lang W (2015) A Multi-Channel, Flex-Rigid ECoG Microelectrode Array for Visual Cortical Interfacing. *Sensors*, 15(1): 832–854.
- Tootell RBH, Hadjikhani N, Hall EK, Marrett S, Vanduffel W, Vaughan JT, & Dale AM (1998) The Retinotopy of Visual Spatial Attention. *Neuron*, 21(6): 1409–1422.
- Tootell RBH, Switkes E, Silverman MS, & Hamilton SL (1988) Functional Anatomy of Macaque Striate Cortex. II. Retinotopic Organization. *J Neurosci*, 8(5): 1531–1568.
- Torrence C, & Compo GP (1998) A Practical Guide to Wavelet Analysis. *Bull Am Meteorol Soc*, 79(1): 61–78.
- Torres Valderrama A, Oostenveld R, Vansteensel MJ, Huiskamp GM, & Ramsey NF (2010) Gain of the Human Dura in Vivo and Its Effects on Invasive Brain Signal Feature Detection. *J Neurosci Methods*, 187(2): 270–279.
- Treder MS, Bahramisharif A, Schmidt NM, Van Gerven MAJ, & Blankertz B (2011a) Brain-Computer Interfacing Using Modulations of Alpha Activity Induced by Covert Shifts of Attention. *J Neuroeng Rehabil*, 8: 24.
- Treder MS, Schmidt NM, & Blankertz B (2011b) Gaze-Independent Brain-Computer Interfaces Based on Covert Attention and Feature Attention. *J Neural Eng*, 8(6): 066003.
- Treue S, & Maunsell JHR (1996) Attentional Modulation of Visual Motion Processing in Cortical Areas MT and MST. *Nature*, 382(6591): 539–541.
- Tulip J, Zimmermann JB, Farningham D, & Jackson A (2017) An Automated System for Positive Reinforcement Training of Group-Housed Macaque Monkeys at Breeding and Research Facilities. *J Neurosci Methods*, 285: 6–18.

11. References

- Ungerleider LG, Galkin TW, & Mishkin M (1983) Visuotopic Organization of Projections From Striate Cortex to Inferior and Lateral Pulvinar in Rhesus Monkey. *J Comp Neurol*, 217(2): 137–157.
- Urigüen JA, & Garcia-Zapirain B (2015) EEG Artifact Removal – State-of-the-Art and Guidelines. *J Neural Eng*, 12(3): 031001.
- Usakli AB (2010) Improvement of EEG Signal Acquisition: An Electrical Aspect for State of the Art of Front End. *Comput Intell Neurosci*, 2010: 630649.
- Van Der Maaten L, & Hinton G (2008) Visualizing Data Using t-SNE *J Mach Learn Res*, 9: 2579–2605.
- Van Essen DC, Lewis JW, Drury HA, Hadjikhani N, Tootell RBH, Bakircioglu M, & Miller MI (2001) Mapping Visual Cortex in Monkeys and Humans Using Surface-Based Atlases. *Vision Res*, 41(10–11): 1359–1378.
- Van Gompel JJ, Worrell GA, Bell ML, Patrick TA, Cascino GD, Raffel C, ... Meyer FB (2008) Intracranial Electroencephalography With Subdural Grid Electrodes: Techniques, Complications, and Outcomes. *Neurosurgery*, 63(3): 498–505.
- Vansteensel MJ, Pels EGM, Bleichner MG, Branco MP, Denison T, Freudenburg Z V, ... Ramsey NF (2016) Fully Implanted Brain-Computer Interface in a Locked-In Patient With ALS. *N Engl J Med*, 375(21): 2060–2066.
- Varela F, Lachaux JP, Rodriguez E, & Martinerie J (2001) The Brainweb: Phase Synchronization and Large-Scale Integration. *Nat Rev Neurosci*, 2(4): 229–239.
- Vaughan Jr HG, Costa LD, & Gilden L (1966) The Functional Relation of Visual Evoked Response and Reaction Time to Stimulus Intensity. *Vision Res*, 6(12): 645–656.
- Vecera SP, & Farah MJ (1994) Does Visual Attention Select Objects or Locations? *J Exp Psychol Gen*, 123(2): 146–160.
- Velliste M, Perel S, Spalding MC, Whitford AS, & Schwartz AB (2008) Cortical Control of a Prosthetic Arm for Self-Feeding. *Nature*, 453(7198): 1098–1101.
- Vetter RJ, Williams JC, Hetke JF, Nunamaker EA, & Kipke DR (2004) Chronic Neural Recording Using Silicon-Substrate Microelectrode Arrays Implanted in Cerebral Cortex. *IEEE Trans Biomed Eng*, 51(6): 896–904.
- Vidyasagar TR (1998) Gating of Neuronal Responses in Macaque Primary Visual Cortex by an Attentional Spotlight. *Neuroreport*, 9(9): 1947–1952.
- Viventi J, Kim D-H, Vigeland L, Frechette ES, Blanco JA, Kim Y-S, ... Litt B (2011) Flexible, Foldable, Actively Multiplexed, High-Density Electrode Array for Mapping Brain Activity in Vivo. *Nat Neurosci*, 14(12): 1599–1605.
- Volkova K, Lebedev MA, Kaplan A, & Ossadtchi A (2019) Decoding Movement From Electrographic Activity: A Review. *Front Neuroinform*, 13: 74.
- Vomero M, Zucchini E, Delfino E, Gueli C, Mondragon NC, Carli S, ... Stieglitz T (2018) Glassy Carbon Electrographic Electrodes on Ultra-Thin and Finger-Like Polyimide Substrate: Performance Evaluation Based on Different Electrode Diameters. *Materials*, 11(12): 2486.
- Wachtler T, Sejnowski TJ, & Albright TD (2003) Representation of Color Stimuli in Awake Macaque Primary Visual Cortex. *Neuron*, 37(4): 681–691.
- Waldert S (2016) Invasive vs. Non-Invasive Neuronal Signals for Brain-Machine Interfaces: Will One Prevail? *Front Neurosci*, 10: 295.
- Waldert S, Pistohl T, Braun C, Ball T, Aertsen A, & Mehring C (2009) A Review on Directional Information in Neural Signals for Brain-Machine Interfaces. *J Physiol Paris*, 103(3–5): 244–254.
- Wandell BA, Dumoulin SO, & Brewer AA (2007) Visual Field Maps in Human Cortex. *Neuron*, 56(2): 366–383.
- Wang PT, King CE, McCrimmon CM, Lin JJ, Sazgar M, Hsu FPK, ... Nenadic Z (2016) Comparison of Decoding Resolution of Standard and High-Density Electrographic Electrodes. *J Neural Eng*, 13(2): 026016.

11. References

- Wang W-L, Li R, Ding J, Tao L, Li D-P, & Wang Y (2015) V1 Neurons Respond to Luminance Changes Faster Than Contrast Changes. *Sci Rep*, 5: 17173.
- Wang W, Collinger JL, Degenhart AD, Tyler-Kabara EC, Schwartz AB, Moran DW, ... Boninger ML (2013) An Electrocorticographic Brain Interface in an Individual With Tetraplegia. *PLoS One*, 8(2): e55344.
- Wang W, Degenhart AD, Collinger JL, Vinjamuri R, Sudre GP, Adelson PD, ... Weber DJ (2009) Human Motor Cortical Activity Recorded With Micro-ECoG Electrodes, During Individual Finger Movements. *Conf Proc 2009 Annu Int Conf IEEE Eng Med Biol Soc, 2009*: 586–589.
- Wang X, Gkogkidis CA, Iljina O, Fiederer LDJ, Henle C, Mader I, ... Ball T (2017) Mapping the Fine Structure of Cortical Activity With Different Micro-ECoG Electrode Array Geometries. *J Neural Eng*, 14(5): 056004.
- Wang Y, Gao X, Hong B, Jia C, & Gao S (2008) Brain-Computer Interfaces Based on Visual Evoked Potentials. *IEEE Eng Med Biol Mag*, 27(5): 64–71.
- Wang Y, Wang Y-T, & Jung T-P (2010) Visual Stimulus Design for High-Rate SSVEP BCI. *Electron Lett*, 46(15): 1057–1058.
- Wässle H (2004) Parallel Processing in the Mammalian Retina. *Nat Rev Neurosci*, 5(10): 747–757.
- Wässle H, Grünert U, Röhrenbeck J, & Boycott BB (1990) Retinal Ganglion Cell Density and Cortical Magnification Factor in the Primate. *Vision Res*, 30(11): 1897–1911.
- Watanabe K, & Funahashi S (2015) A Dual-Task Paradigm for Behavioral and Neurobiological Studies in Nonhuman Primates. *J Neurosci Methods*, 246: 1–12.
- Watanabe M, & Sakagami M (2007) Integration of Cognitive and Motivational Context Information in the Primate Prefrontal Cortex. *Cereb Cortex*, 17(Suppl 1): i101–i109.
- Wegener D, Ehn F, Aurich MK, Galashan FO, & Kreiter AK (2008) Feature-Based Attention and the Suppression of Non-Relevant Object Features. *Vision Res*, 48(27): 2696–2707.
- Wegener D, Freiwald WA, & Kreiter AK (2004) The Influence of Sustained Selective Attention on Stimulus Selectivity in Macaque Visual Area MT. *J Neurosci*, 24(27): 6106–6114.
- Wei Q, Fei M, Wang Y, Gao X, & Gao S (2007) Feature Combination for Classifying Single-Trial ECoG During Motor Imagery of Different Sessions. *Prog Nat Sci*, 17(7): 851–858.
- Wei Q, Lu Z, Chen K, & Ma Y (2010) Channel Selection for Optimizing Feature Extraction in an Electrocorticogram-Based Brain-Computer Interface. *J Clin Neurophysiol*, 27(5): 321–327.
- Westlund K (2015) Training Laboratory Primates – Benefits and Techniques. *Primate Biol*, 2: 119–132.
- Wiesel TN, & Hubel DH (1966) Spatial and Chromatic Interactions in the Lateral Geniculate Body of the Rhesus Monkey. *J Neurophysiol*, 29(6): 1115–1156.
- Williams JC, Rennaker RL, & Kipke DR (1999) Long-Term Neural Recording Characteristics of Wire Microelectrode Arrays Implanted in Cerebral Cortex. *Brain Res Protoc*, 4(3): 303–313.
- Wodlinger B, Downey JE, Tyler-Kabara EC, Schwartz AB, Boninger ML, & Collinger JL (2015) Ten-Dimensional Anthropomorphic Arm Control in a Human Brain-Machine Interface: Difficulties, Solutions, and Limitations. *J Neural Eng*, 12(1): 016011.
- Wolpaw JR, Birbaumer N, McFarland DJ, Pfurtscheller G, & Vaughan TM (2002) Brain-Computer Interfaces for Communication and Control. *Clin Neurophysiol*, 113(6): 767–791.
- Won D-O, Hwang H-J, Kim D-M, Müller K-R, & Lee S-W (2018) Motion-Based Rapid Serial Visual Presentation for Gaze-Independent Brain-Computer Interfaces. *IEEE Trans Neural Syst Rehabil Eng*, 26(2): 334–343.
- Woodman GF (2010) A Brief Introduction to the Use of Event-Related Potentials (ERPs) in Studies of Perception and Attention. *Atten Percept Psychophys*, 72(8): 2031–2046.

11. References

- Wurtz RH (1969) Visual Receptive Fields of Striate Cortex Neurons in Awake Monkeys. *J Neurophysiol*, 32(5): 727–742.
- Xiao Y, Casti A, Xiao J, & Kaplan E (2007) Hue Maps in Primate Striate Cortex. *Neuroimage*, 35(2): 771–786.
- Xing D, Yeh C-I, Gordon J, & Shapley RM (2014) Cortical Brightness Adaptation When Darkness and Brightness Produce Different Dynamical States in the Visual Cortex. *Proc Natl Acad Sci U S A*, 111(3): 1210–1215.
- Xing D, Yeh C-I, & Shapley RM (2009) Spatial Spread of the Local Field Potential and Its Laminar Variation in Visual Cortex. *J Neurosci*, 29(37): 11540–11549.
- Xing X, Wang Y, Pei W, Guo X, Liu Z, Wang F, ... Chen H (2018) A High-Speed SSVEP-Based BCI Using Dry EEG Electrodes. *Sci Rep*, 8: 14708.
- Yabuta NH, Sawatari A, & Callaway EM (2001) Two Functional Channels From Primary Visual Cortex to Dorsal Visual Cortical Areas. *Science*, 292(5515): 297–300.
- Yanagisawa T, Hirata M, Saitoh Y, Goto T, Kishima H, Fukuma R, ... Yoshimine T (2011) Real-Time Control of a Prosthetic Hand Using Human Electrocorticography Signals. *J Neurosurg*, 114(6): 1715–1722.
- Yanagisawa T, Hirata M, Saitoh Y, Kato A, Shibuya D, Kamitani Y, & Yoshimine T (2009) Neural Decoding Using Gyral and Intralcal Electroencephalograms. *Neuroimage*, 45(4): 1099–1106.
- Yang T, Hakimian S, & Schwartz TH (2014) Intraoperative ElectroCorticoGraphy (ECog): Indications, Techniques, and Utility in Epilepsy Surgery. *Epileptic Disord*, 16(3): 271–279.
- Yao Z, Ma X, Wang Y, Zhang X, Liu M, Pei W, & Chen H (2018) High-Speed Spelling in Virtual Reality With Sequential Hybrid BCIs. *IEICE Trans Inf Syst*, E101-D(11): 2859–2862.
- Yau K-W, & Hardie RC (2009) Phototransduction Motifs and Variations. *Cell*, 139(2): 246–264.
- Yeom S-K, Fazli S, Müller K-R, & Lee S-W (2014) An Efficient ERP-Based Brain-Computer Interface Using Random Set Presentation and Face Familiarity. *PLoS One*, 9(11): e111157.
- Yin E, Zhou Z, Jiang J, Chen F, Liu Y, & Hu D (2013) A Novel Hybrid BCI Speller Based on the Incorporation of SSVEP Into the P300 Paradigm. *J Neural Eng*, 10(2): 026012.
- Yoshor D, Bosking WH, Ghose GM, & Maunsell JHR (2007a) Receptive Fields in Human Visual Cortex Mapped With Surface Electrodes. *Cereb Cortex*, 17(10): 2293–2302.
- Yoshor D, Ghose GM, Bosking WH, Sun P, & Maunsell JHR (2007b) Spatial Attention Does Not Strongly Modulate Neuronal Responses in Early Human Visual Cortex. *J Neurosci*, 27(48): 13205–13209.
- Zhang D, Maye A, Gao X, Hong B, Engel AK, & Gao S (2010) An Independent Brain-Computer Interface Using Covert Non-Spatial Visual Selective Attention. *J Neural Eng*, 7(1): 16010.
- Zhang D, Song H, Xu R, Zhou W, Ling Z, & Hong B (2013) Toward a Minimally Invasive Brain-Computer Interface Using a Single Subdural Channel: A Visual Speller Study. *Neuroimage*, 71: 30–41.
- Zhang J, Nguyen T, Cogill S, Bhatti A, Luo L, Yang S, & Nahavandi S (2018) A Review on Cluster Estimation Methods and Their Application to Neural Spike Data. *J Neural Eng*, 15(3): 031003.
- Zhang X, Zhaoping L, Zhou T, & Fang F (2012) Neural Activities in V1 Create a Bottom-Up Saliency Map. *Neuron*, 73(1): 183–192.
- Zhou H, Schafer RJ, & Desimone R (2016) Pulvinar-Cortex Interactions in Vision and Attention. *Neuron*, 89(1): 209–220.

12. Appendix

12.1 Abbreviations

AI	–	Attention index
ALS	–	Amyotrophic lateral sclerosis
AUC	–	Area under the curve
BCI	–	Brain-computer interface
BGP	–	Broadband γ -power
BOLD	–	Blood oxygenation level dependent
C1	–	First visual component of the ERP in the EEG
CC	–	Contrast change
cLIS	–	Classic locked-in syndrome
c-VEP	–	Pseudo-random code modulated VEP
deg	–	Degree of visual angle
dIPFC	–	Dorsolateral prefrontal cortex
dva	–	Degree of visual angle
ECOG	–	Electrocorticography
EEG	–	Electroencephalogram
EFP	–	Epidural field potential
ERF	–	Epidural field potential receptive field
ERP	–	Event-related potential

12.1 Abbreviations

FEF	–	Frontal eye fields
fMRI	–	Functional magnet resonance imaging
FS	–	Fixation square/spot
f-VEP	–	Frequency modulated VEP
HGP	–	High γ -power
iLIS	–	Incomplete locked-in syndrome
ITI	–	Inter-trial interval
ITR	–	Information transfer rate
IQR	–	Inter-quantile range
LCA	–	Luminance change area
LFP	–	Local field potential
LGN	–	Lateral geniculate nucleus
LIP	–	Lateral intraparietal cortex
LIS	–	Locked-in syndrome
MUA	–	Multi unit activity
MEG	–	Magnetoencephalography
MT	–	Middle temporal visual area
N1	–	First negative peak of the ERP
N2	–	Second negative peak of the ERP
NB-PRT	–	Non-binary positive reinforcement training
P1	–	First positive peak of the ERP
PEDOT:PSS	–	Poly(3,4-ethylenedioxythiophene): polystyrene sulfonate
PCA	–	Principle component analysis
PFC	–	Prefrontal cortex

12.1 Abbreviations

PPC	–	Posterior parietal cortex
PRT	–	Positive reinforcement training
RF	–	Receptive field
ROC	–	Receiver-operator characteristic
RT	–	Reaction time / Response time
SC	–	Superior colliculus
SBR	–	Signal-to-background ratio
SD	–	Standard deviation
SE	–	Standard error
SSVEP	–	Steady state visual evoked potential
SUA	–	Single unit activity
SVM	–	Support vector machine
tLIS	–	Total (or complete) locked-in syndrome
t-SNE	–	<i>t</i> -Distributed stochastic neighborhood embedding
t-VEP	–	Time modulated VEP
VEP	–	Visual evoked potential
V1	–	Primary visual cortex
V2	–	Secondary visual cortex
V4	–	Fourth visual area/cortex

12.2 Danksagungen

Als erstes möchte ich meinem Betreuer und Doktorvater Dr. Detlef Wegener danken, der dieses Projekt initiiert hat. Ich danke dir für deine Betreuung. Danke, dass ich mit allen Anliegen zu dir kommen konnte! Danke für all die Gespräche, Diskussionen, innovativen Denkanstöße und die vielfältige Unterstützung.

Danke auch an Prof. Dr. Andreas Kreiter, in dessen Institut ich meine Promotion durchführen durfte. Danke für die Zeit, die Sie sich für mich genommen haben! Danke für all die guten Anregungen und Diskussionen.

Danke an meinen Zweitgutachter Prof. Dr. Michael Koch.

Ich danke der Studienstiftung für ihre finanzielle Unterstützung und die guten Seminare und Workshops, die ich besuchen durfte. Besonderer Dank gilt meinem direkten Ansprechpartner Herrn Antes, der sich immer gewissenhaft um meine Fragen und Anliegen gekümmert hat.

Danke Peter, Katja, Dieter, Maik, Rama und Katrin für die gute Zusammenarbeit im Labor und im Stall und für all die handwerkliche, pflegerische und administrative Unterstützung.

Constantin, I am thankful for your very detailed view. Thanks for the fruitful discussions about computational methods and algorithms. Danke auch dir, Lara, für deine Unterstützung.

Danke an meine Familie und alle Freunde, die mich ge- und ertragen haben, vor allem in den letzten Monaten.

Danke an all die Personen, die die vorläufige Versionen meiner Dissertation gelesen und mir Feedback gegeben haben: Lukas, Eric, Mario, Eben, Jorit und Mama.

Ganz besonderer Dank gilt meiner wunderbaren Frau Angi. Du hast mich die ganze Zeit der Promotion begleitet: Über die Höhenflüge, die du miterlebt und mitgefeiert hast, bis zu den frustrierenden Tiefen, aus denen du mich oft mit deiner Zuversicht und deiner Ermutigung herausgeholt hast. Danke, dass du mir in den letzten Monaten den Rücken freigehalten hast, mein Geschenk!

Versicherung an Eides Statt

Ort, Datum: _____

Versicherung an Eides Statt

Ich, Benjamin Fischer,

versichere an Eides Statt durch meine Unterschrift, dass ich die vorstehende Arbeit selbständig und ohne fremde Hilfe angefertigt und alle Stellen, die ich wörtlich dem Sinne nach aus Veröffentlichungen entnommen habe, als solche kenntlich gemacht habe, mich auch keiner anderen als der angegebenen Literatur oder sonstiger Hilfsmittel bedient habe.

Ich versichere an Eides Statt, dass ich die vorgenannten Angaben nach bestem Wissen und Gewissen gemacht habe und dass die Angaben der Wahrheit entsprechen und ich nichts verschwiegen habe.

Die Strafbarkeit einer falschen eidesstattlichen Versicherung ist mir bekannt, namentlich die Strafandrohung gemäß § 156 StGB bis zu drei Jahren Freiheitsstrafe oder Geldstrafe bei vorsätzlicher Begehung der Tat bzw. gemäß § 161 Abs. 1 StGB bis zu einem Jahr Freiheitsstrafe oder Geldstrafe bei fahrlässiger Begehung.

Unterschrift

Erklärungen zur elektronischen Version und zur Überprüfung einer Dissertation

Ort, Datum: _____

Erklärungen zur elektronischen Version und zur Überprüfung einer Dissertation

Hiermit bestätige ich gemäß § 7, Abs. 7, Punkt 4, dass die zu Prüfungszwecken beigelegte elektronische Version meiner Dissertation identisch ist mit der abgegebenen gedruckten Version.

Ich bin mit der Überprüfung meiner Dissertation gemäß § 6 Abs. 2, Punkt 5 mit qualifizierter Software im Rahmen der Untersuchung von Plagiatsvorwürfen einverstanden.

Unterschrift

Hinweis über den Umfang der Überarbeitung der Dissertation

Diese Dissertation wurde in überarbeiteter Form veröffentlicht. Im Zuge der Überarbeitung wurden einzelne formale Details bearbeitet (z.B. wurde das Datum des Dissertationskolloquiums hinzugefügt) und ein Satz in der Einleitung (Chapter 3) wurde abgeändert.